

Microporous Catalysts for Direct Methane Oxidation to Oxygenates by using H₂O₂ as Oxidant

Von der Fakultät Chemie der Universität Stuttgart
zur Erlangung der Würde eines Doktors der Naturwissenschaften (Dr. rer. nat.)
genehmigte Abhandlung

vorgelegt von
Caiyun Xu
aus Hubei, China

Hauptberichter: Prof. Dr.-Ing. Elias Klemm
Mitberichter: Jun.-Prof. Dr. rer. nat. Deven Estes
Prüfungsvorsitzender: Prof. Dr. rer. nat. Bernhard Hauer

Tag der mündlichen Prüfung: 21.07.2022

Institut für Technische Chemie der Universität Stuttgart
2022

Erklärung über die Eigenständigkeit der Dissertation

Ich versichere, dass ich die vorliegende Arbeit mit dem Titel

“Microporous Catalysts for Direct Methane Oxidation to Oxygenates by using H₂O₂ as Oxidant”

selbständig verfasst und keine anderen als die angegebenen Quellen und Hilfsmittel benutzt habe; aus fremden Quellen entnommene Passagen und Gedanken sind als solche kenntlich gemacht.

Declaration of Authorship

I hereby certify that the dissertation entitled

“Microporous Catalysts for Direct Methane Oxidation to Oxygenates by using H₂O₂ as Oxidant”

is entirely my own work except where otherwise indicated. Passages and ideas from other sources have been clearly indicated.

Name/Name: _____

Unterschrift/Signed: _____

Datum/Date: _____

Acknowledgements

My study in Germany will soon come to an end after the completion of my Ph.D. thesis. I wish to express my sincere appreciation to all those who have offered me invaluable help during the four years of my Ph.D. study here at the Institute of Technical Chemistry (ITC), University of Stuttgart.

First of all, I shall extend my deepest gratitude to my country for offering me a scholarship that provides me the opportunity to study abroad. This experience enriches my knowledge, improves my academic abilities, and expands my horizons.

Secondly, special acknowledgment is given to Prof. Dr.-ing Elias Klemm, my supervisor. He has given me great instructions and encouragements during my study. Especially, he has walked me through all the stages of the writing of this thesis, improving the outline and the argumentation, and correcting the grammatical errors. The thesis could not be finished without his patient guidance. Besides my supervisor, I have benefited a lot from many other professors in ITC, including Dr. Michael Dyballa, Jun.-Prof. Dr. Deven Estes, Apl. Prof. Dr. Michael Hunger, and Frau Apl. Prof. Yvonne Traa. They are very friendly and very professional in scientific research. They have offered me numerous valuable comments and suggestions with incomparable patience and broadened the scope of my knowledge in various fields of literature. The profit that I gained from them will be of everlasting significance to my future research. What is more, I would like to present my thanks to Jun.-Prof. Dr. Deven Estes as the co-reviewer of my thesis and Prof. Bernhard Hauer as the chair of the PhD examination board. Also, I owe many thanks to all the technicians, Heike Fingerle, Barbara Gehring, Dipl.-Ing. (FH) Ines Lauerwald, Ingo Nägele, Andreas Stieber, and Nagme Merdanoglu, who helped me a lot in my experimental set-up and characterizations in my thesis. My thanks also go to my colleagues, Michael Benz, Ann-Katrin Beurer, Osman Bunjaku, Daniel Dittmann, Joachim Hildebrand, Dorothea Häussermann, Zheng Li, Hang Liu, Dr. Ing. Carlos Lobo, Andrea Loi, Sarah Maier, Hoang-Huy Nguyen, Carolin Rieg, Jan Florenski, Maximilian Schmidt, Dr. Qian Song, Marvin Oßkopp, Faeze Tari, Erik Wimmer, and my friends Dr. Junli Xu, Peiwen Wang, Shujin, Hou, Dr.-ing. Hualiang Zuo, Dr. Liu Yang.

Last but not least, I would like to express my thanks to my beloved parents (Xiaoping Wang & Jiayi Xu), my brother (Ruifeng Xu), and my grandmother (Mingying An) for their unfailing love and support. For so many years, they have always been supporting me and respecting me. Their love and care are the greatest fortunes of my life. In particular, I want to express my thanks to my husband Hang Liu, whose name already appeared in the Acknowledgements part of my master

thesis as my boyfriend. Thanks to him for cooking during our life in Germany, we can work hard without being hungry and successfully complete our studies.

Contents

Acknowledgements	I
Contents.....	III
Abbreviations	VII
Abstract	IX
Zusammenfassung.....	XIII
1. State of the art	1
1.1 Introduction.....	1
1.1.1 Conversion of methane to value-added chemicals.....	1
1.1.2 Direct methane conversion to methanol	3
1.2 Direct methane oxidation to methanol (DMTM) with different oxidants	7
1.2.1 N ₂ O as oxidant.....	7
1.2.2 O ₂ as oxidant	9
1.2.3 H ₂ O as oxidant or co-oxidant.....	11
1.3 Direct methane oxidation using H ₂ O ₂ over solid catalysts	13
1.3.1 Nobel metal based catalysts	14
1.3.1.1 AuPd active sites.....	14
1.3.1.2 Single-atom noble metal catalyst (Pd, Rh)	16
1.3.2 Non-noble metal based catalysts	18
1.4 Zeolites for direct methane oxidation with H ₂ O ₂ as oxidant.....	22
1.4.1 Introduction to zeolites	23
1.4.2 Fe/ZSM-5 as catalyst	25
1.4.2.1 Identification of binuclear Fe as active site in Fe/ZSM-5	25
1.4.2.2 Identification of mononuclear Fe as active site in Fe/ZSM-5.....	28
1.4.3 Fe/MOR as catalyst.....	30
1.5. MOFs for direct methane oxidation with H ₂ O ₂ as oxidant.....	31
1.5.1 Introduction to MOFs.....	32
1.5.2 Key Elements of MOFs.....	32
1.5.2.1 Metal nodes and organic bridging ligands	32
1.5.2.2 Flexible structure and topology.....	33
1.5.2.3 Crystalline nature	34
1.5.2.4 Open framework with permanent porosity	34
1.5.3 Advantages of MOFs in Catalysis.....	35
1.5.3.1 Ultrahigh surface area and porosity.....	35
1.5.3.2 Diverse active sites	35
1.5.4 MOFs for direct methane oxidation	37
1.5.4.1 Fe/MIL-53 for methane oxidation by H ₂ O ₂	38
1.5.4.2 Fe/UiO-66 for methane oxidation by H ₂ O ₂	41
1.6 Comparison of state-of-the-art catalysts for direct methane oxidation with H ₂ O ₂ as oxidant.....	42
2. Motivation and objectives	45
3. Experimental methods.....	47

3.1 Chemicals.....	47
3.2 Experimental set-up	48
3.3 The self-decomposition of H ₂ O ₂	49
3.4 The decomposition of organic oxidant TBHP	52
3.5 The calculation of reactor volume.....	53
3.6 Procedure of the catalytic experiments	54
3.7 Analysis of products.....	54
3.7.1 Gas phase analysis	54
3.7.2 Liquid phase analysis	55
3.7.3 H ₂ O ₂ quantification.....	55
3.7.4 The calculation of the performance indicators	56
3.7.5 Proposed reaction scheme in Fe/H ₂ O ₂ -based heterogeneous system.	56
3.8 Characterization of the catalysts.....	57
3.8.1 X-Ray Diffraction.....	57
3.8.2 Chemical Analysis	57
3.8.3 Scanning Electron Microscopy.....	57
3.8.4 Transmission Electron Microscopy.....	58
3.8.5 Nuclear Magnetic Resonance spectroscopy.....	58
3.8.6 Solid state ²⁷ Al MAS NMR measurements.....	58
3.8.7 Pyridine-adsorbed Fourier Transform Infrared Spectroscopy (Py-FTIR)	58
3.8.8 Argon Physisorption	59
3.8.9 ⁵⁷ Fe Mössbauer spectroscopy	59
3.8.10 Diffuse reflectance Ultraviolet-Visible spectroscopy	60
3.8.11 X-ray absorption spectra	60
4. Direct methane oxidation over different MOF catalysts by H ₂ O ₂	61
4.1 CAU-10.....	62
4.1.1 Catalyst design.....	62
4.1.2 Synthesis method	64
4.1.2.1 Synthesis of CAU-10-H and CAU-10-Py.....	64
4.1.2.2 Metal loading of CAU-10-H and CAU-10-Py	64
4.1.3 XRD characterization and activity tests	65
4.2 MOF-74.....	67
4.2.1 Catalyst design.....	67
4.2.2 Synthesis method	68
4.2.3 XRD characterization and activity tests	69
4.3 MIL-100 and MIL-96	71
4.3.1 Catalyst design.....	71
4.3.2 Synthesis method	73
4.3.2.1 Synthesis of MIL-100(Al).....	73
4.3.2.2 Metal loading of MIL-100(Al).....	73
4.3.2.3 Synthesis of MIL-96(Al).....	74
4.3.2.4 Metal loading of MIL-96(Al).....	74
4.3.3 XRD characterization and activity tests	75
4.4 DUT-5.....	77

4.4.1 Catalyst design.....	78
4.4.2 Synthesis method	79
4.4.2.1 Synthesis of DUT-5 and DUT-5-SO ₂	79
4.4.2.2 Metal loading by post-synthesis modification	79
4.4.2.3 Metal loading by direct-synthesis modification	80
4.4.3 XRD characterization and activity test	80
4.5 UiO-66.....	82
4.5.1 Catalyst design.....	82
4.5.2 Synthesis method	83
4.5.2.1 Synthesis of UiO-66	83
4.5.2.2 Metal loading by post-synthetic modification	83
4.5.2.3 Metal loading by direct synthetic modification	84
4.5.2.4 Calcination of Fe/UiO-66	84
4.5.3 XRD characterization and activity tests.....	84
4.6 ZIF-8.....	86
4.6.1 Catalyst design.....	86
4.6.2 Synthesis method	87
4.6.2.1 Synthesis of ZIF-8.....	87
4.6.2.2 In situ synthesis of the ZIF-8 complex host-guest system	87
4.6.2.3 Calcination of the as-synthesized catalysts	88
4.6.3 XRD characterization and activity tests.....	88
4.7 PCN-250.....	90
4.7.1 Catalyst design.....	90
4.7.2 Synthesis method	91
4.7.2.1 Preparation of preformed clusters.....	91
4.7.2.2 Synthesis of PCN-250.....	91
4.7.3 XRD characterization and activity tests.....	92
4.8 Summary	93
5. Direct methane oxidation over Fe/MOR catalysts by H ₂ O ₂	97
5.1 Investigation of different zeolites	97
5.1.1 Preparation method	97
5.1.2 Investigation of the activity.....	98
5.2 Investigation of different metals.....	99
5.2.1 Preparation method	100
5.2.2 Investigation of the activity.....	100
5.2.3 Investigation of the selectivity	101
5.3 Variation of the preparation protocol of Fe/MOR	102
5.3.1 Calcination temperature	103
5.3.1.1 Preparation method	103
5.3.1.2 Investigation of the activity.....	103
5.3.2 Different MOR starting samples.....	104
5.3.2.1 Preparation method	105
5.3.2.2 Investigation of the activity.....	105
5.3.3 Different preparation methods for metal loading	106

5.3.3.1	Preparation method	106
5.3.3.2	Investigation of the activity	108
5.3.3.3	Catalyst characterizations.....	109
5.4	Fe/MOR with different iron loading	111
5.4.1	Preparation method	111
5.4.2	Investigation of the activity	112
5.4.3	Catalyst characterizations	113
5.4.3.1	UV-vis diffuse-reflectance spectroscopy (UV-vis DRS)	113
5.4.3.2	X-ray absorption spectroscopy analysis	115
5.5	PDMS coating of Fe/MOR.....	118
5.5.1	Preparation method	119
5.5.2	Investigation of the activity	120
5.6	Summary.....	121
6.	Direct methane oxidation over Fe/MFI nanosheet catalysts by H ₂ O ₂	123
6.1	Motivation	123
6.2	Synthesis methods.....	128
6.2.1	Synthesis of organic surfactant C ₂₂₋₆₋₆ Br ₂	128
6.2.2	Synthesis of MFI-nanosheet zeolite	129
6.2.3	Fe loading on MFI nanosheets and 3D ZSM-5 zeolite	129
6.2.3.1	Fe loading on MFI nanosheets and 3D ZSM-5 by post-modification.....	129
6.2.3.2	Fe loading on MFI nanosheets by direct modification	130
6.2.4	Pillaring of multilamellar MFI nanosheets.....	131
6.3	Characterizations of 2D MFI nanosheets	131
6.3.1	ICP results	131
6.3.2	SEM and TEM images	133
6.3.3	XRD	134
6.3.4	Physical adsorption.....	135
6.4	Investigation of the activity	135
6.4.1	Catalytic activity of Fe/MFI-nanosheet-550(post) catalysts.....	135
6.4.2	Catalytic activity of Fe/MFI-nanosheet-550(direct) catalysts	136
6.5	Characterizations of catalysts.....	138
6.5.1	XAS analysis	138
6.5.2	UV-vis analysis	140
6.5.3	Solid state ²⁷ Al-MAS-NMR spectroscopy	141
6.5.4	Py-FTIR analysis	142
6.6	Summary.....	144
7.	Conclusion	147
8.	Reference	149

Abbreviations

ALD	Atomic layer deposition	OMSs	Open metal sites
AIM	atomic layer deposition	PCN	Porous Coordination Network
AA	Acetic acid	PSE	Post synthetic exchange
BET	Brunauer-Emmett-Teller	PSM	Post synthetic modification
BAS	Brønsted acid site	pMMO	particulate Methane monooxygenase
CB	Conduction band	POM	Partial oxidation of methane
CVI	Chemical vapour impregnation	PCPs	Porous coordination polymers
CVD	Chemical vapor deposition	PSP	Pore space partition
CUSs	Coordinatively unsaturated metal sites	STEM	Scanning transmission electron microscopy
CNT	Carbon nanotubes	ST	Super tetrahedra
CCP	Cubic close packed	SRM	Steam reforming of methane
CSD	Cambridge Structural Database	sMMO	soluble Methane monooxygenase
DR	Diffuse reflectance	SAC	Single atom catalysis
DRM	Dry reforming of methane	SAs	Single atoms
DRIFTS	Diffuse reflectance infrared Fourier transform spectroscopy	SSIE	Solid state ion-exchange
DMTM	Direct methane to methanol	SBU _s	Secondary building units
DFT	Density functional theory	SC-XRD	Single Crystal-X ray diffraction
EPR	Electron paramagnetic resonance	SALI	Solvent-assisted ligand incorporation
EXAFS	Extended X-ray absorption fine structure	SBU _s	secondary building units
GHG	Greenhouse gas	TOF-MS	Time-of-flight mass spectrometer
HAADF- STEM	High-angle annular dark-field scanning transmission electron microscopy	TOF	Turnover frequency
HSAB	Hard-Soft-Acid-Base	TFA	trifluoroacetic acid
IE	Ion-exchange	T	Tetrahedral
ICP-MS	Inductively coupled plasma mass spectrometry	TPR	Temperature-programmed reduction
IZA	International Zeolite Association	UV-vis	Ultraviolet-visible

IWI	Incipient wetness impregnation	UTSA	University of Texas at San Antonio
LNG	Liquefied nature gas	VB	Valance band
MSA	Methanesulfonic acid	XANES	X-ray absorption near edge structure
MMOs	Methane monooxygenases	ZIF	Zeolitic Imidazolate Framework
MOFs	Metal-organic frameworks	Zr ₆	Hexa-zirconium
MR	Membered rings		
NP	Nanoparticles		

Abstract

As the primary constituent of natural gas and other fossil reserves, methane is an important, highly abundant, and clean fossil fuel. Exploiting an efficient way to convert methane to liquid fuels or chemicals that are transportable and storable represents an essential challenge in catalysis due to the difficulty in activating the strong C–H bond (440 kJ mol^{-1}) in CH_4 . The indirect synthesis route adopted in industry proceeds through syngas generation by methane reforming, which requires considerable energy input and multistage processes. Therefore, direct routes of methane conversion into value-added chemicals, especially CH_3OH , are desirable as they are thermodynamically favorable under relatively mild reaction conditions.

In nature, the methane monooxygenase (MMO) enzyme can achieve direct methane conversion to methanol (DMTM) under ambient conditions based on Fe and Cu-oxo clusters as active sites. Incorporating these metals into zeolitic frameworks with H_2O_2 , O_2 and/or H_2O as oxidants can result in biomimetic activity. Stepwise conversion of DMTM using O_2 and/or H_2O over Cu-containing zeolites was developed to achieve high CH_3OH selectivity, however with relatively low yield. Moreover, repeated heating and cooling during one cycle is cumbersome and time-consuming, extending the cycle time and limiting its applicability.

In the past decade, Fe/ZSM-5 catalyst was found to exhibit unique activity with TOF of up to 2200 h^{-1} towards C1 oxygenates at $50 \text{ }^\circ\text{C}$ using H_2O_2 as an oxidant in a batch autoclave. Exploring advanced catalysts and reaction systems is the key to achieving DMTM under mild conditions. We summarized the most active and selective materials for DMTM reaction in an aqueous H_2O_2 solution in [part 1.6](#). However, the yield of C1 oxygenates over the catalysts with oxides or carbon materials as supports for atomically dispersed metal sites is still not sufficient when considering the high consumption of expensive H_2O_2 . Thus, there is an urgent need for more efficient catalytic systems with higher yields. Immobilizing metal centers in confined space, like micropores, is an effective strategy to restrict the migration and aggregation and thus avoid undesired self-decomposition of H_2O_2 . In the present work, we focused on developing metal-modified zeolite and MOF catalysts for direct methane oxidation to C1 oxygenates using aqueous H_2O_2 as an oxidant in a batch autoclave.

Firstly, considering MOFs structural characteristics and typical modification methods, we mainly adopted three strategies based on the confinement effect, open metal nodes, and tunable organic linkers. Some well-known stable MOFs with Al, Zn and Zr metal nodes that do not have redox ability are chosen as the supports to develop efficient catalytic systems for the methane oxidation reaction. In our work, classic MOFs, CAU-10(Al), MOF-74(Zn), MIL-100(Al), MIL-

96(Al), DUT-5(Al), UiO-66(Zr), ZIF-8(Zn), Fe₂M-PCN-250 were used as supports to fix Fe sites for designing promising catalysts, that carry out the direct oxidation of methane in an autoclave reactor at 50-80 °C with 0.5 M H₂O₂ as oxidant. MOFs catalysts indeed exhibit apparent activity to C1 oxygenates in H₂O₂ aqueous solution. However, special attention should be paid to the stability of the metal-modified MOFs. We found that pristine MOFs without active metal sites, can still maintain good stability under representative reaction condition. Once the Fe active site have been introduced, the generation of active species, •OH from H₂O₂, will cause the damage and oxidation of MOFs framework to CO₂, making it hard to discriminate the actual activity. Taking our results on Fe/DUT-5 as an example, 1.62Fe/DUT-5-SO₂-post exhibited good activity to C1 oxygenates at 60 °C with TOF of 56 h⁻¹ and 77% selectivity, which is the highest activity among MOF catalysts. However, the inevitable framework decomposition during catalysis resulted in an uncertain amount of CO₂ undermining its stability and selectivity.

Secondly, besides active Fe/MFI, we tried to devote more efforts to developing other Fe-modified zeolites. We optimized the synthesis method of Fe/MOR catalysts and explored Fe active sites in MOR in depth. Among the typical metal immobilization methods, incipient wetness impregnation (IWI), liquid ion exchange (IE), solid-state ion exchange (SSIE) and sublimation of FeCl₃ were used to prepare Fe/MOR catalysts with a nominal 0.5 wt.% Fe loading. We developed a modified ion-exchange method to controllably load Fe on MOR with Fe(acac)₃ as a precursor and CH₃CN as a solvent at 85 °C to get around 0.30 wt.% Fe content. In the activity tests of Fe/MOR with different Fe content, we found that around 0.30 wt.% Fe was the optimal loading of Fe/MOR catalysts, which exhibits the best yield and TOFs beyond 500 h⁻¹ to C1 oxygenates. The TEM images and XAS analyses confirmed that the Fe site in 0.30Fe/MOR exists in the form of the mononuclear Fe site. UV-vis measurements indicate that 0.60Fe/MOR obtained by increasing the Fe precursor concentration, showed an apparent band above 400 nm that is ascribed to Fe-oxo nanoparticles. We proposed that the additional Fe in MOR mainly contributed to an increasing fraction of Fe nanoparticles, which tended to trigger undesirable side-reactions, i.e., H₂O₂ decomposition.

Thirdly, since MFI zeolite was reported to be able to host binuclear Fe to exhibit unique activity in direct methane oxidation in H₂O₂, such distinctive performance has only been found in MFI structure. Most follow-up studies concentrated on optimizing synthesis and adjusting reaction parameters. Recently, mononuclear Fe species was also reported as the active site in Fe/ZSM-5 zeolites by correlating a wide variety of characterization results with catalytic performance data. The special topology and microporous structure of MFI that are on one hand necessary to confine atomically dispersed Fe, on the other hand cause a diffusion problem and limit the amount of

accessible active Fe sites. We planned to reduce the diffusion path of 3D MFI by a hierarchical 2D structure, aiming to boost diffusion and increase the amount of accessible Fe active sites further and, thus, improve the productivity of Fe/MFI catalysts. 2D MFI nanosheets were successfully synthesized and characterized by low-angle XRD, SEM, TEM and physical adsorption to prove their structural characteristics. Fe was modified onto 2D MFI nanosheets with high loading of 0.66 wt.%, maintaining highly dispersed Fe sites without obvious aggregation. Both the UV-vis DRS and XAS analysis confirmed that Fe sites in 0.66Fe/MFI-nanosheet existed in the form of a mononuclear Fe sites. However, 2D MFI nanosheet as support was found to be less active than its 3D counterpart, which is contrary to our original idea. We assumed that the nanosheet structure may not be conducive to forming more active binuclear sites. Furthermore, the MFI nanosheet structure was found to cause severe dealumination that causes the decrease in the Brønsted acidity and undermine the activity. Therefore, we concluded that mononuclear Fe is also the active site in Fe/MFI catalyst based on the research in our work.

Zusammenfassung

Als Hauptbestandteil von Erdgas und anderen fossilen Reserven ist Methan ein wichtiger, sehr reichlich vorhandener und recht sauberer fossiler Brennstoff. Die Suche nach einer effizienten Methode zur Umwandlung von Methan in Kraftstoffe oder Chemikalien, die transportabel und lagerfähig sind, stellt eine große Herausforderung für die Katalyse dar, da die Aktivierung der starken C-H-Bindung (440 kJ mol^{-1}) in CH_4 schwierig ist. Die indirekte Syntheseroute, die in der Industrie angewandt wird, verläuft über die Erzeugung von Synthesegas durch Methanreformierung, was einen erheblichen Energieaufwand über mehrstufige Prozesse erfordert. Daher ist die Entwicklung direkter Wege zur Umwandlung von Methan in wertschöpfende Chemikalien, insbesondere CH_3OH , bemerkenswert, da sie unter relativ milden Reaktionsbedingungen thermodynamisch begünstigt ist.

In der Natur kann das Enzym Methanmonooxygenase (MMO) die direkte Umwandlung von Methan in Methanol (DMTM) unter Umgebungsbedingungen auf der Grundlage von Fe- und Cu-Oxo-Clustern als aktive Zentren erreichen. Die Einbindung dieser Metalle in zeolithische Gerüste mit H_2O_2 , O_2 und/oder H_2O als Oxidationsmittel kann zu biomimetischer Aktivität führen. Die schrittweise Umwandlung von DMTM unter Verwendung von O_2 und/oder H_2O über Cu-haltige Zeolithe wurde entwickelt, um eine hohe CH_3OH -Selektivität, aber eine recht geringe Ausbeute zu erzielen. Darüber hinaus ist das wiederholte Erhitzen und Abkühlen während eines Zyklus ein mühsamer und zeitraubender Prozess, der die Zykluszeit verlängert und die Anwendbarkeit einschränkt.

In den letzten zehn Jahren wurde festgestellt, dass der Fe/ZSM-5-Katalysator eine bemerkenswerte Aktivität mit einer TOF von bis zu 2200 h^{-1} gegenüber C1-Oxygenaten bei $50 \text{ }^\circ\text{C}$ unter Verwendung von H_2O_2 als Oxidationsmittel in einem Batch-Autoklaven aufweist. Die Erforschung fortschrittlicher Katalysatoren und Reaktionssysteme ist der Schlüssel zur direkten und milden Herstellung von DMTM. In [Teil 1.6](#) haben wir die aktivsten und selektivsten Materialien für die DMTM-Reaktion in wässriger H_2O_2 -Lösung zusammengefasst. Die Ausbeute an C1-Oxygenaten an Katalysatoren mit Oxiden oder Kohlenstoffmaterialien als Träger für atomar dispergierte Metallzentren ist immer noch nicht ideal, wenn man den hohen Verbrauch von teurem H_2O_2 berücksichtigt. Es besteht daher ein dringender Bedarf an effizienteren katalytischen Systemen mit höherer Ausbeute. Die Verankerung von Metallzentren in sterisch eingeschränkter Umgebung, wie z. B. Mikroporen, ist eine wirksame Strategie zur Vermeidung der Migration und Aggregation, um eine unerwünschte Selbstzersetzung von H_2O_2 zu vermeiden. In unserer Arbeit haben wir uns auf die Entwicklung von metallmodifizierten Zeolith- und MOF-Katalysatoren für

die direkte Oxidation von Methan zu C1-Oxygenaten unter Verwendung von wässrigem H₂O₂ als Oxidationsmittel in einem Batch-Autoklaven konzentriert.

In Anbetracht der strukturellen Eigenschaften und der typischen Modifizierungsmethoden von MOFs haben wir hauptsächlich drei modifizierte Strategien angewandt, die auf dem Confinement-Effekt, offenen Metallknoten und abstimmbaren organischen Linkern in MOFs basieren. Einige bekannte stabile MOFs mit Al-, Zn- und Zr-Metallknoten, die keine Redoxfähigkeit besitzen, wurden als Träger gewählt, um effiziente katalytische Systeme für die Methanoxidsreaktion zu entwickeln. In unserer Arbeit wurden klassische MOFs, CAU-10(Al), MOF-74(Zn), MIL-100(Al), MIL-96(Al), DUT-5(Al), UiO-66(Zr), ZIF-8(Zn), Fe₂M-PCN-250 als Träger zur Fixierung von Eisenstellen zum Entwerfen vielversprechender Katalysatoren verwendet, die die direkte Methanoxidation in einem Autoklavenreaktor bei 50-80 °C mit 0,5 M H₂O₂ als Oxidationsmittel durchführen. Die MOF-Katalysatoren zeigen in der Tat eine offensichtliche Aktivität für C1-Oxygenate in wässriger H₂O₂-Lösung. Besonderes Augenmerk sollte jedoch auf die Stabilität der metallmodifizierten MOFs gelegt werden. Wir haben festgestellt, dass die ursprünglichen MOFs ohne aktive Metallzentren unter den gleichen Reaktionsbedingungen immer noch eine gute Stabilität aufweisen. Nach der Einführung der aktiven Fe-Stelle wird die Erzeugung aktiver Spezies, Hydroxy-Radikale aus H₂O₂, auch zu einer Beschädigung des MOF-Gerüsts zu CO₂ führen, so dass es schwierig ist, die tatsächliche Aktivität zu erkennen. Am Beispiel unserer Forschung an Fe/DUT-5 zeigte 1.62Fe/DUT-5-SO₂-post eine gute Aktivität für C1-Sauerstoffverbindungen bei 60 °C mit einer TOF von 56 h⁻¹ mit 77% Selektivität, was die höchste Aktivität unter den MOF-Katalysatoren ist. Allerdings führte die unvermeidliche Zersetzung des Gerüsts während der Katalyse zu einer nicht bestimmbar Menge an CO₂, die die Selektivität des Katalysators erniedrigt.

Als zweites haben wir versucht, neben dem aktiven Fe/MFI auch andere mit Fe modifizierte Zeolithe zu entwickeln. Wir optimierten die Synthesemethode von Fe/MOR-Katalysatoren und untersuchten eingehend die aktiven Fe-Zentren in MOR. Unter den typischen Methoden zur Nachmodifizierung von Metallen wurden Fe/MOR-Katalysatoren mit einer nominalen Fe-Beladung von 0,5 Gew.-% durch Nassimprägnierung (IWI), Ionenaustausch in Lösung (IE), Ionenaustausch im festen Zustand (SSIE) und Sublimation von FeCl₃ hergestellt. Wir haben ein modifiziertes Ionenaustauschverfahren entwickelt, um die Fe-Beladung mit Fe(acac)₃ als Vorläufer auf MOR in CH₃CN-Lösung bei 85 °C zu kontrollieren, um einen Fe-Gehalt von etwa 0,30 Gew.-% zu erreichen. In den Aktivitätstests von Fe/MOR mit unterschiedlichem Fe-Gehalt fanden wir heraus, dass etwa 0,30 Gew.-% Fe die optimale Beladungsmenge für Fe/MOR-Katalysatoren ist. Diese weisen beste Ausbeuten und TOFs von mehr als 500 h⁻¹ für C1-

Sauerstoffverbindungen auf. Die TEM-Bilder und die XAS-Analyse bestätigten, dass die Fe-Zentren in 0,30Fe/MOR in Form von mononuklearen Fe-Zentren vorliegt. UV-Vis-Messungen zeigten, dass 0,60Fe/MOR, das durch Erhöhung der Fe-Vorläuferkonzentration erhalten wurde, einen deutlich sichtbaren Peak im Bereich von > 400 nm aufweist, der Fe-Oxo-Nanopartikeln zugeordnet wird. Wir schlugen vor, dass das zusätzliche Fe in MOR hauptsächlich dazu beitrug, den Anteil der Fe-Nanopartikel zu erhöhen, die dazu neigten, die unerwünschte Nebenreaktion, d.h. die H_2O_2 -Zersetzung, auszulösen.

Als drittes wurde berichtet, dass MFI-Zeolithe in der Lage sind, zweikerniges Fe zu beherbergen, und deshalb eine einzigartige Aktivität in der direkten Methanoxidation in H_2O_2 zeigen. Solch eine ausgeprägte Leistung wurde nur in der MFI-Struktur gefunden. Die meisten Folgestudien konzentrierten sich auf die Optimierung der Synthese und die Anpassung der Reaktionsparameter. Kürzlich wurde auch über mononukleare Fe-Spezies als aktive Zentren in Fe/ZSM-5-Zeolithen berichtet, indem eine Vielzahl von Charakterisierungsergebnissen mit katalytischen Leistungsdaten korreliert wurden. Die besondere Topologie und mikroporöse Struktur von MFI, die atomar dispergiertes Fe einschließen kann, litt auch unter dem Diffusionsproblem, das die Menge der aktiven Fe-Zentren begrenzt. Wir planten, den 3D-MFI auf eine hierarchische 2D-Struktur zu reduzieren, um den Stofftransport zu verbessern und die Anzahl der aktiven Fe-Zentren zu erhöhen, um die Produktivität des Fe/MFI-Katalysators weiter zu steigern. 2D-MFI-Nanoblätter wurden erfolgreich synthetisiert und durch Röntgen-Kleinwinkel-Streuung, REM, TEM und Physisorption charakterisiert, um ihre strukturellen Eigenschaften nachweisen. Fe wurde auf 2D-MFI-Nanoblätter mit einer hohen Beladung von 0,66 Gew.-% modifiziert, die immer noch hoch dispergierte Fe-Zentren ohne sichtbare Aggregation beibehalten können. Sowohl die UV-vis DRS- als auch die XAS-Analyse bestätigten, dass die Fe-Zentren im 0,66Fe/MFI-Nanoblatt in Form von einkernigen Fe-Zentren vorliegen. Das 2D-MFI-Nanoblatt als Träger erwies sich jedoch als weniger aktiv als sein 3D-Gegenstück, was unseren ursprünglichen Vorstellungen widerspricht. Wir nahmen an, dass die Nanoblattstruktur für die Bildung aktiverer zweikerniger Zentren nicht förderlich ist. Darüber hinaus wurde festgestellt, dass die MFI-Nanoblattstruktur einer starken Dealuminierung verursacht, die zu einer Verringerung der Brønsted-Säurezahl führt und die Aktivität verringert. Daher schlossen wir basierend auf der Forschung in unserer Arbeit, dass einkerniges Fe auch das aktive Zentrum im Fe/MFI-Katalysator ist.

1. State of the art

1. 1 Introduction

The utilization of alternative environmental-friendly fuels is a crucial solution to the energy crisis, including but not limited to petroleum depletion. Methane, an abundant and clean fossil energy source, which consists of approximately 70 to 90% of natural gas and shale gas [1], is widespread throughout the earth. As of 2020, Russia's proven natural gas reserves alone were 37.4 trillion cubic meters [2]. Methane has been widely used in industry for chemical synthesis and in our daily life as fuel for its highest geometric energy density of $\sim 56 \text{ kJ g}^{-1}$ compared with other hydrocarbons [3]. Considering the remote reserves, long-distance natural gas transportation in the gaseous form through pipelines appears impractical. Natural gas is mainly stored and transported as liquefied natural gas (LNG). Due to the harsh requirements for LNG storage, as the boiling point of methane is 109 K, the resulting leakage of LNG is inevitable. As a result, a large amount of gas is simply flared or otherwise lost to the environment during transportation and gas extraction [4]. However, methane is classified as the second most abundant greenhouse gas (GHG) after carbon dioxide [5]. Moreover, its superior heat-trapping capacity confers a global warming potential of 72 times that of carbon dioxide over 20 years [6]. When flaring to CO_2 equivalents, methane from anthropogenic sources accounts for nearly 20% of the world's GHG warming potential each year [7]. Flaring and venting of associated gas is very dangerous and harmful, while significantly contributing to the potential for climate change. Therefore, the high availability of methane calls for the development of efficient methods for its conversion into commodity chemicals, which allows for more accessible and more economical transportation and contributes to the mitigation of GHG emissions.

1.1.1 Conversion of methane to value-added chemicals

Besides the combustion as fuel, methane upgrading into value-added chemicals or liquid fuels can be achieved through direct and indirect routes, as summarized in [Figure 1-1](#). The indirect synthesis routes proceed through the generation of syngas (a mixture of carbon monoxide and hydrogen) by steam reforming of methane (SRM) ([Equation \(1-1\)](#)), dry reforming of methane (DRM) ([Equation \(1-2\)](#)), and partial oxidation of methane (POM) ([Equation \(1-3\)](#)), which is subsequently transformed to C_{n+} products through Fischer-Tropsch synthesis-albeit with a high energy input [8]. In addition, the syngas can be catalytically converted to methanol, which

establishes the indirect route for methanol synthesis from methane (Equation (1-4)). However, the production of the syngas intermediate is a high-temperature, high-pressure, endothermic, and costly process. Under these circumstances, the present survey explores new catalytic systems for direct and efficient methane conversion to bypass the syngas as an intermediate [4]. Direct conversion routes, including pyrolysis and aromatization, oxidative and nonoxidative coupling and partial oxidation have been proposed and tested (Figure 1-1). The possible products from the direct conversion of methane are mainly limited to a few components such as C₂ hydrocarbons, benzene (aromatics), methanol and formaldehyde et al. C₁ oxygenates in addition to synthesis gas.

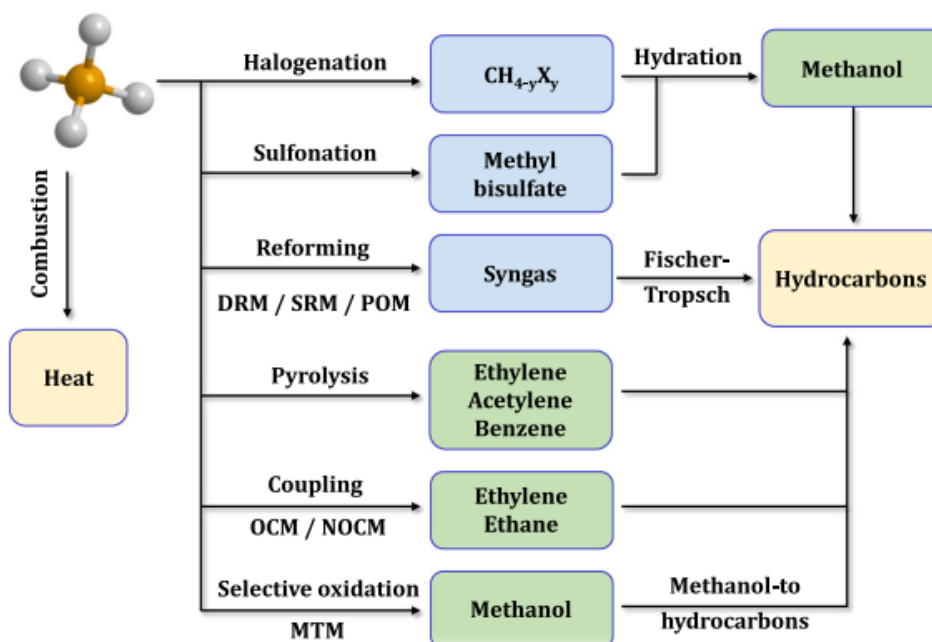
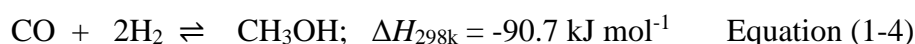
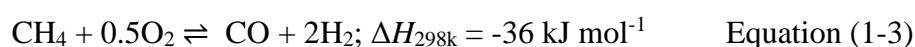
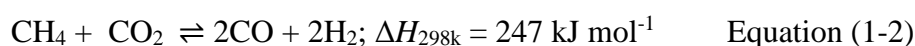
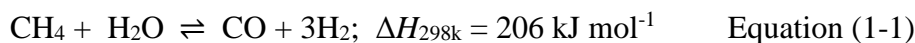


Figure 1-1. Flowsheet of the significant pathways for the valorization of methane.[8]

Conceptually, direct routes should have a distinct economic advantage over indirect routes. However, despite a lot of effort in the research of direct methane conversion during the last decades, no direct processes have progressed to a commercial-stage. The challenges associated with the direct conversion of methane to fuel and chemicals arise from the fact that methane has an entirely symmetrical tetrahedral structure with a high C-H bond energy of 438.8 kJ mol⁻¹. Methane has no functional groups, dipole moment to promote chemical attack, meaning the cleavage of the C-H bond requires very aggressive reactants and harsh conditions such as high temperatures and

pressures. Consequently, under such reaction conditions, products that are more reactive than methane are easily over-oxidized, resulting in a loss of selectivity toward desired products.

1.1.2 Direct methane conversion to methanol

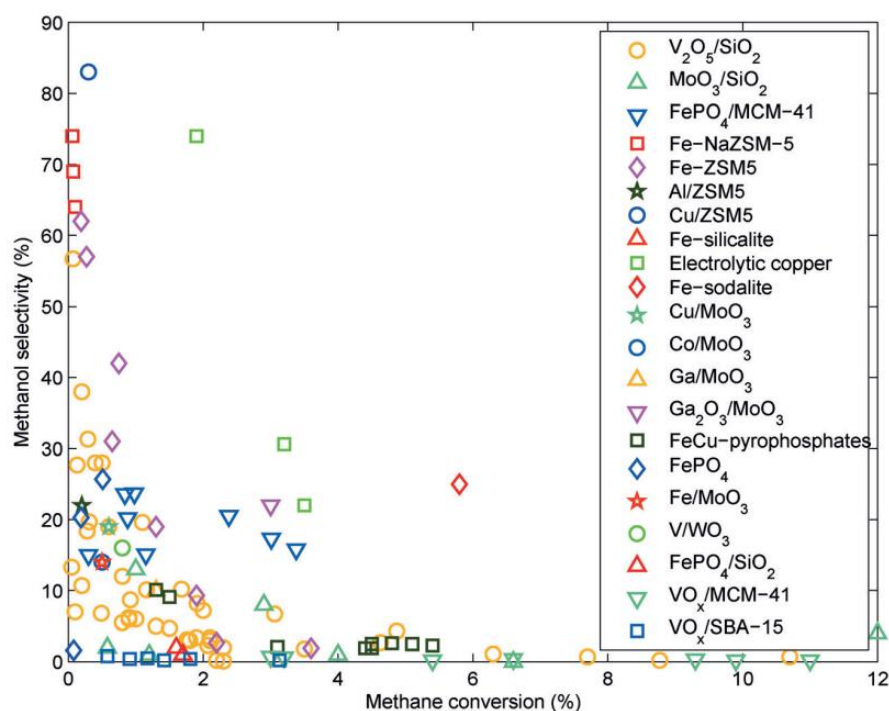


Figure 1-2. Methanol selectivity versus methane conversion over a number of solid catalysts.[11]

Among a number of direct routes to high-value chemicals, direct methane to methanol (DMTM) conversion receives particular attention as methanol can be economically transported and directly used as a feedstock for the production of chemicals such as dimethyl ether, formaldehyde, and propylene [9]. However, DMTM is extremely difficult to master and has emerged as one of the 'Holy Grails of catalysis' [10]. This dream reaction remains a grand challenge because of two distinct problems: the large energy barrier for the activation of C-H bond that is perceived as the rate-determining step in DMTM and simultaneously the inevitable over-oxidation of the products to CO₂, making it still far from practical for use in industry. These two barriers decide methane's low conversion at mild conditions and the low methanol selectivity. Figure 1-2 shows the correlation between methanol selectivity and methane conversion for a number of solid catalysts [11]. A lower selectivity for methanol at a higher methane conversion is found for all catalysts, indicating the limits of the catalytic DMTM process.

In the 1970s, homogeneous catalysts (e.g., platinum, molybdenum, vanadium and palladium complexes, et al.) were first reported for liquid-phase methane conversion [12]. The products were mainly methyl esters, which need to be further hydrolyzed to methanol. Periana et al. [13] used

the platinum(II)-bidiiazine catalyst to convert methane to methanol in concentrated sulfuric acid (102%) with SO_3 as the oxidant. They achieved a yield above 70% at 81% selectivity of the methanol precursor methyl bisulfate. [Figure 1-3](#) shows the reaction mechanism that can explain the high yield in this molecular catalyst system. The key to success for high yields is that no free methanol occurs throughout the process. The bisulfate acts as a protecting group, making the methoxy substances much less prone to over-oxidation than methanol. Therefore, high selectivity can be achieved by stabilizing the product at high conversion. In 2019, Díaz-Urrutia & Ott [\[14\]](#) reported in *Science* that sulfonation for DMTM conversion with >99% selectivity of methanesulfonic acid (MSA) can be achieved in a tandem reactor and can get the pilot stage for as high as 20 metric tons per year of MSA ([Figure 1-4](#)). Despite the outstanding selectivity of methanol derivatives, there are still several intrinsic disadvantages. This process makes use of expensive platinum catalysts and highly corrosive concentrated acid media such as sulfuric and trifluoroacetic acid, which both suffer from both economic and environmental concerns.

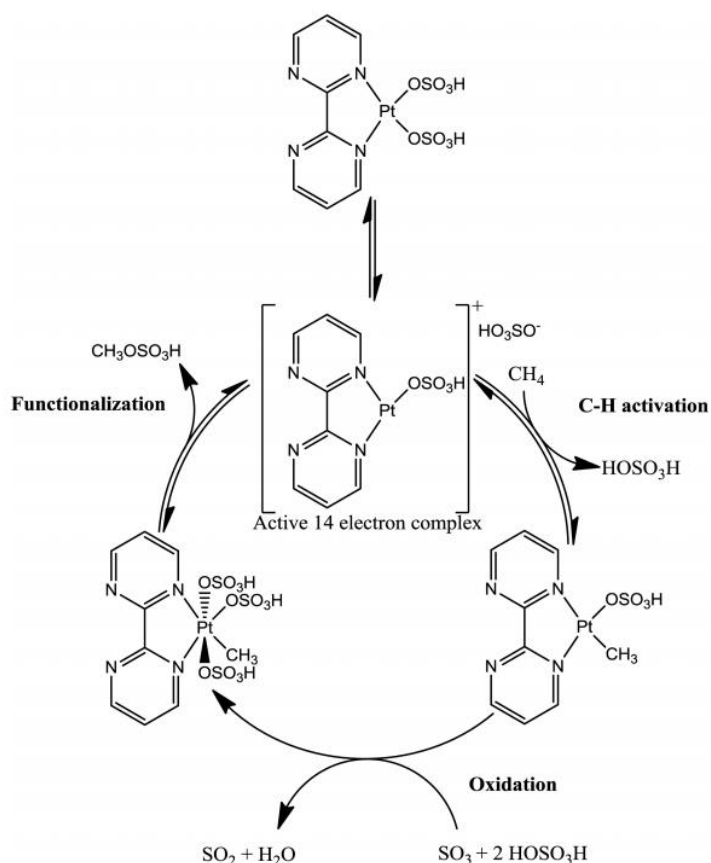


Figure 1-3. Reaction scheme for the oxidation of methane to methyl bisulfate proposed by Periana et al.[\[13\]](#)

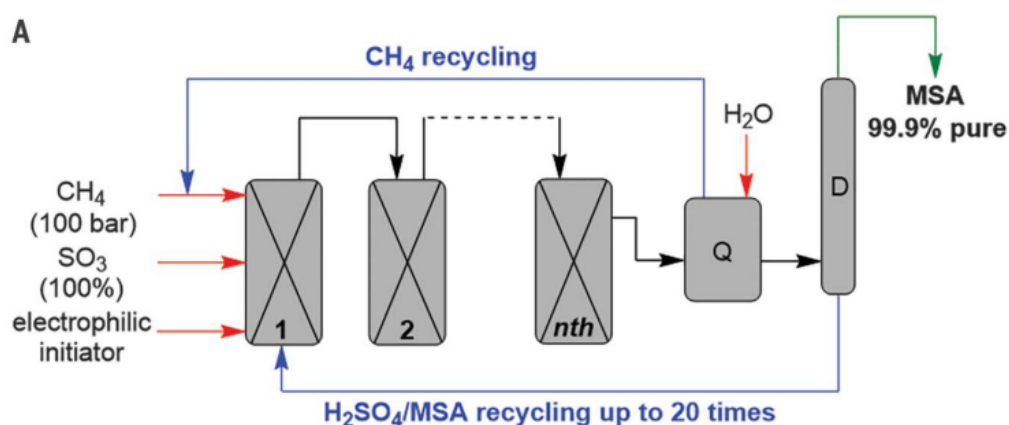


Figure 1-4. The sulfonation process proceeds as a cascade through reactors connected in series.[14]

In nature, methanotrophic bacteria using enzymes called methane monooxygenases (MMOs) are able to activate O_2 and selectively oxidize methane to methanol at ambient pressure and temperature (Equation (1-5)) [15]. There are two types of MMO: a particulate, membrane-bound methane monooxygenase (pMMO) and a soluble methane monooxygenase (sMMO). pMMO, is copper-dependent, but the identity of its copper active site and mechanism remains unclear. By contrast, sMMO uses a diiron active site, which is well understood due to its soluble nature. Several excellent reviews about the structure and mechanism of MMOs have been written over the years to help us understand how enzymes perform DMTM, which offers guidance to the development of catalysts that function under mild conditions [16].

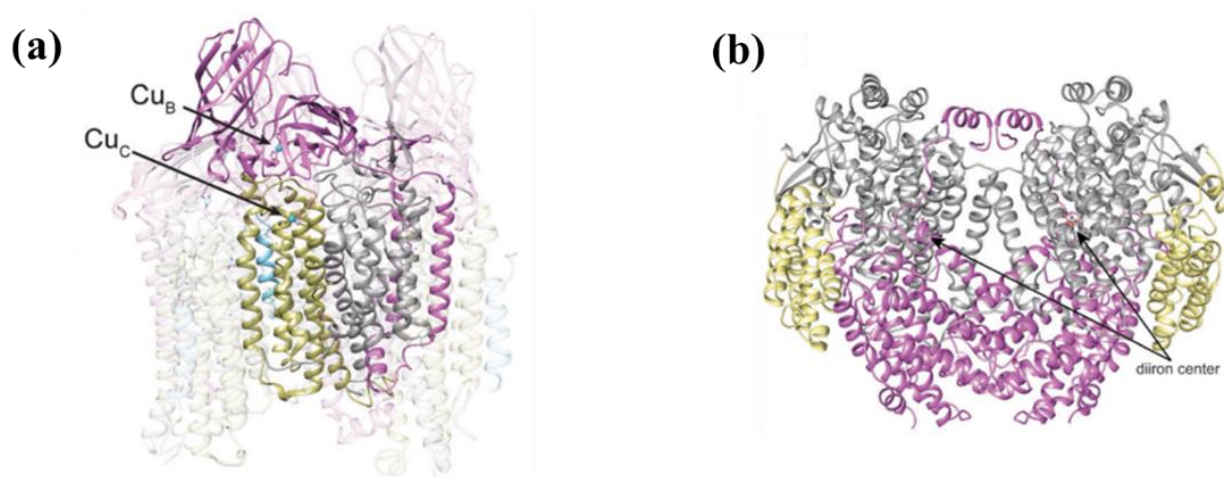
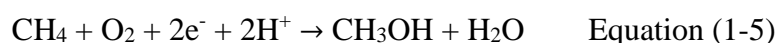


Figure 1-5. Structures of (a) pMMO and (b) sMMO.[16b]

pMMO enzyme consists of three subunits encoded by PmoA (α), PmoB (β), and pmoC (γ) to form an $\alpha\beta\gamma$ protomer [17]. The pMMO crystal structures reveal up to three copper-binding sites per protomer. These sites are referred to as the bis-His, CuB, and CuC sites (Figure 1-5a). The CuB site has been the focus of most discussions. Computational studies and advanced

spectroscopic techniques have recently suggested that both a dinuclear [18] and a mononuclear [19] copper site at this location would be the active site for DMTM. However, extensive evaluation of the related proteins revealed that the methanol is not produced by their CuB-like site, and the nature of the CuB site has been controversial owing to seemingly contradictory biochemical, spectroscopic, and crystallographic results. Two recent experimental findings are consistent with a CuC active site and CuB may still play a functional or stabilizing role, meeting the requirement of more than one copper ion for activity [20].

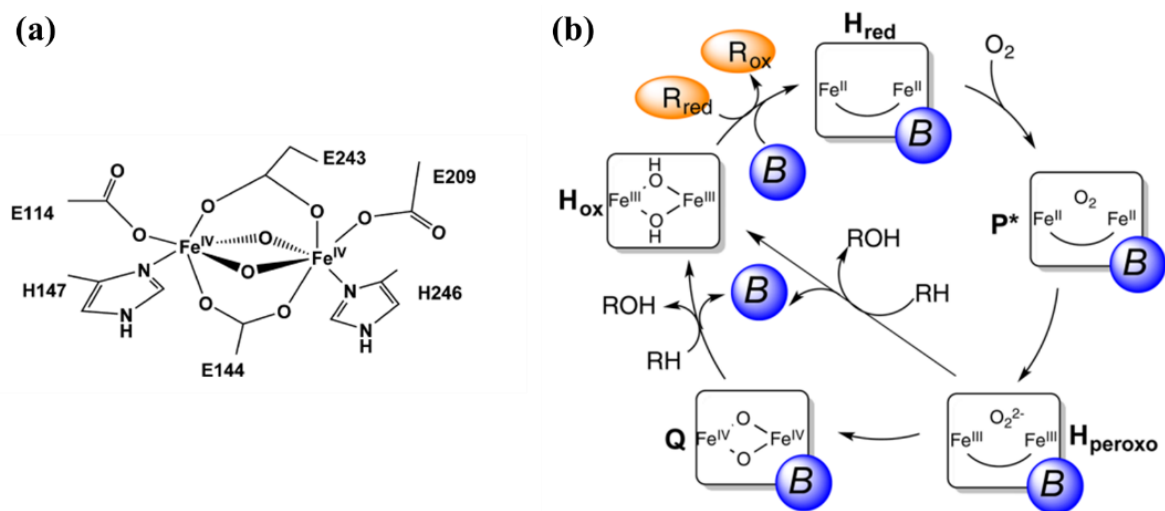


Figure 1-6. (a) Diamond-core structure of compound Q proposed in sMMO, having two irons (Fe^{IV}) bridged by oxygen atoms. H, histidine residues; E, glutamate residues.[21a] (b) The catalytic cycle of sMMO. R_{red} and R_{ox} represent the reduced and oxidized reductase MMOR, respectively, and B represents the regulatory component MMOB.[21b]

As the most well-understood methane-oxidizing enzyme [21], sMMO is arguably the most viable target for the biological conversion of methane to methanol. sMMO has three components: a regulatory protein (MMOB), a reductase (MMOR) to deliver electrons to the active site, and hydroxylase (MMOH) to perform substrate oxidation [22]. MMOH is an $(\alpha\beta\gamma)_2$ homodimer, of which the α subunit contains a diiron center (Figure 1-5b), where dioxygen is activated and substrate hydroxylated. Recent works revealed the structure of the key intermediates in the sMMO catalytic cycle through extensive kinetic, spectroscopic, and computational studies (Figure 1-6). Briefly, the diiron(III) center of MMOH (MMOH_{ox}) is reduced by two sequential electrons from MMOR to the diiron(II) state (MMOH_{red}). Oxygen reacts with MMOH_{red} to form the peroxo intermediates P^* , a diiron(II) species, and P, a peroxo-bridged diiron(III) species, both of which are short-lived, little is known about their structures. The key intermediate of the catalytic cycle is termed compound Q [21a], as shown in Figure 1-6b, and is formed by the decay of H_{peroxo} . The recent study about the time-resolved resonance Raman spectroscopy assigned intermediate Q as a

diamond di-(μ -oxo) diferryl core compared to model compound data [21a]. Other recent studies have focused on how MMOR and MMOB together control the delivery of electrons, protons, and methane to the diiron site. Particularly, outstanding studies by Lippard and Cho et al. [21b] showed that the gating of delivery pathways regulates access of each substrate to the diiron active site during a timed sequence and is coordinated by dynamic interactions with the other component proteins. This gating mechanism, thus, facilitates the removal of methanol to prevent its complete oxidation, enabling their near-perfect selectivity to methanol.

Discovering MMO enzymes and decoding their structure and mechanism for the DMTM process provides an elegant example of an enzyme-catalyzed process and is crucial to developing catalysts that function under mild conditions. This discovery dramatically triggers biomimetic methane direct activation over transition metal ions stabilized by zeolite matrices, such as ZSM-5 and mordenite, while stabilizing binuclear iron and copper centers in a form analogous to that found in MMO enzymes. With dioxygen, water, hydrogen peroxide (H_2O_2), or nitrous oxide as oxidants, methane has been selective oxidation to methanol.

1.2 Direct methane oxidation to methanol (DMTM) with different oxidants

Direct conversion of methane (CH_4) to oxygenated products such as formic acid (HCOOH), formaldehyde (HCHO), methanol (CH_3OH) and methyl hydroperoxide (CH_3OOH) under mild reaction conditions is of great interest in catalysis. Many researchers have investigated metal-catalyzed oxidation systems to convert methane into useful oxygenates directly. The use of oxidants such as H_2O_2 (the only by-product being H_2O), O_2 and even H_2O recently that are atom efficient is favorable to the environment.

1.2.1 N_2O as oxidant

In the early 1990s, Panov and coworkers discovered a new form of surface oxygen (called α -oxygen (α -O)) generated through nitrous oxide (N_2O) decomposition in Fe/ZSM-5 [23]. The iron species in the ZSM-5 matrix are able to dissociate N_2O at a temperature below 573 K to get a reactive surface oxygen α -O, that is active for the direct methane oxidation to C1-oxygenates. They later proposed a possible mechanism of α -site formation based on the binuclear iron complex found in several Fe containing zeolites Fe-ZSM-5, Fe-silicalite and Fe- β (Figure 1-7) [24]. But α -O could not be formed when using O_2 as the oxidant. Owing to the existence of inactive spectator iron sites, the elucidation of the nature of the active site that determines reactivity has been challenging. Snyder et al. overcame this problem and elucidated the structural and electronic information about both the α -Fe and α -O site in zeolite BEA (Figure 1-8) [25]. They reported that

α -Fe is a mononuclear, high spin Fe^{II} species residing within a square planar environment of a β -6MR, and α -O site is a mononuclear, high spin $\text{Fe}^{\text{IV}}=\text{O}$ species having a square pyramidal geometry within the same β -6MR.

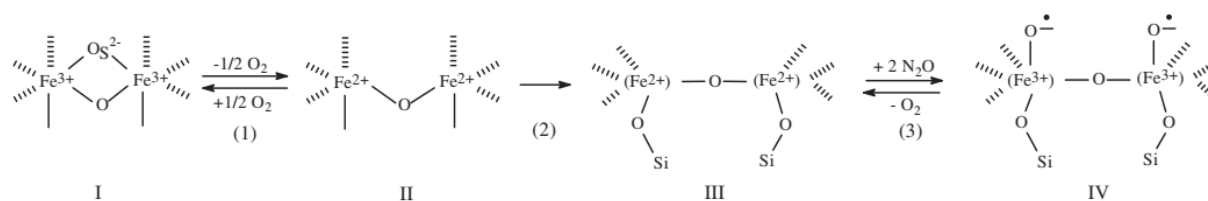


Figure 1-7. An assumed mechanism of the α -sites' formation based on binuclear iron complex in Fe/ZSM-5.[24]

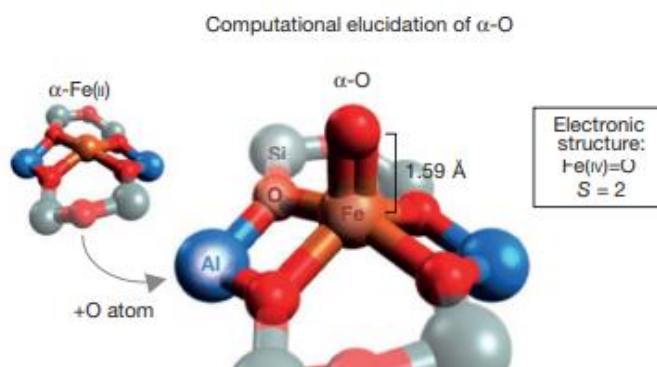


Figure 1-8. The structure of α -Fe(IV)=O in the $S = 2$ ground state and its formation after DFT optimization.[25]

Activation of N_2O and subsequent DMTM process is not limited to MFI framework types alone with literature over Fe/BEA, Fe/CHA, Fe/FER [26] and Cu-zeolites (Cu-BEA, Cu-SSZ) [27] having also been reported. Methanol formation is still debated in this process, as shown in Figure 1-9 [28b]. The methoxy groups may then either hydrolyze to methanol by adding water vapor or may 'rebound' to form an associated $\text{Fe}^{\text{II}}-\text{O}(\text{H})-\text{CH}_3$, which may then desorb, forming CH_3OH . Due to the binding of methanol and methoxy groups on the catalyst surface, both proposed routes require an additional extraction procedure to obtain methanol, which inhibits its industrial applications. In addition, the use of N_2O as an oxidant that is not readily available also dramatically limits the applicability of this process.

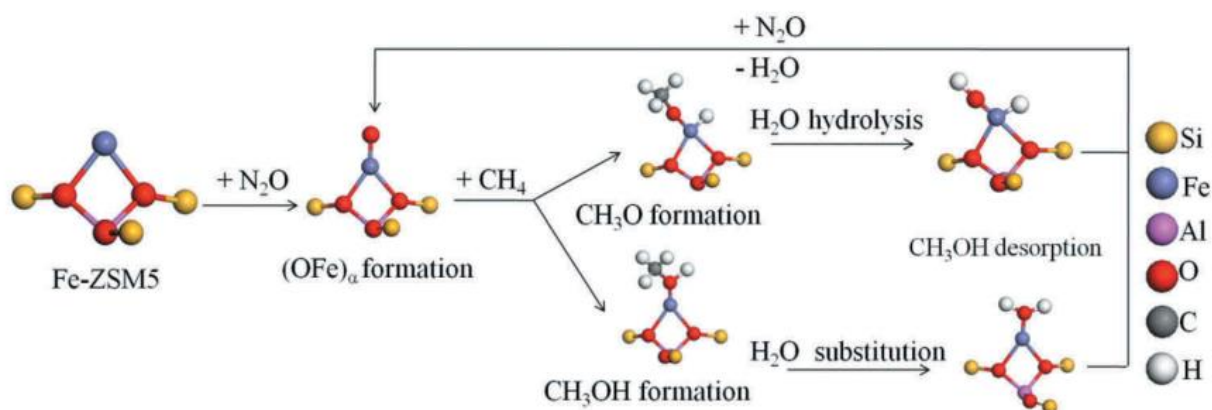


Figure 1-9. The possible pathways of the direct methane oxidation to methanol using N_2O over Fe-ZSM-5.[28b]

1.2.2 O_2 as oxidant

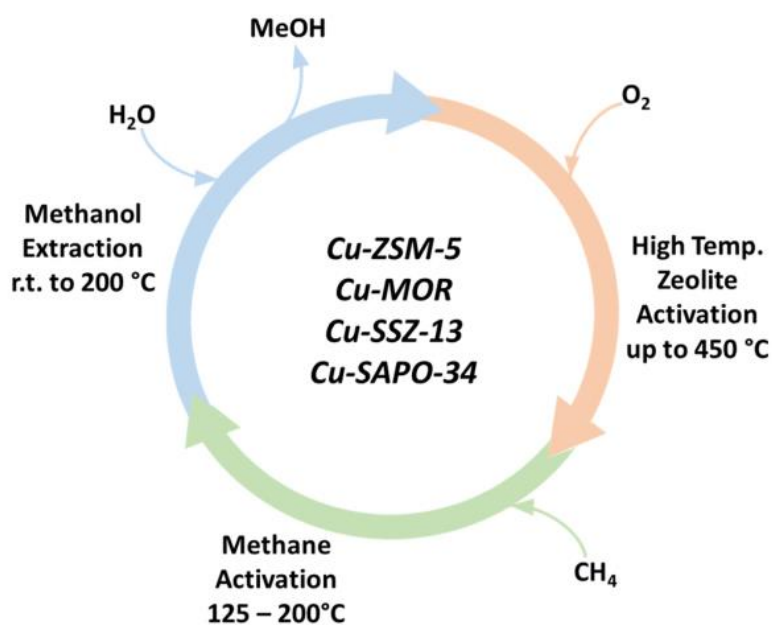


Figure 1-10. The typical stepwise conversion of methane to methanol including (i) the activation process with oxidant (eg. O_2), (ii) oxidation of methane to form surface-bound methanol precursor, and (iii) the extraction of methanol via water steam.[30]

Unlike Fe-zeolites or other Fe-modified catalysts on which methane activation sites cannot be formed with O_2 , copper-containing catalysts, especially Cu-zeolites, can be activated by both N_2O and O_2 . A decade ago, a chemical looping system was developed based on a bis(μ -oxo)dicopper site within Cu-ZSM-5 to convert methane into methanol with a yield up to $8.9 \mu\text{mol}\cdot\text{g}^{-1}$ and 98% selectivity [29]. In the stepwise reaction (Figure 1-10) [30], the first step is activating the catalyst material at a high temperature, typically 450 °C, using either O_2 or N_2O as the oxidant. In the second step, oxygen is then removed from the reactor by He flushing, and methane is introduced

and reacted with the activated catalyst at temperatures from 125 to 200 °C. Finally, methanol is either extracted from Cu-zeolites with a liquid or desorbed by steam. Similar to the conversion of methane to methyl sulfate, oxygen and methane avoid appearing in the reactor with methanol simultaneously. In the past decade, the vast majority of scientific attention has been put on the research of reaction mechanisms and active sites in the conversion process. Throughout the development, methanol formation has been shown to be possible over a wide array of copper-modified zeolite frameworks, including MAZ, MOR, FER, FAU, CHA, MFI, AEI, BPH, AFX, LTL, EON, MEI, BEA [31]. A wide variety of active sites have been proposed for DMTM reaction within these frameworks. In terms of turnover frequency (TOF) to methanol, MOR, CHA, ZSM-5 and MAZ zeolites have the best catalytic performance. In 2021, Li and his coworkers [32] substantially boosted the TOF to methanol to 0.543 h^{-1} with a selectivity up to 91% over a classic Cu/CHA catalyst. Their result shows excellent significance considering that it was obtained in a one-step catalytic process with continuous production of methanol by the use of O_2 together with H_2O as oxidant, and shows extraordinary stability of Cu/CHA.

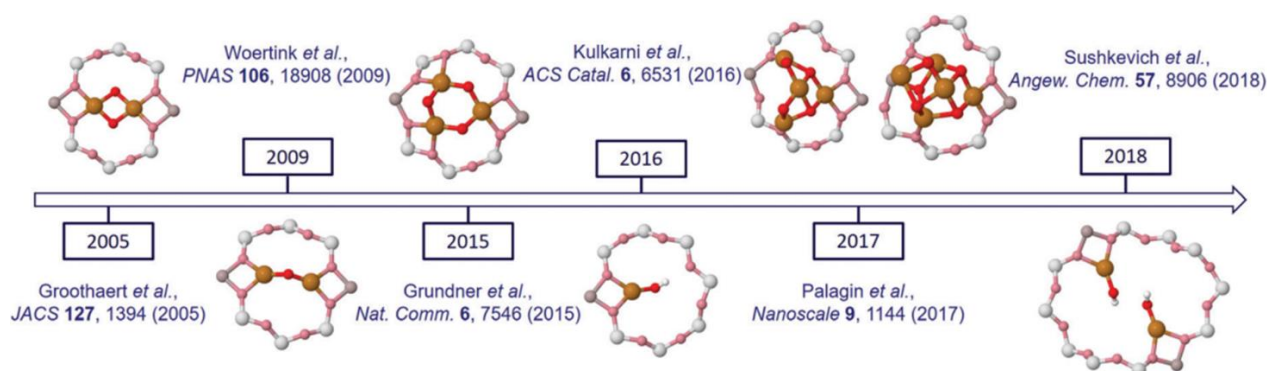


Figure 1-11. Timeline of various suggested configurations of the copper oxide active species in Cu/MOR.[31]

The nature of the active site is still very controversial, spanning from mononuclear copper sites to large copper clusters. Figure 1-11 shows the timeline of various suggested configurations of the copper oxide active species in Cu/MOR [31]. Dimers and trimeric copper centers such as bis μ -oxo di-copper, mono(μ -oxo) di-copper species, and trimeric ($[\text{Cu}_3(\mu\text{-O})_3]^{2+}$) sites, were proposed as active structures because they are suggested to be present in MMO enzymes. However, as discussed above, whether they are present in MMOs is a matter of ongoing debate in the biological community. Based on DFT calculations on different copper clusters, from dimers to pentamers, Palagin et al. [31] showed that $\text{Cu}_4\text{O}_4^{2+}$ and $\text{Cu}_5\text{O}_5^{2+}$ embedded in an 8 MR channel of MOR, which have not been observed experimentally so far, exhibit higher relative stability and activity compared to smaller clusters. Kulkarni et al. [31] discovered that mono-copper species $[\text{CuOH}]^+$ in the 8 MR channel are responsible for the experimental activity of Cu-SSZ-13. Researchers

believe methane can be converted to methanol through various copper active sites, only a portion of which was determined experimentally. Considering that considerable zeolite frameworks can host different active copper sites, it becomes extremely challenging to unravel the configuration of active centers. A stepwise process for DMTM conversion has been proposed and developed; however, there is still a long way before industrial application. Typically, it takes several hours to complete a reaction cycle, and the methanol output per cycle is very limited. In addition, the catalyst activation (regeneration) temperature is usually higher than the reaction temperature, resulting in large temperature fluctuations, which is a challenge for industrial operations involving complex heat exchange systems. Albeit recently reported a non-stepped process in Cu/SSZ-13/O₂/H₂O system [33], an isothermal cyclic process in Cu/MOR/O₂ system [34] for DMTM has been reported, the methane conversion is still far from industrial practicability.

1.2.3 H₂O as oxidant or co-oxidant

So far, although there has not been a commercial process for DMTM, various new routes with efficient solid catalysts have been suggested. Studies [28,35] have found that the addition of water in whether liquid/gas phase will improve the activity, selectivity, and stability of the solid catalysts and benefit the extraction of methanol. In Fe/zeolites/N₂O systems for DMTM, methanol desorption is the rate-limiting step below 473 K. Water vapor addition to Fe/ZSM-5/N₂O was found to accelerate the methanol desorption from the surface, react with methoxy groups for fast hydrolysis to methanol, and restrain the formation of coke on the Fe/ZSM-5 for better stability [36,37]. The Senanayake group [38] revealed the key roles played by H₂O to tune selectivity from CO and CO₂ to methanol over a well-defined CeO₂/Cu₂O/Cu(111) catalyst for CH₄ oxidation with O₂ (Figure 1-12). Firstly, it favorably blocked O₂ activation on the interfacial Ce sites from deep oxidation of CH₄ to CO or CO₂ (Figure 1-12A). More importantly, H₂O can dissociate at Ce sites to produce the active •OH, acting as the actual O-provider and enabling direct CH₄ to CH₃OH conversion (Figure 1-12B). In this system, O₂ dominantly helped to reoxidize CeO_x, which was partially reduced during the reaction. Finally, as previously proposed, H₂O facilitated the hydrogenation of •CH₃O to extract CH₃OH (Figure 1-12C).

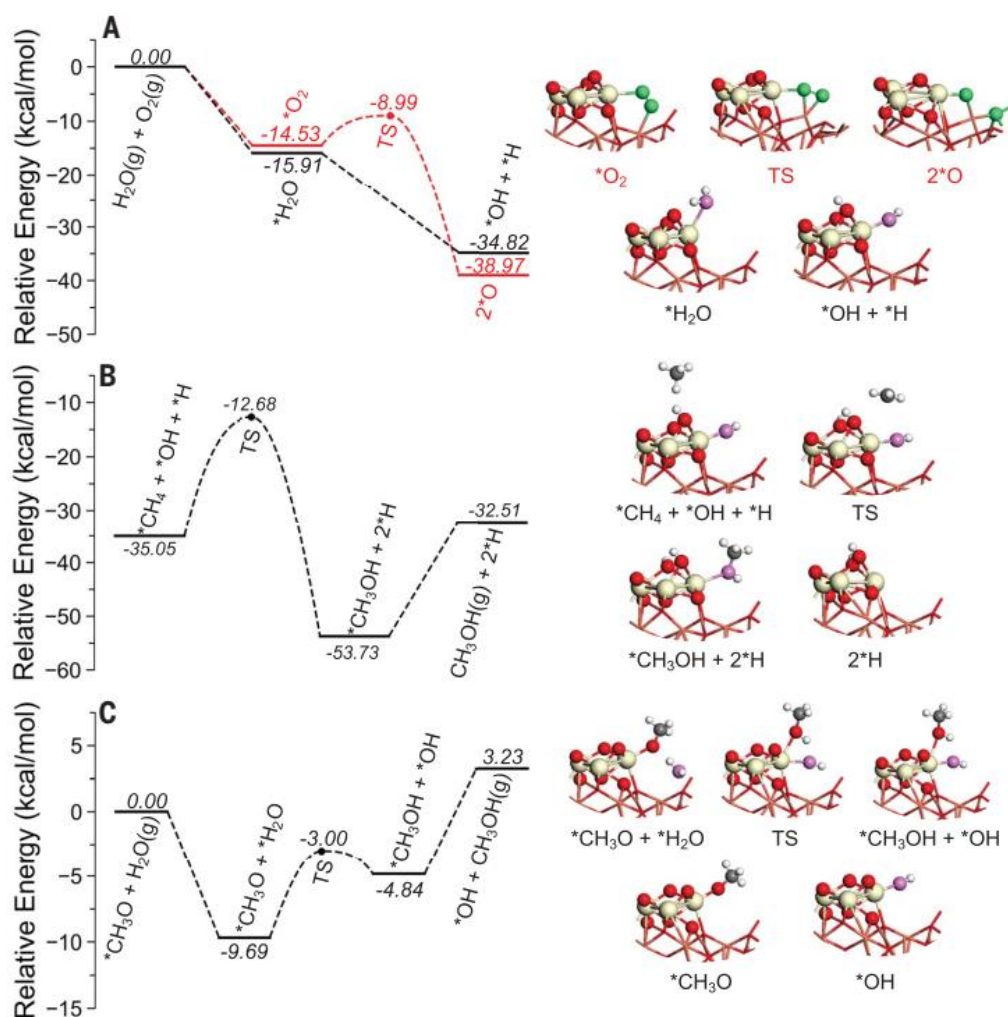


Figure 1-12. DFT-calculated potential energy diagrams for the three important steps involved in CH_4 oxidation by O_2 and H_2O on $\text{CeO}_2/\text{Cu}_2\text{O}/\text{Cu}(111)$. green, O in O_2 ; purple, O in H_2O ; gray, C; white, H.[38]

Recently, Sushkevich et al. [39] reported a new ‘anaerobic’ direct oxidation of methane to methanol over Cu/MOR catalyst, where water is used as the oxidant instead of O_2 . They presented a direct stepwise method (Figure 1-13). The catalyst Cu/MOR was activated in He at 673K first, consecutively reacted with methane and then purged with water at 473K, which produced 0.204 moles of CH_3OH per mole of Cu. Isotopic labeling with H_2^{18}O that inserts labeled oxygen into methanol confirmed water as the source of oxygen to regenerate the zeolite active centers and to make methanol desorption energetically favorable. Combining the experimental data, in situ XAS and IR with DFT calculations, the authors proposed a reaction mechanism involving methane oxidation at Cu^{II} oxide active centers, followed by Cu^{I} reoxidation through the water with concurrent formation of hydrogen. In 2020, Koishybay [40] showed that the water vapor, not dioxygen, is the main source of the oxygen in the methanol obtained over $\text{Cu}\text{-SSZ-13}$ in a continuous-flow reactor. However, it was demonstrated that not all the copper-exchanged materials are active in the anaerobic oxidation of methane. For copper-oxo oligomers, such as

dimers and trimers, water is required to stabilize the newly formed Cu(II) species and reoxidize Cu(I). Copper monomers are more selective in the conventional “aerobic” oxidation with dioxygen.

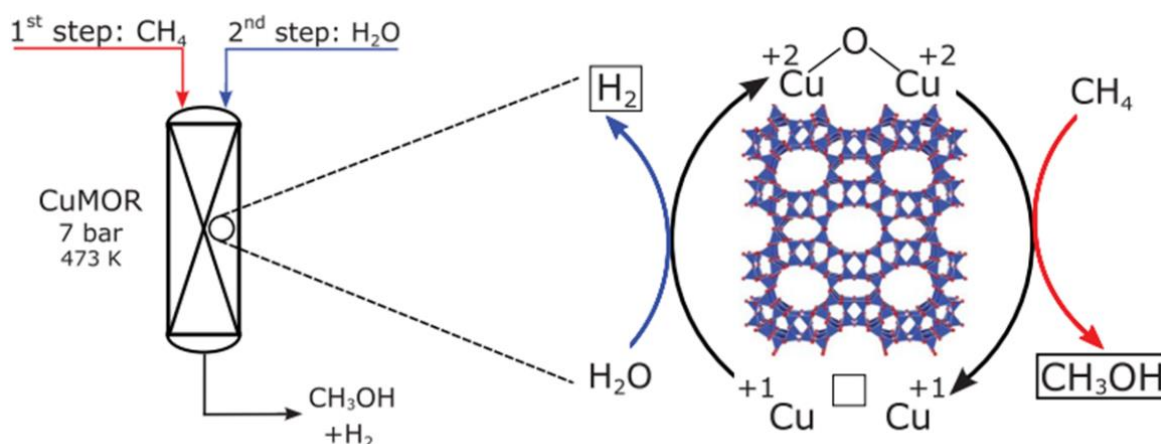
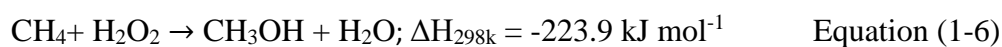


Figure 1-13. Schematic representation of the reaction conditions of the direct methane oxidation by water.[39]

1.3 Direct methane oxidation using H₂O₂ over solid catalysts

As an important industrial oxidant, hydrogen peroxide (H₂O₂) has a wide range of uses, from the provision of clean water to the synthesis of valuable chemicals. The benefit of H₂O₂ as an oxidant is that water is the only product of H₂O₂ decomposition, which is environmentally friendly. Significantly, H₂O₂ has already been proven as a highly efficient oxidant for the liquid-phase direct methane to methanol (DMTM) process under mild conditions (Equation (1-6)). Despite that some catalysts with N₂O, O₂ and H₂O as oxidants, mainly Fe- and Cu-based zeolites, are capable of reaching more than 90% methanol selectivity, the minimal CH₄ conversion, CH₃OH yield, and activation ability of the C-H bond of CH₄ require the use of H₂O₂ as a stronger oxidant. Herein, we mainly want to focus on typical active sites for DMTM process with H₂O₂ as the oxidant in an aqueous solution. In addition to classic Fe-based zeolite catalysts (Fe/MOR, Fe/ZSM-5), AuPd nanoparticle based catalysts (e.g. AuPd/TiO₂), the other newly emerged single-site catalysts (SACs), such as Fe, Co, Rh, Pd, Pt, etc. have also been found active for direct methane oxidation by using H₂O₂. These single-site catalysts with novel active structures can activate the C-H bond at low or even room temperature.



1.3.1 Nobel metal based catalysts

1.3.1.1 AuPd active sites

Edwards et al. [41] observed that Au-Pd nanoparticles (NP) showed highly efficient activity for the direct synthesis of H₂O₂ from H₂ and O₂, which is effective for the further oxidation reaction. They found that Au-Pd nanoparticles supported on TiO₂ (Au-Pd/TiO₂) are active for the oxidation of CH₄ to CH₃OH through a radical process under mild aqueous conditions with H₂O₂ as oxidant and even show better selectivity when using the in situ generated H₂O₂ by adding H₂/O₂ gas mixture as the oxidant [42]. In their further experiments [43], colloidal Au-Pd, instead of Au-Pd/TiO₂, catalyzed methane oxidation, showing much higher activity and methanol selectivity, and much lower consumption of H₂O₂ (Table 1-1). The oxygenate productivity was 29.4 mol·kgcat⁻¹·h⁻¹ at a selectivity of 90% for Au-Pd colloid (entry 2), which is much higher than that of the Au-Pd/TiO₂ (0.03 mol·kgcat⁻¹·h⁻¹, 26%) (entry 1). When 5 bar of oxygen was added additionally as oxidant (entry 3), the product yield was further increased to 53.6 mol kgcat⁻¹·h⁻¹ while maintaining high selectivity to 88%. In entry 5, with much less H₂O₂ (only 50 μmol) and 5 bar of O₂ as oxidant, Au-Pd colloid still achieved 39.4 mol·kgcat⁻¹·h⁻¹ with 92% CH₃OH selectivity. Experiments using isotopically labeled oxygen (O₂) as the oxidant in the presence of H₂O₂ demonstrated that the resulting methanol incorporated a substantial fraction (70%) of gas-phase O₂. More oxygenated products were formed than the amount of H₂O₂ consumed. It was suggested that O₂ can react with •CH₃ generated via H abstraction by •OH from H₂O₂ as the initiation step of CH₄ activation (Figure 1-14).

Table 1-1. Catalytic activity of colloidal Au-Pd catalysts for methane oxidation. Test conditions: reaction time = 0.5 hours; stirring speed = 1500 rpm; CH₄ pressure = 30 bar; reaction temperature = 50 °C.[43]

Entry	Catalyst	H ₂ O ₂ amount (μmol)	O ₂ pressure (bar)	Amount of product (μmol)				Primary oxygenate selectivity (%)	Oxygenate productivity (mol kg _{catalyst} ⁻¹ hour ⁻¹)	H ₂ O ₂ consumed (%)	Gain factor
				CH ₃ OOH	CH ₃ OH	HCOOH	CO ₂				
1*	1%Au-Pd/TiO ₂	1000	0	0.0	0.4	0.00	1.2	26	0.03	73	2 × 10 ⁻³
2†	Au-Pd colloid	1000	0	11.8	3.3	0.6	1.1	90	29.4	38	3 × 10 ⁻²
3‡	Au-Pd colloid	1000	5	17.4	7.6	1.8	1.5	88	53.6	27	9 × 10 ⁻²
4†	Au-Pd colloid	0	5	0	0	0	0.2	0	0	0	–
5†	Au-Pd colloid	50	5	15.7	2.8	1.2	0.3	92	39.4	44	1.2
6†	Pd colloid	50	5	0	0	0	0.7	0	0	22	0
7†	Au colloid	50	5	0	0	0	0.1	0	0	12	0
8‡	PdCl ₂	50	5	0	0	0	0.3	0	0	5	0
9‡	HAuCl ₄	50	5	0	0	0	0.2	0	0	10	0

*Entry 1: Sol-immobilized solid catalyst, 100 mg (6.6 μmol of metal in 10 ml of water)
†Entries 2 to 7: Colloidal catalysts (10 ml, 6.6 μmol of metal)
‡Entries 8 and 9: Homogeneous metal precursor solutions (6.6 μmol of metal in 10 ml of water)

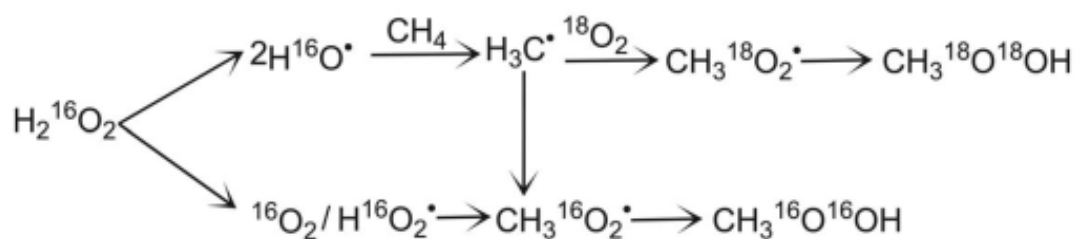


Figure 1-14. Proposed reaction scheme for direct methane oxidation in the presence of H_2O_2 and molecular O_2 . [43]

When H_2O_2 is used as an oxidant, the high consumption rate and low utilization rate of H_2O_2 make the reaction uneconomical. Jin et al. [44] reported a AuPd@ZSM-5-C_{16} catalyst for efficient methane oxidation at 70°C by in situ generated H_2O_2 from H_2 and O_2 , which can prevent H_2O_2 dilution, and thereby keep a high local concentration of H_2O_2 around the Au-Pd nanoparticles. The hydrophobic catalyst was synthesized by fixation of Au-Pd alloy nanoparticles within aluminosilicate zeolite crystals, where the external surface was modified by organosilanes with different organic chains C_3 , C_6 and C_{16} , as depicted in Figure 1-15. The hydrophobic silanes appear to allow H_2 , O_2 , and CH_4 diffusion to the catalyst active sites, while confining the generated peroxide diffused through the encapsulated AuPd nanoparticles to increase the local H_2O_2 concentration and enhance its reaction probability. Figure 1-15 shows the molecular diffusions in the methane oxidation process. The AuPd@ZSM-5-C_{16} catalyst exhibited the best catalytic performance with 17.3% CH_4 conversion and 92% methanol selectivity, corresponding to methanol productivity up to 91.6 millimoles per gram of AuPd per hour.

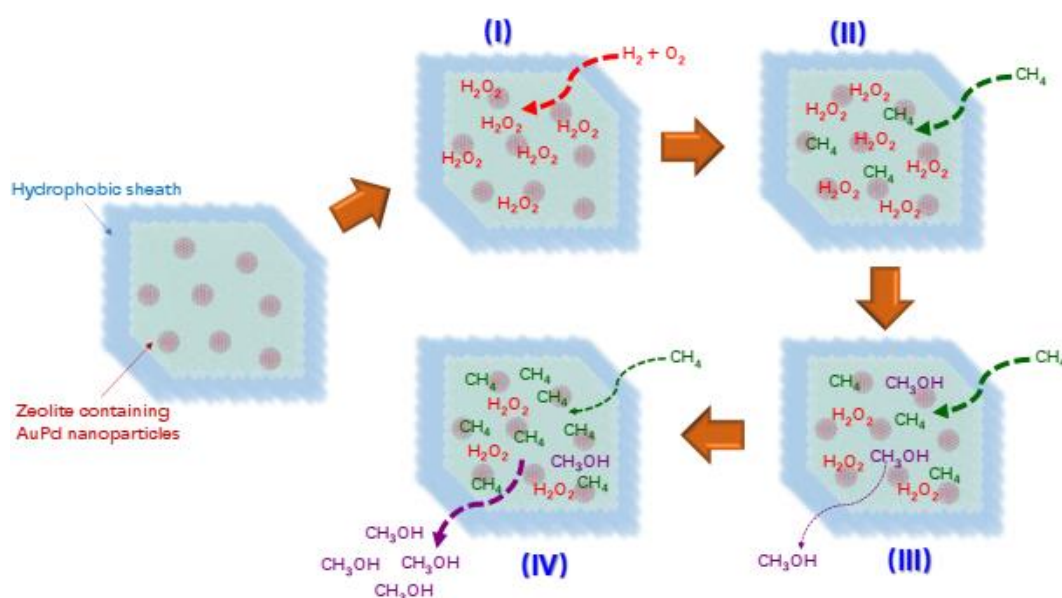


Figure 1-15. Scheme showing the molecular diffusions in the methane oxidation process. The thickness of the arrows represents the diffusion amount. [44]

1.3.1.2 Single-atom noble metal catalyst (Pd, Rh)

Single-atom catalysis (SAC), which indicates surface-supported single atoms in heterogeneous catalysis, has been explored for various reactions [45]. Singly dispersed noble metal atoms anchored on metal oxides as active sites could offer great potential for achieving a distinct catalytic activity or/and selectivity due to their distinctly different electronic state in contrast to their bulk metal nanoparticles [46]. It has been found that based on density functional theory (DFT) calculations, metal sites with a low coordination number like Rh or Pt clusters can stabilize the $\bullet\text{CH}_3$ species to prohibit the successive dehydrogenation of methane [47]. Because the $\bullet\text{CH}_3$ species is a crucial intermediate for CH_3OH formation by combining with $\bullet\text{OH}$ during the reaction, noble metal-based SAC can be promising for selective methane oxidation.

Lee and co-workers [48] reported an atomically dispersed Rh_1/ZrO_2 catalyst in the coordination form of Rh_1O_5 for the selective oxidation of CH_4 to CH_3OH . The Rh SACs on ZrO_2 could activate CH_4 using aqueous H_2O_2 as an oxidant at 70°C , in which the property of Rh single sites significantly affected the CH_4 oxidation. In their work, an atomic Rh (0.3 wt.%) could achieve the highest CH_3OH productivity, whereas Rh nanoparticles on SiO_2 produced only a tiny amount of CO_2 without forming C1 oxygenates (Figure 1-16a). The recyclability of the 0.3 wt.% Rh_1/ZrO_2 catalyst was tested, and the activity of oxygenated products could maintain up to the fourth cycle, as shown in Figure 1-16b. The atomic Rh_1/ZrO_2 was confirmed to be able to stabilize $\bullet\text{CH}_3$ intermediates by diffuse reflectance infrared Fourier transform spectroscopy (DRIFTS) measurement and DFT calculation.

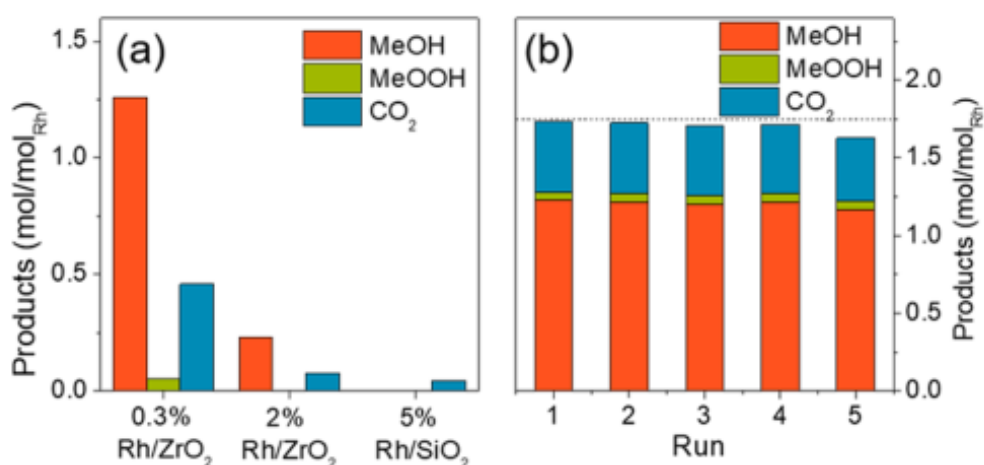


Figure 1-16. (a) Catalytic performance for direct methane oxidation using H_2O_2 as an oxidant over the 0.3 wt.% Rh/ZrO_2 (SAC), 2 wt.% Rh/ZrO_2 (NP), and 5 wt.% Rh/SiO_2 (NP) catalysts. (b) Recyclability test results performed with the 0.3 wt. % Rh/ZrO_2 (SAC) catalyst. Reaction condition: 30 bar of 95% CH_4/He , 70°C , 1 h, 0.5 M H_2O_2 , and 30 mg of catalyst.[48]

Tao and co-workers [49] reported Pd₁O₄ single-sites anchored on the internal surface of micropores of ZSM-5 showed excellent performance for direct CH₄ oxidation. The Pd₁O₄@ZSM-5 catalyst could activate CH₄ using aqueous H₂O₂ as an oxidant at low temperature (50-95 °C) with formic acid as the major product. With 2.0 wt.% CuO used as a co-catalyst, the major product can be shifted into methanol with a selectivity of 86.4% and TOF of 2.78 molecules per Pd₁O₄ site per second at 95 °C. In their work, different Pd loadings (from 0.01 to 2.0 wt.%) on Pd/ZSM-5 catalysts showed similar yields and product distribution, as shown in Figure 1-17, which indicated that the excess Pd, present at the external surface of the zeolite, did not contribute to the activity.

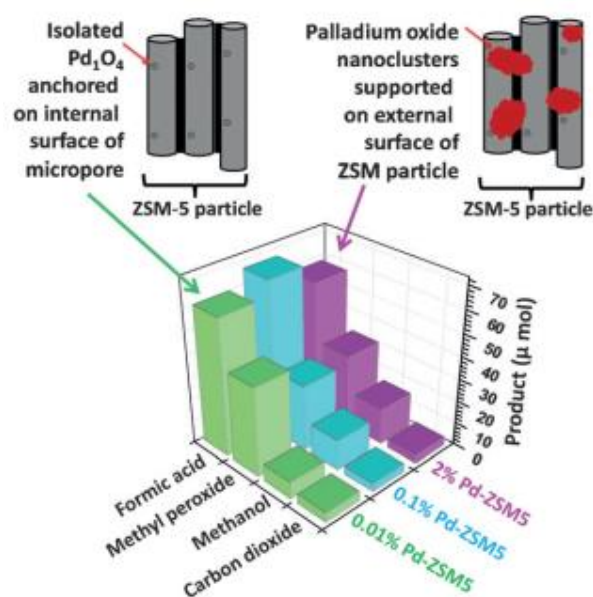


Figure 1-17. Yields of products of transformation of CH₄ catalyzed by 0.01, 0.10, and 2.0 wt.% Pd/ZSM-5 for direct methane oxidation. Reaction was conducted at 50 °C for 30 minutes in 30 bar of CH₄, 5 mmol H₂O₂ and 10 mL of deionized water, and 28 mg of catalyst.[49]

Besides ZrO₂, cerium dioxide nanowires (CeO₂ NWs, 6.2 × 260 nm) were employed to support rhodium (Rh) single-atom via a simple hydrothermal process that can serve as an efficient catalyst for selective methane oxidation to oxygenates (i.e., CH₃OH and CH₃OOH) in aqueous H₂O₂ at 50 °C. The obtained catalyst SAs Rh-CeO₂ NWs [50] exhibited the catalytic performance of 1231.7 mmol g_{Rh}⁻¹ h⁻¹ of oxygenates with 93.9% selectivity, which is 6.5 times higher than that of Rh/CeO₂ nanowires (Rh clusters, 189.4 mmol g_{Rh}⁻¹ h⁻¹) prepared by a conventional wet-impregnation method, as shown in Figure 1-18a. The in-situ DRIFTS measurements in Figure 1-18b and theoretical calculations confirmed that CeO₂ NWs in H₂O₂ triggered the formation of •OOH and •OH. The adsorbed •OH on neighboring Ce(III) atoms oxidized the adsorbed CH₄ at the Rh atoms into •CH₃, which further combines with •OOH and •OH to form CH₃OH and CH₃OOH.

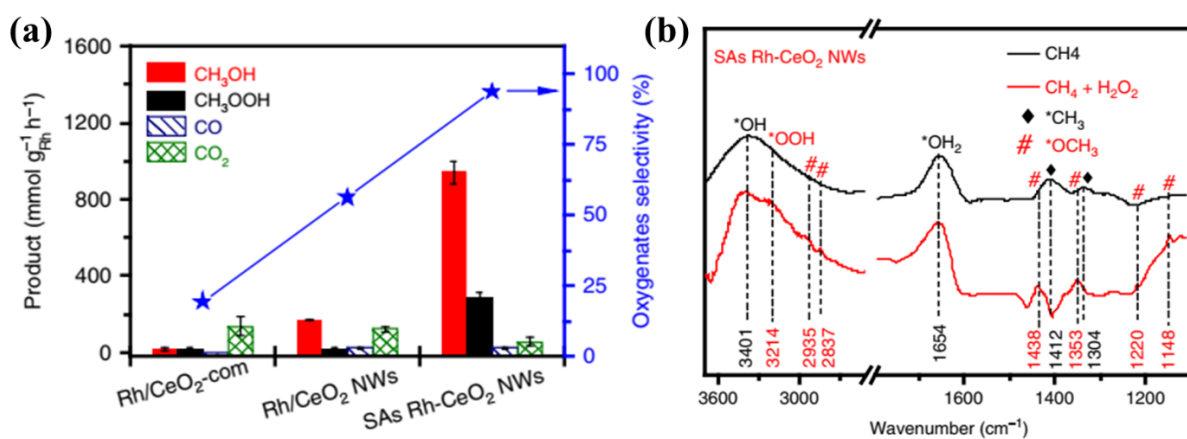


Figure 1-18. (a) The yield and selectivity of oxygenates from Rh/CeO₂-com, Rh/CeO₂ NWs, and SAs Rh-CeO₂ NWs. Reaction conditions: 0.5 MPa of CH₄, 20 mL of 1 M of H₂O₂, 50 °C, 1 h, 10 mg of catalyst. (b) In situ CH₄-DRIFTS measurements on SAs Rh-CeO₂ NWs.[50]

1.3.2 Non-noble metal based catalysts

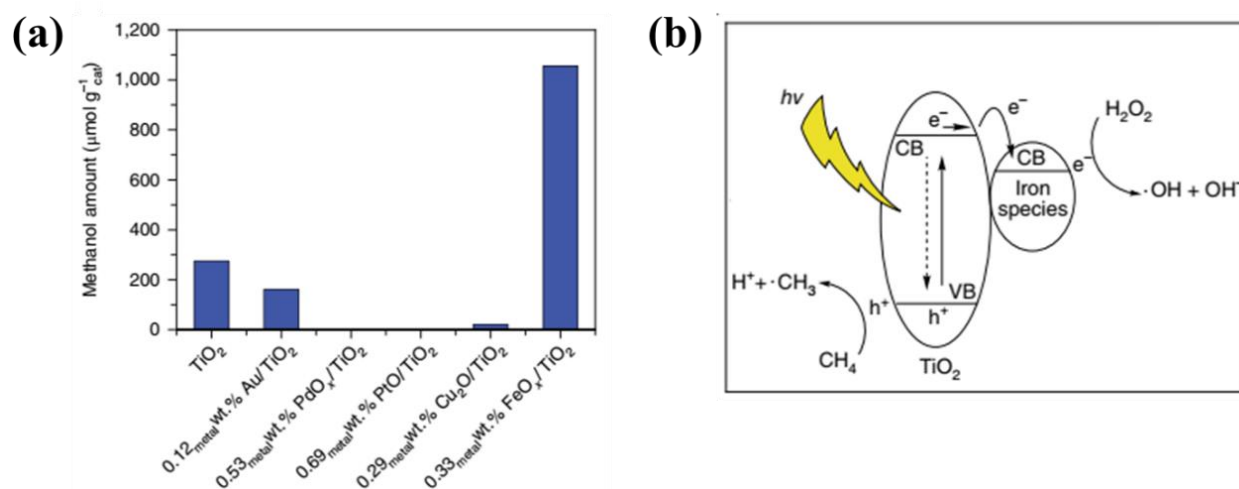


Figure 1-19. (a) Methanol yields for a series of metal modified TiO₂ samples of photocatalytic methane oxidation after 3 h of full arc irradiation. (b) Schematic of charge transfer during methane partial oxidation on 0.33_{metal}Wt.% FeO_x/TiO₂.(hν represents photons, VB is the top of the valance band and CB is the bottom of the conduction band.)[51]

In addition to noble metal, some non-noble metal catalysts (Fe, Cr, Cu, Ni, etc.) decorated on metal oxides or carbon materials have also been studied in direct methane oxidation using H₂O₂ as an oxidant. Xie et al. [51] discovered that with 0.8mM H₂O₂, atomically dispersed iron oxide species anchored on TiO₂ (named as FeO_x/TiO₂) could efficiently convert methane to methanol at ambient conditions and moderate light irradiation (close to one Sun). The optimized FeO_x/TiO₂ catalyst afforded 15% CH₄ conversion and a high methanol yield of 1056 μmol g⁻¹ with an alcohol selectivity over 97% (CH₃OH selectivity over 90%) after 3 h of 300 W Xe lamp irradiation (Figure 1-19a) in a batch reactor purged with 70 mmol CH₄. The iron species could remarkably improve

photo-generated electron-hole separation, lower the reduction potential of H_2O_2 , resulting in the generation of $\cdot\text{OH}$ in Figure 1-19b. The photo-generated holes in the valence band of TiO_2 could react with methane to form methyl radicals ($\cdot\text{CH}_3$), which then combine with $\cdot\text{OH}$ to obtain CH_3OH .

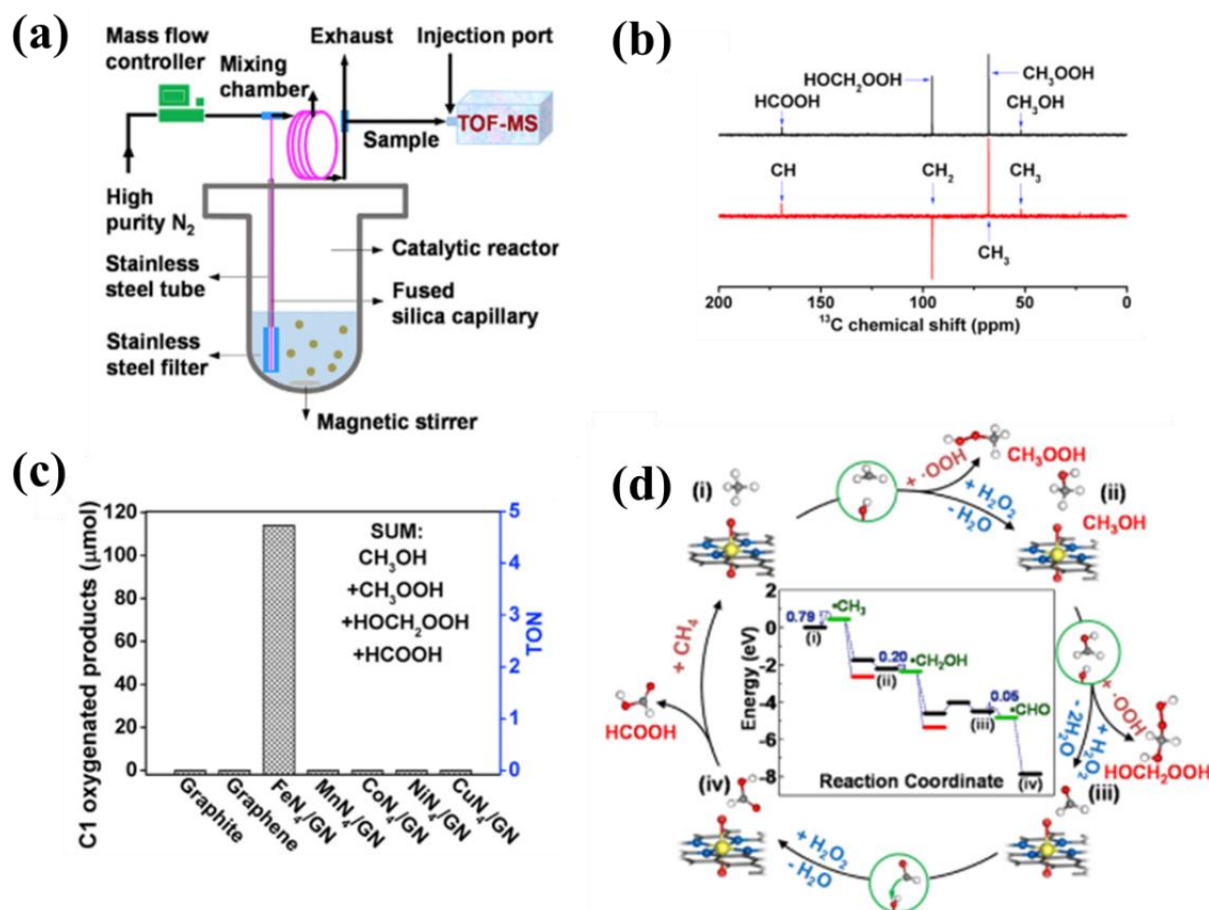


Figure 1-20. (a) A scheme of the designed operando TOF-MS. (b) ^{13}C NMR and ^{13}C DEPT-135 spectra obtained from typical reaction products of $^{13}\text{CH}_4$ oxidation. (c) Catalytic performance of graphite, graphene, FeN_4/GN , and other metal- N_4/GN for CH_4 oxidation. Reaction conditions: 50 mg catalyst, 5 mL of H_2O , 5 mL of H_2O_2 (30%), and 2 MPa of CH_4 (89.9%, N_2 as balance gas) at 25 °C for 10 hours. (d) Reaction pathway of methane conversion to CH_3OH , CH_3OOH , HOCH_2OOH , and HCOOH .^[52]

Bao and coworkers [52] reported that graphene-confined single Fe atoms (FeN_4/GN) could be used as an efficient non-precious metal catalyst to directly oxidize methane to C1 oxygenates at room temperature (25 °C) using H_2O_2 as oxidant. The direct CH_4 oxidation reaction was conducted in a high-pressure reactor connected with a specifically designed online operando time-of-flight mass spectrometer (TOF-MS) (Figure 1-20a), which can qualitatively and quantitatively identify reaction products in real-time that are crucial to following the steps of methane oxidation. Screening from a series of 3d metal- N_4 (Mn, Fe, Co, Ni, and Cu) catalysts, only O- FeN_4 -O structure was found to be unique and could convert methane to C1 oxygenated products with 94%

selectivity after 10 hours of reaction with a turnover frequency (TOF) of 0.47 h^{-1} (TOF = mol of the product (mol of Fe) $^{-1} \text{ h}^{-1}$) (Figure 1-20c). HOCH₂OOH was for the first time identified as a reaction intermediate in methane oxidation. Combined with TOF-MS, ¹³C NMR, and DFT calculations, Bao and coworkers proposed that methane is activated by the O–FeN₄–O to form a methyl radical, which is first converted into CH₃OH and CH₃OOH, and CH₃OH can be further converted to HOCH₂OOH and HCOOH (Figure 1-20b and d).

Zhou et al. [53] reported a two-step strategy to load Ni nanoparticles (NPs) on modified carbon nanotubes (CNT) and transform them into Ni single atoms to obtain sintering-resistant Ni SAs (single-atoms) for efficient CH₄ oxidation to CH₃OH at a low temperature of 50°C using H₂O₂ as oxidant. They modified the CNTs with an N-containing polymer layer that was subsequently transformed into an amorphous N-rich carbon layer after carbonization treatment (denoted as CNT@NC). Ni NPs with different loading can be atomically dispersed on the surface of the amorphous NC layer after thermal treatment, via the strong coordination interaction between N-rich defects and surface-exposed Ni atoms. By continuously increasing the annealing temperature to 900°C, the sink Ni NPs could be converted in situ into Ni SAs in Ni-N₄ architecture through thermal atomization within the surface holes, which is referred to as CNT@PNC/Ni SAs (Figure 1-21a and b). Figure 1-21c and d show the yield and product distribution of the prepared metal-free CNT@NC, Ni NPs and Ni SAs samples with different Ni loading (0.31, 0.68, 1.07 wt.%). The Ni SAs catalyst with a loading of 0.68 wt.% could reach $1.063 \mu\text{mol}\cdot\text{h}^{-1}\cdot\text{mg}^{-1}_{\text{cat}}$ with 94.2% CH₃OH selectivity.

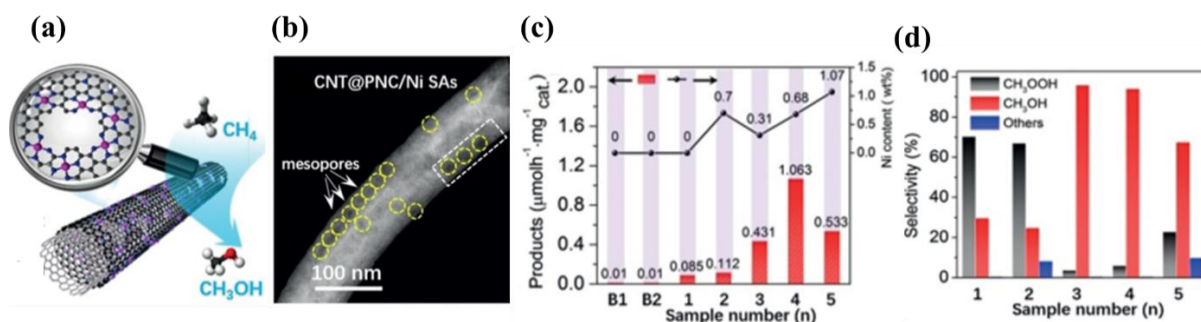


Figure 1-21. (a) The proposed structure of CNT@PNC/Ni SAs catalyst. (b) HAADF images of CNT@PNC/Ni SAs catalyst. (c) and (d) The yield and selectivity of methane oxidation for the prepared catalysts. The sample labeled as B₁ and B₂ is blank comparison. 1 to 5 refers to CNT@NC, CNT@NC@Ni NPs, CNT@PNC/Ni SAs (0.31 wt.% Ni), CNT@PNC/Ni SAs (0.68 wt.% Ni), and CNT@PNC@Ni NPs/SAs (1.07 wt.% Ni), respectively.[53]

Wu et al. [54] reported the facile synthesis of atomically dispersed Cu atoms embedded in a porous C₃N₄ matrix (denoted as Cu-SAs/C₃N₄) for direct methane oxidation, as shown in Figure 1-22a. The as-synthesized Cu SAs catalyst can convert methane mainly into CH₃OOH, CH₃OH at

room temperature (25°C) using H₂O₂ as the oxidant in an autoclave reactor. Among the various kinds of metals, including Cu, Fe, Co and Mn, Cu-SAs/C₃N₄ exhibited the highest yield for the C1 products (153 μmol) for 5 h with a very good TOF (6.7 h⁻¹) and 95% selectivity of oxygenates, as shown in Figure 1-22b. When decreasing the reaction time from 5 h to 2 h, the productivity was still up to 100 μmol over Cu-SAs/C₃N₄ with 11 h⁻¹ TOF. Furthermore, there was no noticeable decrease in the yield after 3 runs over Cu-SAs/C₃N₄ (Figure 1-22c). Various advanced characterization techniques and DFT calculations confirmed that the Cu site in the form of a CuN₄ architecture contributed to the activity.

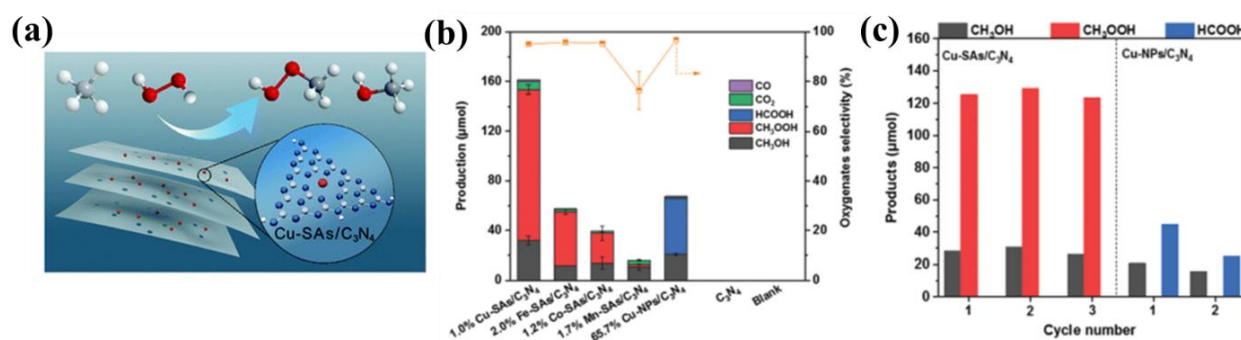


Figure 1-22. (a) Graphic representation of the work. (b) Catalytic results over C₃N₄ and M/C₃N₄ catalysts. (c) Recyclability tests over Cu-SAs/C₃N₄ and Cu-NPs/C₃N₄ catalysts. Reaction conditions: 5 h, 15 mL of H₂O, 5 mL of 40 wt.% H₂O₂, 3 MPa of CH₄ and 30 mg of catalyst.[54]

Shen et al. [55] showed that single chromium atoms supported on titanium dioxide nanoparticles (denoted as Cr₁/TiO₂) as a synergistic catalyst can directly convert methane to C1 oxygenates with H₂O₂ as oxidant under mild conditions, as shown in Figure 1-23a. With 1 wt.% Cr loading, the optimized catalyst reached the highest yield for C1 oxygenates of up to 57.9 mol mol_{Cr}⁻¹ with around 93% selectivity at 50°C after 20 h (Figure 1-23b). Based on the advanced characterization techniques, the Cr(VI) species (possibly the Cr₁-O_x active sites) played a vital role in activating CH₄ and H₂O₂ to get •CH₃ and •OH (Figure 1-23c). The generated •CH₃ and •OH could react with surface-bound Ti-OOH of TiO₂ to form CH₃OOH and CH₃OH by synergistic effect, and the CH₃OH is further oxidized to HOCH₂OOH and HCOOH.

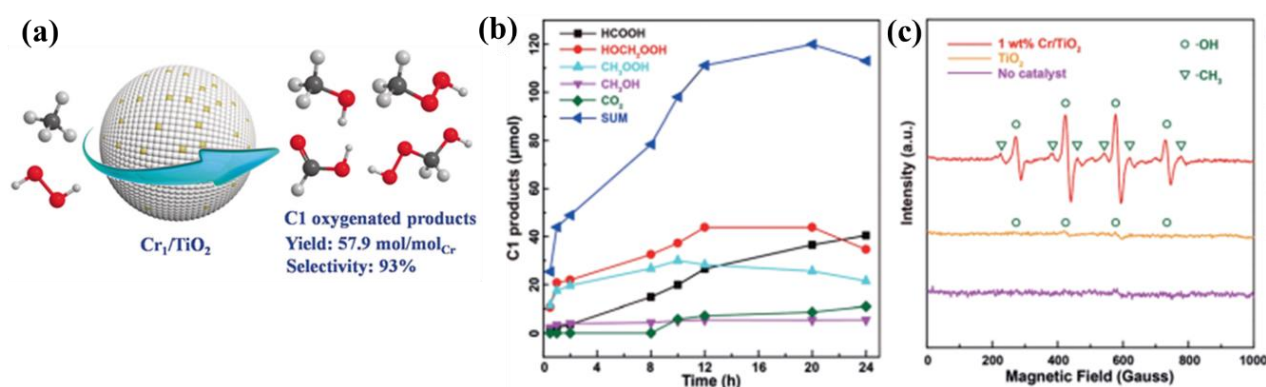


Figure 1-23. (a) Graphic representation of the work. (b) Catalytic performance of the 1 wt.% Cr/TiO₂ catalysts for CH₄ oxidation with different reaction time. (c) Electron paramagnetic resonance (EPR) experiments oxygenated products in liquid phase with different catalysts.[55]

1.4 Zeolites for direct methane oxidation with H₂O₂ as oxidant

In the above-mentioned [part 1.3](#), H₂O₂ has proven a green, environmentally-friendly, highly-efficient oxidant for direct methane oxidation to CH₃OH and other C1 oxygenates through a radical reaction pathway. Highly reactive hydroxyl radicals (\bullet OH) have been confirmed to recombine with \bullet CH₃ to form CH₃OH in the above typical reaction systems with different active sites. However, the productivity of C1 oxygenates over catalysts with mainly oxides or C₃N₄ as the metal carrier is still relatively low when considering the high consumption of rather expensive H₂O₂. In addition, some authors presumed that the metal-support interface was largely responsible for the excessive decomposition of H₂O₂, resulting in the low efficiency of its use to oxidize methane effectively [30b,43]. Many works still avoid mentioning and discussing the consumption of H₂O₂ during the reaction. This drawback is always the core issue that hampers the large-scale application of direct methane oxidation. Thus, a more efficient catalytic system with considerable productivity is urgently needed.

Based on the experience from the active catalysts for direct methane oxidation, atomically dispersed metal sites, especially for iron/copper-based catalysts, are favored for promoting the DMTM process. The tiny metal particles of nanometers or sub-nanometers mainly promote undesirable side-reactions, i.e., H₂O₂ decomposition, which undermines the reaction efficiency [56]. In [part 1.3](#), many examples show the fabrication of single-atom catalysts on metal oxides or carbon materials by surface reactions. One major problem of these catalysts is the leaching and aggregation of active metal sites especially when applied in liquid phase reaction. Anchoring metal centers at confined space, like micropores, is an effective strategy to restrict the migration and aggregation of catalytic metal sites [57]. Meanwhile, by the analogy with the reaction process of MMOs, we assumed that the confinement of reactants would be a favorable factor for bringing important small-molecule reactants together with the active sites. Thus, zeolites and metal-organic frameworks (MOFs) materials, with their microporous structure and large specific surface area, have been widely used as supports to fabricate stable atomically dispersed metal catalysts [58]. These motifs have unusual electronic and chemical properties and display exceptional catalytic performance.

Zeolites, a class of crystalline microporous aluminosilicates, are undoubtedly one of the most important groups of solid catalysts, showing paramount industrial importance for several decades.

More importantly, compared with other crystalline porous materials, zeolites exhibit superior thermal and chemical stability, up to 800 °C or higher. Moreover, zeolites have proven to be excellent porous supports for incorporating metal sites for efficient heterogeneous catalysis. The most promising candidates for C-H activation thus far are Fe- and Cu-based zeolites, where atomically dispersed Fe and Cu sites are believed to be key active-site motifs for the direct methane oxidation to CH₃OH/HCOOH. Particularly, both Fe/MOR and Fe/MFI catalysts have been confirmed to show activity towards direct methane oxidation reaction by using H₂O₂ as an oxidant.

1.4.1 Introduction to zeolites

Zeolites are a class of crystalline microporous silicate materials with large specific surface areas, ordered channels of molecular dimensions, and adjustable acidity and basicity, which are already extensively utilized for refinery and petrochemical processes. The elementary building units of zeolites are SiO₄ and AlO₄ tetrahedra (T), that are linked at their corners by a sharing O atom resulting in a structurally distinct three-dimensional (3D) structure. According to the International Zeolite Association (IZA) [59], there are over 250 zeolite frameworks recognized by IZA. Except for a few natural zeolites, most zeolite structures are synthetic. The structures are denoted with three-capital-letter codes, such as MFI and MOR (see [Figure 1-24](#)) [60]. A defining feature of zeolites is the presence of ordered distributed pores and cages with diameters of less than 2 nm built up from the network of 6-, 8-, 10- and 12-membered rings (MR), which gives them characteristic microporosity. The rings are symbolized with the notation nMR with n the number of TO₄ tetrahedra involved in the corresponding ring. Different pore diameters, channel dimensionality (from 0 D to 3 D), cages, pockets, and other structural characteristics result in different pore structures ([Figure 1-24](#)). MOR pore structure consists of elliptical and non-interconnected 12-MR main channels ($7 \times 6.5 \text{ \AA}$) with parallel 8-MR channels ($5.7 \times 2.6 \text{ \AA}$). The two channels are connected by another 8MR channel called “side pockets” with a window size of $3.4 \times 4.8 \text{ \AA}$. Considering this structure, MOR, therefore, can be described as a 1D zeolite because the molecule diffusion mainly happens in only the 12-MR channel. MFI type framework corresponds to several different zeolite materials, namely, zeolite ZSM-5 and pure-silica zeolite silicalite-1, because of their different chemical properties. ZSM-5 has a 3-dimensional pore structure consisting of straight 10 MR channels ($5.1 \times 5.5 \text{ \AA}$) and interconnected sinusoidal 10 MR channels ($5.3 \times 5.6 \text{ \AA}$), ensuring good diffusion.

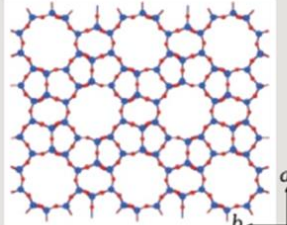
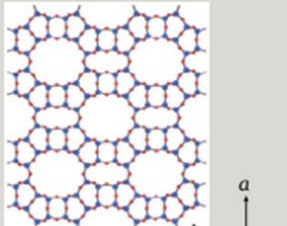
Framework type	Channel system (window size)	Typical material	Projection of framework structure
MFI	5.1 × 5.5 Å (10-ring); 5.3 × 5.6 Å (10-ring)	ZSM-5, silicalite-1, TS-1	
MOR	6.5 × 7.0 Å (12-ring); 2.6 × 5.7 Å (8-ring)	Mordenite	

Figure 1-24. The framework structure of classic MFI and MOR type.[60]

Another feature of zeolites is the isomorphous substitution of Si^{4+} by Al^{3+} in the framework because of their similar values of ionic radii, T–O bond lengths, and T–O–T bond angles. Due to the incorporation of trivalent Al^{3+} that carries one positive charge less than Si^{4+} , there is an excess negative charge that positively charged cations must compensate for electroneutrality. These negative framework charges are balanced by the introduction of protons (H^+) as bridging [Al–OH–Si] hydroxyls between neighboring Si^{4+} and Al^{3+} forming strong Brønsted acid sites (BAS), which are responsible for the catalytic activity of zeolite catalysts. Besides Al, other trivalent elements, such as B, Fe, and Ga can also be applied. There are several well-established methods to generate BAS in zeolites. The most important procedure is the introduction of ammonium ions by ion exchange, which is followed by thermal de-ammoniation to form the bond of a hydroxyl proton at the bridging oxygen of [Al–OH–Si]. The second procedure is the introduction of multivalent metal cations, such as Mg^{2+} , Ca^{2+} , La^{3+} , or mixed rare-earth cations, by ion exchange in aqueous suspension followed by thermal dehydration. BAS are formed based on the generally accepted Hirschler-Plank mechanism [61]. In zeolites containing multivalent cations, heat treatment results in the removal of most of the water initially present in the pores, and these cations have to balance typically two or three negative framework charges in the zeolite with significant distances from each other that form the strong electrostatic fields inside the zeolite pores. In the local electrostatic fields, residual water molecules dissociate to form hydroxyl protons bound to bridging oxygen of [Al–OH–Si].

Besides acting as important Brønsted acid catalysts, zeolite catalysts modified with transition metals, such as Fe, Cu, Ni, Co, Pt, Ti, Pd, and Mo et al., are also critical catalytic materials. [Figure 1-25](#) schematically illustrates three conceptually different transition metal confined zeolite

composites: (i) Isolated metal nanoparticles. (ii) Ion-exchanged cations stabilized on the $[\text{AlO}_4]^-$ tetrahedra. (iii) Isomorphous substitution into the zeolite framework [62]. Many well-established methods have been developed to prepare transition metals modified zeolite catalysts, such as wet impregnation, ion exchange, chemical vapor deposition (CVD), isomorphous substitution, direct encapsulation of metal complexes. Wet impregnation is easy to perform by mixing the solid with metal precursor solutions and subsequently drying to remove the absorbed solvent. Ion exchange methods, typically liquid ion exchange in aqueous solution and solid-state ion exchange (SSIE), are the most used methods to introduce the transition-metal sites inside the pores of the zeolites. CVD is performed by reacting the volatile metal precursors with zeolites under anhydrous conditions, leading to a well-defined catalyst. The isomorphous substitution method allows forming framework metal sites.

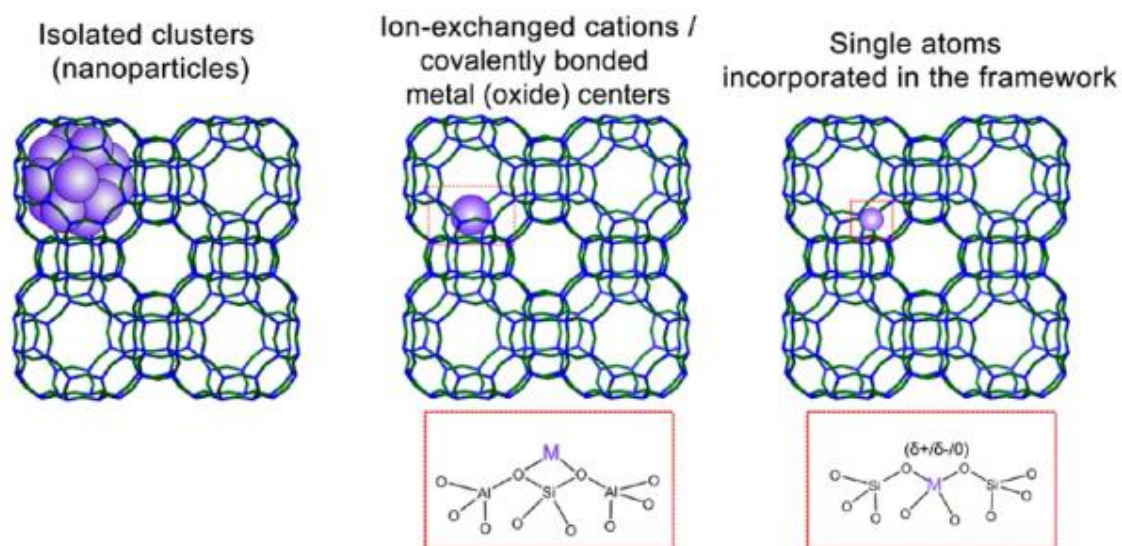


Figure 1-25. Possible zeolite–metal composite configurations.[62]

1.4.2 Fe/ZSM-5 as catalyst

1.4.2.1 Identification of binuclear Fe as active site in Fe/ZSM-5

In 2011, Rahman et al. [63] found that protonated pentasil-type zeolites (H-ZSM-5) were highly active and selective for the direct CH_4 oxidation to HCOOH by the addition of triphenylphosphine ($(\text{C}_6\text{H}_5)_3\text{P}$) using H_2O_2 as oxidant. High yield (13.0%, based on CH_4) with 66.8% selectivity for HCOOH was achieved over H-ZSM-5 catalyst ($\text{SiO}_2/\text{Al}_2\text{O}_3 = 23.8$) under the reaction temperature of 373 K and a CH_4 pressure of 2.6 MPa. A considerable amount of CO_2 was generated as a deep oxidation product. They observed the increasing amount of byproduct O_2 caused by H_2O_2 decomposition ($\text{H}_2\text{O}_2 \rightarrow \text{H}_2\text{O} + \frac{1}{2}\text{O}_2$) with increasing reaction temperature. And they concluded that the acid sites in H-ZSM-5 seem to be the active sites for the direct methane oxidation by investigating the effects of different Si:Al ratios, which determine acidity. Hereafter, Hammond et

al. have conducted comprehensive research on H₂O₂-mediated MTM conversion over iron- and copper-containing MFI zeolites in a batch reactor [56,64,65]. They confirmed that the trace amounts of Fe impurity (0.014 wt.%) in commercial ZSM-5 are the active centers that oxidized CH₄ to C1 oxygenates (mainly HCOOH, CH₃OOH, CH₃OH) with 95% selectivity. H-ZSM-5 (SiO₂/Al₂O₃ = 30) after 550 °C calcination was found to have the most active Si/Al ratio from a range of ZSM-5 catalysts and showed amazing TOFs of 2200 h⁻¹ under standard conditions (50 °C, 0.5h, 30.5 bar of CH₄) [64].

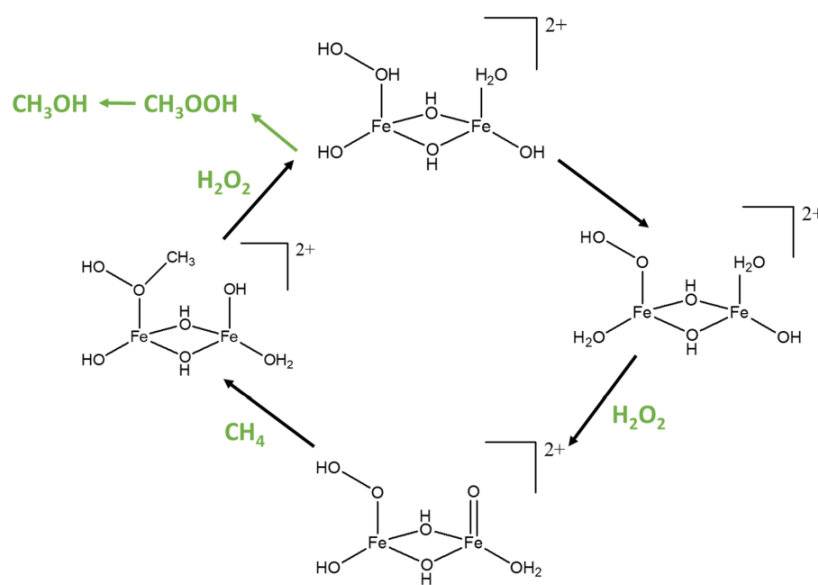


Figure 1-26. Proposed catalytic cycle for direct methane oxidation by a binuclear iron species in ZSM-5.[64]

The level of activity exhibited by commercial H-ZSM-5 has proven to be unique. The author concluded three factors that mainly determine the amazing activity, which are the Si:Al ratios, the activation procedure with a heat pre-treatment at 550°C, and the unique structure of ZSM-5. Other zeolites (i.e., Ferrierite, Beta, Silicalite-1 and TS-1) with similar compositions, but different pore structures, are almost inactive for direct methane oxidation. The authors believed that despite that Al was not the active component in H-ZSM-5, its presence in the framework is essential to anchor iron and prevent aggregation to larger iron oxide clusters. To further elucidate the specific geometrical environment of the extra-framework Fe species, extended X-ray absorption fine structure (EXAFS) analysis and DFT calculations were carried out and revealed that Fe existed in the ZSM-5 in the form of a positively charged di-iron complex $[\text{Fe}_2(\mu_2\text{-O})_2(\text{OH})_2(\text{H}_2\text{O})_2]^{2+}$, containing antiferromagnetically coupled high-spin octahedral Fe³⁺ centers. They used this model to propose a closed catalytic cycle for selective methane oxidation, as shown in Figure 1-26.

Furthermore, they detected the potential radical species formed during the reaction by EPR spectroscopy with 5,5-dimethylpyrroline-N-oxide (DMPO) as a radical trapping agent. They

found significant quantities of $\bullet\text{OH}$ were produced during the reaction, which are involved in the over-oxidation of methanol. The absence of $\bullet\text{CH}_3$ signals in the EPR spectra differed the reaction mechanism from α -oxygen derived from N_2O , or Fenton's chemistry leading to a low oxygenate selectivity, in which $\bullet\text{CH}_3$ have been observed as a key intermediate. Combining with the Time on-line analysis, they proposed that methyl hydroperoxide (CH_3OOH) is the primary reaction product, and that methanol, formic acid, and CO_2 are formed consecutively (Figure 1-27). Although copper does not have a direct effect on methane activation, it improved the methanol selectivity by inhibiting the overoxidation of HCOOH and CO_2 by minimizing the formation of $\bullet\text{OH}$ that was confirmed by EPR measurement. By combining the effect of Cu with the high activity of Fe, they found that a physical mixture of Cu/silicalite-1 and Fe-silicalite-1 synthesized by the SSIE (solid-state ion exchange) method achieved 93% selectivity to methanol with 70 h^{-1} TOF.

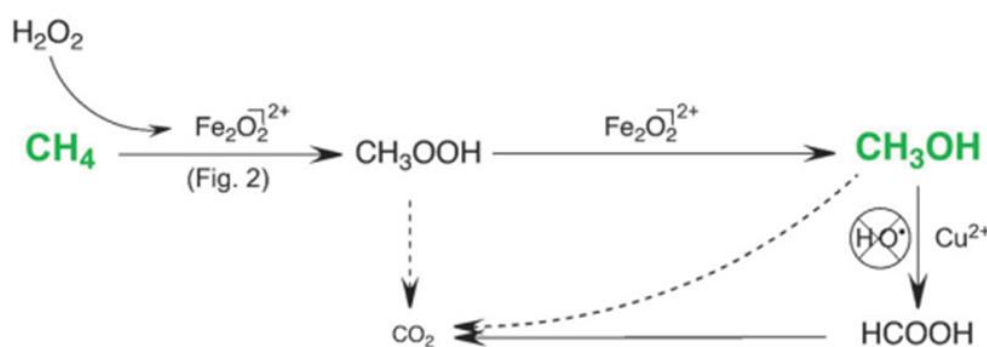


Figure 1-27. A potential reaction scheme for the direct methane oxidation over Fe/ZSM-5 catalyst.[64]

In the last decade, most of the research focused on the influence of reaction parameters, calcination conditions, the Si/Al ratio and acidity on the activity. Al^{3+} was proposed to behave as a structural promoter for facilitating the extraction of Fe^{3+} species to the extra-framework that contributes to the activity. The incorporation of Al also provides an associated negatively charged framework, that is beneficial to the dispersion of the extra-framework Fe species responsible for avoiding the formation of undesirable clusters and bulk oxides [56]. Meysam et al. [66] prepared a series of trivalent heteroatoms ($\text{M} = \text{Ga}, \text{Al}, \text{B}$) substituted into Fe-MFI zeolite ($\text{SiO}_2/\text{M}_2\text{O}_3 = 30$) by hydrothermal method. The key finding in their work is that the strong acidity in ZSM-5 is crucial to H_2O_2 activation under mild conditions and manipulates the product selectivity to formic acid.

1.4.2.2 Identification of mononuclear Fe as active site in Fe/ZSM-5

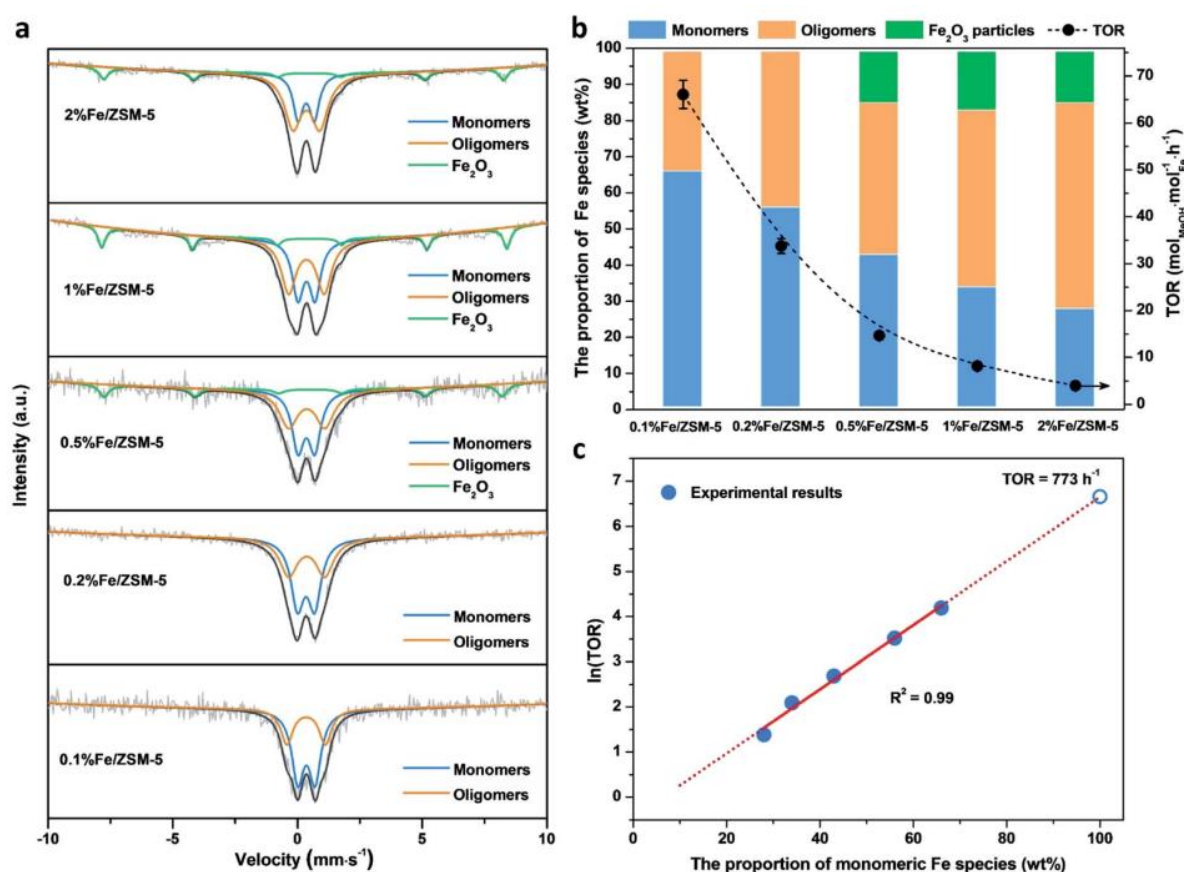


Figure 1-28. (a) Under ambient conditions ^{57}Fe Mössbauer spectra of the Fe/ZSM-5 zeolites with different Fe loadings obtained. (b) The relative proportion of different Fe species in different Fe/ZSM-5 zeolites with the apparent TORs of five Fe/ZSM-5 zeolites. $\text{TOR} = \frac{\text{Number of methanol molecules}}{\text{Number of Fe atoms} \times \text{reaction time}}$ (c) Correlation between the natural logarithm of TORs and the relative proportion of monomeric Fe species quantified by ^{57}Fe Mössbauer spectroscopy.[67]

The actual active sites of Fe/ZSM-5 catalyst for direct methane oxidation are still intensively debated. Recently, Luo and coworkers [67-69] proposed that mononuclear Fe species are the active sites in the Fe/ZSM-5 zeolites by correlating a wide variety of characterization results with catalytic performance data. A set of Fe/ZSM-5 catalysts containing different contents of active components were prepared by a wet impregnation method on commercial H-ZSM-5 (Si/Al= 13.5) [67]. ^{57}Fe Mössbauer spectroscopy was applied to quantify and identify the three Fe species (mononuclear, oligonuclear (Fe_xO_y clusters, $x \geq 2$) clusters and metal oxide nanoparticles), as shown in Figure 1-28a and b. The Mössbauer spectroscopy indicated that the Fe species become less monomeric and more polymeric as the Fe loading increases, which was entirely consistent with the results of HAADF-STEM (High-angle annular dark-field scanning transmission electron microscopy), UV-vis DR and H_2 -TPR (Temperature-programmed reduction). They found that

only the proportion of mononuclear Fe species is positively correlated with the methanol productivity of the Fe/ZSM-5 catalysts among different Fe species (Figure 1-28b and c). With the aid of adjacent Brønsted acid sites (BAS), the 0.1% Fe/ZSM-5 catalyst with dominant mononuclear Fe species possess an excellent turnover rate (TOR) of $66 \text{ mol}_{\text{MeOH}} \text{ mol}_{\text{Fe}}^{-1} \text{ h}^{-1}$.

Despite Luo and coworkers having proven that monomeric Fe is the intrinsic active site and exhibits good CH₃OH productivity, it is still challenging to achieve high CH₃OH selectivity for 0.1Fe/ZSM-5 catalyst having the highest proportion of monomeric Fe due to the overoxidation of CH₃OH to HCOOH. In their further work, they systematically studied the influence of Cu species on the activity and selectivity of 0.1Fe/ZSM-5. A series of Cu-modified 0.1Fe/ZSM-5 catalysts with different Cu loadings from 0.1 to 3 wt.% has been prepared by the co-impregnation method. As shown in Table 1-2, the optimal Cu-Fe(2/0.1)/ZSM-5 catalyst containing dominant mononuclear Fe species, afforded a maximum TOR value of $431 \text{ mol}_{\text{MeOH}} \text{ mol}_{\text{Fe}}^{-1} \text{ h}^{-1}$ and 80% methanol selectivity without HCOOH observed. Based on multiple characterizations, they proved that Cu is present in Cu-Fe(2/0.1)/ZSM-5 mainly in the form of isolated Cu species located at the extraframework position of ZSM-5 with some CuO_x nanoparticles on the external surface of the zeolite. EPR measurements (Figure 1-29a) showed that a weak •OH signal was distinguished over 0.1Fe/ZSM-5, implying that Fe species slightly contributed to the generation of •OH, while an intense •OH signal peak was generated over 2Cu/ZSM-5 and Cu-Fe(2/0.1)/ZSM-5, indicating that Cu species rather than Fe promoted the formation of •OH. A quick decrease of •OH signal was observed over Cu-Fe(2/0.1)/ZSM-5 after the introduction of CH₄ into the reaction solution for 5 min (Figure 1-29b), along with the production of a significant amount of CH₃OH (659 μmol) observed from the time-on-line analysis. Based on this, they proposed that for CuFe(2/0.1)/ZSM-5 the reaction proceeded predominantly via route 1 in Figure 1-29c. In contrast, over 0.1Fe/ZSM-5 the main pathway follows route 2.

Table 1-2. Catalytic performances for the as-prepared catalyst.[68]

Catalyst	C1 products (mol/molFe)					TOR /h ⁻¹ ^a	CH ₃ OH Sel./% ^b
	CH ₃ OH	CH ₃ OOH	OHCH ₂ OOH	HCOOH	CO ₂		
Cu-Fe(0.1/0.1)/ZSM-5	66.8	25.9	21.7	113.3	10.3	134	27
Cu-Fe(0.5/0.1)/ZSM-5	169.9	20.2	20.4	118.5	6.9	340	49
Cu-Fe(1/0.1)/ZSM-5	209.4	18.5	28.6	84.6	9.3	419	60
Cu-Fe(2/0.1)/ZSM-5	215.6	16.6	29.7	0.0	9.1	431	80
Cu-Fe(3/0.1)/ZSM-5	160.9	15.3	26.5	0.0	8.6	322	76

Test conditions: 0.3 g of catalyst; 80 mL of 0.5 M H₂O₂ aqueous solution; 30 bar of CH₄; 50 °C, 0.5 h, 1500 rpm; 160 mL autolae reactor. ^aTOR is defined as mole (methanol)/mole (Fe)/time (h).

^bMethanol selectivity is calculated as moles (CH₃OH)/moles (produced) × 100.

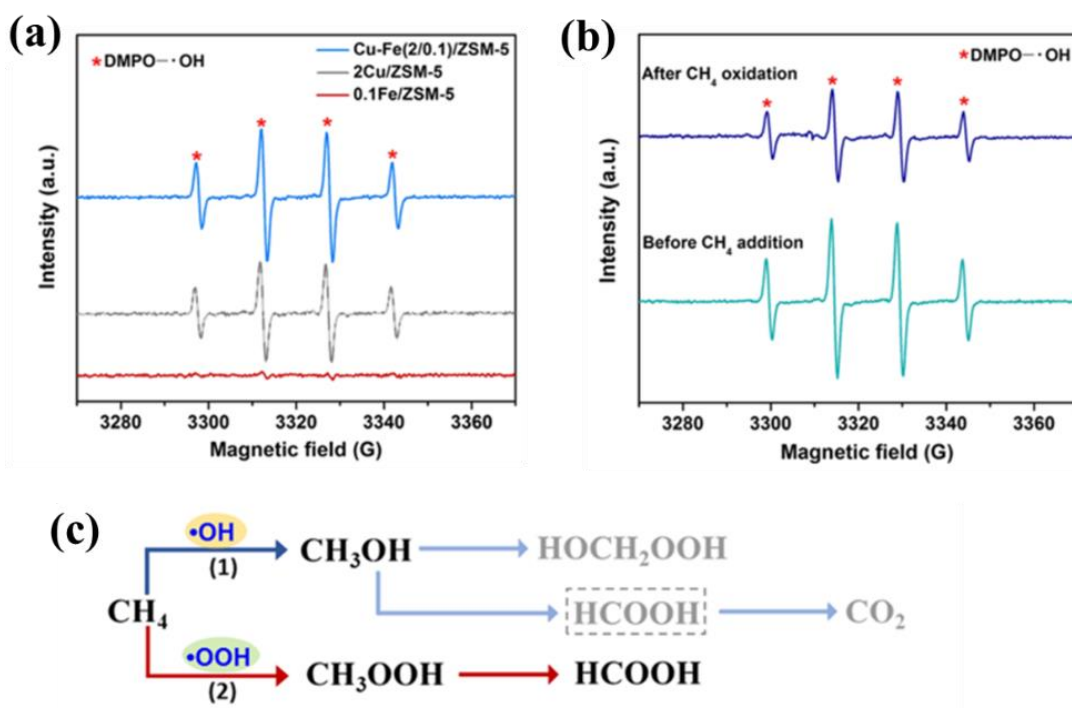


Figure 1-29. (a) EPR spectra obtained from a liquid sample after H_2O_2 decomposition over the 0.1Fe/ZSM-5, 2Cu/ZSM-5, and Cu-Fe(2/0.1)/ZSM-5 catalysts. (b) EPR trapping experiment with DMPO as the radical trapping agent over the Cu-Fe(2/0.1)/ZSM-5 catalyst with H_2O_2 as the oxidant. (c) Proposed reaction scheme for the oxidation of methane in a H_2O_2 -based heterogeneous system.[68]

1.4.3 Fe/MOR as catalyst

Zeolite topology is essential to the activity, which provides the appropriate geometric constraint around Fe or Cu to maintain ultrafine Fe-oxo or Cu-oxo sites that act as active sites. Mordenite (MOR), a natural zeolite, is attractive in catalysis because of its excellent ion exchange properties, thermal stability, availability and low cost [70]. Moreover, MOR micropores have been proven to provide a confined environment that helps stabilize trinuclear copper-oxo clusters for direct methane oxidation by a stepwise process [71]. As stated in [part 1.2.2](#), Cu-exchanged MOR zeolites have proposed active sites for CH_4 to CH_3OH conversion in the stepwise process involving monocopper, dicopper, tricopper species and larger Cu-oxo clusters. However, to the best of our knowledge, a metal-exchanged MOR catalyst is still relatively rare for mild methane oxidation using H_2O_2 under a batch reactor system.

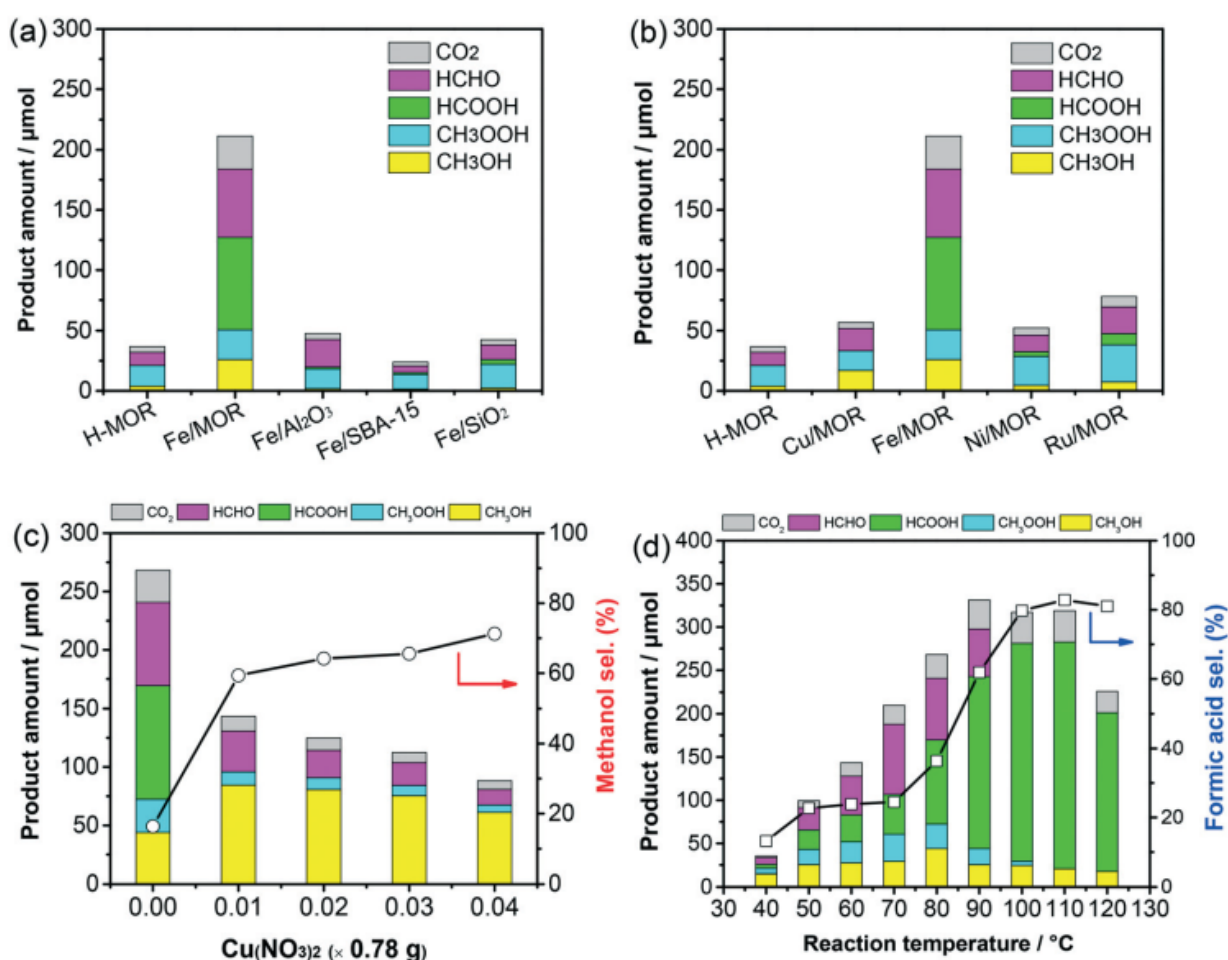


Figure 1-30. (a) Catalysts with 0.5 wt.% Fe loaded on different supports; (b) Different metals with 0.5 wt.% amount loaded on H-MOR catalyst; (c) Effect of the addition of different amounts of $\text{Cu}(\text{NO}_3)_2$ on the methanol selectivity of 0.5 wt.% Fe/MOR- H_2 catalyst; (d) Effect of the reaction temperature on 0.5 wt.% Fe/MOR- H_2 . Reaction condition: 20 mL of 0.5 M H_2O_2 solution, 30 bar of 95% CH_4/N_2 , 30 mg of catalyst, 1 h and 80 °C for a–c.[72]

In 2019, Liu and coworkers [72] reported that an active Fe/MOR catalyst synthesized via simple solid-state ion exchange proved to be active in the selective oxidation of methane with H_2O_2 as oxidant at 80 °C. In their work, they investigated the influence of different supports, different metals (like Cu, Ni, Ru), the addition of copper salt on the methanol selectivity, and the reaction temperature (see Figure 1-30). The authors hold that dimeric octahedral Fe^{3+} species $[\text{Fe}_2(\mu\text{-O})_2]$ in extra-framework position are the active sites as confirmed by XPS, XAS, UV-vis DRS, and HAADF-STEM in combination with DFT calculations. With 30 mg of 0.5 wt.% Fe/MOR- H_2 catalyst at 80 °C for 1 h, they could achieve around 240 μmol of C1 oxygenates with 89% selectivity and a TOF of 90 h^{-1} .

1.5. MOFs for direct methane oxidation with H_2O_2 as oxidant

1.5.1 Introduction to MOFs

MOFs, also known as porous coordination polymers (PCPs), have emerged as one of the most important advances in chemistry and materials since the first concept formulation in 1995 by O. M. Yaghi [73-76]. Metal-based nodes and organic bridging ligands construct MOFs to form crystalline frameworks with open and permanent porosities [75-78]. Unlike the traditional ordered porous materials (e.g., zeolites), various constituent units account for the enormous diversity of the MOF family. Based on the Cambridge Structural Database (CSD) collection, there are over 10,000 structures by March 2021, the number of which is still growing rapidly. Due to their high porosity and flexible and well-defined structure, MOFs have been used in versatile applications, such as gas storage and separation, chemical sensors, and optical or catalysis [78,79-81]. Among these applications, exploring MOFs as heterogeneous catalysts is one of the most promising research areas, which has received tremendous interest and achieved significant progress.

Modern developments of catalysis require deeply understanding of the mechanism and structure-activity relationship to improve catalytic performance, which facilitates rational catalyst development. An excellent example from nature is enzymes, presenting superior catalytic performance in many fields (e.g., methane oxidation). Therefore, mimicking enzymes (such as MMO enzymes) by artificial catalyst design has been a coveted target and attracted much attention and effort [82-83]. In general, besides central metal sites, allosteric sites from pockets of enzymes play a key role in activating substrates, highlighting the influence of secondary coordination environments.

Compared to other traditional catalysts (such as zeolites or inorganic metal oxides), MOFs are considered to possess the following advantages. (1) Ultrahigh porosity facilitates a good dispersion of the active sites, which is highly favorable for superior activity, selectivity. (2) MOFs are structurally diverse and can provide various catalytic sites. (3) Flexible structures can allow for fine-tuning of catalytic microenvironments. Whether coming from pristine frameworks or pore environments, the surrounding of the active site in MOFs can be regarded as a secondary coordination environment, influencing the catalytic behavior [84]. (4) Crystalline nature of the MOFs guarantees a well-defined structure, reducing the difficulty in characterization.

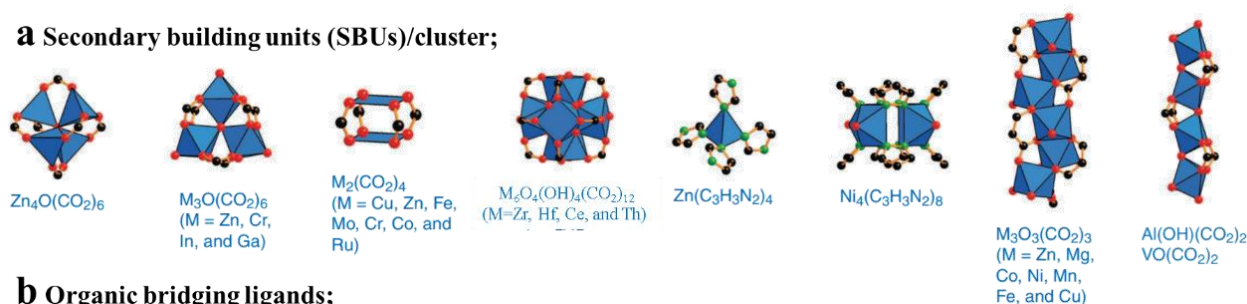
1.5.2 Key Elements of MOFs

1.5.2.1 Metal nodes and organic bridging ligands

As the inorganic part of MOFs, metal nodes are polynuclear metal clusters, also called secondary building units (SBUs), rather than single metal sites. Common SBUs are shown in

Figure 1-31a. SBUs generally possess good stability, which is thermodynamically favorable and can promote the formation of robust frameworks. However, the stability of the whole framework also depends a lot on the strength of the coordination bonds. Hard-Soft-Acid-Base (HSAB) theory is a practical tool to assess the stability of a MOF (**Figure 1-32**). Generally, high-valent metal ions (hard acids, such as Al^{3+} , Zr^{4+}) would prefer to coordinate with O atoms (hard base, mostly from carboxylic acid) (see **Figure 1-31b**), giving strong bonding. On the other hand, low-valent metal ions (soft base, such as Zn^{2+} , Cu^{2+}) tend to form stable bonding with N sites (soft base, mostly from azoles). Versatile ligands contribute a lot to the diversity of MOFs.

a Secondary building units (SBUs)/cluster;



b Organic bridging ligands;

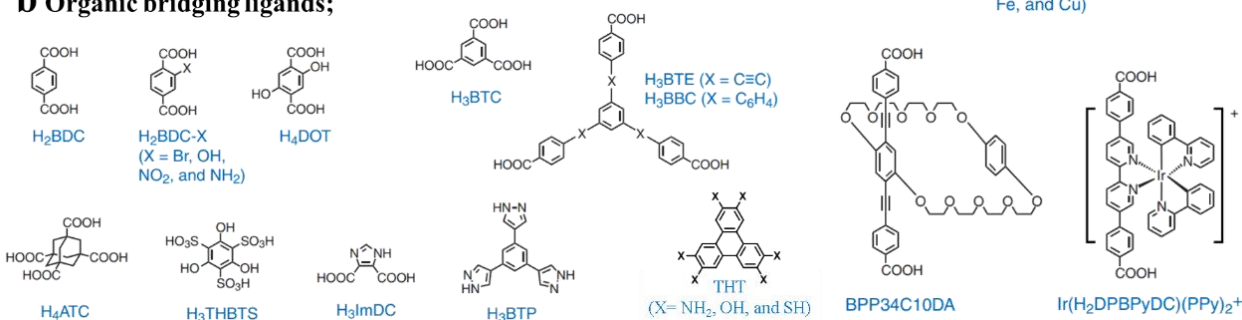


Figure 1-31. Typical SBUs (a) and organic ligands (b).^[75]

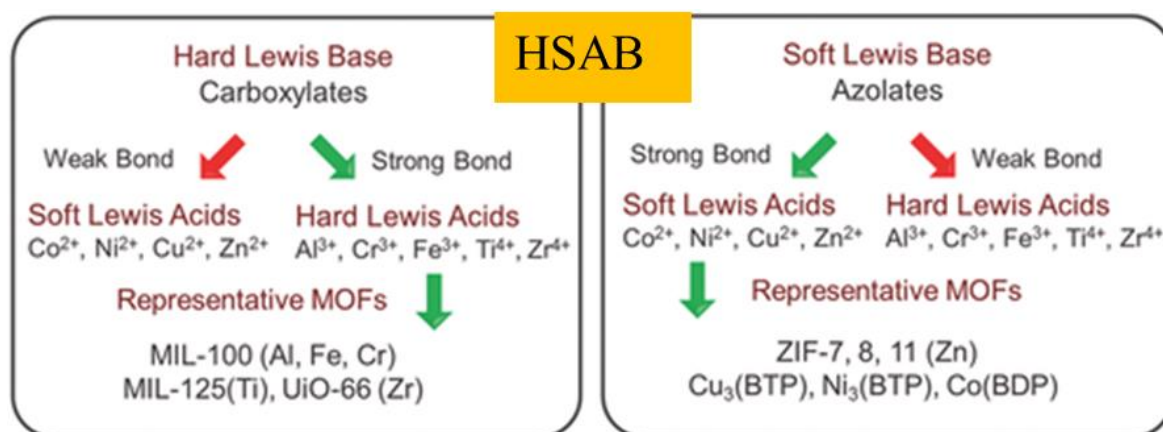


Figure 1-32. HSAB theory upon MOFs.^[85]

1.5.2.2 Flexible structure and topology

MOFs inherit the structural features of their inorganic and organic components. Their building units, including ligands and metal SBUs, can be replaced by counterparts with similar structures

to develop a series of isorecticular MOFs. For example, the ligand was replaced by equally linear but longer ligands to possess larger pore channels. Besides the replaceable ligands, the metal SBUs can also be tailored. Hexa-zirconium (Zr_6) cluster, a well-adopted SBU for its superior stability, can also be replaced by Cerium (Ce), Hafnium (Hf), and some of Lanthanide (Ln) group metals to form similar MOF structure.

1.5.2.3 Crystalline nature

Most MOFs can form single crystals, indicating their ordered periodic structure. The structure can be determined by single Crystal-X ray diffraction (SC-XRD), one of the most effective ways to elucidate the structure. Generally, coordination bonds are the main bonding type in MOFs, regarded as secondary covalent bonds with weak bonding energy. Weaker bonding also means larger reversibility, indicating flexible bonding. Solvothermal methods are the most common methods for MOFs synthesis. Considering the reversible bonding and enthalpy driven crystallization process, the key to MOFs crystallization is that components undergo multiple bonding-breaking-rearrangement steps to grow into a perfect crystal (Figure 1-33) [86].

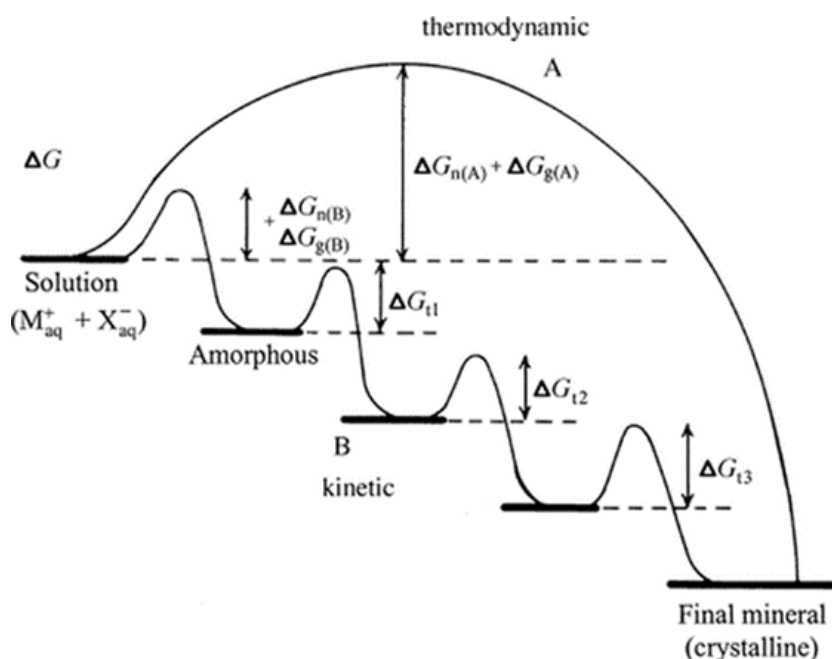


Figure 1-33. Crystallization pathways of MOFs considering multiple steps.[86]

1.5.2.4 Open framework with permanent porosity

One key parameter to distinguish MOFs from inorganic-organic hybrids or coordination polymers is maintaining an open and porous structure, even after removing filler. Even when possessing rigid frameworks, frameworks with too short ligands (such as metal-cyanide frameworks) are not regarded as open frameworks. Frameworks constructed by very soft or

unstable ligands can shrink and lose porosity upon removing the filler. All these materials will not be regarded as MOFs.

1.5.3 Advantages of MOFs in Catalysis

1.5.3.1 Ultrahigh surface area and porosity

Compared with a traditional porous material, MOFs possess superior surface area and porosity (Figure 1-34) [75]. The new record of MOFs material in porosity is DUT-60, which possesses a BET area of $7839 \text{ m}^2 \cdot \text{g}^{-1}$ and pore volume of $5.02 \text{ cm}^3 \cdot \text{g}^{-1}$ [87]. Ultrahigh surface area and porosity allow a high dispersion of active sites. If the active sites are part of pristine MOFs, their dispersion can be very close to homogenous catalysts. Moreover, the relatively large pore textures can offer smooth mass transport of substrates.

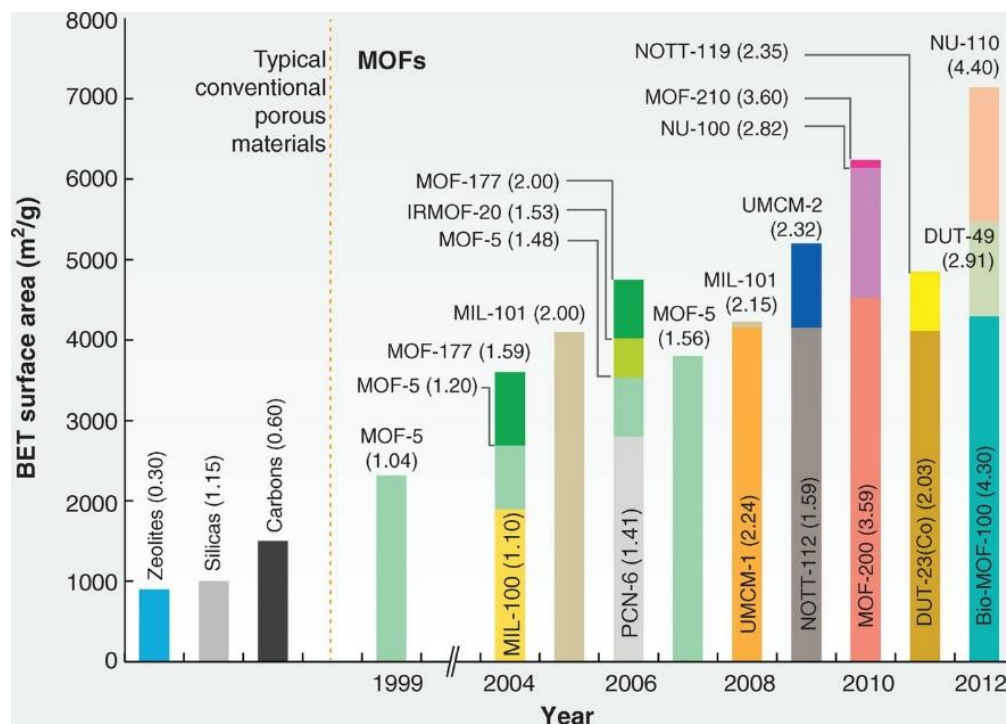


Figure 1-34. Comparison of MOFs with traditional porous materials. The pore volume ($\text{cm}^3 \cdot \text{g}^{-1}$) is listed in brackets. [75]

1.5.3.2 Diverse active sites

MOFs own abundant active sites, either from their pristine structure or the guest molecules. To be specific: (Figure 1-35) [81]

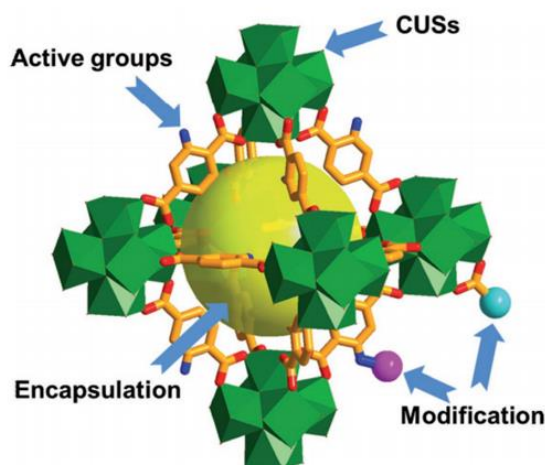


Figure 1-35. Strategies to incorporations of active sites in MOFs. CUSs means coordinatively unsaturated metal sites.[81]

(1) Metal cluster from pristine MOFs. Some SBUs have open sites, also called coordinatively unsaturated metal sites (CUSs), regarded as Lewis acid sites. Even though the metal SBUs are fully coordinated, defect sites are inevitable and CUSs can also be created on purpose by facile treatments. Besides, coordinating atoms, generally bridging oxygens, can serve as Lewis bases. Some bridging -OH or μ_3 -OH groups also have weak Brønsted acidity. What's more, the metal center in SBUs can be served as an electron acceptor or donor to drive redox reaction.

(2) Ligands from pristine MOFs. Functional groups on the ligand can supply various active sites. For example, sulfonic acid group/amino groups can serve as acid/base sites. Some ligands themselves are functional molecules such as metal-porphyrins, salens, metal-bipyridine complex.

(3) Post-modification based on SBUs or ligands. Besides the direct synthesis of isorecticular MOFs, flexible structures of MOFs allow the post-modifications based on pristine MOFs. The post-modifications can be applied to every component in MOF (Figure 1-36), such as post-synthetic Exchange (PSE),[88] post synthetic modification (PSM),[89] atomic layer deposition in MOF (AIM), solvent-assisted ligand incorporation (SALI) [90].

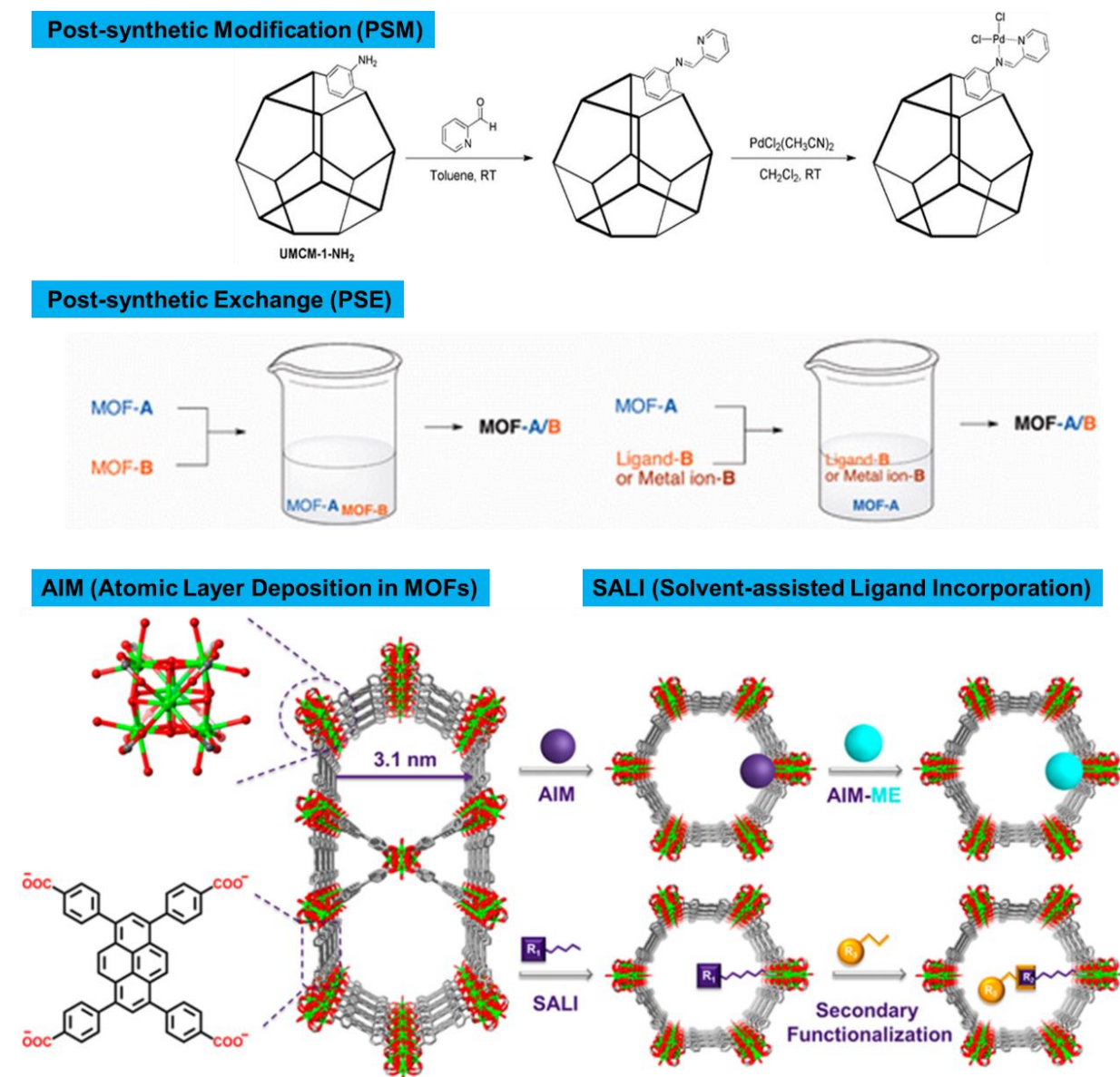


Figure 1-36. Some examples or scheme of PSM, PSE, AIM and SALI. [88-90]

(4) Encapsulated guest molecules: The pore volume is suitable for hosting guest compounds, either prepared by one-pot synthesis or post-casting [91]. The large pore volume can increase the loading. Confinement effects can also stabilize guest compounds and influence catalytic activity. A synergistic effect between guests and MOFs can also be expected.

1.5.4 MOFs for direct methane oxidation

Zeolites stabilize binuclear iron and copper centers in a form similar to that found in methane monooxygenase (MMO) enzymes. Especially ZSM-5 and mordenite, artificially mimic the activity of MMOs with great success. However, the relatively poor adjustability of active sites in zeolites results in ill-defined active sites. The nature of the active sites in iron- and copper-containing zeolites remains largely a matter of speculation. These weaknesses can be conquered

to some degree by using MOF support materials. Like zeolites, MOFs have high porosity, and they have customizable pore microenvironments via post-synthetic modification of linkers, nodes, and guest molecules. Additionally, MOFs are typically highly crystalline with ordered structures suited for characterization by single crystal and/or powder diffraction techniques. It facilitates the design of well-defined heterogeneous catalysts, making them appealing in this regard. Up to now, there are still very limited examples of MOF-based catalysts for selective methane oxidation to methanol. However, each example is representative and provides instructive design and structure regulation of MOF catalysts for future work.

1.5.4.1 Fe/MIL-53 for methane oxidation by H₂O₂

Dmitrii et al. [92] introduced isolated, well-dispersed Fe sites into the Al-based chain MOF MIL-53 to get MIL-53(Fe, Al) mixed-metal catalyst, which showed good activity and selectivity in the oxidation of methane to methanol with H₂O₂ as the oxidant at 60 °C and 30 bar of CH₄. The selected support matrix MIL-53(Al) is built from non-redox-active AlO₆ octahedral chains connected by 1,4-benzodicyclohexadiene acid struts to form well-defined 1D channels (Figure 1-37) [93]. They speculated that such a metal–oxo chain structure of MIL-53 should be able to accommodate isolated Fe species with a coordination environment close to that of the sMMO active site (as shown in Figure 1-37b and c). An electrochemical synthesis method achieved a highly homogeneous distribution of Fe sites within the lattice of MIL-53 with Fe content in the range from 0.3 to 5.5 wt.%. The catalyst displays a good activity with TOFs in 90 h⁻¹ and selectivities to oxygenates of ca. 80%.

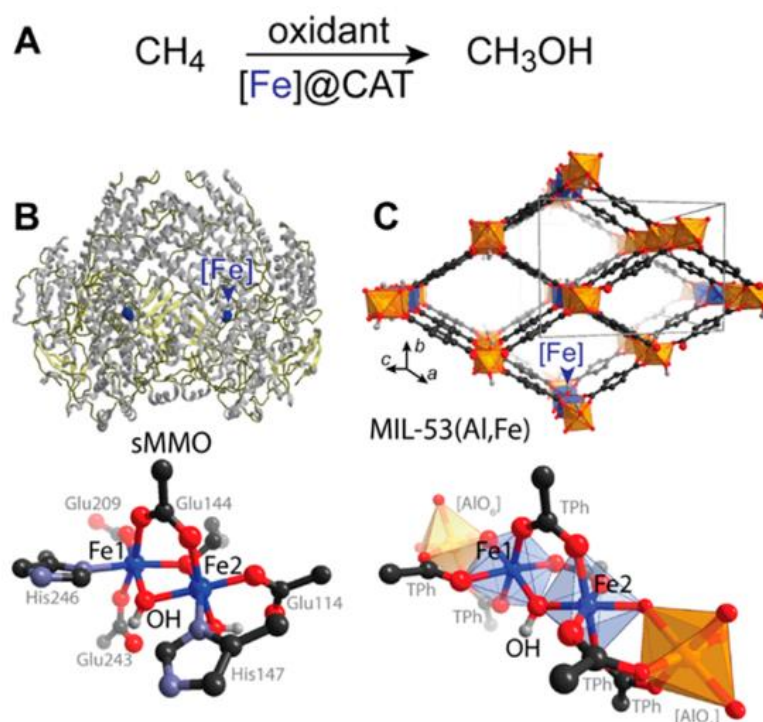


Figure 1-37. (A) Reaction system of the direct methane oxidation; (B) Structure of sMMO enzyme, where each $\alpha_2\beta_2\gamma_2$ dimer contains two diiron active sites; (C) MIL-53(Al, Fe) catalyst with a site-isolated Fe within the MIL-53 octahedral $[\text{AlO}_6]$ chain. (Blue spheres represent Fe.)[92]

After a comprehensive characterization, Zhao et al. revealed that the dimeric (Fe_2 -MIL-53(Al)) and monomeric (Fe_1 -MIL-53(Al)) Fe complexes generated from isomorphous substitution of Al by Fe ions in MIL-53 are the active sites. Such Fe sites are located in a unique octahedral weak ligand field environment that is expected to be favorable for C–H bond activation [94]. DFT calculations indicated that despite different oxidation states, the activities of monomeric and dimeric species are comparable, and they promote the same reaction steps. Based on spectroscopic characterization and DFT calculations, they proposed a possible minimum energy reaction pathway from CH_4 to CH_3OH with H_2O_2 over the dimeric Fe sites in MIL-53(Al, Fe) (as shown in Figure 1-38). The mechanistic studies were later extended, using the same methodology, considering the full reaction network, including the formation of the active sites, overoxidation of methane to CO_2 , and decomposition of H_2O_2 to H_2O and O_2 [95].

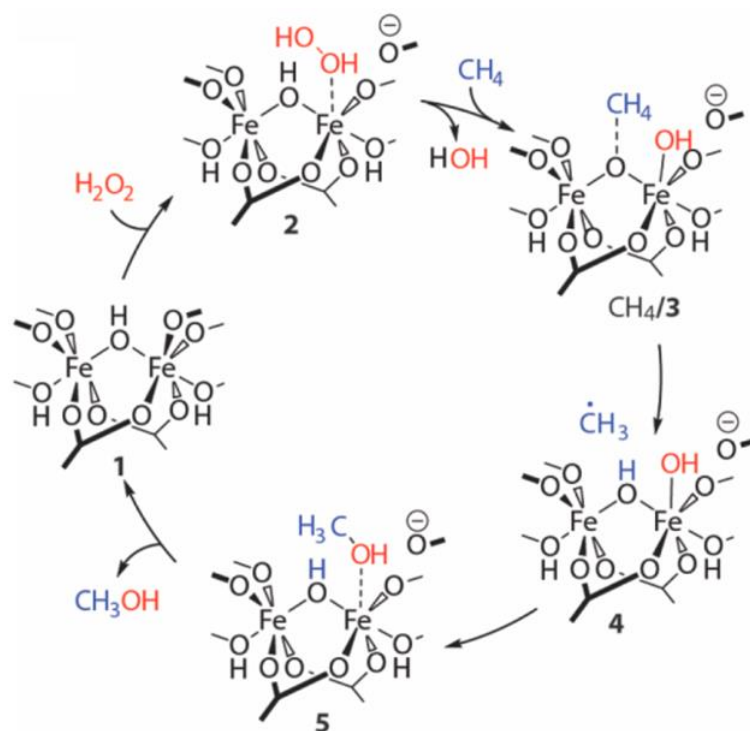


Figure 1-38. Proposed mechanism of methane to methanol oxidation with H_2O_2 over the dimeric Fe site in MIL-53(Al,Fe).[95]

In their work, they raised two problems concerning Fe-based MOF catalysts for methane selective oxidation with H_2O_2 as oxidant, which provides strong reference for later work. Firstly, it is about the stability issue of MIL-53 catalyst during catalytic reactions. The catalytic reaction was performed below $60\text{ }^\circ\text{C}$, because the MIL-53(Al,Fe) catalysts were not stable in aqueous H_2O_2 at higher temperatures ($>80\text{ }^\circ\text{C}$). They also prepared the counterpart MIL-53(Al,Fe) catalysts (named HTS) using the direct hydrothermal synthesis method as control experiments. The Fe leaching into the H_2O_2 aqueous solution and the formation of lots of peroxidation products for HTS samples with high Fe content (5.4 and 16.6 Fe wt.%, respectively) was observed. Furthermore, the presence of dissolved linker in solution and partial decomposition of MOF structure was observed. To obtain high MOF catalyst stability, using a non-redox scaffold is crucial. Secondly, it is about the competing self-decomposition reaction of H_2O_2 to H_2O and O_2 , which undermines H_2O_2 utilization efficiency and limits the overall efficiency of the catalytic system. The catalytic reaction is inevitably accompanied by the self-decomposition of H_2O_2 , which is used as the oxidant. Based on the DFT calculations, the computed reaction energy diagrams indicate that the self-decomposition of H_2O_2 is strongly kinetically favored over methane activation. Typically, the H_2O_2 utilization efficacy of Fe/Zeolites (around 20-50%) is about one order of magnitude higher than that of the Fe/MOF catalyst (around 1-5%).

1.5.4.2 Fe/UiO-66 for methane oxidation by H₂O₂

Due to their superior stability, Zr₆ based MOFs are widely studied in heterogeneous catalysis. In particular, -OH and -OH₂ groups on the metal nodes of Zr₆ based MOFs could act as the anchoring sites for active components, offering precise catalyst design of the catalyst at the molecular level [96]. Zhao et al. [97] reported that Fe-O clusters on Zr₆ nodes of UiO-66 (Zr₆(OH)₄O₄(BDC)₆, BDC =benzene-1,4-dicarboxylate) modulated with trifluoroacetic acid (TFA) can successfully catalyze methane oxidation with H₂O₂ as the oxidant at 50 °C in the autoclave reactor. Figure 1-39 shows the synthesis steps of UiO-66(2.5TFA)-Fe (with a composition of Zr₆O_{4.17}(OH)_{3.83}(BDC)_{4.29}(HCOO)_{0.75}(TFA)_{2.50}) catalysts and contrast sample UiO-66(0.37AA)-Fe (AA represents acetic acid), involving: (1) competitive coordination of Zr⁴⁺ ion with monocarboxylic modulator (TFA or AA) over bicarboxylic H₂BDC ligand to form the variant UiO-66,[98] (2) abstracting hydrogen atoms from -OH/-OH₂ groups in UiO-66, (3) anchoring Fe-O clusters to obtain the catalysts with 2.2 wt.% and 3.0 wt.% Fe inside, respectively.

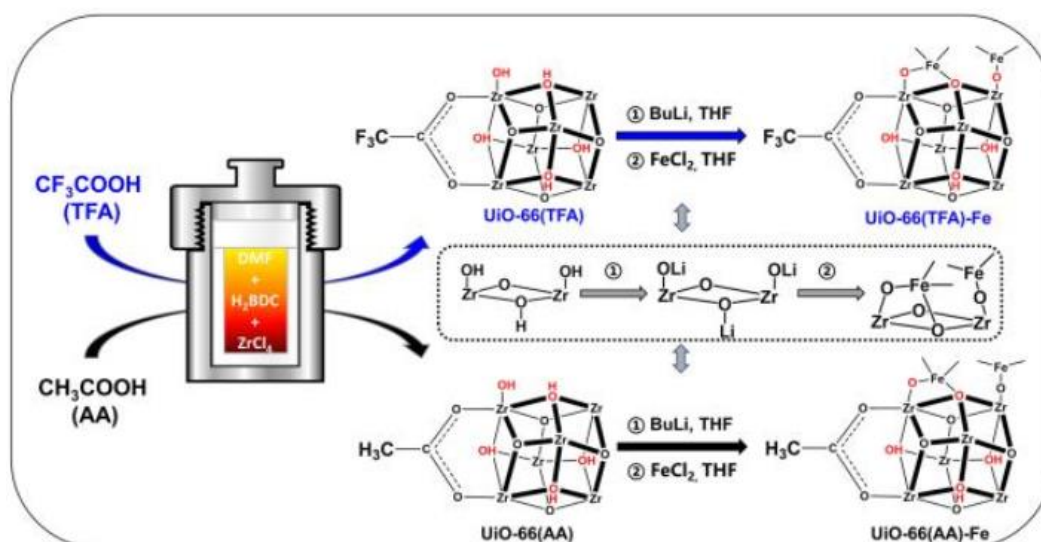


Figure 1-39. Scheme of synthesizing Zr₆ nodes coordinated with TFA or AA and then anchoring Fe sites on Zr₆ nodes.[97]

Based on XPS and XAS measurements, the authors argued that the TFA group coordinated to the Zr₆ node of UiO-66 enhances the oxidation state of the adjacent Fe-O cluster due to its electron-withdrawing ability originating from the higher electronegativity of F (4.1) in TFA than H (2.1) in AA. The experiments and theoretical calculation results further proved that the TFA groups promoted the activation of the C-H bond of methane and significantly enhanced catalytic activity of the adjacent Fe-O clusters, thus leading to the high C1 oxygenated yield of 4799 μmol gcat⁻¹ h⁻¹ with 97.9% selectivity, ~8 times higher than those modulated with AA. The theoretical

calculation results and EPR detection of active oxygen species show the reaction pathway for direct methane oxidation catalyzed by UiO-66(TFA)-Fe in [Figure 1-40](#).

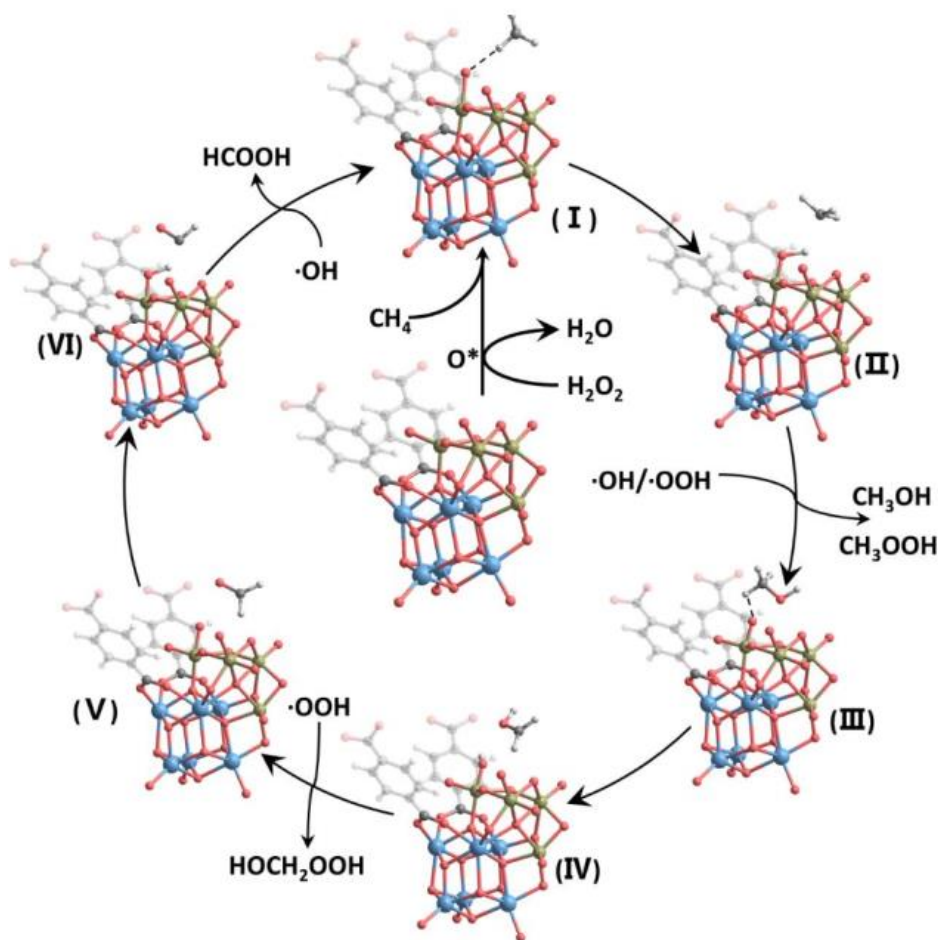


Figure 1-40. Scheme of reaction pathway for methane oxidation with H_2O_2 as oxidant catalyzed by UiO-66-Fe. Color scheme: light gray for hydrogen, dark gray for carbon, red for oxygen, blue for zirconium and brown for iron.[97]

1.6 Comparison of state-of-the-art catalysts for direct methane oxidation with H_2O_2 as oxidant

[Table 1-3](#) summarizes the catalytic performance of the representative catalysts discussed in part [1.3](#), [1.4](#) and [1.5](#).

Table 1-3. The representative catalysts of low-temperature methane oxidation with H_2O_2 as oxidant.

Catalyst (Metal loading)	Reaction condition	Oxygenates selectivity (%)	Product distribution (%)	P_{cat} ($\text{h}^{-1} \text{mg}^{-1}$) ^a P_{metal} ($\text{h}^{-1} \text{mg}^{-1}$) ^b	TOF (h^{-1}) ^c	Ref.
AuPd/TiO ₂ (1wt.%)	30.5bar CH ₄ , 0.5M H ₂ O ₂ , 50°C, 0.5h	85.4%	MeOH (12.1%) MeOOH (73.4%)	0.50 μmol 5.9 μmol	6.85	[42]

Au-Pd colloids (6.6 μmol of metal)	30bar CH_4 , 5bar O_2 , 50 μmol H_2O_2 , 50 $^\circ\text{C}$, 0.5h	92%	MeOH (14%) MeOOH (78.5%)	/ 39.4 μmol	9.2	[43]
AuPd@ZSM-5- C_{16} (3.24 wt.% Au, 1.76 wt.% Pd)	30bar (3.3% H_2 , 6.6 O_2 , 1.6 CH_4), 0.5h, 70 $^\circ\text{C}$	100%	MeOH (92%) HCOOH (8%)	4.6 μmol 91.6 μmol	14.8	[44]
Rh_1/ZrO_2 (0.3 wt.%)	~30bar CH_4 , 0.5M H_2O_2 , 70 $^\circ\text{C}$, 0.5h	78.5%	MeOH (64.1%) MeOOH (14.4%)	0.036 μmol 12 μmol	2.6	[48]
$\text{Pd}_1\text{O}_4/\text{ZSM-5}$ (0.01 wt.%)	30bar CH_4 , 0.5M H_2O_2 , 50 $^\circ\text{C}$, 0.5h	96.2%	MeOH (6.6%) MeOOH (35.3%) HCOOH (54.3%)	7.7 μmol $7.7 \times 10^4 \mu\text{mol}$	8820	[49]
SAs Rh-Ce O_2 NWs (0.29 wt.%)	0.5 MPa CH_4 , 1 M H_2O_2 , 50 $^\circ\text{C}$, 1h, 10 mg	93.9%	MeOH (71.7%) MeOOH (22.8%)	3.57 μmol 1231.7 μmol	126.7	[50]
$\text{FeO}_x/\text{TiO}_2$ (0.33 wt.%)	atmospheric pressure CH_4 , 0.8 mM H_2O_2 , 25 $^\circ\text{C}$, light irradiation, 3h	97%	MeOH (90%)	0.35 μmol 107 μmol	6	[51]
Fe-NC SACs (2.7 wt.%)	20bar (CH_4 , N_2), 4.9M H_2O_2 , 25 $^\circ\text{C}$, 10h	93.7%	MeOH (4.8%) MeOOH (35.6%) OHCH $_2$ OOH (27%) HCOOH (30.5%)	0.23 μmol 8.4 μmol	0.47	[52]
CNT@PNC/ Ni SAs (~0.68 wt.%)	20bar CH_4 , 4.9M H_2O_2 , 50 $^\circ\text{C}$, 10h	100%	MeOH (94.2%) MeOOH (5.8%)	1.1 μmol 156.3 μmol	1.4	[53]
Cu-SAs/ C_3N_4 (1 wt.%)	30bar CH_4 , 3.4M H_2O_2 , 25 $^\circ\text{C}$, 5h	95%	MeOH MeOOH	1.02 μmol 102 μmol	6.7	[54]
Cr_1/TiO_2 (1 wt.%)	30bar CH_4 , 0.5M H_2O_2 , 50 $^\circ\text{C}$, 1h	93%	MeOOH (37.1%) OHCH $_2$ OOH (44%)	4.39 μmol 439 μmol	22.8	[55]
H-ZSM-5 (0.014 wt.%)	30bar CH_4 , 0.5M H_2O_2 , 50 $^\circ\text{C}$, 0.5h, 27mg	95%	MeOH (20%) MeOOH (23.0%) HCOOH (57%)	$2.85 \times 10^3 \mu\text{mol}$ $2.03 \times 10^7 \mu\text{mol}$	2278	[64]
0.1%Fe/ H-ZSM-5	30bar CH_4 , 0.5M H_2O_2 , 50 $^\circ\text{C}$, 0.5h, 0.3g	97%	MeOH (16.4%) MeOOH (23.0%) OHCH $_2$ OOH (18%) HCOOH (40%)	$3.5 \times 10^3 \mu\text{mol}$ $3.5 \times 10^6 \mu\text{mol}$	209	[67]
Fe/MOR- H_2 0.5 wt.%)	30bar CH_4 , 0.5M H_2O_2 , 80 $^\circ\text{C}$, 1h	89	MeOH (16%) HCOOH (40%) HCHO (32%)	$8 \times 10^3 \mu\text{mol}$ $1.6 \times 10^6 \mu\text{mol}$	90	[72]
MIL-53(Fe,Al) 0.34 wt.%)	30 bar CH_4 , 60 $^\circ\text{C}$, 1h, 0.5M H_2O_2 ,	80%	MeOH (60%) HCOOH (20%)	5 μmol 804 μmol	90	[92]
UiO-66(2.5TFA)-Fe (2.2 wt.%) Fe)	30bar CH_4 , 0.5M H_2O_2 , 50 $^\circ\text{C}$, 1h	97%	OHCH $_2$ OOH (21%) HCOOH (63%)	4.8 μmol 218 μmol	12	[97]

^aProductivity_{cat}(h⁻¹ mg⁻¹) = molar mass of C1 oxygenates(μmol)/[mass of catalyst(mg) \times reaction time(h)]; ^bProductivity_{metal}(h⁻¹ mg⁻¹) = molar mass of C1 oxygenates(μmol)/[mass of active metal(mg) \times reaction time(h)]; ^cTOF(h⁻¹) = molar mass of C1 oxygenates(μmol)/[molar mass of active metal(μmol) \times reaction time(h)].

2. Motivation and objectives

Among a number of direct CH₄ conversion routes to high-value chemicals, methanol as a target product has received particular attention as methanol can be economically transported and directly used as a feedstock for the production of chemicals. However, this dream reaction remains a grand challenge because it is tough to achieve high CH₄ conversion and CH₃OH selectivity simultaneously, making it still far from industrially usable. H₂O₂ has been proved a green, environmental-friendly, highly-efficient oxidant for CH₄ oxidation to C1 oxygenates, including CH₃OH, CH₃OOH, OHCH₂OOH and HCOOH, through a radical reaction pathway under mild conditions. However, as summarized in [Table 1-3](#), the productivity of C1 oxygenates over the known catalysts with mainly oxides or carbon materials as supports is still relatively low when considering the high consumption of more expensive H₂O₂. This drawback is always the core issue that hampers the large-scale application of direct methane oxidation. Thus, a more efficient catalytic system with considerable productivity is urgent. Learning from the known active catalysts, atomically dispersed metal sites, especially for iron/copper-based catalysts, are favored for promoting the methane oxidation. The tiny metal particles of nanometers or sub-nanometers mainly promote the undesirable side reactions, i.e., H₂O₂ decomposition. Anchoring metal centers in confined space, like micropores, effectively restricts migration and aggregation. Meanwhile, by the analogy with the reaction process of MMOs, the confinement of reactants will be a favorable factor for bringing important small-molecule reactants together with the active sites. Thus, zeolites and MOFs materials with a microporous structure, large specific surface and high exposure to active sites have been widely used as supports to fabricate stable atomically dispersed metal catalysts. These motifs have unusual electronic and chemical properties and display exceptional catalytic performances, including direct methane oxidation. What's more, both zeolites and MOFs have proven capable of duplicating the Fe or Cu sites similar to the configuration found in MMOs, exhibiting impressive reactivity on DMTM.

The work presented in this thesis focused on the direct methane oxidation to C1 oxygenates using aqueous H₂O₂ as an oxidant over mainly metal-modified zeolite and MOF materials. They are briefly summarized as follows:

① MOFs, constructed from metal sites coordinated with functional organic linkers, are a new class of porous crystalline materials. Different from the rigid structure and debated active sites after heat treatment of zeolite catalysts, either metal nodes or organic linkers in MOFs can be easily functionalized and designed to create well-defined catalytic sites. So far, there are still minimal examples of MOF-based catalysts for DMTM reaction. By screening for stable MOF catalysts, we

could design and construct an efficient active site in these frameworks adopting diversified modification methods based on the confinement effect, open metal nodes and tunable organic linkers of MOFs to discover more catalytic systems for the DMTM reaction.

② Fe and Cu based zeolites have distinctive advantages in the DMTM process. Compared with a wide array of zeolite frameworks that have been shown to host copper and exhibit impressive CH₃OH selectivity using O₂, only Fe/MFI catalyst in H₂O₂ system has received broad interest in the last decade. Although Fe/MOR catalyst has been confirmed to be active, it still lacks sufficient exploration. We hope to further optimize the synthesis of Fe/MOR catalysts and give in-depth exploration of active sites.

③ In recent years, several renowned groups have contributed to figuring out the precise configuration of Cu/zeolite. However, since it was first discovered that MFI could host binuclear iron to exhibit unique activity with TOF of up to 2200 h⁻¹ on direct methane conversion in H₂O₂, such distinctive performance has only been found in MFI and most follow-up studies concentrated on optimizing synthesis and adjusting reaction parameters. The special topology and microporous structure of MFI that can confine atomically dispersed Fe, will also suffer the diffusion problem to limit the number of active Fe sites. We hope to reduce the MFI from 3D to 2D, aiming to boost mass transfer to improve its performance further.

3. Experimental methods

3.1 Chemicals

All the chemicals used in this work are listed in [Table 3-1](#). All the chemicals were used as received without further purification.

Table 3-1 Chemicals used in this work.

Chemical	Purity, Producer
Methane 4.5, CH ₄	99.995 vol. %, Westfalen AG
Deionized water, DI-H ₂ O	In-house made
Double-distilled water, DD-H ₂ O	In-house made
Deuterium oxide, D ₂ O	99.9 atom % D, Sigma-Aldrich
Deuterium oxide with 0.75wt.% TMSF	99.9 atom % D, D ₂ O with 3-(trimethylsilyl)propionic-2,2,3,3-d ₄ acid, sodium salt, Sigma-Aldrich
Hydrogen peroxide solution, H ₂ O ₂	≥ 30%, Sigma-Aldrich
Methanol, MeOH	HPLC Plus, ≥99.9%, Sigma-Aldrich
Formaldehyde solution, HCHO	37 wt. % in H ₂ O, Sigma-Aldrich
Formic acid, HCOOH	For hplc, Sigma-Aldrich
Acetone	p.a. In-house chemical store
Acetonitrile, MeCN	p.a., In-house chemical store
Ethanol, EtOH	p.a., In-house chemical store
Toluene	p.a., In-house chemical store
Diethyl ether	p.a., In-house chemical store
N, N-Dimethylformamide, DMF	p.a., In-house chemical store
Sulfuric acid, H ₂ SO ₄	98%, In-house chemical store
Nitric acid, HNO ₃	65%, In-house chemical store
Acetic acid, CH ₃ COOH	≥99%, Sigma-Aldrich
Ferroun indicator solution	Fluka
Polydimethylsiloxane, PDMS	SYLGARD® 184, Sigma-Aldrich
1-bromodocosane	98%, Sigma-Aldrich
<i>N,N,N',N'</i> -tetramethyl-1,6-diaminohexane	99%, Sigma-Aldrich
1-bromohexane	98%, TCI
1,4-benzenedicarboxylic acid, H ₂ BDC	98%, ACROS
1,3-benzenedicarboxylic acid, 1,3-H ₂ BDC	99%, AlfaAesar
2,6-pyridinedicarboxylic acid	99%, Sigma-Aldrich
1,3,5-benzenetricarboxylic acid (H ₃ btc)	98%, AlfaAesar
4,4'-Biphenyldicarboxylic acid, H ₂ BPDC	97%, Sigma-Aldrich,
trimethyl-1,3,5-trimesate, btcMe ₃	98%, TCI
2-methylimidazole, H-MeIM	99%, Sigma-Aldrich
2,5-dihydroxy-1,4-benzenedicarboxylic acid, H ₂ -DHBDC	98%, TCI
3,3',5,5'-azobenzenetetracarboxylate, ABTC	97%, Sigma-Aldrich
Sodium acetate trihydrate, CH ₃ COONa·3H ₂ O	p.a., In-house chemical store
Sodium hydroxide, NaOH	p.a., In-house chemical store

Aluminium Sulfate Octadecahydrate, $\text{Al}_2(\text{SO}_4)_3 \cdot 18\text{H}_2\text{O}$	98%, Carl Roth
Aluminum nitrate nonahydrate, $\text{Al}(\text{NO}_3)_3 \cdot 9\text{H}_2\text{O}$	98%, Sigma-Aldrich
Iron (III) acetylacetonate, $\text{Fe}(\text{acac})_3$	p.a., In-house chemical store
Iron(II) chloride, $\text{FeCl}_2 \cdot 4\text{H}_2\text{O}$	p.a., 99%, Sigma-Aldrich
Iron(III) chloride hexahydrate, $\text{FeCl}_3 \cdot 6\text{H}_2\text{O}$	99+%, AlfaAesar
Iron(III) nitrate nonahydrate, $\text{Fe}(\text{NO}_3)_3 \cdot 9\text{H}_2\text{O}$	$\geq 99\%$, Fluka
Chromium(III) acetylacetonate, $\text{Cr}(\text{acac})_3$	98%, TCI
Chromium(III) chloride, CrCl_3	p.a., In-house chemical store
Chromium(III) chloride hexahydrate, $\text{CrCl}_3 \cdot 6\text{H}_2\text{O}$	p.a., In-house chemical store
Cobalt(II) acetylacetonate, $\text{Co}(\text{acac})_2$	99%, Sigma-Aldrich
Cobalt(II) acetate tetrahydrate, $\text{Co}(\text{CH}_3\text{COO})_2 \cdot 4\text{H}_2\text{O}$	99%, Fluka
Cobalt(II) nitrate hexahydrate, $\text{Co}(\text{NO}_3)_2 \cdot 6\text{H}_2\text{O}$	98%, Sigma-Aldrich
Cerium(IV) sulfate tetrahydrate, $\text{Ce}(\text{SO}_4)_2 \cdot 4\text{H}_2\text{O}$	p.a., In-house chemical store
Copper(II) acetylacetonate, $\text{Cu}(\text{acac})_2$	98%, Sigma-Aldrich
Copper(II) nitrate trihydrate, $\text{Cu}(\text{NO}_3)_2 \cdot 3\text{H}_2\text{O}$	p.a., In-house chemical store
Manganese(II) chloride tetrahydrate, $\text{MnCl}_2 \cdot 4\text{H}_2\text{O}$	99%, Fluka
Manganese(II) acetylacetonate, $\text{Mn}(\text{acac})_2$	98%, TCI
Zinc chloride, ZnCl_2	98%, Fluka
Zinc nitrate hexahydrate, $\text{Zn}(\text{NO}_3)_2 \cdot 6\text{H}_2\text{O}$	98%, Sigma-Aldrich
Zirconium(IV) chlorid, ZrCl_4	98%, AlfaAesar
Vanadium(IV) oxide sulfate pentahydrate, $\text{VO}_2 \cdot \text{SO}_4 \cdot 5\text{H}_2\text{O}$	97%, Sigma-Aldrich
Tetraethyl orthosilicate, TEOS	$\geq 99\%$, Sigma-Aldrich
Zeolite SAPO-34(H)	Catalyst Plant of Nankai University (Tianjin, China), Al/P/Si = 1/0.93/0.1
Zeolite Y(H)	Alfa Aesar, Si/Al=2.6
Zeolite Mordenite(NH_4)	Alfa Aesar, Si/Al=9
Zeolite Mordenite(Na)	ZEOCAT FM-8, Si/Al=6
Zeolite Mordenite(H)	ZEOCAT FM-8/25 H, Si/Al=12
Zeolite ZSM-5(H)	Tricat Inc., Hunt Valley, USA, Si/Al=23

3.2 Experimental set-up

The selective oxidation of methane was carried out in an autoclave reactor equipped with a Teflon liner vessel and a PTFE stirrer. A flow diagram of the experimental setup is shown in [Figure 3-1](#). The tightness of the system was checked through a pressure retention test by pressurizing with N_2 to 35 bar and then checking the pressure drop over 12 hours. The pressure drop was less than 2 % over 12 hours, which confirms the tightness of the reactor. The reaction was conducted according to the following steps. Step 1: After adding the catalyst and liquid, the reactor was sealed and filled in CH_4 up to 30 bar for 3 times to exclude residual air inside. Step 2: After the reactor was heated to the desired temperature, the reaction started by switching on the stirrer at around

600 rpm. Step 3: the vessel was quickly cooled in an ice-water bath below 11°C to minimize the evaporation of volatile products after finishing the reaction. Step 4: before releasing the reactor's pressure, the air in the pipe was removed with the help of a vacuum pump until the pressure dropped below 4 mbar. The gas products (CH₄, CO, CO₂, N₂, O₂) were collected with a gas bag and analyzed by GC-FID. The liquid reactor content was filtered and analyzed by a combination of ¹H-NMR, HPLC or titration to quantify the liquid products HCOOH, HCHO, CH₃OH, CH₃OOH, OHCH₂OOH and the consumption of H₂O₂.

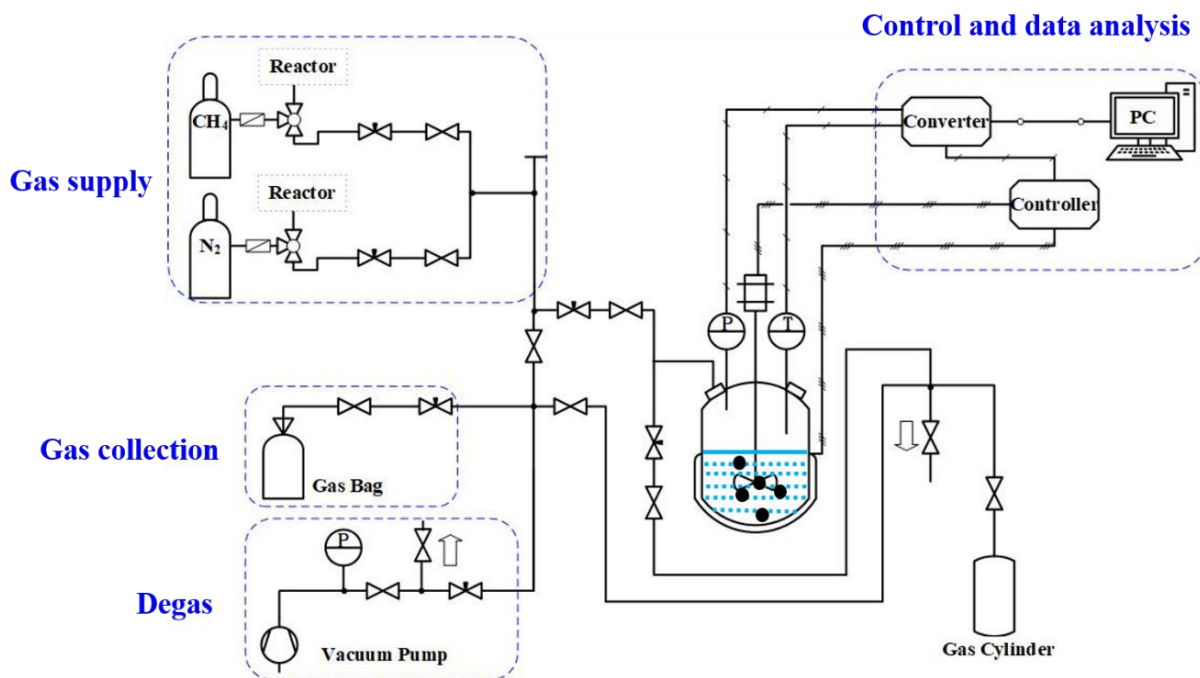


Figure 3-1. The flow diagram of the experimental set-up in this work.

3.3 The self-decomposition of H₂O₂

The utilization rate of H₂O₂ is an essential factor in evaluating the performance of catalysts. During the activity tests, we found that the self-decomposition process consumed a lot of H₂O₂ to generate the byproduct O₂ without prevention (see following [Equation \(3-1\)](#)). Multiple factors have been proved to impact the self-decomposition of H₂O₂, such as the temperature, atmosphere, the metal components from the reactor, and pH value of the solution [99]. [Table 3-2](#) shows the result of the self-decomposition of H₂O₂ without adding solid catalysts under different reaction conditions. In [entries 1-3](#), we learned that the reaction temperature and time greatly influence the self-decomposition, which increases with higher temperature and longer reaction time. In [entry 2](#), 50 °C and 1 h will cause almost 25% H₂O₂ conversion and generate a significant amount of byproduct O₂ with negligible 2~3 μmol C1 products. The carbon balance value of around 97% is not perfect, mainly because of the instrumental error from GC. The total gas content calculated

based on GC calibration curves of different gas, is less than 100%. However, with more than 95% of carbon balance, it still has high accuracy. In [entry 3](#), when the reaction was conducted at 80 °C for 1 h, almost half of the H₂O₂ in the solution will decompose to generate 1.5 mmol O₂ with a non-negligible amount of C1 products and CO₂, which will strongly interfere the evaluation of the catalyst activity. In [entry 4](#), when changing the reaction atmosphere from CH₄ to N₂, there is a strong decomposition of H₂O₂ with around 80% conversion. We propose that without the competitive interaction of CH₄ with H₂O₂, the self-decomposition of H₂O₂ will happen easily in N₂. In [entry 5](#), the HCl solution was added to adjust the pH value of the solution to 4.3. The acidic solution would promote the decomposition of H₂O₂ to generate around 65 μmol C1 products and 13 μmol CO₂.



Table 3-2. The self-decomposition of H₂O₂ in the reaction condition without catalysts.^a

No.	Reaction Condition	T (°C)	t (h)	Products yield (μmol)						H ₂ O ₂ Conv. (%)	Carbon Balance (%)
				MeOH	MeOOH	OHCH ₂ OOH	HCOOH	CO ₂	O ₂ (×10 ³)		
1	30 bar CH ₄	50	0.5	0.4	0.5	0	0.2	0	0.3	9.1	99.2
	30 bar CH ₄	50	0.5	0.4	0.6	0	0.1	0	0.2	3.9	98.3
2	30 bar CH ₄	50	1	0.6	1.5	0	0.9	0	0.5	21.7	98.4
	30 bar CH ₄	50	1	0.7	1.1	0	1.5	0	0.8	27.0	98.2
	30 bar CH ₄	50	1	0.2	1.8	0	0.3	0	0.4	24.6	96.3
3	30 bar CH ₄	80	1	6.3	0	0	24.8	15.5	1.5	46.8	98.2
	30 bar CH ₄	80	1	4.7	12.5	0	4.7	0	1.3	48.8	99.8
	30 bar CH ₄	80	1	4.3	14.0	0	4.2	17.6	1.6	59.2	96.8
4	30 bar N ₂	80	1	0	0	0	0	0	2.4	82.2	98.4
5	HCl (pH=4.3) ^b	80	1	19.2	20.3	0	25.1	13.0	2.3	82.0	97.7

^a**Reaction condition:** without solid catalyst, 10 mL of 0.5 M H₂O₂, autoclave reactor, 600 rpm, 30 bar of CH₄ or N₂;^b30 bar of CH₄.

In addition to the factors mentioned above, we also found that the metal components of the autoclave reactor, such as the stirrer, inner wall of the autoclave and thermowell, which are made of zirconium Grade 702, also cause the consumption of H₂O₂. [Table 3-3](#) shows the results of H₂O₂ decomposition caused by the metal components of the autoclave reactor. In [entry 1](#), without the protection of the metal components of the reactor, the reactor itself causes a huge consumption of H₂O₂ under room temperature and 30 bar N₂ or CH₄ atmosphere. In [entry 2](#), regardless of the N₂ pressure, removing the metal stirrer without stirring and covering the thermowell with silicone will significantly inhibit the self-decomposition of H₂O₂, which indicates that protection is necessary. In [entry 3](#), wrapping the thermowell with a thin polytetrafluorethylene (PTFE) band is better and is more durable. In [entry 4](#), when we removed the metal stirrer, put a smaller glass cylinder inside

as the reactor and wrapped the thermowell with a PTFE band, there was almost no decomposition of H_2O_2 , which confirms our suspicions that the protection of metal components will eliminate decomposition. Figure 3-2 shows our homemade PTFE cylinder, stirrer that fits the reactor well and PTFE band wrapped on thermowell. In entry 5, under this condition, there is no extra decomposition of H_2O_2 .

Table 3-3. The self-decomposition of H_2O_2 caused by the metal components of the autoclave reactor.^a

No.	T (°C)	Atmosphere (bar)	Time (min)	Special condition	Theoretical peak area ^b	Actual peak area ^c
1	50	30 N_2	40	-	3,124,500	0
	r.t. ^d	30 N_2	40	-	2,755,661	0
	r.t.	30 CH_4	40	-	2,755,661	620,000
2	r.t.	30 N_2	40	removing stirrer; thermowell covered with silicone	2,850,000	2,000,000
	r.t.	5 N_2	40	removing stirrer; thermowell covered with silicone	2,850,000	2,100,000
	r.t.	1 N_2	40	removing stirrer; thermowell covered with silicone	2,850,000	2,100,000
3	r.t.	1 N_2	40	removing stirrer; thermowell covered with PTFE band	2,950,000	2,290,000
4	r.t.	1 N_2	40	removing stirrer; glass cylinder; thermowell covered with PTFE band	2,920,000	2,920,000
5	r.t.	1 N_2	60	PTFE stirrer, PTFE cylinder, thermowell covered with PTFE band	3,233,169	3,230,249

^a**Reaction condition:** without solid catalyst, 10 mL 0.5 M H_2O_2 , autoclave reactor, 30 bar of CH_4 or N_2 ; ^bTheoretical peak area: the peak area of H_2O_2 before reaction indicated by HPLC. ^cActual peak area: the peak area of H_2O_2 after reaction indicated by HPLC; ^dr.t. represents room temperature.

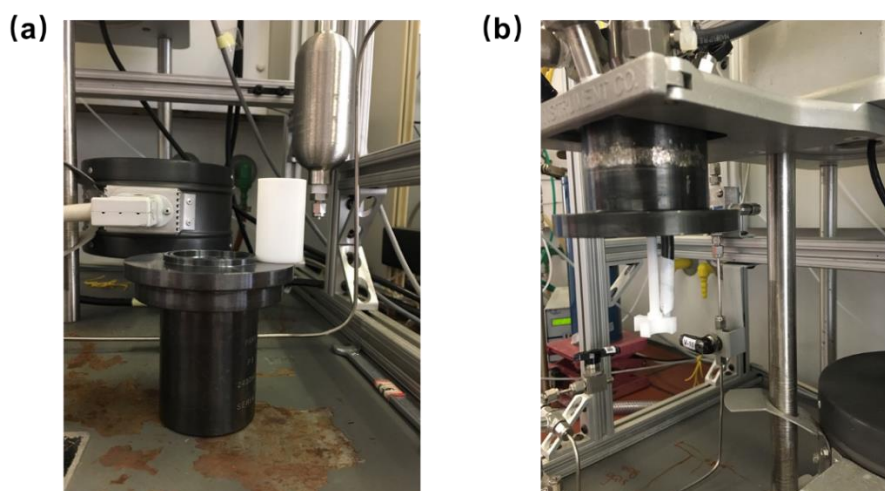


Figure 3-2. (a) The homemade PTFE cylinder; (b) The homemade PTFE stirrer and the thermowell covered with PTFE band.

After eliminating the self-decomposition caused by the autoclave reactor, we try to figure out how much H₂O₂ will be consumed in the blank experiment. Two representative support materials MOF (UiO-66) and zeolite (MOR) without modified active sites like Fe were chosen as the catalysts to observe the consumption of H₂O₂. Table 3-4 shows the catalytic results of H₂O₂ conversion for two blank catalysts at 50 °C for 1 h under 600 rpm stirring. In both entry 1 and entry 2, the conversion of H₂O₂ is much suppressed under this condition. We proposed that the existence of solids in the solution would inhibit the self-decomposition of H₂O₂ by blocking its chain reaction. For both reactions, the conversion of H₂O₂ was quite low with ignorable C1 products, which greatly reduced the interference. The choice of the reaction temperature is also very important, where high temperature causes a too fast self-decomposition of H₂O₂ and low temperature cannot trigger the reaction. 50 °C is a good choice. If necessary, 80 °C also can have a try.

Table 3-4. The self-decomposition of H₂O₂ in the blank experiments.^a

No.	Cat.	Product yield (μmol)					O ₂ (×10 ³)	H ₂ O ₂ Conv. (%)	Carbon Balance (%)
		MeOH	MeOOH	OHCH ₂ OOH	HCOOH	CO ₂			
1	UiO-66	0.5	0.8	0	2.3	0	0.1	0.04	100.5
2	MOR	0.5	0.1	0	0.5	0	0.2	2.6	101.5

^a**Reaction condition:** 10 mL of 0.5 M H₂O₂ aqueous solution, 30 bar of CH₄, 50 °C, 1 h, 10 mg of solid catalysts.

3.4 The decomposition of organic oxidant TBHP

Many researchers are interested in applying organic oxidant TBHP (tert-butyl hydroperoxide) for oxidation reactions. TBHP is a strong oxidant, often more effective than hydrogen peroxide or atmospheric oxygen. ^tBuO• and ^tBuOO• radicals generated from the decomposition of TBHP was believed to be the key active species for the oxidation reaction [100]. TBHP was found to be a highly effective organic oxidant for the methane to methanol reaction [101,102]. MOF catalyst Fe-DUT-5-SO₂ (see part 4.4) was studied for methane oxidation reaction in a 0.5 M TBHP aqueous solution. Table 3-5 shows the catalytic results with TBHP as an oxidant. In entry 1, 1.62Fe/DUT-5-SO₂ MOF catalyst was found to have quite good catalytic activity and selectivity for selective methane oxidation at 60 °C for 0.75 h. Blank experiments are essential to confirm the actual activity of the catalyst. In entry 2, the blank reaction without catalyst in the reaction solution was

performed under the same reaction condition. Unexpectedly, the reaction proceeded even without our test catalyst, which indicated that the catalyst did not trigger the generation of oxygenated products. In [entry 3](#), the reaction of 1.62Fe/DUT-5-SO₂ in N₂ was conducted to investigate the origin of the oxygenated products, which confirmed that they were not from methane. In [entry 4](#), the reaction proceeded without catalyst in N₂, which further confirmed that the decomposition of TBHP caused the generation of oxygenated products. The above experiments reminded us the utilization of organic oxidants must be cautious for selective methane oxidation.

Table 3-5. The self-decomposition of TBHP in catalytic reaction.^a

No.	Cat.	Reaction Condition	Product yield(μmol)/Selectivity(%)						
			MeOH	OHCH ₂ OOH	MeOOH	HCHO	HCOOH	CO ₂	O ₂ (×10 ³)
1	1.62Fe/DUT-5-SO ₂ -post syn.	60 °C, 0.75 h 5 mg, CH ₄	39.2	40.5	45.0		27.6	13.2	0.23
			23.7%	24.4%	27.2%	/	16.7%	8.0%	
2	without catalyst	60 °C, 0.5 h, CH ₄	21.9	5.8	15.7	14.7	1.7	16.7	0.24
			28.6%	7.5%	20.5%	19.2%	2.3%	26.9%	
3	1.62Fe/DUT-5-SO ₂ -post syn.	60 °C, 0.5 h 5 mg, N ₂	43.6	34.7	49.3	64.5	20.8	31.3	0.26
			17.8%	14.2%	20.2%	26.4%	8.5%	17.4%	
4	without catalyst	60 °C, 0.5 h N ₂	33.8		30.6	2.0	6.9	17.9	0.31
			37.0%	0	33.5%	2.3%	7.6%	20.0%	

^a**Reaction condition:** 10 mL of 0.5 M TBHP aqueous solution, 30 bar of N₂ or CH₄, 600 rpm.

3.5 The calculation of reactor volume

The measurement of the real gas volume of the reactor after we equipped the set-up with the homemade PTFE stirrer and cylinder is crucial to correctly consider the gaseous products in the calculation of the key performance indicators. The nominal size of the reactor is 25 mL, which corresponds to the liquid hold-up. We connected the U-type gas-measuring device ([Figure 3-3a](#)) to the autoclave reactor. The measuring points of the reactor can record the temperature and pressure change ΔP accurately. The device can be used to measure the gas volume V released from the reactor. The calculating formula is based on the ideal gas law and is shown in [Figure 3-3b](#). We repeated the measurement for 8 times to get the average gas volume of the reactor. The gas volume was determined as 55.25 mL.

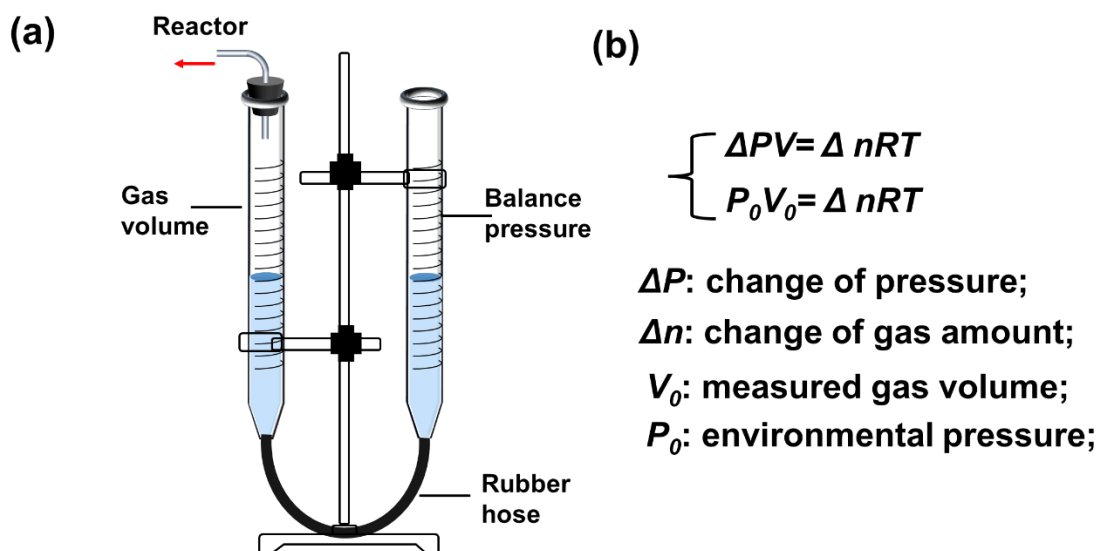


Figure 3-3. (a) Schematic diagram of the U-type gas measuring device; (b) The formula for calculation the reactor gas volume V_0 .

3.6 Procedure of the catalytic experiments

In a typical reaction, the vessel was loaded with 10 mL of 0.5 M H_2O_2 aqueous solution and the desired amount of catalyst, which subsequently was purged 30 bar methane three times to remove residual air and finally charged with methane to 30 bar. The reaction mixture was heated to the desired temperature (50 °C or 80 °C) with a slow stirring speed of 200-300 rpm at the beginning, which usually takes around 10 min or 15 min to reach the desired temperature of 50 °C or 80 °C, respectively. Once the temperature was achieved, the stirring speed was raised to the maximum 600 rpm, taking as the reaction's starting point. After the reaction was finished, the vessel was quickly cooled in an ice-water bath below 11 °C to condense the products into liquid. The resultant solution was filtered and analyzed using $^1\text{H-NMR}$, HPLC, and titration. The gas product was collected using an aluminum gas bag and analyzed by GC-FID.

3.7 Analysis of products

3.7.1 Gas phase analysis

The gaseous phase products were analyzed by gas chromatography (GC, Agilent 7890A), equipped with PLOT&MOLESIEVE columns, a thermal conductivity detector (TCD) and a flame ionization detector (FID), using He as carrier gas. The gaseous products CH_4 , O_2 , CO and CO_2 were quantified against a calibration curve constructed from commercial standards.

3.7.2 Liquid phase analysis

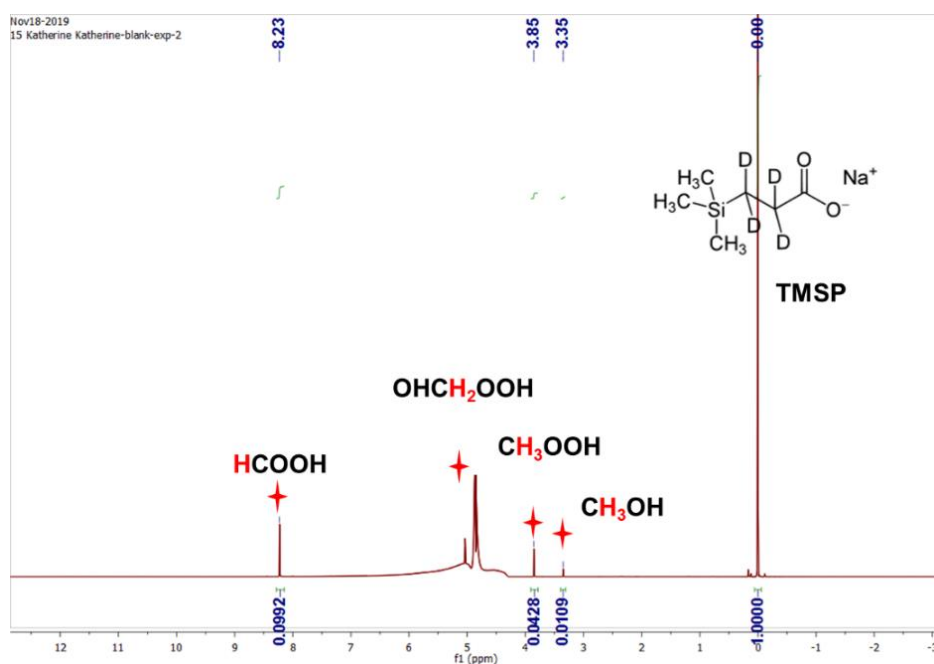


Figure 3-4. Example of the product quantification by ^1H NMR with solvent suppression program.

The liquid phase products were analyzed and quantified by ^1H NMR on a 400 MHz Bruker AVANCE III NMR spectrometer. ^1H NMR spectra were recorded with a $\pi/2$ pulse width of 10 μs , a recycle delay of 5 seconds and 20 scans. Typically, 500 μL of the sample, 100 μL of D_2O with TMSP internal standard (0.12 wt.% Trimethylsilylpropanoic acid) were placed in an NMR tube together and mixed thoroughly. A solvent suppression program (ZGPR) was run to minimize the signal arising from the solvent H_2O . The oxygenated products identified were methanol ($\delta = 3.35$ ppm, s), methyl hydroperoxide ($\delta = 3.86$ ppm, s), HOCH_2OOH ($\delta = 5.04$ ppm, s) and formic acid ($\delta = 8.23$ ppm, s). An illustrative spectrum is provided in Figure 3-4. The chemical shift for HOCH_2OOH matches well with that reported by Cui et al [52].

3.7.3 H_2O_2 quantification

Method 1:

The amount of H_2O_2 remaining at the end of a reaction was quantified by titration of aliquots of the final solution against acidified $\text{Ce}(\text{SO}_4)_2$ solution using the Ferroin indicator.

Method 2:

The consumption of H_2O_2 can also be quantified by high-performance liquid chromatography (HPLC, Agilent 1260 Infinity) equipped with a column of NUCLEOGEL Sugar 810 H column and a RID detector, using 0.5 mM H_2SO_4 as eluent. The concentration can be calculated using a calibration plot.

3.7.4 The calculation of the performance indicators

1. The selectivity of product was defined in Equation (1):

$$\text{Selectivity}_{(\text{MeOH})} = \frac{n(\text{MeOH})}{n(\text{MeOH}) + n(\text{MeOOH}) + n(\text{OHCH}_2\text{OOH}) + n(\text{HCOOH}) + n(\text{CO}_2)} \times 100\% \quad \text{Equation (3-2)}$$

$n(\text{MeOH})$ refers to the molar amount of MeOH in the reactor after reaction obtained by NMR test.

2. The conversion of H_2O_2 was defined in Equation (2) or Equation (3):

$$\text{Conversion}_{(\text{H}_2\text{O}_2)} = \frac{\text{peak area of H}_2\text{O}_2 \text{ of reaction solution after reaction}}{\text{peak area of H}_2\text{O}_2 \text{ aqueous solution before reaction}} \times 100\% \quad \text{Equation (3-3)}$$

The peak areas of H_2O_2 solution before and after reaction were obtained by HPLC measurements.

$$\text{Conversion}_{(\text{H}_2\text{O}_2)} = \frac{\text{the consumed Ce(SO}_4)_2 \text{ volume of reaction solution}}{\text{the consumed Ce(SO}_4)_2 \text{ volume of H}_2\text{O}_2 \text{ solution before reaction}} \times 100\% \quad \text{Equation (3-4)}$$

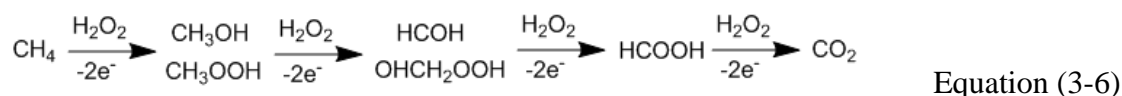
4)

The consumed volume of $\text{Ce(SO}_4)_2$ for reaction solution were obtained by titration.

3. The utilization ratio of H_2O_2 was defined in Equation (4):

$$\text{Utilization}_{(\text{H}_2\text{O}_2)} = \frac{n(\text{MeOH}) + n(\text{MeOOH}) + 2n(\text{OHCH}_2\text{OOH}) + 3n(\text{HCOOH})}{n(\text{the total consumption of H}_2\text{O}_2)} \times 100\% \quad \text{Equation (3-5)}$$

The consumption of H_2O_2 of the C1 oxygenates in Equation (4) is based on the the reaction Equation (5):



4. Turnover frequencies (TOFs) were defined as micromoles of C1 oxygenates per micromole of iron and hour (h^{-1}), as shown in Equation (6).

$$\text{TOF} = \frac{n(\text{MeOH}) + n(\text{MeOOH}) + n(\text{OHCH}_2\text{OOH}) + n(\text{HCOOH})}{(\text{mass of catalyst (20mg)} \times \text{mass fraction of Fe (wt\%)} / 56 \text{g/mol}) \times \text{reaction time (0.5h)}} \quad \text{Equation (3-7)}$$

3.7.5 Proposed reaction scheme in Fe/ H_2O_2 -based heterogeneous system.

Based on literatures [52,67], the proposed reaction scheme for direct methane oxidation in Fe/ H_2O_2 -based heterogeneous system was that CH_4 was first oxidized to CH_3OOH and CH_3OH , and then CH_3OH was further converted into HOCH_2OOH and consecutively oxidized by $\bullet\text{OH}$ into HCOOH and CO_2 (Figure 3-5). This is also consistent with our work. The self-decomposition of H_2O_2 to O_2 as a byproduct influenced mainly by temperature and reactor was already discussed in part 3.3. In our reaction system, besides that the reaction temperature (50-80 °C) will trigger the thermal decomposition of H_2O_2 , this reaction can also be carried out because of the Fe ion in the presence of most of our tested catalysts based on Fenton's reaction [99], see following Equation (3-8),(3-9),(3-10):

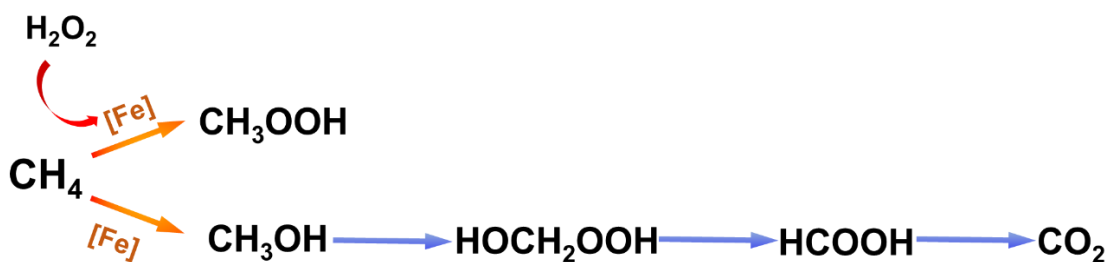
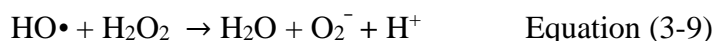
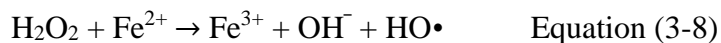


Figure 3-5. Proposed reaction scheme for direct methane oxidation in the H_2O_2 -based heterogeneous system.



3.8 Characterization of the catalysts

3.8.1 X-Ray Diffraction

X-ray diffractometry (XRD) analysis was carried out on a BrukerD8 Advance diffractometer at an excitation voltage of 35 kV and a current intensity of 40 mA using a $\text{Cu K}\alpha$ ($\lambda = 0.154 \text{ nm}$) radiation.

3.8.2 Chemical Analysis

The chemical compositions of the catalysts were determined by a Varian optical emission spectrometer Vista-MPX CCD with an inductively coupled plasma optical emission spectrometry (ICP-OES). Silicon, aluminum, and metals were determined by ICP-OES. The acid digestion of the zeolite materials was performed as follows: around 20 mg of sample was digested in a mixture of 1 mL 49 wt.% HF, 2 mL 36.5 wt.% HCl, 2 mL 65 wt.% HNO_3 , and 8 mL double-distilled water. MOF samples were entirely digested in a mixture of nitric acid and hydrofluoric acid. Heike Fingerle from Institute of Technical Chemistry at University of Stuttgart did the measurements.

3.8.3 Scanning Electron Microscopy

Scanning electron microscopy (SEM) images were collected by TESCAN VEGA3 XM with a tungsten filament electron source and SE (secondary electron) detector. Hang Liu from Institute of Technical Chemistry at University of Stuttgart did the measurements.

3.8.4 Transmission Electron Microscopy

Transmission electron microscopy (TEM) images were collected by Philips CM-200 FEG TEM. The sample for the TEM study was prepared by suspending the sample powder in acetone with a 2 min ultrasound treatment and then dropping the mixture on a carbon-coated Cu grid (TEM grid) and drying in the air. The applied voltage was 200 kV and the camera was a TVIPS TEMCAM F224HD. Hang Liu from Institute of Technical Chemistry at University of Stuttgart did the measurements.

3.8.5 Nuclear Magnetic Resonance spectroscopy

Nuclear Magnetic Resonance spectroscopy (NMR) experiments were performed on Bruker AVANCE III 400 MHz equipped with with solvent suppression method (ZGPR). ^1H NMR spectra were recorded with a $\pi/2$ pulse width of 10 μs , a recycle delay of 5 s, and 20 scans. Institute of Organic Chemistry at University of Stuttgart did the measurements.

3.8.6 Solid state ^{27}Al MAS NMR measurements

The solid state ^{27}Al MAS NMR measurements were carried out on a Bruker Avance III 400WB spectrometer using a 4.0 mm MAS NMR probe with a spinning rate of 8 kHz. ^{27}Al MAS NMR spectra were recorded at the resonance frequencies of 104.2 MHz, with a single-pulse $\pi/6$ (^{27}Al) excitation, and repetition times of 0.5 s for ^{27}Al nuclei. Dr. Zheng Li from ITC did the measurements.

3.8.7 Pyridine-adsorbed Fourier Transform Infrared Spectroscopy (Py-FTIR)

In the Py-FTIR experiments, sample powders were pressed to obtain rectangular wafers, which were subsequently degassed at 500 °C for 120 min in an in-situ IR cell and then cooled to room temperature. IR spectra were collected using an FT-IR spectrometer (Nicolet iS50) with 32 scans and 4 cm^{-1} resolution for each spectrum. N_2 flow saturated with pyridine was flowed into the FTIR cell at room temperature for 30 min to ensure that all acid sites were covered. Before measurement, the physisorbed and weakly bound pyridine molecules were desorbed for 30 min under vacuum at the same temperature [103]. After that, the samples were consecutively heated to 150, 250, 350, 450, and 550 °C with the rate of 4 °C min^{-1} , and Py FTIR absorption spectra were measured at these temperatures. M.Sc. Nagme Merdanoglu from ITC did the measurements.

3.8.8 Argon Physisorption

Argon physisorption measurements were conducted to determine the surface areas and pore volumes on an Autosorb 3B (Quantachrome) operating at 87.45 K. The samples were outgassed at 350 °C under vacuum for 15 h prior to the measurements. Brunauer-Emmett-Teller (BET) surface areas were determined by the adsorption isotherm within the pressure range $0.05 < P/P_0 < 0.3$. Micropore volumes were determined by t-plot analysis, and pore size distribution was obtained from the adsorption isotherm using the Barrett-Joyner-Halenda (BJH) method. Dr. Dorothea Häussermann from ITC did the measurements.

3.8.9 ^{57}Fe Mössbauer spectroscopy

Mössbauer spectroscopy provides an excellent tool for probing the local environment of the Fe atoms present in such materials. Some groups [67,104] reported the validation and quantification of the three identified Fe species (mononuclear, oligonuclear clusters and metal oxide nanoparticles) in Fe/ZSM-5 zeolite catalysts synthesized by different methods is accomplished by applying ^{57}Fe Mössbauer spectroscopy. A major difficulty in characterizing the Fe sites among the catalysts for selective methane oxidation by ^{57}Fe Mössbauer spectroscopy was the low fraction of active Fe. In most cases, the catalyst with 0.5 wt.% Fe is very typical. Higher Fe content in zeolite mainly contributes to the formation of metal oxide nanoparticles, which is not helpful for effectively selective methane oxidation [105]. Thus, in order to get better results, samples with low iron concentrations are prepared from enriched ^{57}Fe . In our case, we decided to try the measurement of 0.524Fe/MOR_{SSIE} zeolites with the highest Fe content among our catalysts to detect the signal. ^{57}Fe Mössbauer spectrum of the 0.524Fe/MOR_{SSIE} catalyst was measured on a homemade spectrometer based on an RCPTM MS-96 Mössbauer spectrometer equipped with a Ritverc Co57 in an Rh-matrix source, a YAP:Ce scintillating crystal detector, and a Janis SVT-400 helium-bath cryostat. Velocity calibration was carried out at room temperature using an α -Fe foil [106]. Figure 3-6 shows the result of the 0.524Fe/MOR_{SSIE} zeolite catalysts. It is quite disappointing that we did not detect any ^{57}Fe Mössbauer signal after almost 5 days of measurement under room temperature. Dr. Mario Winkler from Institute of Physical Chemistry at University of Stuttgart did the measurements.

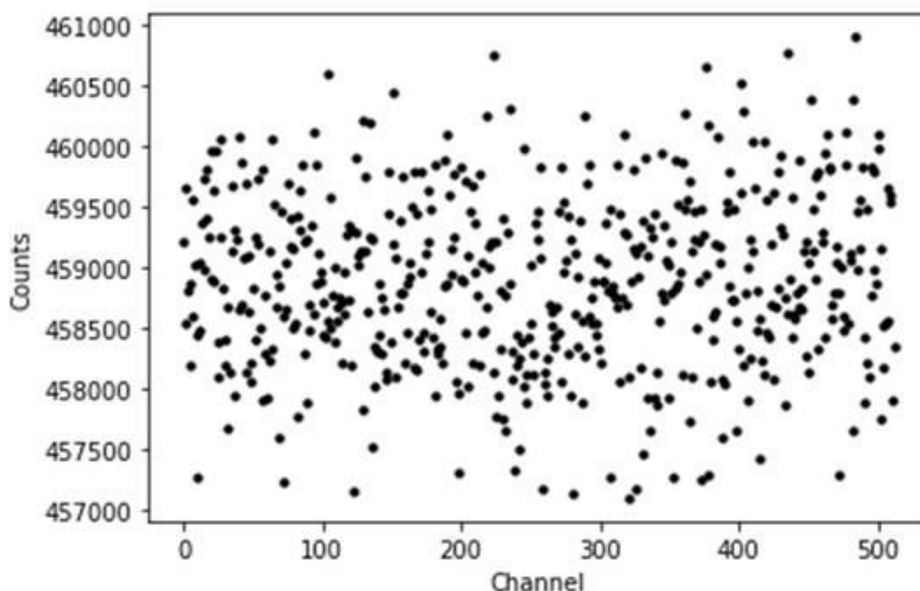


Figure 3-6. ^{57}Fe Mössbauer spectra of the 0.524Fe/MOR_{SSIE} zeolites obtained at ambient temperature.

3.8.10 Diffuse reflectance Ultraviolet-Visible spectroscopy

UV-visible (UV-vis) spectra of zeolite Fe/MOR catalysts were recorded on a Lambda950 spectrometer in the diffuse reflectance (DR) mode at room temperature. The baseline was corrected using BaSO₄ as reference material. Samples were scanned between 190 and 800 nm at a scan rate of 200 nm/min. The intensity of the UV-vis DR spectra was presented in the form of the Kubelka-Munk function. Dr Shujin Hou from the department of physics at Technical University of Munich did the measurements.

3.8.11 X-ray absorption spectra

The X-ray absorption spectra (XAS), including X-ray absorption near-edge structure (XANES) and extended X-ray absorption fine structure (EXAFS) of the samples at Fe K-edge, were collected at the beamline 1W1B station of the Beijing Synchrotron Radiation Facility (BSRF), China. A double Si(111)-crystal monochromator was used for energy selection. The Fe K-edge XAFS data were recorded in fluorescence mode. Fe foil, Fe₂O₃ were used as references. All spectra were collected in ambient conditions. The Athena software package was used to analyze the data.

4. Direct methane oxidation over different MOF catalysts by H₂O₂

Soluble MMO enzymes can selectively oxidize methane into methanol with remarkable selectivity under ambient conditions by Fe-oxo species that require a series of gating mechanisms to control access to the active site to avoid methanol over-oxidation [16a]. Mimicking the features of Fe-oxo active sites in enzymes within solid supports is one of the important strategies to design promising catalysts [107]. MOF materials possess both organic and inorganic constituents, abundant topologies and highly porous structures, making them an ideal platform for active metal sites. Part 1.5 showed that MOF catalysts successfully catalyzed selective methane oxidation to methanol and formic acid with H₂O₂ as an oxidant. So far, however, the examples of MOF as a catalyst are still minimal. Combining the study of the active catalysts from literature, we mainly design MOF catalysts based on three strategies: Firstly, open metal sites; Open metal sites (OMSs) with unsaturated coordination within the framework endow MOFs with excellent catalytic features. In addition, the highly dispersed open metal sites within MOFs are very significant for catalysts' efficiency. The introduction of active metal atoms such as Fe in MOFs with open coordination can activate H₂O₂ to oxidize the C-H bond of light alkanes. Examples like MIL-53(Fe, Al) [92] have been confirmed to contain biomimetic mono- and di-nuclear iron sites that activate ethane/methane. Furthermore, computational studies suggested an expanded library of MOFs containing sites capable of affecting light alkane activation [108]. Secondly, confinement of metal sites in the framework; MOFs can serve as a scaffold based on the coordination effect of N and O atoms in the organic groups to confine and fix metal-oxo sites to catalyze organic transformations. Thirdly, regulation of the microenvironments of frameworks; Flexible structures and multiple components of MOFs offer enormous potential for tunable microenvironments for catalysis by post-modification methods to introduce metal sites with the desired configuration. For a UiO-66(2.5TFA)-Fe catalyst [97], trifluoroacetic acid (TFA) groups substituting original terephthalic acid ligands of UiO-66 coordinated with Zr₆ node of UiO-66 to enhance the oxidation state of adjacent Fe-O cluster, promoting the activation of C-H bond of methane.

MOF catalysts can conduct the methane oxidation to methanol in fixed-bed reactors. However, typically, they are operated in a stepwise manner: (1) catalyst oxidation with N₂O or O₂, (2) methane activation, and (3) methanol extraction with water vapor, each step conducted at different reaction temperatures with He rinsing before the next step, thus presenting a challenge for a streamlined catalytic process. Herein, we tried to conduct methane oxidation in the liquid phase, where H₂O₂ is used as an oxidant in a Parr autoclave reactor. There are mainly two problems for MOF catalysts occurring in this reaction system from preliminary work. Firstly, the high-

temperature activation process in case of O₂ as an oxidant and the strong oxidizing ability in case of H₂O₂ as an oxidant, both require stable MOF structures. Thus, metal nodes in MOF structures like Al-based and Zn-based ones without redox ability are appropriate. Secondly, the competing H₂O₂ conversion methane reaction and self-decomposition resulted in low activity and low utilization ratios of H₂O₂, which is still not resolved.

As described in [part 1.5](#), MOFs' stability depends greatly on compositions. Therefore, to select stable MOFs for methane oxidation, the stability of organic ligands and the strength of coordination bonds should be considered. As for ligands, the conjugated ligands with less reductive groups, such as smaller aromatic ligands, are preferred. As for the strength of coordination bonds, HSAB theory is the most common and facile method to judge the stability of the compounds. Based on HSAB theory, couples of high-valence metal species (such as Zr⁴⁺, Al³⁺) and carboxylic acid based ligands (O as coordination atoms) or couples of low-valence metal species (such as Zn²⁺) and azole ligands (N as coordination atoms) are more preferred to give stable coordination. However, the actual stability in methane oxidation can only be assessed once they are applied to catalysis.

4.1 CAU-10

4.1.1 Catalyst design

The MOFs based on aluminum have been proven to be both thermally and chemically stable [109]. What's more, aluminum salts have a low price and toxicity, making these materials popular in industrial research. The Al-based MOF CAU-10-H (CAU = Christian-Albrechts University) is composed of the V-shaped 1,3-benzene dicarboxylic acid (1,3-H₂BDC) as a linker ([Figure 4-1a](#)) and cis-connected, corner-sharing AlO₆ polyhedra as node ([Figure 4-1c](#)) [110]. CAU-10-H exhibits a framework with square-shaped one-dimensional pores with a diagonal opening of ~3.6 Å ([Figure 4-1d](#)). This compound can also be directly synthesized with various functional groups on the linker molecule to synthesize CAU-10-X materials. The rigid framework of CAU-10-H remains intact up to 410 °C under air, indicating good stability [110]. We tried to replace the 1,3-H₂BDC ligand with 2,6-pyridinedicarboxylic acid linker ([Figure 4-1b](#)) to synthesize a new material named CAU-10-Py to further confine the metal sites with coordinated pyridine-N sites of the new linker.

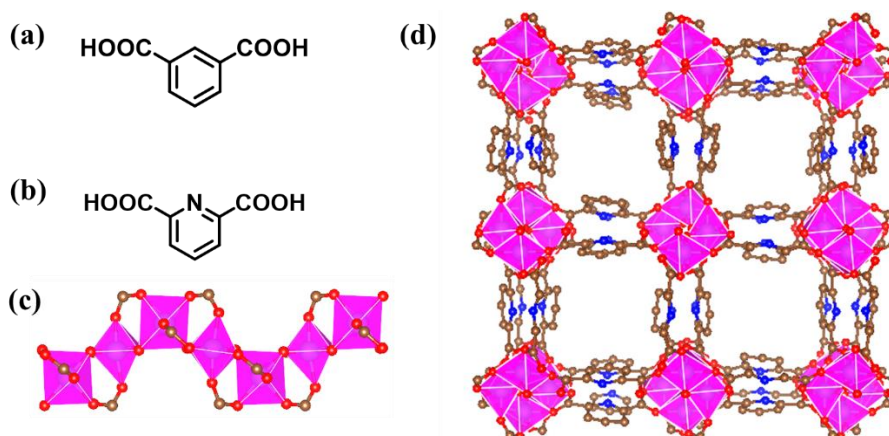


Figure 4-1. (a) The molecular structure of ligand 1,3-benzenedicarboxylic acid (1,3-H₂BDC); (b) The molecular structure of ligand 2,6-pyridinedicarboxylic acid; (c) A chain of cis-connected, corner-sharing AlO₆ polyhedra of CAU-10 viewed along b axis; (d) 2 × 2 × 2 supercell of the framework of CAU-10-Py viewed along the c-axis, showing the 4-fold connectivity of the helices and the square-shaped channels that are formed. Pink = Al, red = O, brown = C, and blue = N.

Since the Fe³⁺ species [Fe₂(μ-O)₂] at the extra-framework position of active Fe/ZSM-5 catalyst after 550 °C calcination were confirmed as the initial active sites by multiple characterizations,[64] researchers tried to construct the Fe₂ cluster active sites in diverse support materials. MOF materials show great advantages by micro-environment adjustment in mimicking enzymes to form active Fe₂ and Cu₂ clusters that are found in MMO enzymes for selective methane oxidation to methanol under mild conditions. We tried to embed Fe ions or other metals like Cu and Co into CAU-10 and CAU-10-Py to catalyze selective methane oxidation to oxygenates. As shown in other literature [111], a new metalation strategy taking advantage of the precise spatial arrangement of organic struts in a MOF to create chelating metal sites is to achieve metal functionalization similar to metalloenzymes [112]. There are three possible ways for Fe, Co or Cu bounding to CAU-10: (1) Single Fe coordinates with O atom on Al cluster, which is not stable and easy to be washed away; (2) Partial substitution of Al, which is quite a low possibility because of the mild conditions (85 °C); (3) As shown in the following figure, it's more stable based on the confinement effect by more coordination atoms. In Figure 4-2, we proposed the structure of [Fe₂(μ-O)₂] fixed in CAU-10 and CAU-10-Py by using organic struts that bear auxiliary chelating sites like O and N atoms. Figures 4-2a and 4-2b show the proposed structures of [Fe₂(μ-O)₂] in CAU-10 and CAU-10-Py with Fe ions chelated by O atoms from the two opposite AlO₆ clusters. Figure 4-2c shows the proposed structure of [Fe₂(μ-O)₂] in CAU-10-Py with Fe ions chelated by O atoms and N atoms from two adjacent 2,6-pyridinedicarboxylic acid linkers.

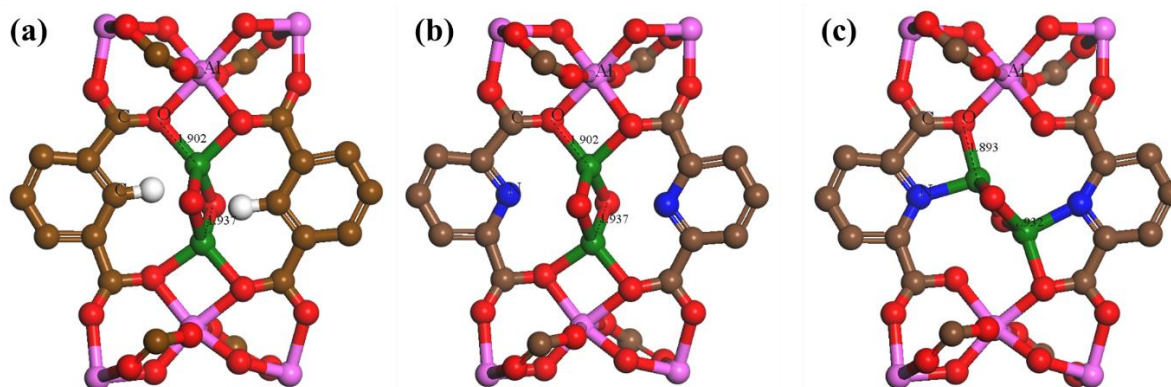


Figure 4-2. (a) and (b) The proposed structure of $[\text{Fe}_2(\mu\text{-O})_2]$ in CAU-10 and CAU-10-Py with Fe ions chelated by O atoms from the two opposite AlO_6 clusters. (c) The proposed structure of $[\text{Fe}_2(\mu\text{-O})_2]$ in CAU-10-Py with Fe ions chelated by O atoms and N atoms from two adjacent 2,6-pyridinedicarboxylic acid linkers. Pink = Al, red = O, brown = C, green = Fe, white = H, and blue = N.

4.1.2 Synthesis method

4.1.2.1 Synthesis of CAU-10-H and CAU-10-Py

CAU-10-H was synthesized according to the literature [113] from a mixture of 200 mg of 1,3- H_2BDC (1.20 mmol), 800 mg of $\text{Al}_2(\text{SO}_4)_3 \cdot 18\text{H}_2\text{O}$ (1.20 mmol), 1 mL of N,N' -dimethylformamid (DMF), and 4 mL of H_2O . The aluminum salt was dissolved in water, and the organic ligand was dissolved in DMF. The reactants were dosed into a Teflon-lined steel autoclave with a volume of 20 mL and placed in an oven for 12 h at 135 °C. After being cooled to room temperature, the product was filtered off, and the obtained solid was re-dispersed in water by sonication and stirring until a homogeneous mixture was obtained. The dispersion was filtered again and the white microcrystalline solid was dried in air. CAU-10-py was synthesized just by changing the ligand to an equivalent 2,6-pyridinedicarboxylic acid linker.

4.1.2.2 Metal loading of CAU-10-H and CAU-10-Py

Synthesis of Fe/CAU-10: A 10 mL glass flask was loaded with 40 mg of CAU-10-H, 10 mg of $\text{Fe}(\text{acac})_3$ and 4 mL of CH_3CN and heated at 85 °C for 1 hour under stirring.

Synthesis of Co/CAU-10: A 10 mL glass flask was loaded with 40 mg of CAU-10-H, 10 mg of $\text{Co}(\text{CH}_3\text{COO})_2 \cdot 4\text{H}_2\text{O}$, and 4 mL of MeCN and heated at 85 °C for 1 hour under stirring.

Synthesis of Cu/CAU-10-Py: A 10 mL glass flask was loaded with 80 mg of CAU-10-Py, 10 mg of $\text{Cu}(\text{acac})_2$ and 5 mL of DMF and heated at 120 °C for 24 hours under stirring.

Synthesis of Fe/CAU-10-Py: A 10 mL glass flask was loaded with 80 mg of CAU-10-Py, 10 mg of $\text{Fe}(\text{acac})_3$ and 5 mL of DMF and heated at 120 °C for 24 hours under stirring.

The metalated material was washed with fresh CH₃CN or acetone for 3 times. The resulting catalysts were dried at 80 °C for 5 hours and activated under a dynamic vacuum at 120 °C for 12 hours.

4.1.3 XRD characterization and activity tests

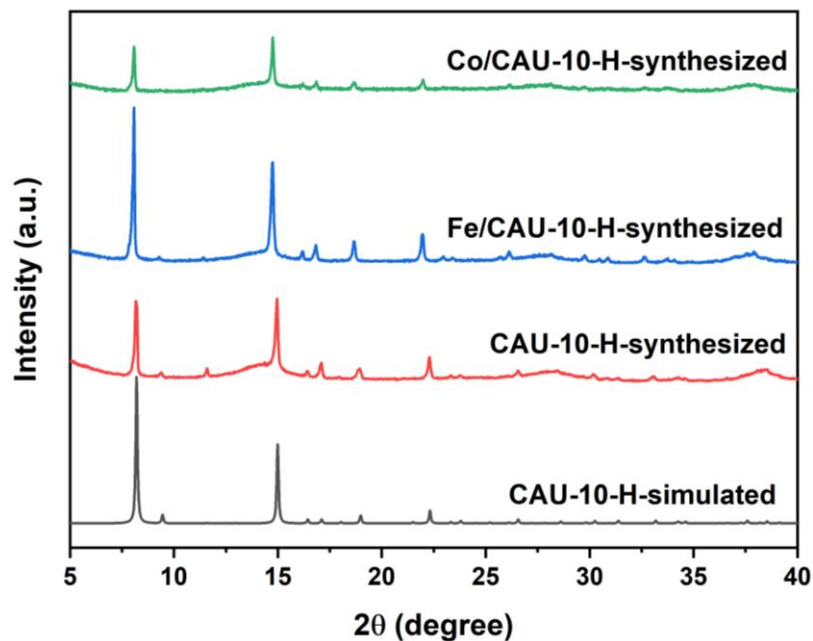


Figure 4-3. PXRD patterns for pristine and metal modified CAU-10-H catalysts.

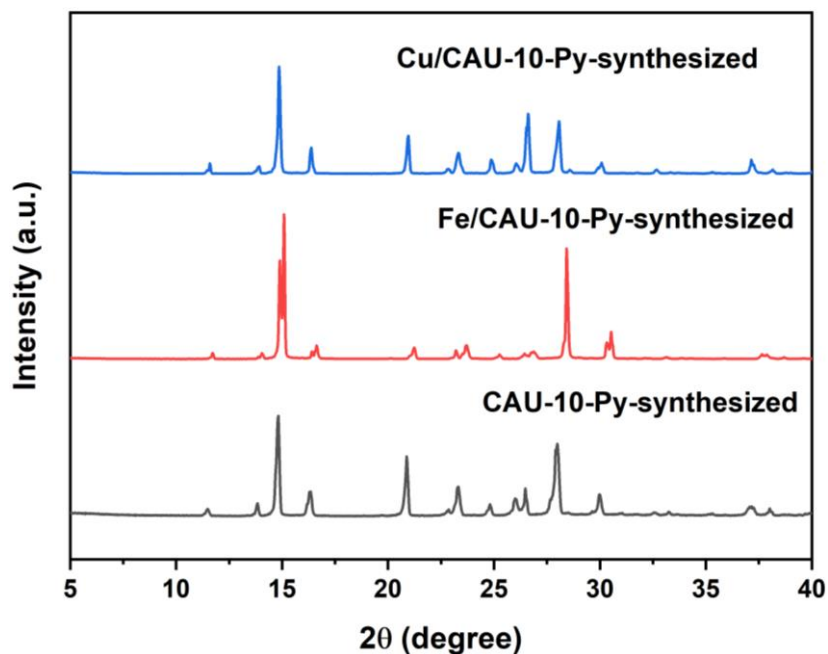


Figure 4-4. PXRD patterns for pristine and metal modified CAU-10-Py catalysts.

Table 4-1. Catalytic performances of the synthesized CAU-10 related catalysts.

Entry	Cat.	React. Condi.	Product yield(μmol)/Selectivity(%)						H_2O_2		TOF (h^{-1})
			Me OH	OHCH ₂ OOH	Me OOH	HCOOH	CO ₂	O ₂ ($\times 10^3$)	Conv. (%)	Util. (%)	
1	0.56Fe/ CAU-10	80°C, 1h 10 mg	5.6 3.8%	15.4 10.5%	17.8 12.1%	9.3 6.3%	99.0 67.4%	1.8	71.5	2.1	45
2	0.46Co/ CAU-10	80°C, 1h 10 mg	4.1 8.1%	6.9 13.6%	5.9 11.6%	0	33.90 66.7%	2.4	87.6	0.5	21
3	0.56Fe/ CAU-10	60°C, 1h 10 mg	2.4 7.5%	3.1 10.0%	8.7 27.8%	3.0 9.4%	14.2 45.3%	0.3	11.1	4.5	17
4	0.38Fe/ CAU-10-Py	70 °C, 1h 20mg	1.3 6.3%	4.9 23.5%	10.6 51.1%	4.0 19.2%	0	0.4	13.0	4.9	16
5	0.66Cu/ CAU-10-Py	70°C, 1h 20 mg	1.0 11.7%	1.7 19.5%	5.6 64.8%	0.4 4.0%	0	0.3	7.9	2.7	4

Reaction condition: 30 bar CH₄, 10 mL of 0.5 M H₂O₂, 600 rpm.

PXRD measurements were performed as a preliminary analysis to confirm agreement of the synthesized and metal-modified CAU-10-H materials to the previously reported PXRD patterns of the parent CAU-10-H in Figure 4-3. It can be seen that the peak positions of the experimental and simulated patterns of the pure CAU-10-H sample are in good agreement. For the Fe/CAU-10 and Co/CAU-10 samples, no visible reflections of metal NPs detected, possibly due to the low content of metal sites, while they showed the same reflections as the pure CAU-10-H sample, which illustrated that the modification with the metal did not disrupt the crystal structure of CAU-10-H. Moreover, 2,6-pyridinedicarboxylic acid linker replaced the original 1,3-H₂BDC ligand to synthesize CAU-10-Py for further metal modification. The crystal orientation has changed to a certain extent because the new linker caused the difference in XRD patterns in Figure 4-4. The prominent peak of CAU-10-H at a 2 θ angle of around 15° has remained.

The catalytic oxidation of methane using H₂O₂ was conducted in a batch system with 30 bar of CH₄ and 0.5 M H₂O₂. Table 4-1 shows the catalytic results of the synthesized CAU-10 based catalysts. The activity tests of the new catalyst require optimization and exploration of test conditions. The reaction temperature has a sensitive parameter, since a too high temperature may cause fast self-decomposition of H₂O₂ while a too low temperature cannot trigger the reaction. Fe/CAU-10 and Co/CAU-10 were firstly used at 80°C for 1 h (entry 1 and 2). Around 48 μmol C1 products were produced with large amounts of CO₂ (67% selectivity) and considerable consumption of H₂O₂. Co active site in entry 2 did not show any advantages in catalytic performance and H₂O₂ utilization. In entry 3, we decreased the reaction temperature to 60°C to check the catalytic performance of Fe/CAU-10. The dramatic drop in H₂O₂ conversion and CO₂ amount without increasing oxygenates formation indicates that 60 °C can not improve the reaction

by Fe/CAU-10. In [entry 4](#) and [5](#), Cu/CAU-10-Py and Fe/CAU-10-Py were tested at 70 °C for 1 h. Because CO₂ generation did not occur, we assume that both catalysts are stable enough under such catalytic conditions to avoid the generation of CO₂ from framework damage. It may also be because the limited activation of H₂O₂ by the catalyst resulted in a small amount of •OH that determines the framework stability and catalytic activity. From the H₂O₂ conversion in [entries 4-5](#), we can learn that Cu and Fe sites dispersed into the CAU-10-Py, did not cause a fast activation of H₂O₂ and increased selectivity to oxygenates slightly. What makes us disappointed is that the desired product's amount is always limited. The reasons for such a bad activity may be the unsuccessful construction of binuclear clusters or the bad stability of the proposed binuclear cluster.

4.2 MOF-74

4.2.1 Catalyst design

Fe_{0.1}Mg_{1.9}(dobdc) (dobdc=2,5-dioxido-1,4-benzenedicarboxylate) was introduced as a catalyst for the conversion of ethane to ethanol and acetaldehyde with nitrous oxide (N₂O) as the oxidant with reaction temperatures below 75 °C [114]. Xiao et al. [114] proposed that Fe_{0.1}Mg_{1.9}(dobdc) with open iron (II) sites could react with N₂O generating a high-spin nonheme iron(IV)-oxo complex that can activate the strong C–H bond of ethane. However, unlike the ethane oxidation to ethanol, methane oxidation by N₂O on Fe_{0.1}Mg_{1.9}(dobdc) did not observe under similar reaction conditions. The MOF M₂(dobdc) (M = Zn, Fe, Mn, Mg, Co, Ni) [115] has a high density of open M²⁺ cation sites lining one-dimensional cylindrical pores of ~1.1 nm diameter ([Figure 4-5c](#)). Despite the abundant open metal sites within the channels of the MOF, thermal stability can reach at least 400 °C. Besides the Fe site, Mn has also been reported to activate H₂O₂ to catalyze the epoxidation of alkenes on MnFe-MOF-74 [116]. Thus, MnZn-MOF-74 and FeZn-MOF-74 were tried to catalyze methane oxidation with H₂O₂ as an oxidant in an aqueous solution under an autoclave reactor.

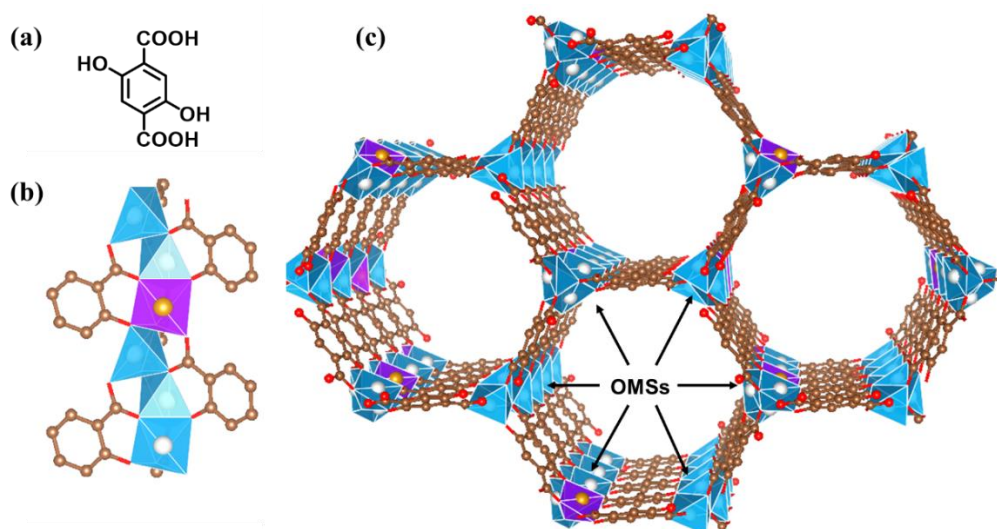


Figure 4-5. (a) The molecular structure of 2,5-dioxido-1,4-benzenedicarboxylate linker which is short for dobdc^{4-} ; (b) SBU with Zn and the second metal (Fe, Mn) shown as polyhedra; (c) Structure of $\text{Fe}_x\text{Zn}_{1-x}$ -MOF-74, showing hexagonal channels lined with five-coordinated divalent Zn and the second metal (Fe, or Mn) sites. The view is down the c axis, along the helical chains of metal ions. Fe randomly dispersed within the framework. (DMF and H_2O guest molecules have been omitted for clarity) Purple = Fe or Mn, red = O, brown = C, and blue = Zn.

4.2.2 Synthesis method

MnZn -MOF-74 and FeZn -MOF-74 were prepared by a one-pot method according to the literature [117]. The shares of Mn and Fe were controlled by adjusting the stoichiometric ratio of corresponding metal precursors. In a typical synthesis procedure, a solid mixture of 2,5-dihydroxy-1,4-benzenedicarboxylic acid (H_2 -DHBDC) (30 mg), $\text{FeCl}_2 \cdot 4\text{H}_2\text{O}$ or $\text{MnCl}_2 \cdot 4\text{H}_2\text{O}$ (10 mg) and ZnCl_2 (80 mg), were dissolved in DMF (10 mL) and EtOH (0.66 mL) in a 25 mL Schlenk flask. The reaction started after Ar purging and sealing by vigorously stirring at 120 °C for 24 hours. After that, the flask was cooled to room temperature. Then the mother liquor was decanted, and the solid was washed with DMF and methanol each for 3 times and was immersed in methanol for 3 days. The methanol was decanted, and the catalysts were vacuum dried, which were used for catalytic tests (see following No. 2 and No. 3 in Table 4-2). The metal loadings of Fe and Mn were decided by ICP measurements.

We further improved the synthesis method to get more stable FeZn -MOF-74 catalysts. A solid mixture of H_2 -DHBDC (100 mg), 5 wt.% $\text{FeCl}_2 \cdot 4\text{H}_2\text{O}$ (17.2 mg) and 95 wt.% $\text{Zn}(\text{NO}_3)_2 \cdot 4\text{H}_2\text{O}$ (429 mg), was dissolved in DMF (10 mL) and deionized H_2O (0.5 mL) in a 25 mL Schlenk flask. The reaction started after Ar purging and sealing by vigorously stirring at 110 °C for 21.5 hours. The following procedures were the same as before (see following No. 4-6 in Table 4-2).

4.2.3 XRD characterization and activity tests

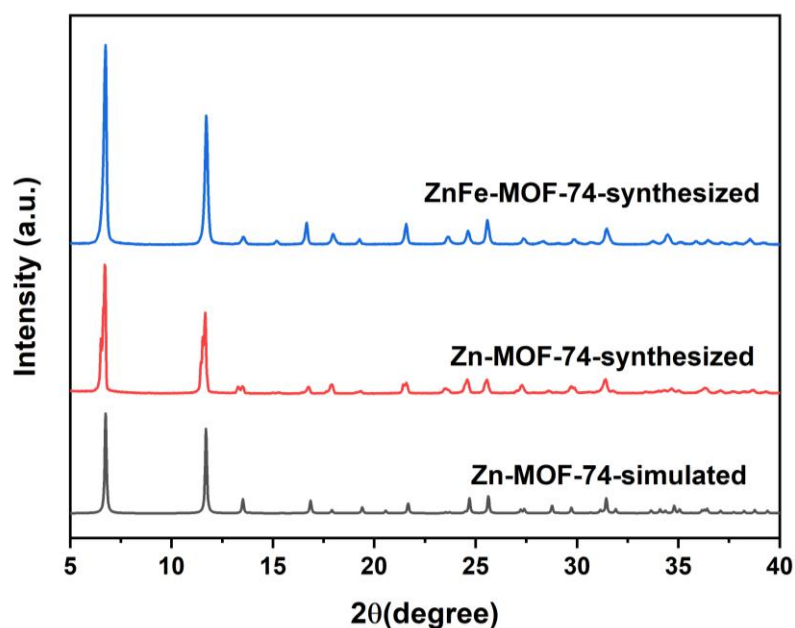


Figure 4-6. PXRD patterns for pristine and Fe modified Zn-MOF-74 obtained by improved method.

Table 4-2. Catalytic performance of the synthesized MOF-74 based catalysts.

No.	Cat.	React. Condi.	Product yield(μmol)/Selectivity(%)					H ₂ O ₂		TOF (h ⁻¹)	
			MeOH	OHCH ₂ OOH	MeOOH	HCOOH	CO ₂	O ₂ ($\times 10^3$)	Conv. (%)		Util. (%)
1	24.9Fe-MOF-74 ^a	70°C, 1h 10 mg	4.4 2.3%	0	17.2 11.6%	42.8 28.8%	83.9 56.6%	1.21	66.0	4.4	1.4
2	2.1FeZn-MOF-74 ^b	50°C, 1h 5 mg	3.2 3.8%	15.5 18.4%	12.8 15.2%	14.0 16.6%	38.7 46.0%	0.2	27.3	6.4	24
3	2.3MnZn-MOF-74	50°C, 1h 10 mg	0	0	0	0	56.9 100%	1.0	41.7	0	0
4	2.4FeZn-MOF-74 ^c	50°C, 1h 5 mg	0	0	0.6 4.9%	4.6 38.9%	6.7 56.2%	0.3	12.0	2.4	2
5	2.4FeZn-MOF-74 ^c	60°C, 0.5h 10 mg	0	0	0.6 1.0%	10.5 17.4%	49.0 81.6%	0.58	23.7	2.7	5
6	2.4FeZn-MOF-74 ^c	50°C, 1h 10 mg	0	0	0.5 1.3%	11.9 32.7%	24.0 66.0%	0.57	21.9	3.3	3

Reaction condition: 30 bar CH₄, 10 mL of 0.5 M H₂O₂, 600 rpm; ^aThe reaction supernatant turned to pale yellow after catalysis. ^bThe reaction supernatant turned to pale yellow and the color of catalyst turned from black to brick red after catalysis. ^cAfter the improvement of synthesis, the reaction solution is colorless after filtration and the color of catalyst turned from green to yellow.

After synthesis improvement, the crystallinity of the MOF-74 materials was confirmed by powder X-ray diffraction (PXRD) analysis (Figure 4-6). The PXRD patterns of Zn-MOF-74 and FeZn-MOF-74 coincided with the simulated MOF-74 structure, which confirmed that the topology was retained and all variations were isostructural. Furthermore, every reflex matches with the simulated PXRD pattern of MOF-74, ruling out the occurrence of other phases, such as ZnO and Fe₂O₃.

The catalytic performance of FeZn-MOF-74 was evaluated in the direct methane oxidation in water using 0.5 M H₂O₂ as the oxidant at 30 bar CH₄ in an autoclave reactor (see Table 4-2). The specific reaction time and temperature were adjusted according to the catalytic result. Fe-MOF-74 with exclusively Fe clusters as the SBU with Fe content of 24.9 wt.% was tested first at 70°C for 1 h. No. 1 shows that 64 μmol C1 oxygenated products were obtained, but lots of CO₂ generated with 56.6% selectivity over Fe-MOF-74. The reaction supernatant also turned pale yellow after catalysis, which implied the iron was leached from the catalyst. The instability of Fe-MOF-74 may lead to the decomposition of the catalyst during the test, which contributed to the strong formation of CO₂.

Thus, we turned to dope active metal species (Fe and Mn) into stable Zn-MOF-74 (see No.2 and No.3). In No. 2, FeZn-MOF-74 with 2.1 wt.% of Fe loading showed better C1 product selectivity with a TOF of 24 h⁻¹ and better H₂O₂ utilization ratio. What's more, after the reaction, the MOF catalyst was observed a drastic color change from black to brick red, which is consistent with the literature [114], indicating the oxidation of Fe(II) to Fe(III). The reaction solution nevertheless turned pale yellow after catalysis, which implied a MOF decomposition and Fe leaching. In No. 3, we found that MnZn-MOF-74 with 2.3 wt.% of Mn loading did not show any activity for selective methane oxidation but still prompted the decomposition of H₂O₂ that caused the damage of the framework to generate CO₂. At that moment, we were worried that the poor selectivity was caused by the lack of sufficient stability of the pristine MOF-74.

After confirming the activity of FeZn-MOF-74 but poor stability to generate a lot of CO₂, we further improved the synthesis method to get a more stable pristine MOF-74 used for Fe modification (No. 4-6). There is no apparent difference in XRD patterns between the old and new MOF-74 that can be observed. The reaction solution for the newly synthesized catalyst indeed is colorless after the reaction. Comparing No. 2 with 4, the more stable MOF framework shows worse performance. As seen in No. 5 and 6, increasing the reaction temperature and catalyst amount did not give better activity. The framework remained from the XRD pattern after the reaction. This result indicates the activity of the FeZn-MOF-74 (No. 2) may result from the defective sites or the solved fragments.

4.3 MIL-100 and MIL-96

4.3.1 Catalyst design

The trigonal trimer, corresponding to the μ_3 -oxo-centered carboxylate-bridged trinuclear unit, is well-known for the formation of the giant pore MOF series MIL-96 [118], MIL-100 [119], and MIL-101 [120] et al. Such a unit has been reported to incorporate many trivalent metals such as V [121], Cr [119,120,122], Fe [23], and Al [118]. Moreover, carboxylate linkers are helpful to build extra-large pore solids with relatively high thermal stability. MIL-100(Fe) [123] is built up from the trimeric Fe(III)-oxo nodes and benzene-1,3,5-tricarboxylic acid (BTC) linkers, forming a porous structure with the MTN zeolitic architecture (MTN=zeolite soconymobil – thirty-nine) (Figure 4-7a), which can be successfully synthesized in gram quantities according to the procedure described in [124]. The corresponding three-dimensional framework exhibits two types of cages with 25 and 29 Å diameter accessible through 5.5- and 8.6-Å diameter windows (Figure 4-7a). More specifically, the trimeric units (Figure 4-7c) are connected to each other on each corner through the trimesate ligands located on each face to form a large super tetrahedron (ST), which is the basic building block of the MIL framework (Figure 4-7b). The trimeric unit (Figure 4-7c) consists of three Fe³⁺ atoms of octahedral coordination bridged by one oxygen vertex. Thermal activation under vacuum or inert flow can create either open Fe(III) sites through the elimination of water or open Fe(II) sites through the elimination of the monovalent anion (Figure 4-7d) [125].

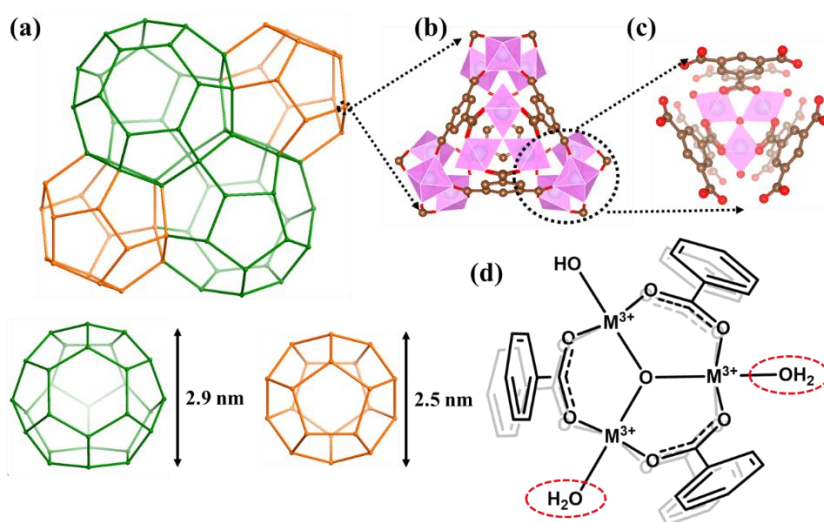


Figure 4-7. (a) Top: Schematic view of the 3D structure of MIL-100 with two types of cages visualized in green and orange delimited by the vertex sharing of the ST (the vertices represent the centers of each ST). Bottom: View and dimensions of the two different cages (orange, 20 tetrahedra; green, 28 tetrahedra); (b) The ST formed by using trimeric unit on each corner and trimesic acid, which occupies the faces of ST. (c) The original building block of the trimeric unit

with a trimer of metal octahedra chelated by three carboxylic functions. (d) Representation of the tri-iron node in which the M metal site is open coordinated by post-treatment to remove the coordinated H₂O or OH groups. Pink = Fe, red = O and brown = C.

Unsaturated Fe(II) species have been reported as the active sites in Fe-exchanged zeolites [25,26] and MOFs (MOF-74-(Mg, Fe) and MIL-53(Al, Fe)) capable of activating light alkanes through the formation of high-spin Fe(IV)=O moiety by N₂O. Also, MIL-100(Fe) having unsaturated Fe(II) species with similar geometry and oxidation state as a catalyst for light alkane activation like propane [126] and methane [127] with N₂O as the oxidant has been demonstrated. In contrast to the higher amount of catalyst applied to the fixed-bed reactor with N₂O or O₂ as the oxidant, the amount required for batch reactors is relatively small, making the screening of new MOF designs as catalysts easier. There is still a lot of room for adjustment and design of the MIL-100 catalyst, such as changing the metal sites or using a more stable Al-based MIL-100 as the support. For example, besides Fe sites, single-site chromium atoms supported on titanium dioxide nanoparticles (denoted as Cr₁/TiO₂) [55] are reported as an efficient heterogeneous catalyst for direct methane oxidation to C1 oxygenated products with H₂O₂ as oxidant under mild conditions.

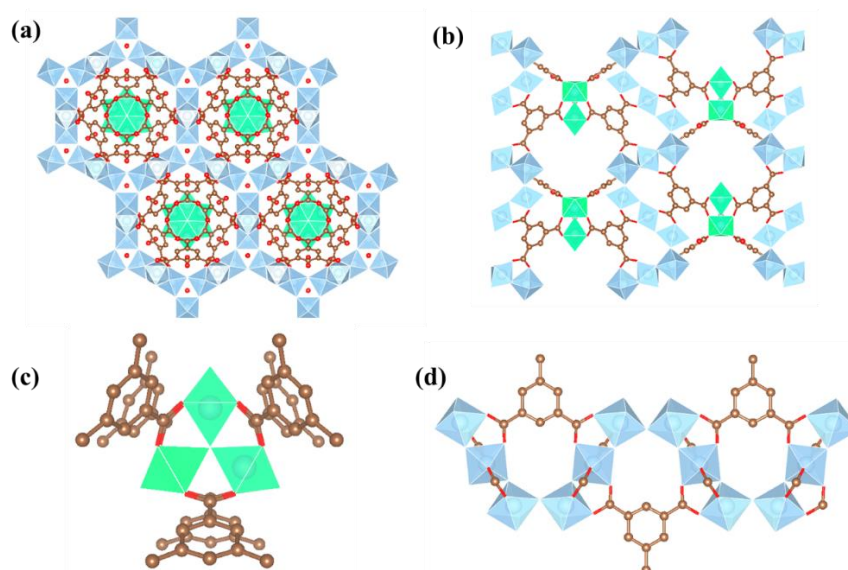


Figure 4-8. (a) Projection of the structure of MIL-96(Al) along the c axis, showing the hexagonal network. (b) Projection of the structure of MIL-96(Al) along the b axis. (c) View of the μ_3 -oxo-centered trinuclear $\text{Al}_3(\mu_3\text{-O})[(\text{O}_2\text{C}-\text{C}_6\text{H}_3-(\text{CO}_2)_2)_6(\text{H}_2\text{O})_3]$ core in MIL-96, showing the three $\text{AlO}_5(\text{H}_2\text{O})$ octahedral units chelated by the trimesate groups. (d) View of the corrugated chains of corner-sharing aluminum octahedral, with the -cis-cis-trans sequence in MIL-96. Green = Al, pale blue = Al, red = O and brown = C.

In addition to MIL-100, MIL-96 [118], with a similar structural configuration, consisting of octahedrally coordinated aluminum linked through the trimesate ligand, can also be viewed as good support for Fe sites. The structure of MIL-96(Al),

[Al₁₂O(OH)₁₈(H₂O)₃(Al₂(OH)₄)[BTC]₆·24H₂O] as the chemical formula contains isolated trinuclear μ₃-O centered aluminum clusters (Figure 4-8c) and infinite chains of aluminum octahedra (Figure 4-8d) forming a hexagonal network with 18-membered rings (Figure 4-8a and 4-8b). Two different types of Al clusters were found in the MIL-96 framework. The first one (Figure 4-8c) is a classic μ₃-oxo-centered trinuclear unit with aluminum octahedrally linked by the trimesate ligand, which is also present in MIL-100(Fe) acting as the active part for partial methane oxidation. The second type of Al cluster consists of a 2D network of aluminum octahedral chains, interconnected to form a hexagonal 18-membered ring in the (a,b) plane (Figure 4-8a). The metal chain structure also accommodates dimeric and monomeric Fe species in MIL-53(Fe,Al) active for selective methane oxidation in H₂O₂ aqueous solution.

4.3.2 Synthesis method

4.3.2.1 Synthesis of MIL-100(Al)

According to Férey et al. [119], MIL-100(Al) was hydrothermally synthesized in an autoclave reactor from a mixture of aluminum nitrate (Al(NO₃)₃·9H₂O), trimethyl 1,3,5-benzenetricarboxylate (C₁₂H₁₂O₆, noted btcMe₃), nitric acid (HNO₃, 1 M) and deionized water. The following composition was placed in a 23 ml Teflon vessel and then in a Parr-type autoclave: Al(NO₃)₃·9H₂O: 740 mg; btcMe₃: 338 mg; 1 M HNO₃: 2.2 mL; H₂O: 9.1 mL. The synthesis was conducted at 210 °C for 3.5 hours in an oven. The resulting powder was separated by filtration, washed with DMF 2 times until colorless and deionized water for 1 time, and then soaked with acetone for 1 day and dried at room temperature.

4.3.2.2 Metal loading of MIL-100(Al)

According to the literature [128], a highly efficient and versatile strategy, namely solvent-assisted metal metathesis, was reported to obtain a variety of metal-modified MOFs, including several well-known MOFs like MIL and PCN series.

Synthesis of V/MIL-100(Al): 100 mg VCl₃, 100 mg MIL-100(Al) and 50 mL DMF were added into a 100 mL glass flask, then heated to 165 °C and refluxed for 2 hours. After the exchange procedure, the solid V/MIL-100(Al) was obtained by decanting the mother liquor and rinsing with deionized water 2 times, acetone 2 times and immersed into acetone for 1 day to exchange DMF. The acetone was decanted, and the catalyst was vacuum dried at 150 °C overnight before catalytic reactions. The metal content was 1.97 wt.% V determined by ICP measurements.

Synthesis of Cr/MIL-100(Al): (20.05.20 batch) 4.5 mg CrCl₃, 100 mg MIL-100(Al) and 50 mL DMF were added into a 100 mL autoclave reactor, then heated to 160 °C for 12 hours. The purple

solid Cr/MIL-100(Al) was obtained by decanting the mother liquor and rinsing with deionized water 2 times, acetone 2 times and immersed into acetone for 1 day to exchange DMF. The acetone was decanted, and the catalyst was vacuum dried at 150 °C overnight before catalytic reactions. The metal content was 0.55 wt.% Cr determined by ICP measurements.

(20.09.07 batch) 3.6 mg $\text{CrCl}_3 \cdot 6\text{H}_2\text{O}$, 60 mg MIL-100(Al) and 10 mL DMF were added into a 25 mL glass flask, then refluxed at 160 °C for 2 h. The pale-yellow solid Cr/MIL-100(Al) was obtained by decanting the mother liquor and rinsing with DMF 1 time, acetone 1 times and immersed into acetone for 1 day to exchange DMF. The acetone was decanted, and the catalyst was vacuum dried at 150 °C overnight before catalytic reactions. The metal content amounted to 0.27 wt.% determined Cr by ICP measurements.

Synthesis of Fe/MIL-100(Al): 30.8 mg $\text{FeCl}_3 \cdot 6\text{H}_2\text{O}$, 70 mg MIL-100(Al) and 10 mL of DMF were added into a 25 mL glass flask, then refluxed at 160 °C for 2 hours. The pale-yellow solid Fe/MIL-100(Al) was obtained by decanting the mother liquor and rinsing with DMF 1 time, acetone 1 time and immersed into acetone for 1 day to exchange DMF. The acetone was decanted, and the catalyst was vacuum dried at 150 °C overnight prior to catalytic reaction. The metal content was 0.94 wt.% Fe determined by ICP measurements.

The obvious color change of the synthesized catalysts after metallization indicated that the metal had been successfully immobilized into the MOF structure.

4.3.2.3 Synthesis of MIL-96(Al)

According to the literature [118], the aluminum trimesate $\text{Al}_{12}\text{O}(\text{OH})_{18}(\text{H}_2\text{O})_3(\text{Al}_2(\text{OH})_4)\text{-}[\text{btc}]_6 \cdot 24\text{H}_2\text{O}$ (MIL-96) was hydrothermally synthesized in an autoclave reactor. Typically, the reaction mixture containing the molar ratio: 1 $\text{Al}(\text{NO}_3)_3 \cdot 9\text{H}_2\text{O}$ (3.5 mmol, 1.314 g)/0.14 H_3btc (0.5 mmol, 0.105 g, 1,3,5-benzenetricarboxylic acid)/80 H_2O (278 mmol, 5 mL) was placed in a 23-mL Teflon-lined steel autoclave at 210 °C for 24 h. After the hydrothermal treatment, a powdery product was obtained, which was filtered off, washed with deionized water until colorless, and dried in air at room temperature.

4.3.2.4 Metal loading of MIL-96(Al)

14.2 mg $\text{CrCl}_3 \cdot 6\text{H}_2\text{O}$ or 38 mg $\text{FeCl}_3 \cdot 6\text{H}_2\text{O}$ was dissolved in 10 mL acetone upon ultrasonication to form Cr^{3+} or Fe^{3+} stock solution. A freshly prepared MIL-96 (about 100 mg) was dispersed in the above solution (10 mL), refluxing at 65 °C for about 1 hour. After the exchange procedure, the solid denoted as Cr/MIL-96 or Fe/MIL-96 was obtained by decanting the mother liquor and rinsing with acetone 2 times and soaked into acetone for 1 day. The acetone was decanted, and the catalyst was vacuum dried. After drying, the colors of Cr/MIL-96 or Fe/MIL-96

were pale blue and dark yellow, respectively. The metal contents were 4.4 wt.% Cr and 2.8 wt.% Fe determined by ICP measurements.

4.3.3 XRD characterization and activity tests

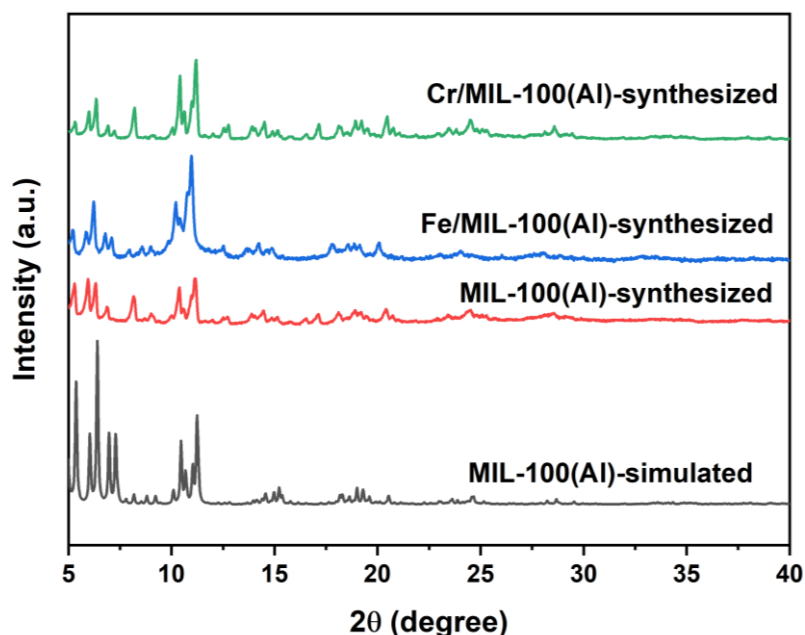


Figure 4-9. PXRD patterns for pristine and metal loaded MIL-100(Al).

Table 4-3. Catalytic performance of the synthesized MIL-100(Al) related catalysts.

No.	Cat.	React. Condi.	Product yield(μmol)/Selectivity(%)						H ₂ O ₂		TOF (h ⁻¹)
			Me OH	OHCH ₂ OOH	Me OOH	HCOOH	CO ₂	O ₂ ($\times 10^3$)	Conv. (%)	Util. (%)	
1	1.97V/MIL-100(Al)	50°C, 0.8h 6 mg	0.6 45.7%	0	0.1 8.7%	0.6 45.7%	0	0.07	0	0	0.7
2	1.97V/MIL-100(Al)	80°C, 0.7h 10 mg	1.2 11.9%	0	7.0 70.6%	1.7 17.4%	0	0.5	12.5	2.0	3.6
3	0.55Cr/MIL-100(Al) ^a	50°C, 1h 10 mg	1.6 8.7%	4.8 26.4%	9.5 52.1%	2.3 12.8%	0	0.6	28.8	1.9	19
4	0.55Cr/MIL-100(Al) ^a	60°C, 1h 9 mg	4.6 3.6%	18.0 13.9%	11.4 8.7%	8.5 6.5%	87.6 67.3%	2.0	87.7	2.2	48
5	0.27Cr/MIL-100(Al) ^b	60°C, 0.5h 5 mg	1.0 9.7%	0	8.4 81.0%	1.0 9.2%	0	0.2	13.5	1.9	80
6	0.27Cr/MIL-100(Al) ^b	60°C, 1h 10 mg	1.3 9.0%	2.9 19.9%	9.3 63.0%	1.2 8.1%	0	0.5	20.6	2.0	28
7	0.94Fe/MIL-100(Al)	50°C, 1h 5 mg	0.5 18.3%	0	1.9 67.7%	0.4 14.0%	0	0.14	5.3	1.4	3.4
8	0.94Fe/MIL-100(Al)	60°C, 1h 10 mg	0.7 9.5%	1.0 14.0%	4.5 62.9%	1.0 13.6%	0	0.27	8.8	2.3	4.2

Reaction condition: 30 bar CH₄, 10 mL 0.5 M H₂O₂, autoclave reactor, 600 rpm; ^a20.05.20 batch, 4.5 mg CrCl₃ as metal precursor, Cr: 0.55 wt.%. ^b20.09.07 batch, 3.6 mg CrCl₃·6H₂O as metal precursor. Cr: 0.27 wt.%.

MIL-100(Al) was prepared using the hydrothermal method. Figure 4-9 shows the XRD patterns of synthesized MIL-100(Al) and Fe, Cr-modified MIL-100(Al) by solvent-assisted metal metathesis. The synthesized sample displayed well-resolved XRD patterns consistent with the simulated one, indicating that the structure of MIL-100(Al) has been obtained. Every index matches with the simulated PXRD pattern of MIL-100, ruling out the presence of other phases, such as the corresponding metal oxides.

The catalytic oxidation of methane using H₂O₂ was conducted in the batch autoclave reactor with 30 bar of CH₄ and 0.5 M H₂O₂ (see Table 4-3). No. 1 and 2 for V/MIL-100(Al) show that V sites could not activate H₂O₂ to catalyze methane oxidation, even when increasing the temperature to 80°C. Comparing No. 3&4 with 5&6, we found that Cr/MIL-100(Al) with CrCl₃ as a metal precursor (No. 3 and 4) showed a stronger ability to activate H₂O₂ than CrCl₃·6H₂O. However, the amount of C1 products is still quite low, around 50 μmol for Cr/MIL-100(Al) in No. 4, with huge amounts of CO₂ and high consumption of oxidant at 60 °C for 1 h. In No. 7 and 8, Fe active sites in Fe/MIL-100(Al) did not show a strong ability to activate H₂O₂.

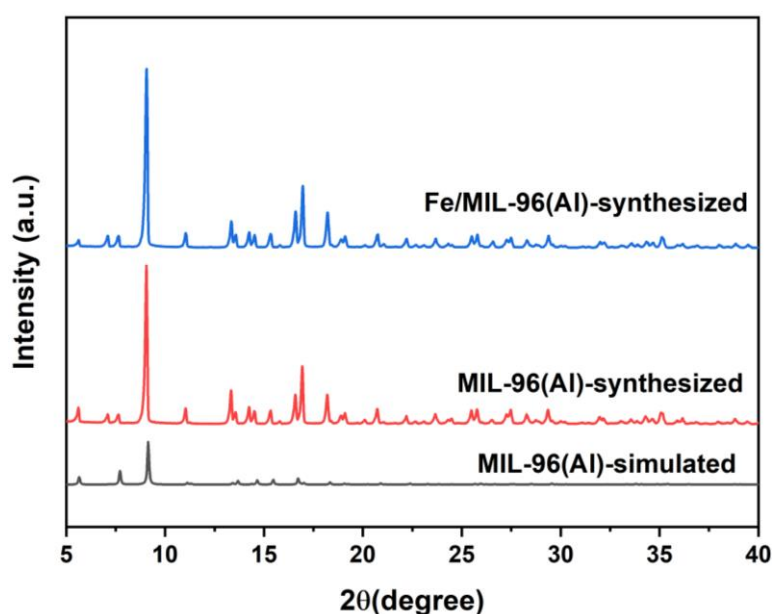


Figure 4-10. PXRD patterns for pristine and Fe modified MIL-96(Al).

Table 4-4. Catalytic performance of the synthesized MIL-96(Al) based catalysts.

No.	Cat.	React. Condi.	Product yield(μmol)/Selectivity(%)					H ₂ O ₂		TOF (h ⁻¹)
			MeOH	OHCH ₂ OOH	MeOOH	HCOOH	CO ₂	O ₂ (×10 ³)	Conv. (%)	

1	4.4Cr/ MIL-96	60°C, 0.5h 5mg	3.0 6.2%	10.2 21.1%	5.5 11.4%	0	29.6 61.3%	2.6	98.4	0.6	8.8
2	4.4Cr/ MIL-96	38°C, 2h 5mg	0.7 15.4%	0	3.8 84.6%	0	0	1.2	80.7	0.1	0.5
3	2.8Fe/ MIL-96	70°C, 0.5h 5mg	2.2 4.9%	11.4 25.0%	14.0 30.7%	0	17.9 39.5%	2.4	88.5	0.9	22

Reaction condition: 30 bar CH₄, 10 mL 0.5 M H₂O₂, autoclave reactor, 600 rpm.

MIL-96 was synthesized according to the literature, followed by treatment with DMF and distilled water to remove the unreacted trimethyl 1,3,5-benzenetricarboxylate. The modified Fe/MIL-96 and Cr/MIL-96 catalysts were prepared through solvent-assisted metal metathesis of MIL-96 with metal chloride salts. The final Fe and Cr loadings in the catalyst were determined as 2.8 wt.% and 4.4 wt.%, respectively, based on the ICP. The powder X-ray diffractions (PXRD) of MIL-96 pattern agree well with the previously reported one (Figure 4-10) [118]. Also, Fe/MIL-96 exhibits no loss of crystallinity (Figure 4-10), indicating that the integrity of the MIL-96 framework is maintained well during the Fe loading. Furthermore, no significant diffraction reflexes of Fe oxide were detected in the PXRD.

The catalytic oxidation of methane using H₂O₂ was conducted in the batch autoclave reactor with 30 bar of CH₄ and 0.5 M H₂O₂ (see Table 4-4). In No. 1, compared to the very limited amount of C1 products of around 20 μmol, huge consumption of H₂O₂ with 98.4% conversion occurred even under very mild reaction conditions of 60 °C for 0.5 h over 4.4Cr/MIL-96. We tried to lower the reaction temperature to around 40 °C with a prolonged reaction time of about 2 h in No. 2. The catalytic result showed almost no C1 products, but with still quite high H₂O₂ conversion of around 80%, which suggested the Cr site in MIL-96 is highly prone to decompose H₂O₂ not activate methane. In No. 3 for 2.8Fe/MIL-96, despite about 90% conversion of H₂O₂, only 27 μmol C1 products were produced, giving a very low H₂O₂ utilization ratio of 0.9%. Remarkably, CO₂ was generated without HCOOH being observed. Considering that methane oxidation can be regarded as multiple consecutive reactions, the CO₂ is typically accompanied by the formation of HCOOH, which is the reactant being oxidized to CO₂. Thus, we speculated that the origin of this CO₂ might not be the over-oxidation of methane, but the decomposition of the BTC linkers in the MOF framework. The BTC linker can undergo mineralization, which gives CO₂ directly. Thus, the overall worse performance has prompted us to stop further research on MIL-96.

4.4 DUT-5

4.4.1 Catalyst design

Sulfolane (a 5-membered cyclic sulfone) is a widely used dipolar aprotic, water-soluble and highly stable industrial solvent [129]. Sulfolane has been reported to have the feature of temporary combination with hydroxyls, which improves phenol selectivity in benzene oxidation to phenol reaction [130]. Balducci et al. [131] showed that the phenol selectivity in sulfolane by using H_2O_2 is twice that in other solvents due to the temporary bonding between phenol and sulfolane to avoid the generation of by-products. Sulfolane has also proven to be an efficient solvent for liquid-phase direct methane oxidation with H_2O_2 . Xiao et al. [132] showed that a sulfolane/ H_2O_2 aqueous solution mixture led to an excellent methanol selectivity and low H_2O_2 conversion over Fe-MFI catalyst at 323 K. In Figure 4-11, when 50 vol% sulfolane was used as the solvent, the yield and selectivity of MeOH reached the maximum with a high yield of oxygenated products and low H_2O_2 conversion. Thus, the author proposed that the temporary adduct formation of hydroxyls with sulfone prevented the overoxidation of methanol. On the other hand, H_2O_2 showed the highest conversion in water but the lowest conversion in sulfolane because sulfolane is an aprotic solvent in contrast with the protic nature of water that provides protons. The author also investigated the stability of sulfone under the typical reaction conditions and found there were no peaks ascribed to the products observed after the blank test in the $^1\text{H-NMR}$ spectrum. However, it is important to point out that the authors did not mention if they detected CO_2 in the blank experiment, which is very likely generated through total oxidation of sulfone by hydroxyl radicals. Considering the high price and toxicity of organic solvent sulfone, we envisage the fixation of sulfone groups in MOF structure which will be highly dispersed to improve the methanol selectivity and H_2O_2 utilization ratio.

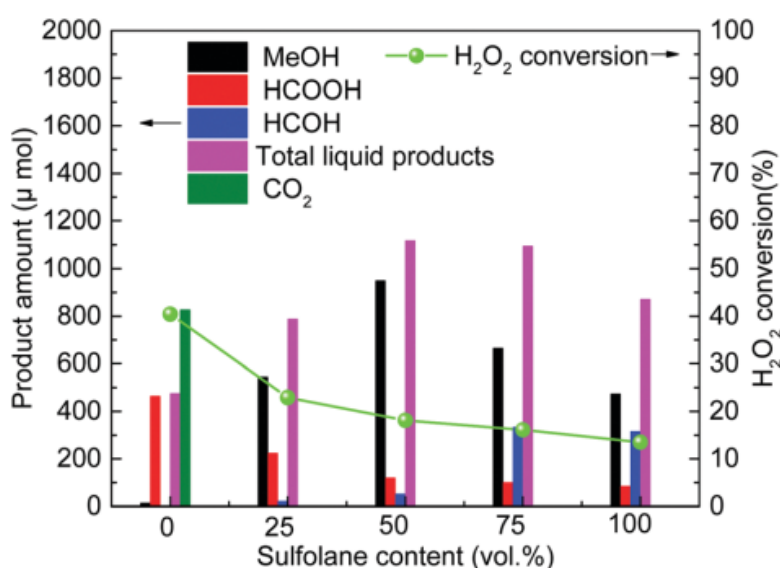


Figure 4-11. The amount of products and H₂O₂ conversion under different proportions of sulfolane content. Reaction conditions: 323 K, 10 mL of solvent, 50 mg of catalyst, 27 mmol of H₂O₂, P(CH₄) = 3 MPa, 2 h.[132]

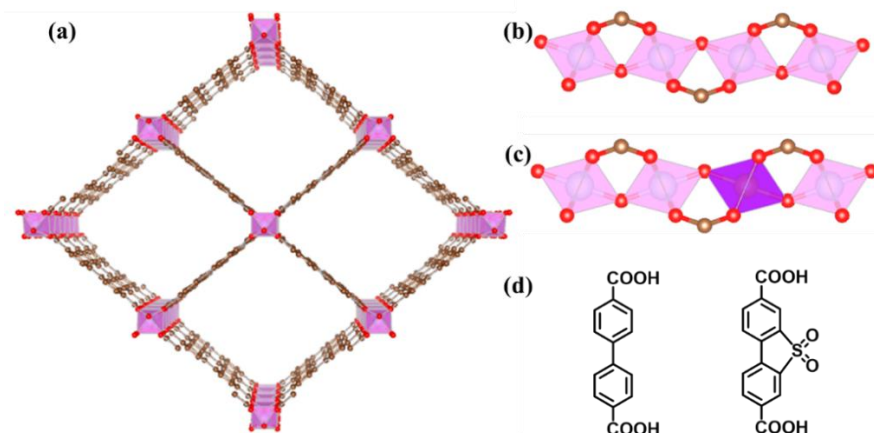


Figure 4-12. (a) Schematic representation of DUT-5 structure viewing along b axis. (b) Schematic representation of the Al chain of DUT-5. (c) Schematic representation of Fe doped Al chain. (d) The ligand molecule of BPDC (4,4'-biphenyl dicarboxylate) and BPDC-SO₂ linkers (4,4'-bibenzoic acid-2,2'-sulfone). Pink = Al, purple = Fe, red = O and brown = C.

A sulfone functionalized MOF DUT-5 (DUT = Dresden University of Technology), denoted as DUT-5-SO₂ was synthesized using 4,4'-bibenzoic acid-2,2'-sulfone (BPDC-SO₂) linkers (see Figure 4-12) [133] The parent material, DUT-5(Al), was first synthesized by the group of Kaskel [134], which consists of aluminum and 4,4'-biphenyl dicarboxylate linkers. DUT-5(Al) has the same topology and metal building blocks as MIL-53(Al), but with a longer linker molecule.

4.4.2 Synthesis method

4.4.2.1 Synthesis of DUT-5 and DUT-5-SO₂

According to the literature [133,134], DUT-5-SO₂ and DUT-5 were synthesized using a mixture of Al(NO₃)₃·9H₂O (0.6 g, 1.6 mmol), organic ligand H₂BPDC (4,4'-bibenzoic acid) (0.63 g, 2.6 mmol) or H₂BPDC-SO₂ (0.8 g, 2.6 mmol) suspended in 60 mL N,N-dimethylformamide (DMF). According to Ref. [133], ligand H₂BPDC-SO₂ was synthesized based on commercial H₂BPDC. The mixture was placed in a 100 mL Schlenk flask sealed and heated to 413 K with stirring and kept for 24 h at this temperature. The white powder obtained was filtered off, washed thoroughly with DMF, methanol and acetone and finally vacuum dried.

4.4.2.2 Metal loading by post-synthesis modification

A certain amount of FeCl₃·6H₂O or CrCl₃·6H₂O was dissolved in 10 mL acetone upon ultrasonication. A freshly prepared DUT-5 or DUT-5-SO₂ (about 100 mg) was dispersed in the

above solution (10 mL), refluxing at 65 °C for about 1 hour. After the exchange procedure, the solids denoted as Fe/DUT-5-SO₂-post or Fe/DUT-5-post were obtained by decanting the mother liquor and rinsing with acetone 2 times and soaked into acetone for 1 day. Finally, the acetone was decanted, and the catalyst was vacuum dried. The color of Fe/DUT-5-SO₂-post after drying was pale yellow.

4.4.2.3 Metal loading by direct-synthesis modification

According to the literature [134], Fe-DUT-5-SO₂-direct and Fe-DUT-5-direct were synthesized using a mixture of Al(NO₃)₃·9H₂O (0.6 g, 1.6 mmol), Fe(NO₃)₃·9H₂O (20.8 mg, 1.0 wt.%), organic ligand H₂BPDC (4,4'-bibenzoic acid) (0.63 g, 2.6 mmol) or H₂BPDC-SO₂ (0.8 g, 2.6 mmol) suspended in 60 mL N,N'-dimethylformamide (DMF). The mixture was placed in a 100 mL Schlenk flask sealed and heated to 413 K with stirring and kept for 24 h at this temperature. The white powder was filtered off, washed thoroughly with DMF, methanol, and acetone, and vacuum dried. The color of Fe-DUT-5-SO₂-direct after drying was brown.

4.4.3 XRD characterization and activity test

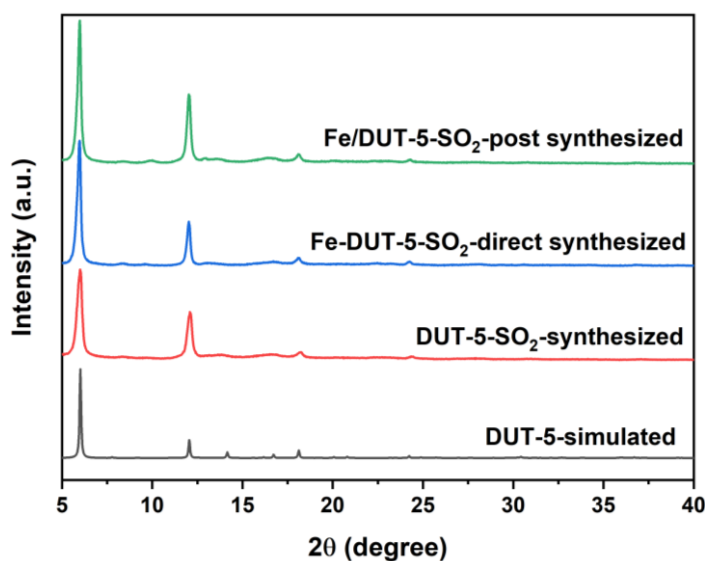


Figure 4-13. PXRD patterns for pristine and Fe modified DUT-5-SO₂(Al).

Table 4-5. Catalytic performance of the synthesized DUT-5 based catalysts.

No.	Cat.	React. Condi.	Product yield(μmol)/Selectivity(%)						H ₂ O ₂		TOF /h ⁻¹
			MeOH	OHCH ₂ OOH	MeO OH	HCO OH	CO ₂	O ₂ (×10 ³)	Conv. (%)	Util. (%)	
1	0.26Fe/DUT-5-SO ₂ -post	60°C, 0.5h 5 mg	0.4 12.5%	0	3.0 87.5%	0	0	0.15	3.7	1.9	-
2	0.26Fe/DUT-5-SO ₂ -post	70°C, 1h 10 mg	1.8 5.1%	2.4 6.8%	10.8 30.6%	2.7 7.8%	17.6 49.7%	0.36	11.3	4.4	37.7

4. Direct methane oxidation over different MOF catalysts by H₂O₂

3	0.50Fe-DUT-5-SO ₂ -direct	70°C, 1h 10 mg	2.7 5.5%	4.2 8.5%	15.5 31.2%	6.4 12.9%	20.8 42.0%	0.45	15.8	5.7	32.1
4	1.62Fe/DUT-5-SO ₂ -post	60°C, 0.5h 5 mg	3.6 6.8%	9.2 17.5%	17.9 34.0%	9.9 18.9%	11.9 22.7%	0.58	22.3	6.1	56.0
5	1.45Cr/DUT-5-SO ₂ -post	60°C, 0.5h 5mg	2.5 6.4%	4.8 12.2%	13.6 34.3%	8.3 20.9%	10.3 26.1%	0.47	16.4	6.0	41.9
6	DUT-5-SO ₂	60°C, 0.5h 5 mg	1.3 32.0%	0	2.7 68.0%	0	0	0.20	3.1	2.5	-
7	3.0Fe-DUT-5-SO ₂ -direct ^a	60, 1h 5mg, N ₂	-	-	-	-	104	1.48	63.6	-	-
8	0.3Fe-DUT-5-SO ₂ -direct ^a	60, 1h 6mg, N ₂	-	-	-	-	11.6	0.38	12.2	-	-
9	3Fe-DUT-5-direct ^a	60, 1h 5mg, N ₂	-	-	-	-	122.8	1.75	74.0	-	-

Reaction condition: 30 bar of CH₄, 10 mL of 0.5 M H₂O₂, autoclave reactor, 600 rpm, 30 bar of CH₄; ^aThe reaction was conducted in N₂ condition to check the CO₂ generation.

The powder XRD patterns of DUT-5-SO₂ obtained from solvothermal synthesis and Fe modified samples by direct or post-synthesized method show good consistency, as can be seen in [Figure 4-13](#). These patterns are further compared with the simulated powder XRD pattern for the crystal structure model of DUT-5 [[134](#)]. All diffractions of experimental patterns shifted slightly to higher 2θ angles, because the sulfone group of the BPDC-SO₂ linker causes a bending of the ligand, changing the angle between the terminal carboxylates from 180° to 163° [[133](#)].

The catalytic oxidation of methane using H₂O₂ was conducted in a batch autoclave reactor at 50 °C with 30 bar of CH₄ and 0.5 M H₂O₂. [Table 4-5](#) shows the catalytic results of the synthesized DUT-5 related catalysts. From [No. 1](#), we found conducting the reaction at 60 °C could not activate catalyst 0.26Fe/DUT-5-SO₂-post that showed almost no H₂O₂ conversion and no C1 products. Further increasing the reaction temperature to 70 °C generated about 18 μmol C1 product with 50% CO₂ selectivity, which showed better activity than direct synthesized 0.50Fe-DUT-5-SO₂-direct catalyst in [No. 3](#). We tried to increase the Fe content in Fe/DUT-5-SO₂-post catalyst and prepare Cr modified catalysts. In [No. 4](#) and [5](#), 1.62Fe/DUT-5-SO₂-post and 1.45Cr/DUT-5-SO₂-post showed similar activity with around 40 μmol C1 product and 56/h TOF at 60 °C. The inevitable generation of CO₂ makes us doubt whether it is from methane or the decomposition of the MOF framework. In [No. 6](#), we conduct the blank experiment over DUT-5-SO₂ without active metal to check the stability of the MOF framework in the reaction condition. It seems DUT-5-SO₂ is quite stable without decomposition to CO₂ in 0.5M H₂O₂ aqueous solution at 60 °C for 1 h. We further test the stability of DUT-5-SO₂ with active metal in N₂ to check the stability when H₂O₂ is activated

by active site Fe in No. 7-9. Without the competition from methane, the MOF framework, especially the organic linker, became the target for the $\bullet\text{OH}$. The carboxylic acid based ligand can undergo mineralization/decarboxylation, which can give CO_2 directly. Compared No. 7 with 8, we learn that the amount of Fe content determines the conversion of H_2O_2 and the degree of framework damage causing the generation of CO_2 . The above experiments make us understand why there is always a certain ratio of CO_2 generated from the framework damage during the reaction. Comparing No. 7 and 9, the lower degree of generating CO_2 and the lower H_2O_2 conversion of 3Fe-DUT-5- SO_2 -direct compared to 3Fe-DUT-5-direct is in accordance with our initial vision that sulfone groups benefit the H_2O_2 utilization to some degree. Even though the positive effect of $-\text{SO}_2$ was verified, the interfering degradation of MOFs will influence our judgment of the catalysts regarding activity/selectivity, which caused us to stop the research on modified DUT- SO_2 catalysts.

4.5 UiO-66

4.5.1 Catalyst design

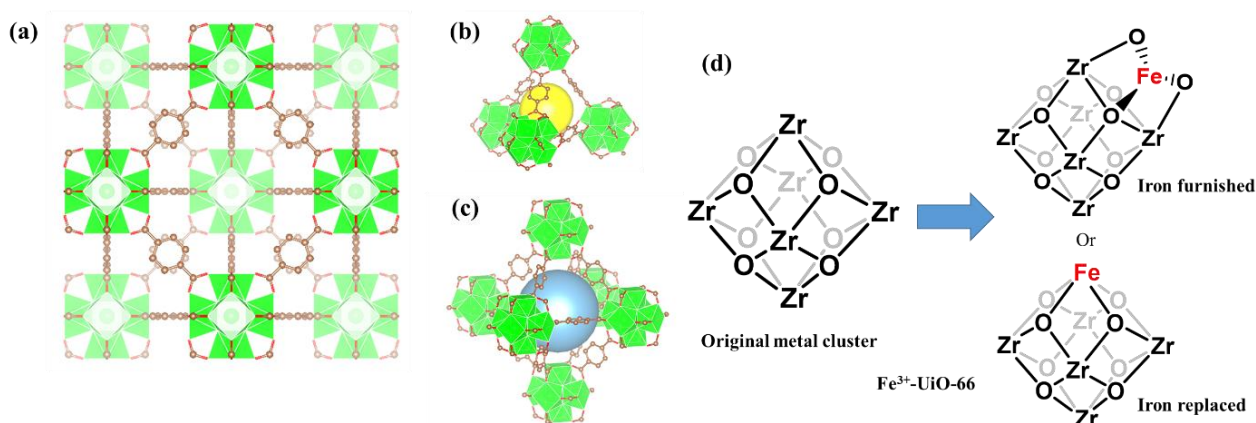


Figure 4-14. (a) Schematic representation of Zr-MOF UiO-66 with 1,4-benzene-dicarboxylate (BDC) as linker viewing along c axis. The Zr-MOF structure is assembled of two types of cages: (b) a super tetrahedron and (c) a super octahedron. (d) Schematic representation of the Fe position on the Zr_6 cluster of UiO-66 after metal functionalization by direct- and post-synthetic modification method. Green = Zirconium, red = O and brown = C.

The stability of the MOF frameworks mainly depends on the inorganic building units and the strength of the chemical bond between the inorganic node and the ligand. We have chosen some Al-based MOFs mentioned above due to their high thermal and chemical stability. Besides Al-based SBUs, Zr-based inorganic building units like in UiO-66 are of utmost importance for getting stable, flexible structures. The UiO-66 structure is formed with linear ligands 1,4-benzene-

dicarboxylate (BDC) and Zr₆O₄(OH)₄(CO₂)₁₂ with 12 coordinations, expanding to the cubic closest packed (CCP) structure (Figure 4-14) [135]. Some simple functionalization strategies at metal-organic framework nodes have been reported to afford coordinatively unsaturated metal centers that can catalyze interesting organic reactions [136]. We tried two different ways to achieve the Fe ion metalation on Zr SBUs of UiO-66, on one hand by direct synthesis and on the other hand by post-synthetic modification. In Figure 4-14d, the proposed structures after Fe modification by the two different methods are exhibited. The metal nodes of hexa-zirconium(IV) MOFs are often coordinated with -OH and -OH₂ groups that could further act as the anchoring sites for active components, which can be used for a broad scope of organic transformations. For the post-synthetic modification, the deprotonation of OH sites of Zr-SBUs followed by reactions with iron afforded Fe- functionalized MOF-materials Fe/UiO-66-post (Figure 4-14d). For the direct-synthetic modification, Fe ion is prone to replace the position of Zr to form the Fe active site after vacuum activation to remove coordinated H₂O or OH sites.

4.5.2 Synthesis method

4.5.2.1 Synthesis of UiO-66

According to the literature [135], the synthesis of UiO-66 was performed by dissolving 372 mg ZrCl₄, 276 mg 1,4-benzenedicarboxylic acid (H₂BDC), 0.2 mL H₂O and 12 mL acetic acid in 100 mL N,N'-dimethylformamide (DMF) (24.9 g, 340 mmol) at room temperature. The thus obtained mixture was sealed and placed in a pre-heated oven at 120 °C for 24 hours. After cooling in air to room temperature, the resulting solid was filtered, repeatedly washed with DMF and acetone, and finally dried at room temperature.

4.5.2.2 Metal loading by post-synthetic modification

10 mg FeCl₃·6H₂O was dissolved in 4 mL acetonitrile with 50 mg UiO-66 upon ultrasonication in a glass vial, which was then heated at 85 °C for and kept at this temperature for 24 hours in an oven. After the exchange procedure, the solids denoted as Fe/UiO-66-post were obtained by decanting the mother liquor and rinsing with acetonitrile 2 times, acetone for 1 time, and soaked into acetone for 2 days. Finally, the acetone was decanted, and the catalyst was vacuum dried.

25 mg VOSO₄·5H₂O was dissolved in the mixture of 5 mL acetonitrile and 3 mL DMF with 50 mg UiO-66 upon ultrasonication in a glass vial, then heated to 85 °C and hold at this temperature for about 24 hours in an oven. After the exchange procedure, the solid denoted as V/UiO-66-post was obtained by decanting the mother liquor and rinsing with acetonitrile 2 times, H₂O until

colorless and acetone 1 time and soaked into acetone for 2 days. The acetone was decanted, and the catalyst was vacuum dried.

4.5.2.3 Metal loading by direct synthetic modification

According to the literature [137], the mixed Fe/Zr UiO-66 material was obtained under solvothermal conditions from a mixture of 166 mg 1,4-benzenedicarboxylic acid (1 mmol), 186.4 mg of zirconium(IV) chloride (0.8 mmol) and 54 mg of Fe(III) chloride hexahydrate (0.2 mmol) in 5 mL N,N-dimethylformamide (DMF) which was filled in a Teflon lined vessel and heated to 120 °C for 24 hours. After cooling, the solution was filtered and the recovered powder was washed with DMF, distilled water and acetone to remove any free, unreacted 1,4-benzenedicarboxylic acid.

4.5.2.4 Calcination of Fe/UiO-66

The obtained Fe-UiO-66-direct and V/UiO-66-post further calcined at 300 °C in an oven achieved with a heating rate of 100 °C/h and kept for 5 hours in air.

4.5.3 XRD characterization and activity tests

Powder X-ray diffraction (XRD) patterns (Figure 4-15) revealed that the crystal structure of the synthesized UiO-66 and Fe modified UiO-66 obtained from direct- and post-synthesized methods is in good agreement with that of typical UiO-66. Furthermore, no obvious XRD peaks of Fe compounds are discerned, likely owing to their extremely small size and low loading. The PXRD patterns obtained for calcined samples indicate that the calcination process has little effect on the overall crystallinity of the material.

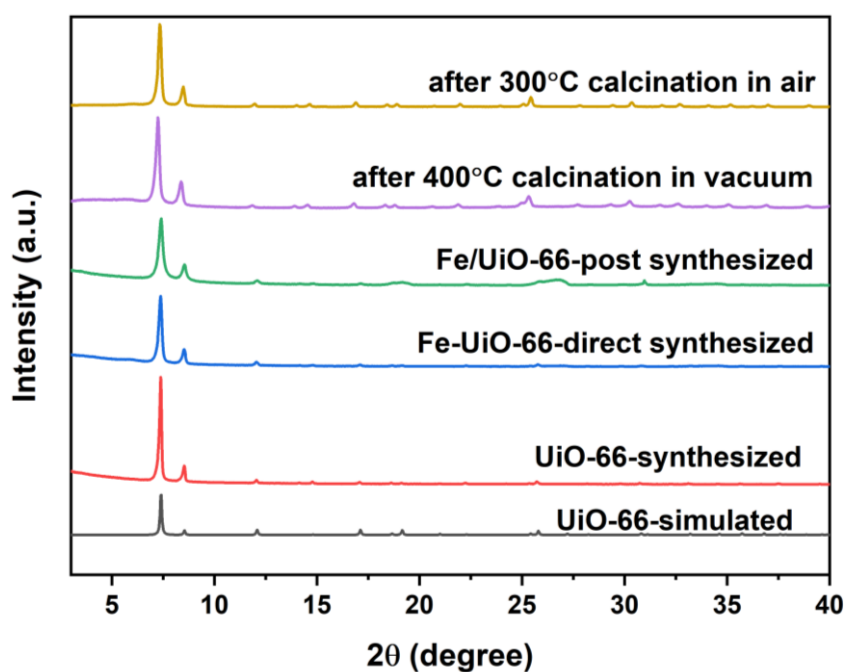


Figure 4-15. PXRD patterns for pristine and Fe modified UiO-66(Zr).

The catalytic oxidation of methane using H₂O₂ was conducted in a batch autoclave reactor at 50 °C with 30 bar of CH₄ and 0.5 M H₂O₂. Table 4-6 shows the catalytic results of the synthesized UiO-66 based catalysts. According to entry 1, 1.6V/UiO-66 did not show any trend to activate H₂O₂ at 50 °C. Further increasing the reaction temperature to 80 °C (entry 2), there was a strong conversion of H₂O₂, but almost no C1 products and CO₂, indicating that the conversion of H₂O₂ is caused mainly by thermal decomposition at 80 °C without degradation of UiO-66. Considering the existence of these iron sites in MOF being mostly a single state, proper calcination without damaging MOFs framework was performed to promote cluster formation as done for zeolites (see part 1.4). According to entry 3, the calcined 1.7V/UiO-66-post-300 did not show an increase in C1 products but with a higher degree of H₂O₂ thermal decomposition to O₂ and generation of CO₂ possibly due to the framework degradation. Fe-modified UiO-66 catalysts obtained by post- and direct-synthetic methods were first tested at 50 °C (see entry 4 and 5). Comparing the catalytic results with the pristine UiO-66 without metal site in entry 6, 0.9Fe-UiO-66-direct did not show any real activity of Fe sites, and 1.0Fe/UiO-66-post obviously can activate H₂O₂ with around 40% conversion to get a very limited amount of C1 products of 19 μmol at 50 °C. The calcined sample 1.2Fe-UiO-66-direct-400-vacuum of entry 7 can activate H₂O₂ with 18% conversion compared to 4% conversion of the uncalcined sample as shown in entry 4, but it did not give any product. Despite increasing the reaction temperature to 80 °C in entry 8, few oxygenates were obtained. Compared with other tested MOF catalysts, UiO-66 based catalysts showed better stability in our test condition. However, they did not show good activity to oxygenates, possibly due to the unsuitable Fe loading conditions.

Table 4-6. Catalytic performances of the synthesized UiO-66 based catalysts.

Entry	Cat.	React. Condi.	Product yield(μmol)/Selectivity(%)						H ₂ O ₂		TOF /h ⁻¹
			MeOH	OHCH ₂ OOH	MeOOH	HCOOH	CO ₂	O ₂ (×10 ³)	Conv. (%)	Util. (%)	
1	1.6V/UiO-66-post	50°C, 1h 10 mg	0.4	0	1.0	1.0	0	0.11	0.9	9.9	-
2	1.6V/UiO-66-post	80°C, 1h 10 mg	1.6 33.5%	0	2.4 50.3%	0.8 16.2%	0	1.5	53.0	0.2	-
3	1.7V/UiO-66-post-300	80°C, 1h 15 mg	2.2 6.2%	0	5.3 15.4%	1.9 5.5%	25.3 72.8%	1.8	67.1	0.4	-
4	0.9Fe-UiO-66-direct	50°C, 1h 10 mg	0.6 15.3%	0	1.1 26.4%	2.4 58.3%	0	0.2	4.1	4.2	-
5	1.0Fe/UiO-66-post	50°C, 1h 10 mg	2.1 5.9%	0	6.9 19.1%	9.7 26.9%	17.4 48.1%	1.0	39.3	1.8	13

6	UiO-66	50°C, 1h 10 mg	0.5 14.1%	0	0.8 23.2%	2.3 62.4%	0	0.13	0.04	-	-
7	1.2Fe- UiO-66- direct-400- vacuum ^a	50°C, 1h 10 mg	0.5	0	2.1	2.2	0	0.55	18.1	1.0	-
8	1.1Fe- UiO-66- direct-300 ^b	80°C, 1h 10 mg	2.6 4.0%	0	8.4 13.0%	5.2 8.0%	48.6 75.0%	1.0	38.0	5.0	-

Reaction condition: 30 bar CH₄, 10 mL 0.5 M H₂O₂, autoclave reactor, 600 rpm; ^aFe-UiO-66-direct treated in vacuum at 400 °C achieved with a heating rate of 3 °C/min and kept for 3 h. ^bFe-UiO-66-direct calcined in air at 300 °C with a heating rate of 3 °C/min and kept for 3 h.

4.6 ZIF-8

4.6.1 Catalyst design

ZSM-5 has proven capable of stabilizing extra-framework Fe species as the active sites through activation at 550 °C, in a form analogous to that found in methane monooxygenase enzymes, to selectively convert methane to mono-oxygenated products in the presence of H₂O₂. However, the characterization and identification of Fe sites in zeolites are nontrivial because of multiple iron species. The exact nature of the active sites in Fe-ZSM-5 remains largely a matter of speculation [138]. Using MOFs to encapsulate single Fe sites or bi-nuclear Fe complexes is a currently unexplored yet promising method to achieve uniformly dispersed and specific Fe sites after calcination to remove the organic part. We selected the zeolitic imidazolate framework-8 (ZIF-8) [139] to act as the nanoporous host material, within which we encapsulate different Fe metal complex guests [140]. This strategy was motivated by the larger internal void size of ZIF-8 at 13.32 Å × 11.18 Å with much narrower pore windows of ~3.4 Å (Figure 4-16a). ZIF-8 could be prepared on the gram scale to allow detailed investigations. The advantage of facile ZIF-8 synthesis [141,142] is that it offers a straightforward route to confine guest molecules larger than the physical dimension permitted by the MOF window opening. More significantly, unlike other MOFs, ZIF-8 has exceptional thermal (up to 550°C in N₂) and chemical stability upon refluxing with organic solvents, water, and aqueous alkaline solution, making it possible to withstand the high-temperature activation to form Fe active sites.

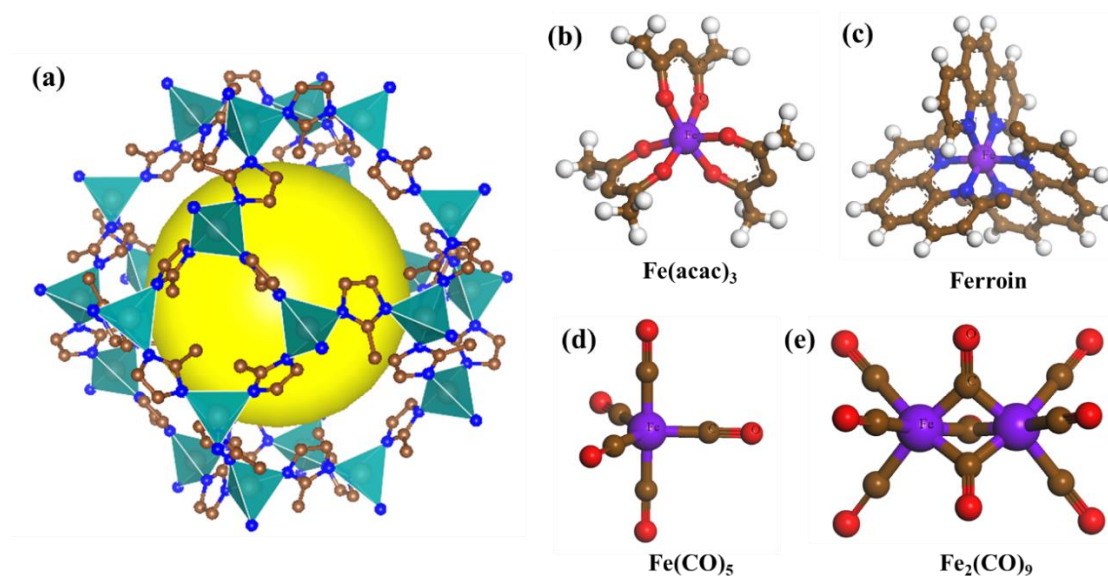


Figure 4-16. (a) The larger internal void volume at the center of the sodalite nanocage of ZIF-8. (c) The molecule structures of Fe(acac)₃, Ferroin, Fe(CO)₅ and Fe₂(CO)₉ represented by ball stick models. Peacock green = Zn, brown = C, blue = N, red = O, purple = Fe, and white = H.

4.6.2 Synthesis method

4.6.2.1 Synthesis of ZIF-8

According to the literature [142], a solid mixture of zinc nitrate tetrahydrate Zn(NO₃)₂·4H₂O (0.210 g) and 2-methylimidazole (H-MeIM) (0.060 g) was dissolved in 18 mL of DMF in a 20 mL glass vial. The vial was capped and heated at a rate of 5 °C/min to 140 °C in a programmable oven and held for 24 h, then cooled to room temperature. After removing the mother liquor from the mixture, chloroform (20 mL) was added to the vial. Colorless crystals were collected from the upper layer, washed three times with DMF, and dried in air for 10 min.

4.6.2.2 In situ synthesis of the ZIF-8⊃complex host–guest system

According to the literature, the hybrid host-guest materials were obtained by in situ synthesis method [140]. Initially, the Fe precursor metal complex (see Figure 4-16) was mixed with Zn(NO₃)₂·4H₂O in a ratio of 0.5:1 mmol in 25 mL of methanol to get solution A. Then, in another flask, 4:16 mmol of Zn²⁺: H-MeIM was added to 25 mL of methanol to get solution B, which was kept stirring for 5 minutes and then was added into solution A slowly. After vigorous stirring, the temperature was increased to 80 °C. The synthesis took about 10 minutes. Finally, the crystalline product was washed thoroughly (4 cycles) using a copious amount of methanol and acetone to remove excess complex and residual soluble products. The final product was separated by centrifugation at 8000 rpm.

4.6.2.3 Calcination of the as-synthesized catalysts

To promote a proper cluster formation of single Fe sites, calcinations were conducted. Thus, the obtained metal complex/ZIF-8 compounds were further calcined in an oven at 350 °C or 400 °C with a heating rate of 100 °C/h and kept for 5 hours in N₂, or at 900 °C for 2 hours in N₂.

4.6.3 XRD characterization and activity tests

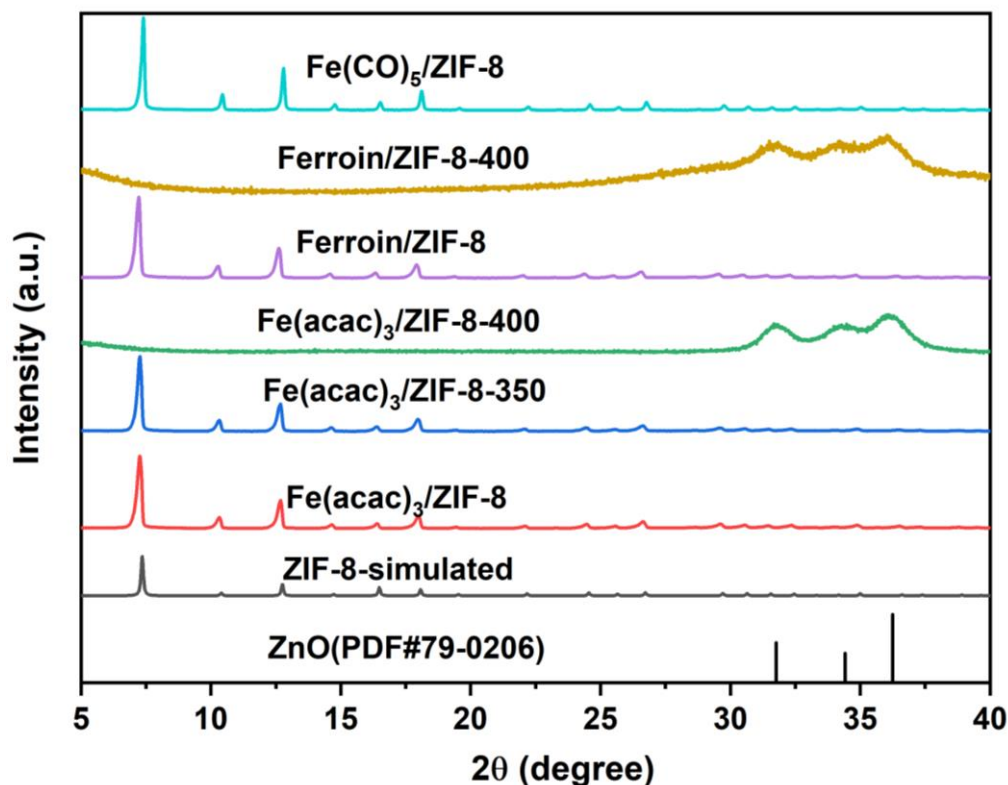


Figure 4-17. PXRD patterns for pristine and Fe modified ZIF-8(Zn).

XRD was used to compare the structural data of the simulated ZIF-8 with its guest-encapsulated counterparts and identify the crystal phase of the as-prepared samples before and after calcination (Figure 4-17). All the diffraction patterns, except for samples calcined at 400 °C, prove the structural integrity of ZIF-8. The XRD pattern of Fe(acac)₃/ZIF-8-350 sample prepared by calcination at 350 °C is similar to that of pure ZIF-8, indicating that the sodalite structure of ZIF-8 crystals was not altered by the addition of Fe precursor and the calcination process. After calcination at 400 °C, the XRD reflexes corresponding to ZIF-8 completely disappeared. The resulting phase were turned out to be ZnO (P63mc, PDF card no. 79-0206) [143]. The reflexes at 2θ values of 31.8, 34.4, 36.2 can be ascribed to (100), (002), and (101) crystal planes of hexagonal ZnO, respectively [144].

Table 4-7. Catalytic performance of the synthesized ZIF-8 based catalysts.

No.	Cat.	React. Condi.	Product yield(μ mol)/Selectivity(%)					H ₂ O ₂		TOF /h ⁻¹	
			Me OH	OHCH ₂ OOH	Me OOH	HCOOH	CO ₂	O ₂ ($\times 10^3$)	Conv. (%)		Util. (%)
1	0.25Fe(acac) ₃ /ZIF-8-400	70°C, 1h 10 mg	0.32 3.7%	0	0.20 2.3%	8.15 94.0%	0	2.12	77.7	0.62	19
2	0.1Fe(acac) ₃ /ZIF-8-350	70°C, 1h 10 mg	0.23 3.3%	0	0	6.77 96.7%	0	0.67	23.0	1.72	38
3	0.5Ferroin/ZIF-8-400	70°C, 1h 10 mg	0.29 1.4%	0	1.33 6.5%	3.73 18.2%	15.2 74.0%	0.89	31.5	0.78	6
4	0.6Ferroin/ZIF-8-900-2h ^a	r.t. 1h 10 mg	0	0	0	0	0	0.12	100	0	-
5	1.2Fe(CO) ₅ /ZIF-8-400	70°C, 1h 10 mg	0.23	0	0	0	0	2.73	98.7	0	-

Reaction condition: 30 bar of CH₄, 10 mL of 0.5 M H₂O₂, autoclave reactor, 600 rpm; ^aGenerating lots of bubbles when adding catalyst into H₂O₂ solution.

The catalytic oxidation of methane using H₂O₂ was conducted in a batch autoclave reactor with 30 bar of CH₄ and 0.5 M H₂O₂. Table 4-7 shows the catalytic results of the synthesized ZIF-8 based catalysts. Comparing No. 1 and 2, samples calcined at 350 °C and 400 °C, respectively, showed different XRD patterns and different catalytic results. Fe(acac)₃/ZIF-8-400 lost ZIF-8 structure and decomposed to ZnO at 400 °C associated with higher conversion of H₂O₂ than Fe(acac)₃/ZIF-8-350 at 70 °C for 1 h. However, both samples generated limited C1 products, which can be attributed to a severe self-decomposition of H₂O₂ under such reaction conditions. Comparing No. 3 and 4, the difference in the H₂O₂ consumption of Ferroin/ZIF-8 samples calcined at 400 °C and 900 °C, respectively, is even more obvious. For the Ferroin/ZIF-8-900-2h sample, a lot of bubbles were generated once it was added to the H₂O₂ solution. In No. 5 of sample 1.2Fe(CO)₅/ZIF-8-400 calcined at 400 °C, the higher loading also decomposed all H₂O₂ even under lower calcination temperature. From the above experimental results, we can learn that the maintained structure of ZIF-8 and suitable Fe content benefit the dispersion of small Fe clusters after calcination. Calcination above 400 °C and too much Fe loading will result in bigger Fe clusters that will cause vigorous decomposition of H₂O₂.

4.7 PCN-250

4.7.1 Catalyst design

After introducing metal sites like Fe, Cu, Mo, Cr, Co, or V, Zeolites have been proven to catalyze selective methane oxidation to mainly formic acid. Inspired by the natural methane monooxygenase (MMO) enzymes, Fe or Cu sites have been introduced into zeolites to mimic the active binuclear Fe found in enzymes. Although many efforts have been devoted to deciphering MMO enzymes' structure and working mechanism [19], the concept of biomimetics has not yet successfully led to new catalysts. The main problem is the presence of multiple iron species after high-temperature calcination. Thus, the nature of the active sites in Fe/zeolites remains largely a matter of speculation. We tried to adjust the introduction strategy of suitable Fe sites and make it more rational. As we know $M_2^{3+}M^{2+}(\mu_3-O)(X)(COO)_6$ ($M = Fe, Cr, Al, Sc, V, In$, where X represents a counteranion that may be present) is one of the most common building blocks [145], which appears in some classic MOFs such as MIL-100(Fe_3, Cr_3) [123,146], MIL-101(Fe_3, Cr_3) [147,148], and PCN-250(Fe_2Mn, Fe_3, Fe_2Co , and Fe_2Ni) [149]. The undercoordinated open metal sites found in these trimetallic nodes [151] make this class of MOFs attractive for oxidation catalysis. We envisaged using defined Fe_2M -PCN-250 composition and crystalline structure as our catalyst to conduct selective methane oxidation in an aqueous H_2O_2 solution. The structure of

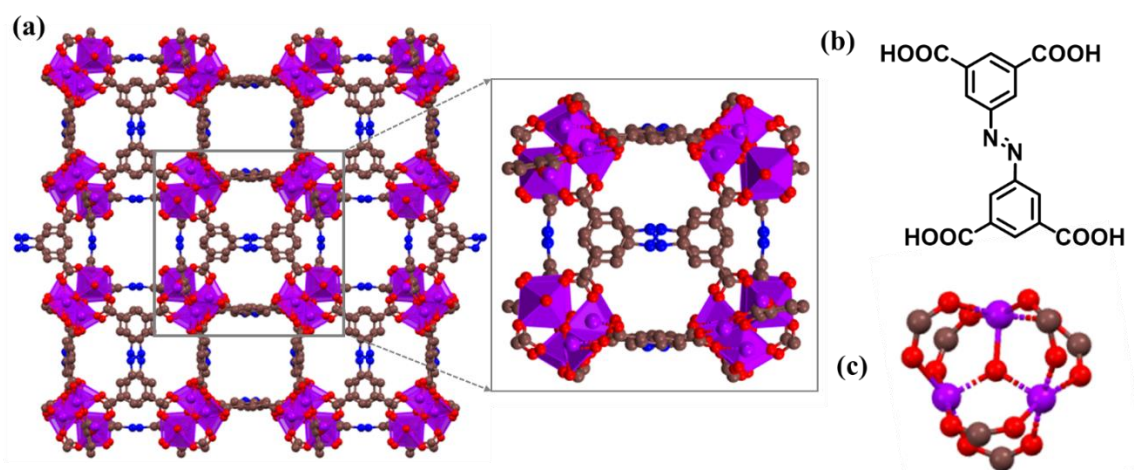


Figure 4-18. (a) Crystallographic structure of Fe_3 -PCN-250 and its unit cell, (b) its ABTC linker (ABTC = 3,3',5,5'-azobenzenetetracarboxylate), and (c) cluster representation of its $Fe_3(\mu_3-O)(COO)_6$ node. Hydrogen atoms are omitted for clarity.

Fe₂M-PCN-250 (M = Fe²⁺,³⁺, Co²⁺, Ni²⁺, Mn²⁺, Zn²⁺) consists of trimetallic Fe₂M nodes ([Fe₂M(μ₃-O)(CH₃COO)₆]) connected by tetratopic azobenzene-based ABTC linkers (ABTC = 3,3',5,5'-azobenzenetetracarboxylate) to produce a soc net (Figure 4-18). This design aims to change the microenvironment of the Fe₂ cluster. We believe that the diverse, mixed-metal trimetallic node is beneficial for systematically studying the effect of the node composition on the catalytic properties of the MOF and developing structure-function relationships. In 2019, Barona et al. [152] did DFT calculations and experimentally confirmed the predicted activity trends of PCN-250 variants towards partial oxidation of propane with N₂O.

4.7.2 Synthesis method

4.7.2.1 Preparation of preformed clusters.

Fe₂M(μ₃-O)(CH₃COO)₆ (abbreviated as Fe₂M) (M = Fe, Mn, Co, Ni, Zn) is prepared according to the reported procedure [153]: A solution of sodium acetate trihydrate (42 g, 0.31 mol) in water (70 mL) was added to a filtered, stirred solution of iron(III) nitrate nonahydrate (8 g, 0.02 mol) and the metal(II) nitrate (0.1 mol) in water 70 mL. The brown precipitate was filtered off, washed with water and ethanol, and finally dried in the air.

4.7.2.2 Synthesis of PCN-250

According to literature [149], ABTC linker (ABTC = 3,3',5,5'-azobenzenetetracarboxylate, 10 mg), Fe₂M cluster (M = Mn, Fe, Co, Ni, Zn) (15 mg) and acetic acid (1 mL) in 2 mL of DMF were ultrasonically dissolved in a Pyrex vial. The mixture was heated in an oven at 140 °C for 12 h. After cooling down to room temperature, dark brown crystals were collected by filtration.

4.7.3 XRD characterization and activity tests

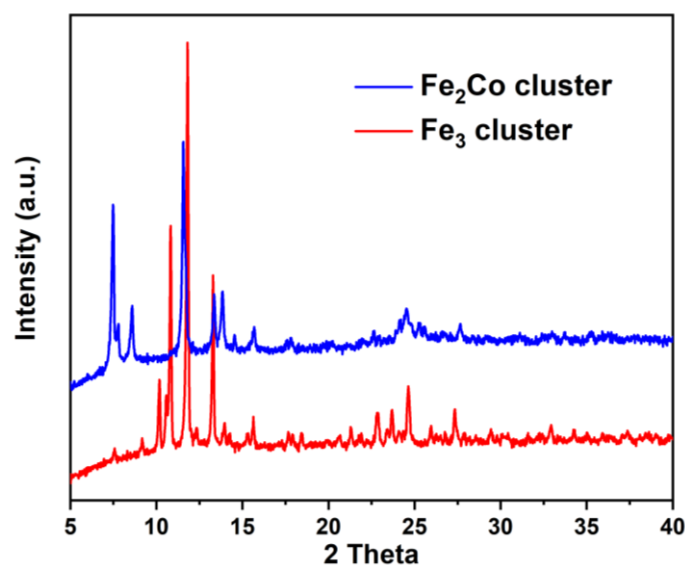


Figure 4-19. PXRD patterns for Fe₂M clusters.

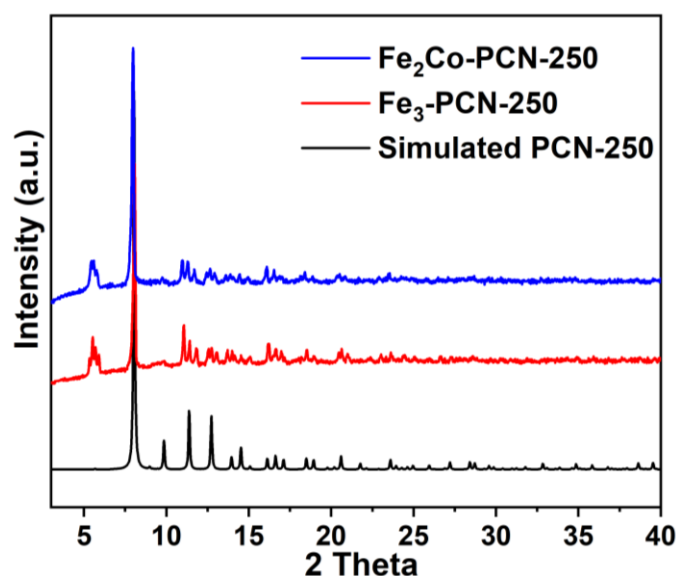


Figure 4-20. PXRD patterns for pristine and Fe₂M-PCN-250.

In the beginning, Fe₂Co and Fe₃ clusters were synthesized, and the mixed metal clusters' PXRD patterns were confirmed their successful synthesis by comparison with the literature (Figure 4-19) [150]. These diffraction indices indicate the ordered structure of the clusters. These clusters were used as SBUs for the synthesis of PCN-250. The XRD patterns are in good agreement with the simulated PCN-250 pattern (Figure 4-20).

Table 4-8. Catalytic performance of the synthesized PCN-250 based catalysts.

Entry	Cat.	React. Condi.	Product yield(μmol)/Selectivity(%)						H ₂ O ₂		TOF /h ⁻¹
			MeOH	OHCH ₂	Me	HCOOH	CO ₂	O ₂	Conv.	Util.	

			OOH				($\times 10^3$)	(%)	(%)		
1	Fe ₂ Co-PCN-250 ^a	50°C, 1h, 10 mg	1.6 1.0%	0	6.7 4.1%	51.1 31.5%	103.0 63.4%	1.1	60.9	5.2	3
2	Fe ₃ -PCN-250 ^b	50°C, 1h, 10 mg	9.2 3.0%	0	11.2 3.7%	83.7 27.7%	197.7 65.5%	1.6	87.0	6.1	3

Reaction condition: 30 bar CH₄, 10 mL 0.5 M H₂O₂, autoclave reactor, 600 rpm. ^aFe₂Co-PCN-250: 11.5wt.% Fe, 3.6 wt.% Co; ^bFe₃-PCN-250: Fe: 16.0 wt.%.

The catalytic oxidation of methane using H₂O₂ was conducted in a batch autoclave reactor at 50 °C with 30 bar of CH₄ and 0.5 M H₂O₂. Table 4-8 shows the catalytic results of the synthesized PCN-250 based catalyts. According to entry 1 and 2, both Fe₂Co-PCN-250 and Fe₃-PCN-250 show obviously activity under 50°C for 1h. Fe₃-PCN-250 generated more C1 oxygenates of 105 μmol and converted more H₂O₂ than Fe₂Co-PCN-250, which proves that the change in the microenvironment of Fe₂ cluster will indeed influence the activity. What makes us disappointed is that the high amount of byproduct CO₂ was inevitably produced at both catalyts even under a low temperature of 50 °C. Additionally, the supernatant showed a yellow color after reaction, indicating the instability of these MOFs under reaction conditions.

4.8 Summary

It is generally known that metal-modified zeolite catalyts show the best catalytic performance for selective methane oxidation to methanol or formic acid to date. However, due to their low porosity, most zeolite-based catalyts can only host a limited number of active sites, generally lower than 0.5 wt.%. Such a low loading of active sites restricts a further enhancement of the overall activity of metal-modified zeolite. Besides, due to the complexity of the synthesis methods, the metal sites in zeolites are present in various forms. Such heterogeneity in Fe species results in difficulties in deciphering the actual active sites and makes the discrimination of active sites among many inactive ones extremely challenging.

In recent decades, MOFs have received much attention as a series of crystalline microporous materials. MOFs exhibit a high degree of uniformity in metal nuclearity, oxidation state, and coordination environment. Based on the well-defined structure and much higher porosity, it was expected to overcome the disadvantages of zeolite-based catalyts. Herein, we seek to utilize some recognized stable MOFs as supports to fix metal sites for designing promising catalyts for selective methane oxidation in the liquid phase reaction system with H₂O₂ as the oxidant. MOFs with metal nodes based on Al, Zn and some Zr-based ones without redox ability are chosen as the supports for their well-known thermal and chemical stability. Combining the study of literature

and our understanding of the structural features and their advantages, we mainly designed metal modified MOF catalysts based on three strategies:

1. Replacing open metal sites in the SBUs with active sites.
2. MOF linkers can serve as a scaffold based on the coordination effect of N and O atoms of the linker to confine and fix metal-oxo sites.
3. MOFs' structures and multiple components offer large potentials for tunable microenvironments for catalysis by post-modification method to introduce metal sites with the desired configuration.

Based on the catalytic results, we hope to share our experience and provide some sincere suggestions to other researchers who want to use MOF materials as catalysts for selective methane oxidation with H_2O_2 aqueous solution as the oxidant. There are some key challenges that all face who want to take advantage of MOF materials for selective methane oxidation under mild reaction conditions:

1. Although MOF-based catalysts are considered charming candidates, the activities achieved yet are still inferior to that of zeolite-based catalysts. The activity of the catalysts is regarded as one of the most important properties to evaluate the catalysts. The development of highly active catalytic sites within MOFs to achieve higher apparent activity is still a challenge for MOFs materials.

2. MOF-based materials are thought to possess lower active sites' heterogeneity due to their high crystallinity and well-defined structures. This advantage is theoretically applied to MOF crystals or intrinsic MOFs. However, introducing heterogeneous species (such as nanoparticles) into MOFs to form composites still leads to certain heterogeneity. Therefore, adequate structural characterizations are still essential for such MOF-based composites. The structural resolution of the catalyst plays a crucial role in exploring the structure-activity relationship, which could guide the design and synthesis of high-performance catalysts.

3. The stability of MOF-based catalysts needs to be carefully verified. The flexibility of MOFs facilitates tailorable and diverse structures while foreshadowing the drawback of worse stability compared to traditional inorganic compounds (such as zeolites). The examination with PXRD and physical sorption experiments after the reaction are necessary to check the stability in terms of structures and porosities of MOF-based materials. And our experiments told that the supernatant after reaction should also be analyzed to determine if the existence of leakage and degraded fractions from MOFs.

4. It is also essential to clarify the origin of the activity. There are two possible interfering contributions: (1) fractions of the degraded MOFs may cause additional activity; (2) degradation

products of MOFs may be erroneously calculated on products. For example, carboxylic acid based ligands can undergo oxidative degradation to give additional CO₂. If necessary, control experiments with isotope labeling by ¹³C and ¹⁷O should be carefully conducted to track the origin of the products and the reaction pathway.

5. One drawback of MOF-based catalysts is the lack of proper theoretical calculations. Considering MOFs are crystalline structures, common Density Functional Theory (DFT) calculations are unsuitable. This is because DFT calculations are for molecules and are not adapted to crystal structures. Decomposing the MOF structures into molecular fractions for DFT calculations may cause unpredictable errors in results. The Vienna Ab initio Simulation Package (VASP) is more suitable for crystalline structure. However, there will be too many atoms in the crystal unit of MOFs, which requires too much computing time for VASP calculations. Overall, successfully applying theoretical calculation to MOF based materials is still a challenge.

5. Direct methane oxidation over Fe/MOR catalysts by H₂O₂

Compared to the much in-depth research of Fe/ZSM-5 catalysts for direct methane oxidation with H₂O₂, such as studies on specific active sites, reaction mechanisms, zeolite preparation methods, and reaction parameters, it is quite necessary to conduct some further work to understand the structure of the active sites and optimize the catalyst preparation in Fe/MOR catalyst.

5.1 Investigation of different zeolites

The varying topologies and compositions of Fe-modified zeolites are thought to have a large effect on not only their ability to produce C₁ products but also the nature of the active sites. The level of activity exhibited by ZSM-5 containing trace amounts of Fe has proven to be unique. In 2012, Hammond et al. [64] found that, following high-temperature calcination, commercial ZSM-5 with 0.014 wt.% Fe impurity displays significant catalytic activity with a TOF as high as 2200 h⁻¹ for the direct methane oxidation using 0.5 M H₂O₂ aqueous solution at 50 °C. They hold that the active iron site is an extra-framework binuclear core that forms a Fe-OOH intermediate upon activation with H₂O₂, which they deduced from EXAFS measurements and DFT calculations. In 2021, Zhu et al. [105] found that 0.03 wt.% Fe/ZSM-5(66) synthesized via ion-exchange triggered the highly efficient conversion of methane to formic acid (HCOOH) at 80 °C with 15% H₂O₂ aqueous solution, reaching 8% methane conversion with a TOF of 84200 h⁻¹ and selectivity for C₁ oxygenates of 91%. On the basis of a series of experimental characterizations and density functional theory (DFT) calculations, they found that both mononuclear and binuclear Fe species confined in the channel of the ZSM-5 can generate Fe-O centers, which are highly active for the dissociation of C-H bonds. Methane can be successfully oxidized to formic acid via free radical pathways under mild conditions. The Fe modified ZSM-5 catalyst has been considered the most active catalyst, with HCOOH as the main product in the batch-reactor system with H₂O₂ aqueous solution as the oxidant. Other zeolites with similar compositions, but different pore structures, are an order of magnitude less active. Besides Fe/ZSM-5, other classic zeolites are worth investigating Fe modification for direct methane oxidation to understand the structural characteristics and Fe sites formation in zeolites.

5.1.1 Preparation method

Commercial NH₄-MOR (Si/Al=9, Alfa Aesar), H-ZSM-5 (Si/Al=23, Tricat Inc., Hunt Valley, USA), H-Y (Si/Al=2.6, Alfa Aesar), and H-SAPO-34 (Al/P/Si = 1/0.93/0.1, Catalyst Plant of

Nankai University, Tianjin, China) catalysts were purchased from Sigma-Aldrich. The zeolites were loaded with Fe by a modified liquid ion-exchange (IE) method with $\text{Fe}(\text{acac})_3$ as a precursor corresponding to a nominal 0.5 wt.% Fe content (see [Figure 5-1](#)). 200 mg commercial MOR powder and a certain amount of $\text{Fe}(\text{acac})_3$ containing 0.5 wt.% Fe were added into a glass vial with 8 mL of CH_3CN . The vials were treated with ultrasound for 2 mins and placed in an oven at 85 °C for 24 h. After the heat treatment, the samples were centrifuged and washed with a sequence of acetone, deionized water, and acetone and were subsequently dried in an oven at 80 °C for 5 h. Finally, the samples were calcined in an oven at 500 °C with a heating ramp of 100 K/h for 5 h in air.

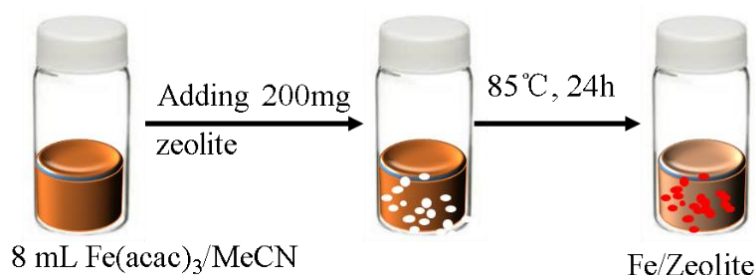


Figure 5-1. (a) Scheme of the Fe loading procedure by modified liquid ion-exchange (IE) method using CH_3CN as solvent.

5.1.2 Investigation of the activity

[Table 5-1](#) and [Figure 5-2](#) show the catalytic performance of various Fe-zeolites for direct methane oxidation. [Entry 1](#) shows that commercial ZSM-5 containing 0.05 wt.% Fe impurity after heat-treatment has an excellent activity with a TOF as high as 4293 h^{-1} for the methane oxidation using 0.5 M H_2O_2 aqueous solution at 80 °C for 0.5 h. However, loading more iron (0.24 wt.%) on ZSM-5 zeolite ([entry 2](#)) did not show any increase of the C1 productivity but came with a much higher CO_2 yield and lower H_2O_2 utilization. The reason is speculated to be the Fe species aggregation during high-temperature calcination (around 500 °C) due to the addition of much exogenous Fe [[105](#)]. Despite not being as active as ZSM-5 zeolites in terms of TOF values ([entries 1 and 3](#)), the research on Fe/MOR can be helpful to understand the formation and structure of Fe active sites in zeolites for direct methane oxidation in H_2O_2 . For Fe/MOR catalysts, after loading more Fe ([entries 3 and 4](#)), Fe/MOR still maintained the activity with an even higher TOF value, which means the uniform formation of Fe active sites without apparent aggregation. Besides ZSM-5 and MOR zeolites, other classic zeolites SAPO-34 and Y ([entry 6](#) and [entry 7](#)) did not show significant activities.

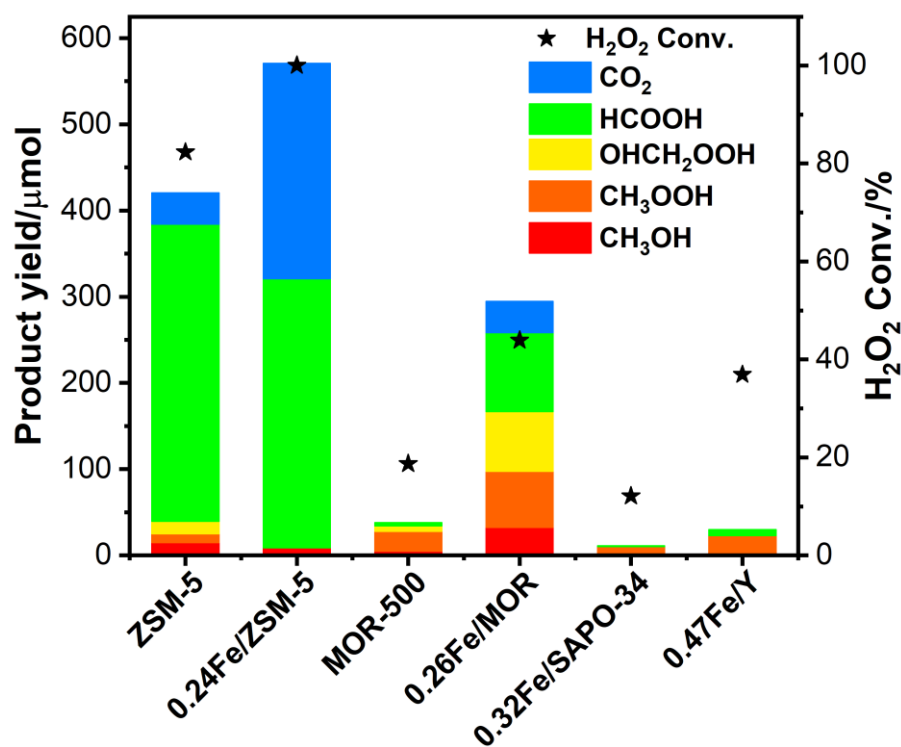


Figure 5-2. The activities and product distributions over different catalysts and corresponding H₂O₂ conversion.

Table 5-1. Catalytic activity of various Fe-zeolites for direct methane oxidation.

Entry	Catalyst	Product yield(μmol)/Selectivity(%)					H ₂ O ₂		TOF /h ⁻¹
		MeOH	MeOOH	OHCH ₂ OOH	HCOOH	CO ₂	Conv. (%)	Util. (%)	
1	ZSM-5-500	14.9 3.5%	10.3 2.4%	14.6 3.5%	344.6 81.9%	36.1 8.6%	82.3	25.5	4293
2	0.24Fe/ZSM-5-500	9.0 1.6%	0	0	312.2 54.7%	249.3 43.7%	100	19.2	747
3	MOR-500	5.0 13.3%	22.9 60.6%	6.5 17.1%	3.4 8.9%	0	18.7	5.4	352
4	0.26Fe/MOR-500	32.7 11.1%	64.8 22.0%	69.6 23.6%	91.4 31.1%	36.0 12.2%	43.9	22.3	555
5	0.32Fe/SAPO-34-500	1.2 10.7%	9.1 82.2%	0	0.8 7.1%	0	12.1	2.1	19
6	0.47Fe/Y-500	3.2 10.8%	19.9 66.5%	0	6.8 22.7%	0	36.9	2.4	36

Reaction condition: 30 bar of CH₄, 10 mL of 0.5 M H₂O₂, 600 rpm, 80 °C, 0.5 h, 20 mg of catalyst. The used commercial zeolites ZSM-5 and MOR contain 0.05 wt.% and 0.06 wt.% Fe impurity, respectively.

5.2 Investigation of different metals

5.2.1 Preparation method

Commercial H-MOR (Si/Al=12, ZEOCAT FM-8/25 H) with only 0.003 wt.% Fe impurity was used as the support for loading different metals to reduce the interference from Fe impurity found in NH₄-MOR. For metal loading, 200 mg of commercial H-MOR powder and a certain amount of Cu(acac)₂, Cr(acac)₃, Co(acac)₂ or Mn(acac)₂ metal precursors corresponding to a nominal metal loading of 0.5 wt.% were added to 8 mL of CH₃CN in a glass vial. The vials had ultrasonic dispersion for 2 minutes and were put in an oven for 24 h at 85 °C. After the heat treatment, the sample was filtered off, and washed with ethanol/deionized water/ethanol and then dried in an oven for 5 h at 80 °C. After fully ground, the powder was calcined in an oven at 500 °C with a heating ramp of 100 °C/h and kept for 5 h in air. FeCu/MOR catalysts were prepared by adding certain amounts of Fe(acac)₃ and Cu(acac)₂ corresponding to nominal 0.1 wt.% Fe and 0.1 wt.% Cu to obtain 0.088Fe0.089Cu/MOR(H), and nominal 0.15 wt.% Fe and 2.5 wt.% Cu to obtain 0.156Fe1.43Cu/MOR(H). All other steps and the calcination procedure are the same as before.

5.2.2 Investigation of the activity

Table 5-2. Catalytic activity of various metal/MOR zeolites for direct methane oxidation.

Entry	Catalyst	Product yield(μmol)/Selectivity(%)					H ₂ O ₂		TOF /h ⁻¹
		MeOH	MeOOH	OHCH ₂ OOH	HCOOH	CO ₂	Conv. (%)	Util. (%)	
1	0.46Cu/MOR(H)	9.6 50.6%	4.9 26.0%	4.0 21.1%	0.4 2.3%	0	33.4	1.4	26
2	0.03Cr/MOR(H)	2.3 17.8%	7.6 58.4%	2.6 19.7%	0.5 4.0%	0	19.4	1.6	-
3	0.47Co/MOR(H)	1.3 15.1%	2.4 26.9%	5.0 57.0%	0.1 1.0%	0	23.3	1.1	11
4	0.36Mn/MOR(H)	1.9 4.6%	5.8 14.4%	31.2 77.1%	1.6 3.9%	0	43.9	3.3	62
5	0.31Fe/MOR(H)	28.8 8.8%	55.5 16.9%	72.6 22.2%	130.6 40.0%	39.9 12.2%	63.4	19.5	527

Reaction condition: 30 bar of CH₄, 10 mL of 0.5 M H₂O₂, 600 rpm, 80 °C, 0.5 h, 20 mg of catalyst.

Various kinds of metals, such as Cu, Cr, Co and Mn, were screened for the oxidation reaction of methane, of which Fe/MOR showed the highest activity (Table 5-2, Figure 5-3). Considering H₂O₂ conversion, all M/MORs (M= Cu, Cr, Co and Mn) can activate H₂O₂ to some degree without producing significant C1 products, resulting in a quite low H₂O₂ utilization ratio. Therefore, the presence of Fe species in MOR was crucial for substantial catalytic activities and a higher H₂O₂ utilization ratio.

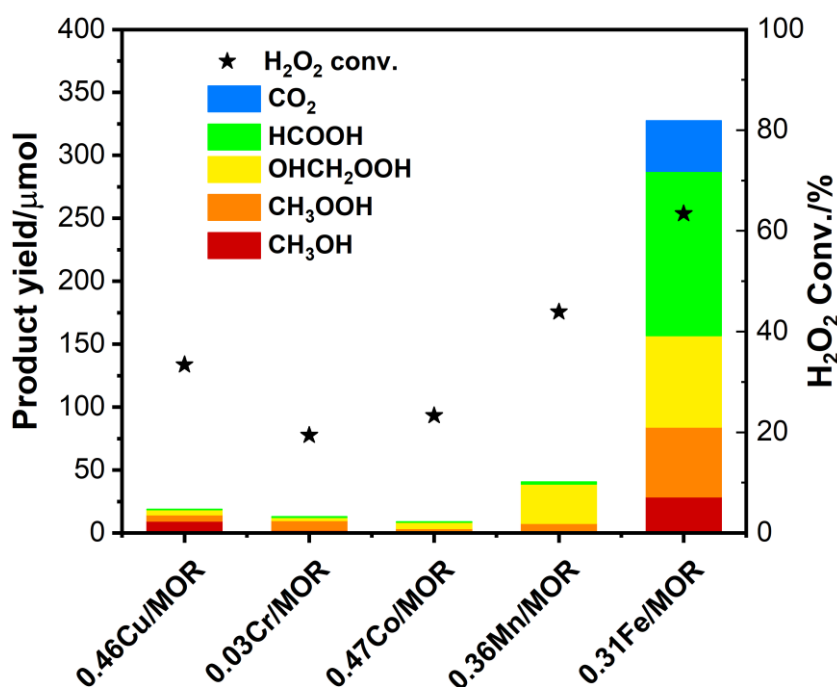


Figure 5-3. The activities and product distributions over different metals modified MOR(H) catalysts and their corresponding H₂O₂ conversion.

5.2.3 Investigation of the selectivity

The Cu addition to the reaction system, either as a co-component of the catalyst or as a solid catalyst in a physical mixture, or even as Cu²⁺ ions in the reaction solution, was reported to suppress the over-oxidation of methanol and improve the methanol yield [64]. As shown in Table 5-3 and Figure 5-4, MOR(H) samples loaded with/without different metal species were added as modulators to investigate their influence on selectivity over 0.26Fe/MOR(NH₄) catalyst. The yield of formic acid and CO₂ decreased apparently after adding these additives (entries 1 to 5), indicating the suppressed over-oxidation. Thus, even though the amount of CH₃OH and CH₃OOH did not change, the corresponding selectivity increased. It is proposed that these variable-valence metal species could scavenge •OH to suppress over-oxidation. Among these, Cr/MOR(H) with 0.03 wt.% of Cr has the strongest scavenging effect (see entry 5). Copper was the most preferred one due to increased methanol yield and selectivity (see entry 3). When introducing Cu sites as co-component and preparing CuFe/MOR catalysts, even higher selectivities towards CH₃OH and CH₃OOH can be achieved, namely 65.3%, but at the expense of their yields and H₂O₂ utilization ratio (see entry 6 and 7). This may be due to Cu's largely scavenging active •OH, thus inhibiting the activity.

Table 5-3. Addition of a second metal to suppress the over-oxidation in direct methane oxidation with Fe/MOR.

Entry	Cat.	Product yield(μmol)/Selectivity(%)	H ₂ O ₂	TOF
-------	------	------------------------------------	-------------------------------	-----

		MeOH	MeOOH	MeOH +MeOOH	OHCH ₂ OOH	HCOOH	CO ₂	Conv. (%)	Util. (%)	/h ⁻¹
1	0.26Fe/MOR	32.7 11.1%	64.8 22.0%	33.3%	69.6 23.6%	91.4 31.0%	36.0 12.2%	44.6	22.3	555
2	0.26Fe/MOR +MOR(H)	30.7 11.7%	66.6 25.2%	36.9%	52.0 19.7%	87.6 33.2%	26.8 10.2%	40.6	21.9	509
3	0.26Fe/MOR+ 0.46Cu/MOR(H)	58.0 24.4%	37.0 15.6%	40.0%	60.8 25.6%	56.6 23.9%	25.0 10.5%	50.1	14.5	456
4	0.26Fe/MOR+ 0.36Mn/MOR(H)	27.2 11.9%	58.4 25.5%	37.4%	48.5 21.1%	74.7 32.6%	20.5 8.9%	44.1	21.1	449
5	0.26Fe/MOR+ 0.03Cr/MOR(H)	27.4 14.4%	59.7 31.3%	45.7%	53.7 28.2%	37.8 19.8%	12.1 6.3%	38.8	14.5	384
6	0.088Fe0.089Cu/ MOR(H)	15.3 27.7%	17.6 31.2%	58.9%	12.3 22.3%	10.0 18.1	0	27.9	6.2	350
7	0.156Fe1.43Cu/ MOR(H)	42.7 44.7%	19.7 20.6%	65.3%	14.1 14.8%	0	18.9 19.8%	38.7	8.5	285

Reaction condition: 30 bar of CH₄, 10 mL of 0.5 M H₂O₂, 600 rpm, 80 °C, 0.5 h, 20 mg of catalyst and/or 20 mg of co-catalyst.

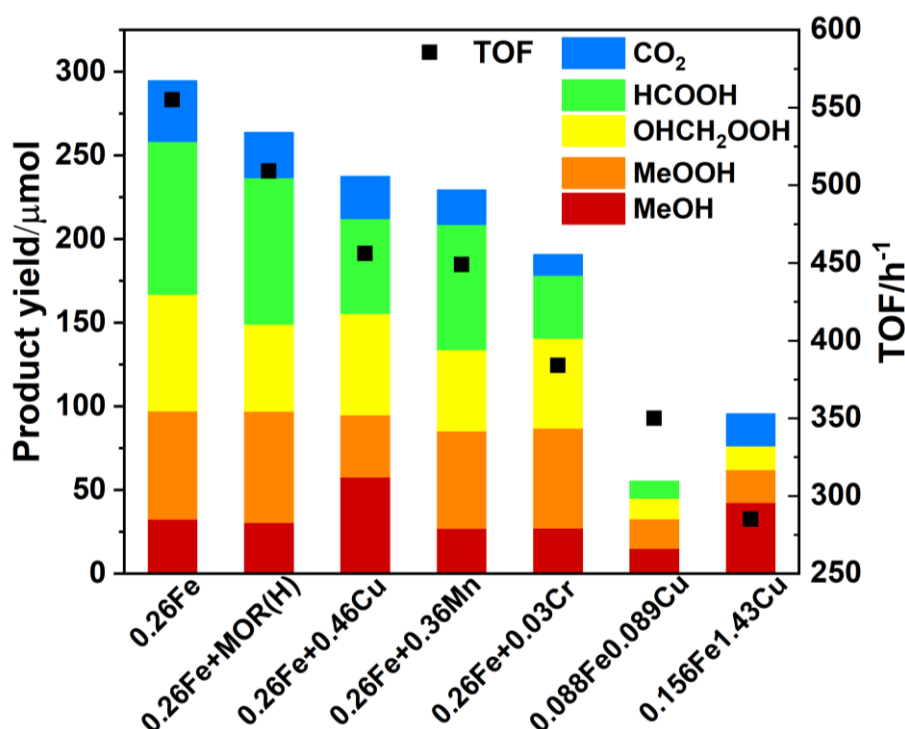


Figure 5-4. Catalytic studies of the addition of a second metal by physical mixture or as co-component on the catalyst to suppress the over-oxidation by Fe/MOR in the direct methane oxidation.

5.3 Variation of the preparation protocol of Fe/MOR

5.3.1 Calcination temperature

Several research groups have shown that high-temperature heat treatment is favorable for the migration of Fe ions and the formation of extra-framework Fe clusters [105], which are responsible for the methane to methanol/formic acid conversion in Fe-ZSM-5 [154]. Therefore, we studied the influence of the heat-treatment temperature of Fe/MOR catalysts on the formation of the Fe active sites and their catalytic properties in direct methane oxidation. Zeolite mordenite was calcined at different temperatures to study the influence of thermal treatments. The ammonium type mordenite was used as the starting material for all subsequent thermal treatments.

5.3.1.1 Preparation method

A commercial NH₄-MOR (Si/Al ratio = 9, Alfa Aesar) with 0.06 wt.% Fe impurity was purchased. The catalyst was activated before catalytic measurement, typically by calcination in air at different temperatures achieved with a heating rate of 100 °C/h and kept for 5 h. Prepared catalysts were denoted as MOR, MOR-500, MOR-700 and MOR-900, according to the calcination temperatures, without calcination, 500 °C, 700 °C and 900 °C.

In addition to parent MOR(NH₄), Fe modified 0.35Fe/MOR(NH₄) catalyst obtained by a modified liquid ion-exchange method with Fe(acac)₃ as a precursor was also used to investigate the influence of calcination temperature. The samples were calcined in an oven in the air at 500 °C or 700 °C achieved with a heating ramp of 100 °C/h and kept for 5 h, which are denoted as 0.35Fe/MOR-500 and 0.35Fe/MOR-700.

5.3.1.2 Investigation of the activity

Table 5-4 shows the effect of heat-treatment temperature on the selective methane oxidation reaction. We discovered that, following high-temperature heat treatment (entry 3), MOR-500 using H₂O₂ as oxidant at 80 °C displays obvious catalytic activity. Compared with the catalytic results without the calcination procedure (entries 1 and 2), the H₂O₂ conversion and TOF increased to 18.7% and 352 h⁻¹, respectively, after a heat pre-treatment at 500 °C for 5 h in air. Thus, high-temperature calcination contributed to the formation of Fe active sites, which can activate H₂O₂ at 80 °C and exhibit productivity and selectivity to C1 oxygenates. In-framework Fe species migrated into the channels of the MOR zeolite and formed extra-framework Fe species as active sites during calcination. According to entry 4, extending the reaction time further increased the product yield and TOF slightly. Increasing the calcination temperature to 700 °C (entry 5), the TOF increased significantly from 352 h⁻¹ to 1633 h⁻¹. Further increasing the calcination temperature to 900 °C (MOR-900) (entry 6), the TOF decreased slightly and the CO₂ yield and selectivity increased

significantly. These catalytic tests demonstrated that higher temperature pre-treatments result in higher oxygenation yields, reaching a maximum at 700 °C. Conducting the reaction over MOR-900 at 50 °C (entry 7), the low activity and H₂O₂ conversion proved that Fe/MOR catalyst needs 80 °C to activate the H₂O₂. As for the exogenous Fe species, 0.35Fe/MOR(NH₄) zeolite calcinated at 500 °C (entry 8) and 700 °C (entry 9) were tested and compared. 500 °C for the higher Fe loading Fe/MOR catalyst was chosen due to the lower CO₂ selectivity and higher H₂O₂ utilization ratio. Thus, we concluded that high-temperature calcination possibly generated more active sites to improve activity. However, too high calcination temperature can lead to the aggregation of the iron species, resulting in weakening the catalytic performance for direct methane oxidation.

Table 5-4. The effect of heat-treatment temperature on the performance of the Fe/MOR and MOR with Fe impurity.

Entry	Cat.	React. Condi.	Product yield(μmol)/Selectivity(%)					H ₂ O ₂		TOF /h ⁻¹
			MeOH	MeOOH	OHCH ₂ OOH	HCOOH	CO ₂	Conv. (%)	Util. (%)	
1	MOR	50°C, 1h	0.5 43.6%	0.1 10.3%	0	0.5 46.1%	0	2.6	1.5	11
2	MOR	80°C, 1h	0.7 32.4%	0.9 43.2%	0	0.5 24.3%	0	5.9	1.0	7
3	MOR-500	80°C, 0.5h	5.0 13.3%	22.9 60.6%	6.5 17.1%	3.4 8.9%	0	18.7	5.4	352
4	MOR-500	80°C, 1h	20.0 24.0%	32.1 38.6%	21.4 25.7%	9.7 11.7%	0	32.2	7.2	373
5	MOR-700	80°C, 0.5h	21.6 11.2%	59.7 31.0%	48.3 25.1%	45.8 23.8%	17.3 9.0%	30.4	21.1	1633
6	MOR-900	80°C, 0.5h	9.5 4.6%	34.7 16.9%	35.1 17.1%	62.0 30.3%	63.6 31.0%	58.1	10.5	1315
7	MOR-900	50°C, 0.5h	1.9 14.3%	9.8 75%	0	1.4 10.7%	0	2.7	11.9	122
8	0.35Fe/MOR-500	80°C, 0.5h	23.6 8.0%	53.5 18.2%	52.9 18.0%	111.2 37.9%	52.5 17.9%	57.2	25.0	385
9	0.35Fe/MOR-700	80°C, 0.5h	9.3 2.4%	9.5 2.4%	6.7 1.7%	142.5 36.6%	221.4 56.8%	97.1	9.6	268

Reaction condition: 30 bar of CH₄, 10 mL of 0.5 M H₂O₂, 600 rpm, 20 mg of catalyst.

5.3.2 Different MOR starting samples

It has been shown that the type of the counter cations has a large effect on the catalytic performance of metal-zeolites. For instance, during the ion exchange of MOR with copper salts, sodium ions added into the solution can occupy the ion exchange positions in 8-membered rings of the zeolite, suspending the formation of active copper-oxo species [155]. Similarly, methane oxidation using N₂O as an oxidant over iron-substituted molecular sieves showed that Brønsted

acidity is required to stabilize the Fe-based α -oxygen active site [156]. What's more, Brønsted acid sites (BAS) were reported to boost the activity for direct methane oxidation over Fe/ZSM-5 zeolite with H₂O₂ aqueous solution [67]. Thus, MOR zeolites in the ammonium (NH₄), sodium (Na), and protonic (H) forms as starting samples are studied in the direct methane oxidation reaction.

5.3.2.1 Preparation method

Commercial NH₄-MOR (Si/Al=9, Alfa Aesar), H-MOR (Si/Al=12, ZEOCAT FM-8/25 H), Na-MOR (Si/Al=6, ZEOCAT FM-8) catalysts were purchased. The Fe was loaded by the modified liquid ion-exchange (IE) method with Fe(acac)₃ as a precursor corresponding to a nominal 0.5 wt.% Fe content. 200 mg commercial MOR powder and a certain amount of Fe(acac)₃ corresponding to a nominal loading of 0.5 wt.% Fe were added to 8 mL of CH₃CN in a glass vial. The vials were treated with ultrasound for 2 min and were placed in an oven for 24 h at 85 °C. After the heat treatment, the samples were centrifuged and washed with acetone, deionized water, and acetone and then dried in an oven for 5 h at 80 °C. Finally, the samples were calcined in an oven in the air at 500 °C achieved with a heating ramp of 100 °C/h and kept for 5 h.

5.3.2.2 Investigation of the activity

Table 5-5 and Figure 5-5 show the effect of MOR zeolites with different counter cations on the catalytic reactivity. As shown in Table 5-5, when using Fe/MOR(Na) (entry 4), the yield of C1 oxygenates was greatly reduced compared to Fe/MOR(NH₄) (entry 2) and Fe/MOR(H) (entry 6). With the aid of adjacent Brønsted acid sites (BAS), methane can be oxidized to C1 oxygenates. Our catalytic investigations show that BAS in MOR can indeed enhance the activity of methane oxidation, in line with previous reports [67].

Table 5-5. The effect of MOR zeolites with different counter cations on the catalytic reactivity.

Entry	Cat.	Fe loading (wt.%)	Product yield(μmol)/Selectivity(%)					H ₂ O ₂		TOF /h ⁻¹
			MeOH	MeOOH	OHCH ₂ OOH	HCOOH	CO ₂	Conv. (%)	Util. (%)	
1	MOR(NH ₄)	0.06	5.0 13.3%	22.9 60.6%	6.5 17.1%	3.4 8.9%	0	18.7	5.4	352
2	Fe/MOR (NH ₄)	0.26	32.7 11.1%	64.8 22.0%	69.6 23.6%	91.4 31.0%	36.0 12.2%	44.6	21.8	555
3	MOR(Na)	0.02	0.4 28.6%	0.5 35.7%	0.2 14.3%	0.3 21.4%	0	16.1	0.2	-
4	Fe/MOR (Na)	0.22	0.9 25.6%	2.0 57.3%	0	0.6 17.1	0	17.7	0.5	8.7
5	MOR(H)	0.003	1.5 25.0%	3.0 49.9%	0.9 15.0%	0.6 10.1%	0	17.1	0.7	-
6	Fe/MOR (H)	0.31	28.8 8.8%	55.5 16.9%	72.6 22.2%	130.6 40.0%	39.9 12.2%	63.4	19.5	527

Reaction condition: 30 bar of CH₄, 10 mL of 0.5 M H₂O₂, 600 rpm, 80 °C, 0.5 h, 20 mg of catalyst.

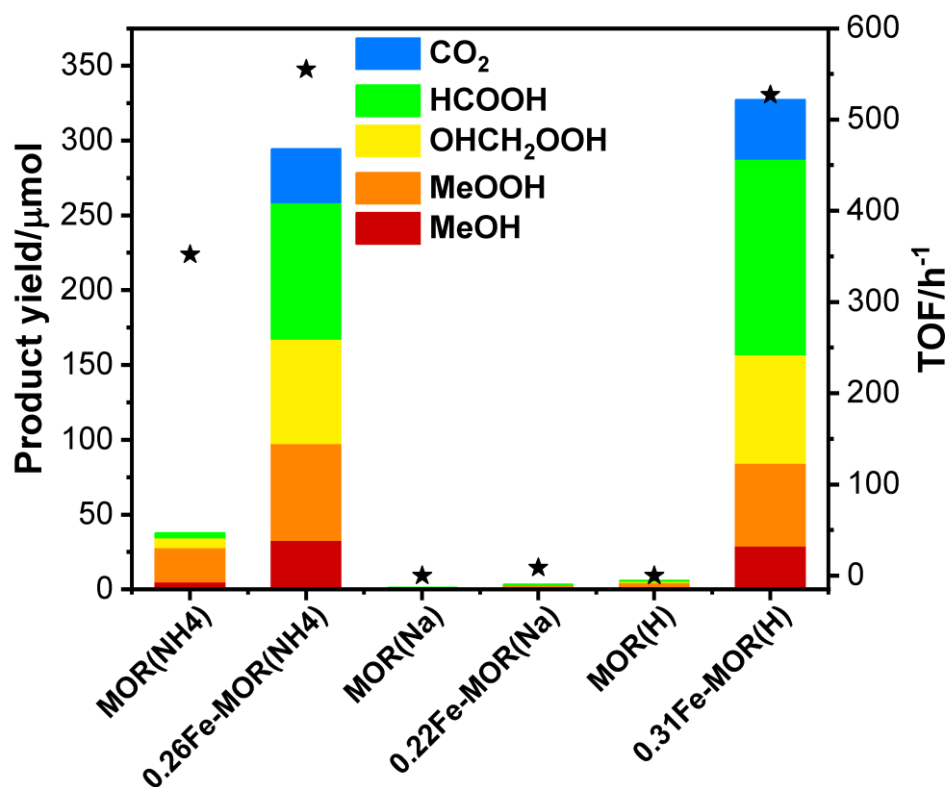


Figure 5-5. The activities and product distributions over different type of Fe/MOR catalysts and corresponding TOFs.

5.3.3 Different preparation methods for metal loading

Four different preparation methods, namely incipient wetness impregnation (IWI), liquid ion exchange (IE), solid-state ion exchange (SSIE) and sublimation of FeCl_3 , were applied to obtain Fe/MOR catalysts.

5.3.3.1 Preparation method

The Fe/MOR catalysts with nominal 0.5 wt.% Fe loading were obtained by using commercial NH_4 -MOR catalyst with 0.06 wt.% Fe impurity ($\text{Si}/\text{Al} = 9$, Alfa Aesar) and iron (III) nitrate nonahydrate ($\text{Fe}(\text{NO}_3)_3 \cdot 9\text{H}_2\text{O}$), iron (III) acetylacetonate ($\text{Fe}(\text{acac})_3$) and iron(III) chloride ($\text{FeCl}_3 \cdot 6\text{H}_2\text{O}$) as iron precursors. Different methods were employed as follows:

For the modified liquid ion-exchange (mIE) method, 200 mg NH_4 -MOR powder and a certain amount of Fe salts ($\text{Fe}(\text{acac})_3$, $\text{Fe}(\text{NO}_3)_3 \cdot 9\text{H}_2\text{O}$ or $\text{FeCl}_3 \cdot 6\text{H}_2\text{O}$) corresponding to a nominal 0.5 wt.% Fe loading were added to 8 mL of CH_3CN in a glass vial. The vials were treated with ultrasound for 2 min and were placed in an oven for 24 h at 85 °C.

For the standard liquid ion exchange (sIE) method, 200 mg NH_4 -MOR powder and a certain amount of Fe salts ($\text{Fe}(\text{NO}_3)_3 \cdot 9\text{H}_2\text{O}$) corresponding to a nominal 0.5 wt.% Fe content were added

to 8 mL of H₂O in a glass flask. The vials were treated with ultrasound for 2 min and were placed in an oven for 24 h at 85 °C.

After the Fe loading procedure by liquid ion-exchange method, the samples were centrifuged and washed with a sequence of acetone, deionized water, and acetone and were then dried at 80 °C in an oven for 5 h. Finally, the samples were calcined in an oven in air at 500 °C achieved with a heating ramp of 100 °C/h, and kept at this temperature for 5 h. The obtained catalysts are denoted as xFe/MOR_{IE} (x equals to the actual Fe content (wt.%) obtained by inductively coupled plasma optical emission spectrometry (ICP-OES) measurements). The used solvents (CH₃CN or water) and iron precursors were listed in the reaction condition column in [Table 5-6](#).

For the solid-state ion-exchange (SSIE) method, 400 mg NH₄-MOR powder was mixed and intensively grounded with a certain amount of Fe salts (Fe(acac)₃ or Fe(NO₃)₃·9H₂O) corresponding to a nominal 0.5 wt.% Fe in an agate mortar for 1 h under ambient condition. Then, the obtained uniform mixture was calcined in an oven in air at 500 °C achieved with a heating ramp of 100 °C/h and kept at this temperature for 5 h. The obtained catalysts are denoted as xFe/MOR_{SSIE}.

For the incipient wetness impregnation (IWI) method, 200 mg NH₄-MOR powder was charged into a 25 mL round bottom flask equipped with a magnetic stirring bar. A certain amount of Fe salt (Fe(acac)₃ or Fe(NO₃)₃·9H₂O) corresponding to a nominal 0.5 wt.% Fe loading was dissolved in the liquid mixture of 2 mL ethanol/1 mL CH₃CN/0.5 mL H₂O, which was then added into the flask. The flask was stirred vigorously and then kept at 30 °C for 24 h. Or, a certain amount of Fe(NO₃)₃·9H₂O corresponding to a nominal 0.5 wt.% Fe loading was dissolved in 3.5 mL deionized water, and the flask was then submerged in a 50 °C water bath for 24 h with vigorous stirring. The obtained material was then dried at 80 °C in an oven for 5 h and the powder was calcined in an oven at 500 °C in the air achieved with a heating ramp of 100 °C/h and kept at this temperature for 5 h. The obtained catalysts are denoted as xFe/MOR_{IWI}.

For the FeCl₃ sublimation method [157], the catalyst was prepared by chemical vapor deposition using FeCl₃·6H₂O as the iron precursor. In the experiment, 50 mg FeCl₃·6H₂O and 100 mg NH₄-MOR were placed on the upstream and downstream sides, respectively, in a porcelain boat, then transferred into the tube furnace with flowing N₂. Subsequently, the reactor was heated to 300 °C with a heating ramping of 2 °C/min and kept for 3 h, and then heated to 600 °C with a ramping rate of 5 °C/min and kept for 3 h. After the heat treatment, the sample was washed in the sequence of acetone, deionized water, and acetone and finally dried at 80 °C in an oven for 5 h. The obtained catalysts are denoted as xFe/MOR_{subl}.

5.3.3.2 Investigation of the activity

Table 5-6 and Figure 5-6 show the catalytic performance in direct methane oxidation for Fe/MOR samples prepared by different methods in a batch autoclave at 80 °C, with 30 bar of CH₄ and 10 mL of 0.5 M H₂O₂ aqueous solution. Yu et al. proposed [69] that the SSIE method, employing no solvent, avoids the preparation of the precursor solution and drying process to remove the solvent, which could thus prevent the hydrolysis and subsequent aggregation of Fe species and formation of bulk Fe oxides species, resulting in a better activity. But in our case, we did not see a clear advantage of the SSIE method, which exhibited similar yields to other methods (see entries 5 and 6). Among the catalysts prepared by IWI method (see entries 7-9), entry 8 with Fe(NO₃)₃ solved in the mixture of organic solvents (CH₃CN and ethanol) and deionized water showed the best yield and TOF value. According to entry 10, FeCl₃ sublimation method showed much lower productivity and H₂O₂ utilization ratio and higher CO₂ selectivity than the SSIE, IE and IWI methods. In Figure 5-6, one can clearly see that Fe/MOR catalysts obtained by the other three typical Fe loading methods all gave an excellent yield of C1 oxygenates around 250 μmol under suitable conditions, which proved the superiority of MOR zeolite as iron support for direct methane oxidation by using H₂O₂ as oxidant. Notably, the 1-0.260Fe/MOR_{IE} (entry 1), synthesized using Fe(acac)₃ as a precursor and MeCN as a solvent in the liquid ion exchange (mIE) process, exhibited a TOF of 555 h⁻¹, significantly exceeding the TOFs obtained by all other preparation methods. This highlights the high potential of the MOR-based catalyst in direct methane oxidation, other than MFI type zeolite.

Table 5-6. Catalytic performance of Fe/MOR catalysts prepared by different methods.

Entry	Cat.	Prep. Condi.	Product yield (μmol)/Selectivity (%)					H ₂ O ₂		TOF /h ⁻¹	C1 Yield /μmol
			MeOH	OHCH ₂ OOH	MeOOH	HCOOH	CO ₂	Conv. (%)	Util. (%)		
1	0.260Fe/MOR _{mIE}	Fe(acac) ₃ CH ₃ CN	32.7	69.6	64.8	91.4	36.0	43.9	22.3	555	259
			11.1%	23.6%	22.0%	31.0%	12.2%				
2	0.590Fe/MOR _{mIE}	Fe(NO ₃) ₃ CH ₃ CN	23.8	61.0	50.9	87.7	45.6	53.9	17.1	211	223
			8.8%	22.7%	18.9%	32.6%	16.9%				
3	0.150Fe/MOR _{mIE}	FeCl ₃ CH ₃ CN	12.2	18.6	28.0	16.9	6.8	67.4	3.8	282	76
			14.8%	22.6%	34.0%	20.5%	8.2%				
4	0.510Fe/MOR _{sIE}	Fe(NO ₃) ₃ H ₂ O	26.7	62.3	58.8	79.1	25.6	42.9	22.2	249	227
			10.6%	24.7%	23.3%	31.3%	10.1%				
5	0.524Fe/MOR _{SSIE}	Fe(acac) ₃	20.9	53.1	42.7	117.6	59.8	67.0	15.9	250	235
			7.1%	18.1%	14.5%	40.0%	20.3%				
6	0.547Fe/MOR _{SSIE}	Fe(NO ₃) ₃	26.6	62.7	51.0	110.3	45.4	57.7	19.7	256	253
			9.0%	21.2%	17.2%	37.2%	15.3%				
7	0.423Fe/MOR _{IWI}	Fe(acac) ₃	23.5	51.1	54.0	59.2	17.1	35.2	20.7	248	189
			11.5%	25.0%	26.4%	28.9%	8.3%				
8	0.518Fe/MOR _{IWI}	Fe(NO ₃) ₃	26.3	59.5	53.4	113.5	45.3	59.6	18.4	272	253
			8.8%	20.0%	17.9%	38.1%	15.2%				

9	0.554Fe/ MOR _{IWI}	Fe(NO ₃) ₃ H ₂ O	23.9 10.9%	50.4 23.0%	54.0 24.7%	71.7 32.7%	19.0 8.7%	39.3	20.4	202	199
10	0.229Fe/ MOR _{subl}	FeCl ₃	15.8 12.8%	22.3 18.1%	35.6 29.0%	29.8 24.2%	19.5 15.9%	58.4	9.5	252	104

Reaction condition: 30 bar of CH₄, 10 mL of 0.5 M H₂O₂, 600 rpm, 80°C, 0.5 h, 20 mg of catalyst.

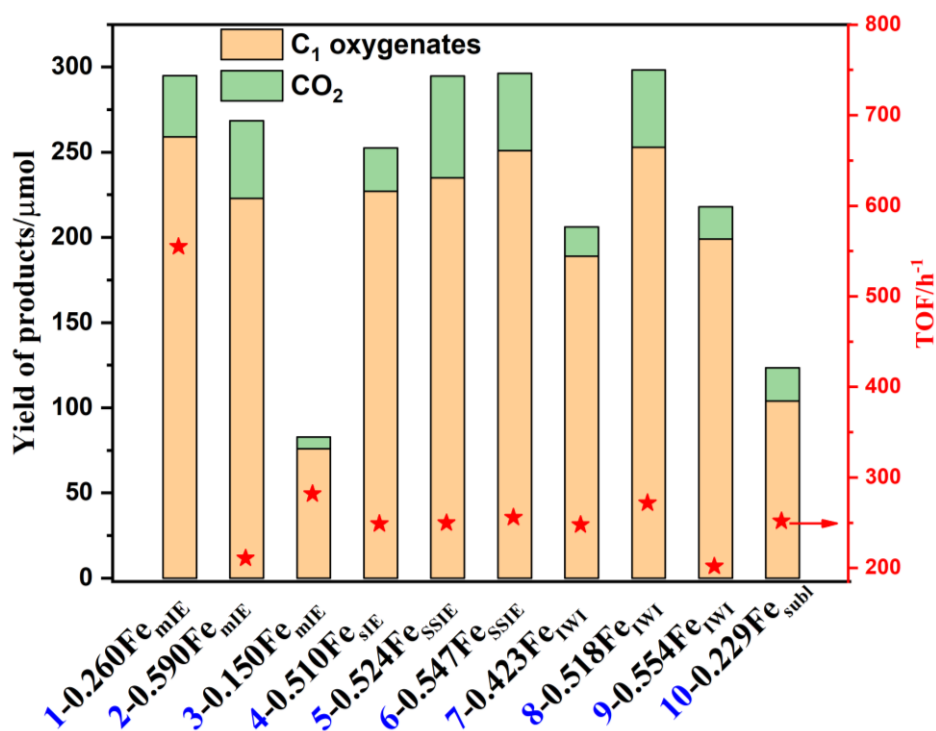


Figure 5-6. Dependence of performances on synthesis methods.

5.3.3.3 Catalyst characterizations

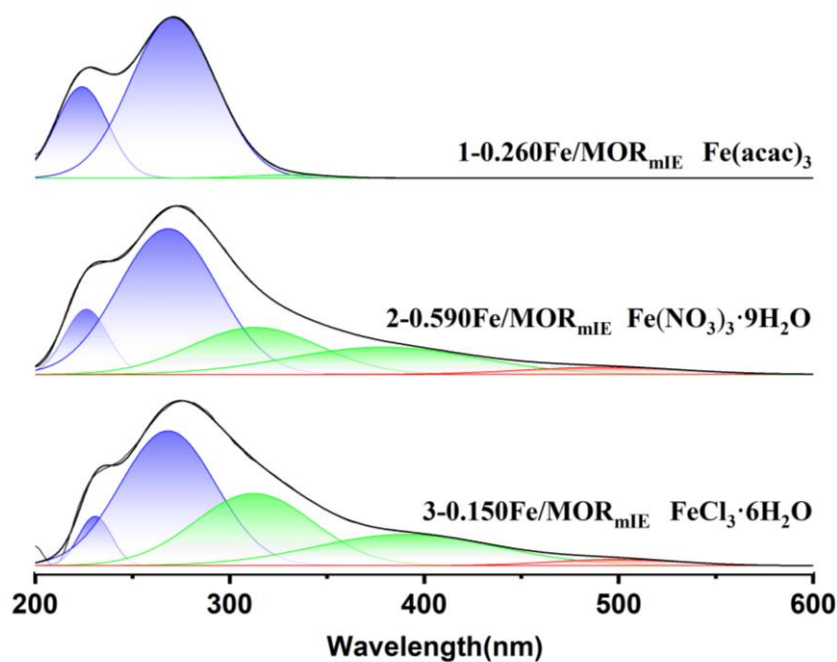


Figure 5-7. UV-vis DRS spectra of Fe/MOR catalysts prepared by the liquid ion-exchange method in CH₃CN as solvent with different iron precursors Fe(acac)₃, Fe(NO₃)₃·9H₂O and FeCl₃·6H₂O, respectively.

Table 5-7. Deconvolution data of Fe/MOR_{mIE} prepared by different iron precursors.

Catalysts ^b	Relative contribution of different range (%) ^a		
	I ₁ (200~300 nm)	I ₂ (300~400 nm)	I ₃ (>400 nm)
1-0.260Fe/MOR _{mIE}	98.7	1.3	0
2-0.590Fe/MOR _{mIE}	72.2	25.4	2.4
3-0.150Fe/MOR _{mIE}	62.7	35.2	2.1

^aObtained by using Origin software (GaussAmp Fit), R² > 0.99. ^bEntry 1: Fe(acac)₃, Entry 2: Fe(NO₃)₃·9H₂O, Entry 3: FeCl₃·6H₂O.

The effect of different Fe precursors for the liquid ion-exchange process was further examined. UV-vis DRS was used to investigate the nature of Fe(III) species in the catalysts, as depicted in [Figure 5-7](#). The deconvolution of the absorbance spectra into subbands was made based on the assignments described in the following. UV-vis DRS spectra of Fe containing zeolites can be divided into three regions, <300 nm, 300-400 nm, and >400 nm, corresponding to isolated mononuclear Fe³⁺ species with different coordination, oligomeric Fe_xO_y clusters, and Fe₂O₃ nanoparticles, respectively [158,159]. Nevertheless, UV-vis analysis provides a semiquantitative distribution of these species rather than accurate quantities [160]. The relative percentages of various Fe species determined in [Table 5-7](#) do not take into account the wavelength dependence of extinction coefficients. Despite this fact and the inherent uncertainty of the deconvolution process, the quantifications in [Table 5-7](#) provide a valuable indication of the relative amounts of various Fe sites in the catalysts studied. The Fe distribution listed in [Table 5-7](#) showed that for 1-0.26Fe/MOR prepared by liquid ion-exchange in acetonitrile, around 98.7% of the iron was present as mononuclear sites of different coordination. As for the samples prepared by Fe(NO₃)₃·9H₂O and FeCl₃·6H₂O in acetonitrile, additional spectral features in the >300 nm regions appear and develop, attributed to the presence of more oligomeric Fe clusters and particles. Thus, it can be concluded that the Fe precursor used during synthesis determines the nature and proportion of Fe species, which in turn will affect the catalytic performance. Thus, we proposed that the advance of ion exchange with Fe(acac)₃ consists in the suppressed Fe aggregation in acetonitrile, achieving controllable loading with mononuclear Fe species, which might be due to the capping effect of acetylacetonate counter ions. These findings provide valuable insights into the design of highly

efficient Fe/MOR catalysts for the methane activation. Adopting MeCN as the solvent allows for suppression of the hydrolysis of the Fe(acac)₃ to achieve selective loading of mononuclear Fe species.

5.4 Fe/MOR with different iron loading

Recently, different groups have claimed that binuclear Fe clusters or monomeric Fe species in Fe/ZSM-5 are the intrinsic active sites for direct methane oxidation based on a combination of catalytic experiments and in situ characterizations [64,67]. Inevitably, the presence of disparate Fe species, such as mononuclear, oligonuclear clusters and metal oxides particles, are experimentally confirmed in Fe containing zeolites [104,161], and a majority of the Fe species show limited activity as spectator species in the low-temperature methane oxidation [65]. The nature and proportion of Fe species of Fe-containing zeolites depend critically on many factors, such as the preparation method, Fe content, calcination temperature, and procedure used for their activation [69]. In order to determine the optimal loading and the underlying structure-performance relation, different Fe loadings were investigated.

5.4.1 Preparation method

To obtain different Fe contents of the catalysts, 200 mg commercial NH₄-MOR powder and the specific amounts of Fe(acac)₃ corresponding to nominal Fe loadings of 0.1, 0.5, 1.0, 1.5, and 5.0 wt.%, respectively, were added to 8 mL MeCN as a solvent in glass vials. The vials were treated with ultrasound for 2 min and were placed in an oven for 24 h at 85 °C. After the heat treatment, the samples were centrifuged and washed with acetone, deionized water, and acetone and then dried in an oven for 5 h at 80 °C. Finally, the samples were calcined in an oven at 500 °C with a heating ramp of 100 °C/h and kept at this temperature for 5 h in the air. Despite the increasing amount of Fe precursor, the actual Fe loading did not increase proportionally, which is probably due to a diffusion limitation of Fe(acac)₃ inside the pores of the zeolite (see Figure 5-8).

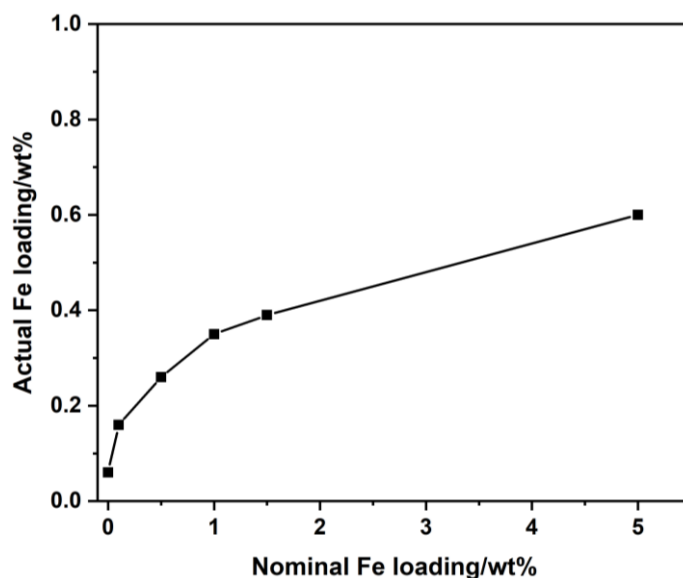


Figure 5-8. The loading effect of $\text{Fe}(\text{acac})_3$ precursor on commercial $\text{NH}_4\text{-MOR}$ zeolite containing 0.06 wt.% Fe impurity in CH_3CN solution.

5.4.2 Investigation of the activity

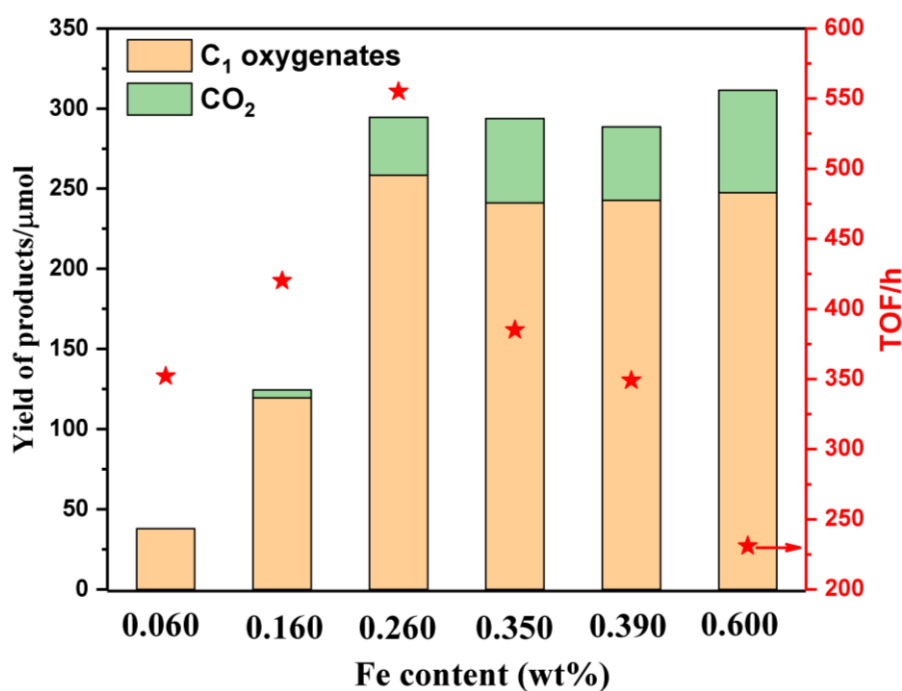


Figure 5-9. Catalytic performance of Fe/MOR catalysts with different Fe loadings prepared by $\text{Fe}(\text{acac})_3$ in CH_3CN solution via liquid ion-exchange method. Reaction condition: 30 bar of CH_4 , 10 mL of 0.5 M H_2O_2 , 600 rpm, 80 °C, 0.5 h, 20 mg of catalyst.

Table 5-8. Performance of Fe/MOR with different Fe loadings.

Entry	Cat.	Product yield(μmol)/Selectivity(%)					H_2O_2		TOF /h ⁻¹	C1 Yield/ μmol
		MeOH	OHCH ₂ OOH	MeOOH	HCOOH	CO ₂	Conv. (%)	Util. (%)		

1	MOR-500	5.0 13.3%	6.5 17.1%	22.9 60.6%	3.4 8.9%	0	18.7	5.4	352	37.8
2	0.160Fe/MOR	16.8 13.5%	31.5 25.3%	48.0 38.6%	23.1 18.6%	5.0 4.0%	16.9	16.2	420	119.4
3	0.260Fe/MOR	32.7 11.1%	69.6 23.6%	64.8 22.0%	91.4 31.1%	36.0 12.2%	43.9	22.3	555	258.5
4	0.350Fe/MOR	23.6 8.0%	52.9 18.0%	53.5 18.2%	111.2 37.9%	52.5 17.9%	57.2	25.0	385	241.2
5	0.390Fe/MOR	21.3 7.4%	57.3 19.9%	48.8 16.9%	115.3 40.0%	45.9 15.9%	60.1	21.2	349	242.7
6	0.600Fe/MOR	23.2 7.5%	45.2 14.5%	42.4 13.6%	136.8 43.9%	63.9 20.5%	68.5	15.9	231	247.6

Reaction condition: 30 bar of CH₄, 10 mL of 0.5 M H₂O₂, 600 rpm, 80 °C, 0.5 h, 20 mg of catalyst.

Catalysts with different Fe content were obtained by increasing the addition of Fe(acac)₃ according to nominal loadings of 0, 0.1, 0.5, 1.0, 1.5, and 5.0 wt.% Fe, respectively. The catalytic performance was evaluated by the product yield and TOF of Fe/MOR catalysts with a series of Fe loadings (Figure 5-9 and Table 5-8). Figure 5-9 shows that the optimal active loading was around 0.260 wt.% Fe, because this catalyst exhibited the best yield and maximal TOF. Fe loaded beyond 0.260 wt.% did not contribute to the increase of product yield to C1 oxygenates, but to a higher amount of CO₂ and lower H₂O₂ utilization ratio (Table 5-8).

5.4.3 Catalyst characterizations

5.4.3.1 UV-vis diffuse-reflectance spectroscopy (UV-vis DRS)

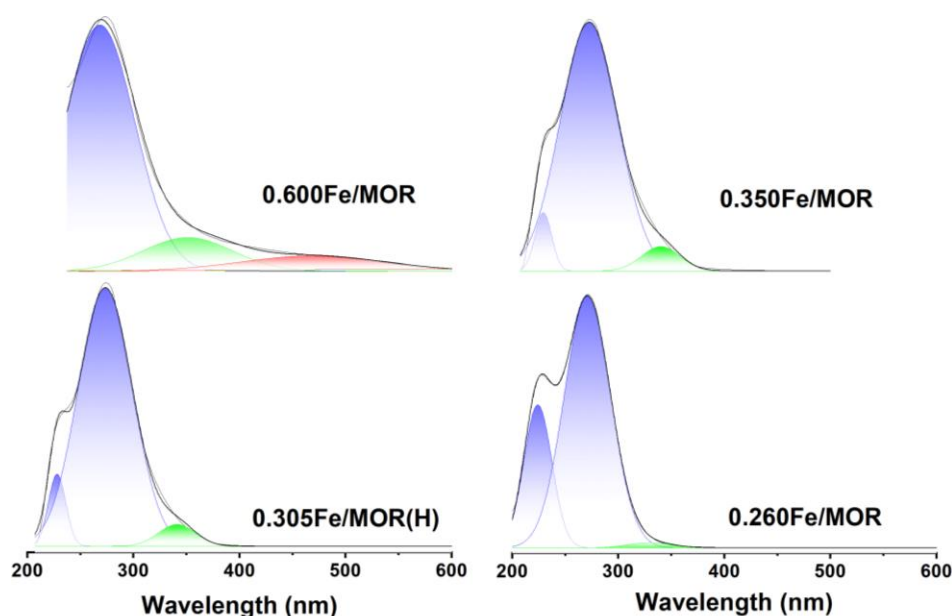


Figure 5-10. UV-vis DRS of Fe/MOR catalysts prepared by modified liquid ion-exchange method with different Fe contents. Except from 0.305Fe/MOR(H) all other catalysts were obtained using NH₄-MOR as support.

Table 5-9. Deconvolution data of Fe/MOR with different Fe content.

Catalysts	Relative contribution of different range (%) ^a		
	I ₁ (200~300 nm)	I ₂ (300~400 nm)	I ₃ (>400 nm)
0.260Fe/MOR	98.7	1.3	0
0.305Fe/MOR(H)	95.2	4.8	0
0.350Fe/MOR	92.6	7.4	0
0.600Fe/MOR	83.4	11.4	5.2

^aObtained by using Origin software (GaussAmp Fit), R² > 0.99.

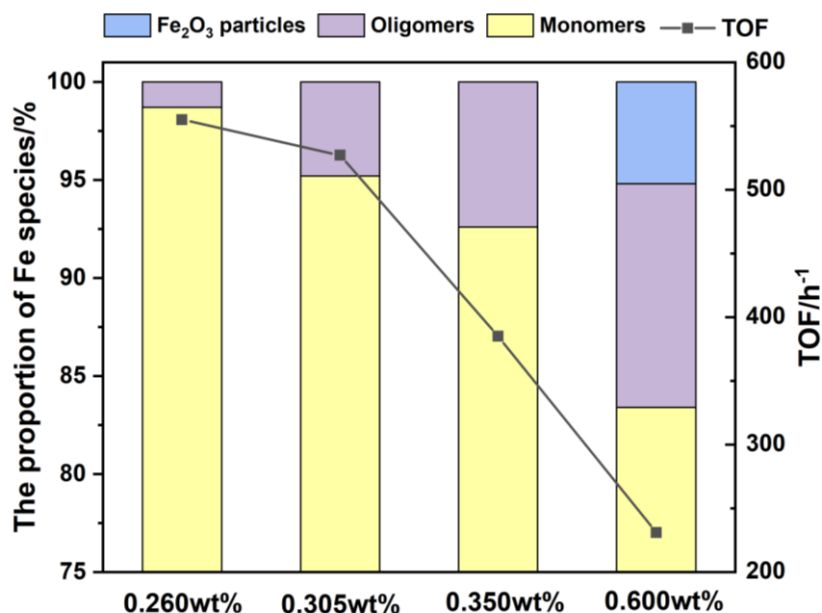


Figure 5-11. The relative proportion of different Fe species in different Fe/MOR zeolites with the TOFs to C1 oxygenates.

Spectroscopic studies were conducted to distinguish the Fe species (see Figure 5-10 and Table 5-9). UV-vis DR spectra showed that 98.7% of the iron at a loading of 0.260 wt.% was present as mononuclear sites of different coordination. When further increasing the Fe content, significant aggregation can be observed due to a higher proportion of the oligomeric clusters and even the appearance of Fe₂O₃ nanoparticles. By comparing the TOFs with the fractions of Fe sites as determined from UV-vis DRS, it can be assumed that mononuclear Fe ions are the active sites for direct methane oxidation (see Figure 5-11). An increasing Fe loading in MOR above the optimal value of 0.260 wt.% mainly led to the increase of Fe aggregates, which seem to catalyze the undesirable side-reactions (H₂O₂ decomposition and over-oxidation), resulting in a significant

decrease in TOF values. It needs to be noted that an apparent drop in TOF can be observed between 0.260 wt.% and 0.350 wt.%. Considering that no serious aggregation at 0.350 wt.% loading as well as at 0.260 wt.% occurred, the drop in the TOF might be caused by diffusion limitation in the batch reactor. This also explains why the yield of C1 oxygenates approached a limiting value for loadings beyond 0.260 wt.%.

5.4.3.2 X-ray absorption spectroscopy analysis

Further characterizations were used to elucidate the structure of Fe species in MOR. TEM images did not show any evidence for Fe nanoparticles based on the diffraction contrast, indicating the existence of sub-nanometer Fe species in MOR below the detection limit of TEM (Figure 5-12). To further investigate the coordination environment of Fe in MOR zeolite, X-ray absorption spectroscopy (XAS) was performed. The X-ray absorption near-edge structure (XANES) spectrum of Fe/MOR shows a Fe K-edge, which sits quite close to Fe₂O₃ but has a bit lower adsorption edge than Fe₂O₃, suggesting a little reduced valence of Fe in Fe/MOR (Figure 5-13a). The Fourier transform-extended X-ray absorption fine structure (FT-EXAFS) spectrum shows two dominant peaks below $R = 2 \text{ \AA}$, that can be ascribed to two kinds of Fe-O scattering paths (Figure 5-13b). There are no apparent observations of the Fe-Fe scattering path, contrasted by Fe foil (2.21 \AA) and Fe₂O₃ (2.56 \AA), confirming the absence of Fe-Fe bonds and atomic dispersion of Fe sites in Fe/MOR. The fitting of FT-EXAFS is further conducted to determine the coordination environments (Figure 5-13c, 5-13d). The best fit is achieved by FeO₆ coordination with two types of Fe-O bonds (Figure 5-14b), excluding binuclear clusters, trinuclear clusters, and Fe₂O₃ (Figure 5-15). The bond lengths of 1.85 and 2.04 \AA correspond to Fe-O-Al/Si and Fe-OH/H₂O, respectively [68,162]. The corresponding fitting parameters are summarized in Table 5-10. Furthermore, wavelet transformed (WT) EXAFS spectrum also indicates the atomic state of Fe species in MOR (Figure 5-14a), which gives a more descriptive evaluation.

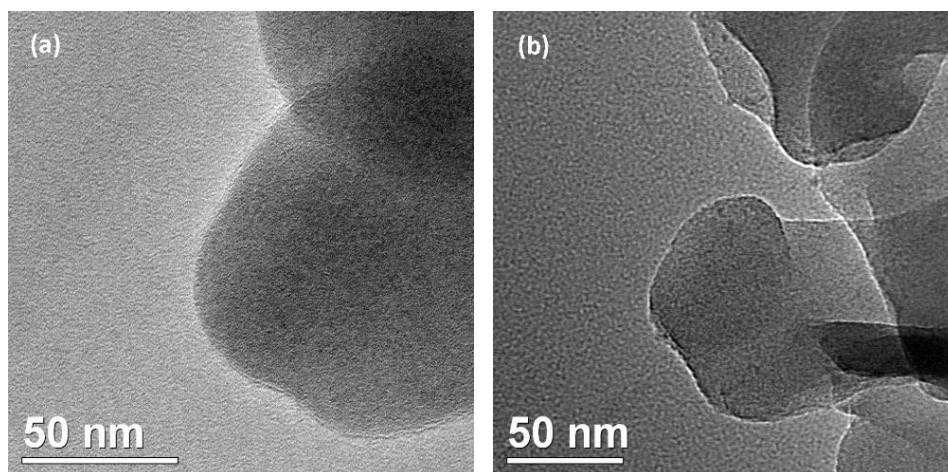


Figure 5-12. TEM images of the (a) 0.35Fe/MOR-500 and (b) 0.60Fe/MOR-500 catalysts.

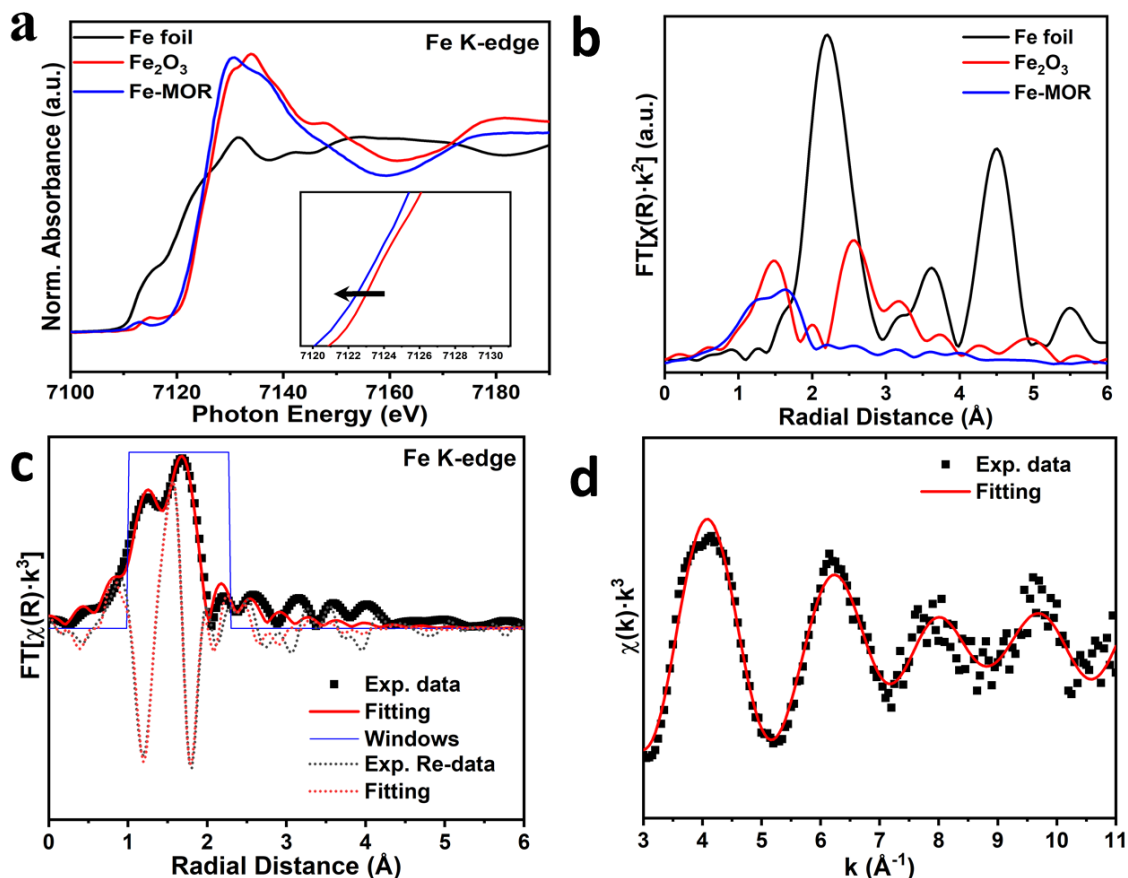


Figure 5-13. (a) Fe K-edge XANES spectra and (b) FT-EXAFS spectra of 0.35Fe/MOR, Fe foil and Fe₂O₃. EXAFS fitting in R-space (c) and in k-space (d).

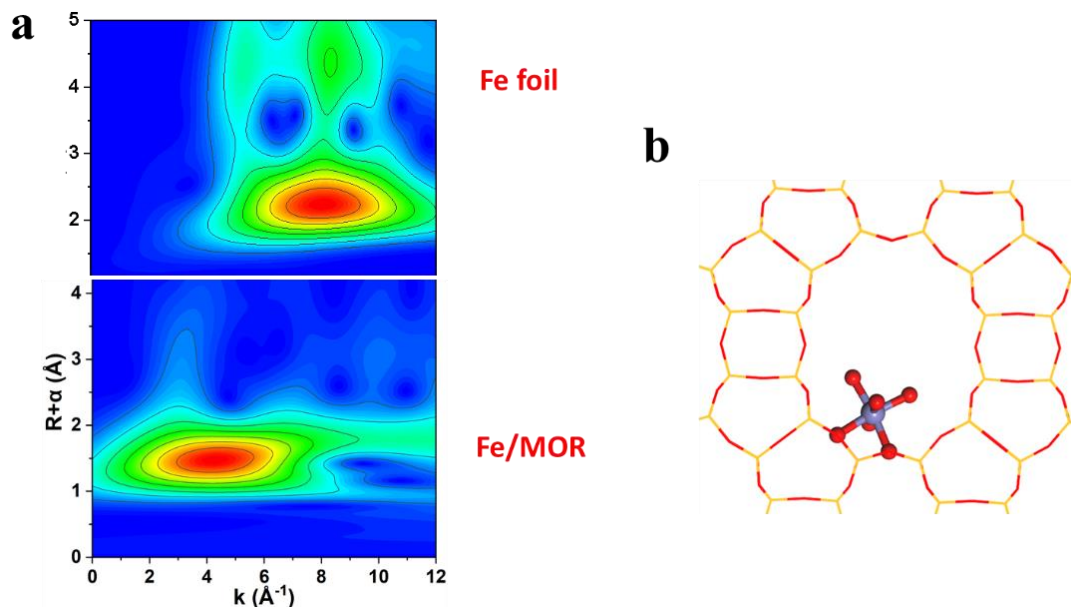


Figure 5-14. (a) WT-EXAFS of 0.35Fe/MOR and Fe foil. (b) The proposed structure of the mononuclear Fe in MOR, viewing along *c* axis. Pink: Al; Yellow, Si; Red: O; Purple: Fe.

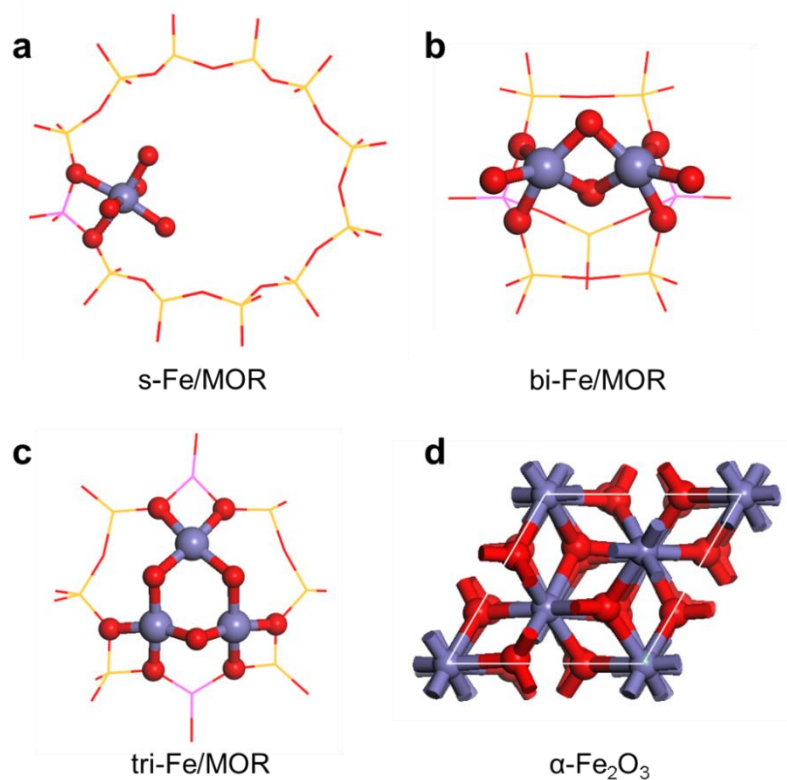


Figure 5-15. Potential Fe structures hosted in MOR zeolite considered in XAS fitting. (a) single atom Fe in 12 MR. (b) binuclear Fe in 6 MR. (c) trinuclear Fe in 8 MR. (d) α -Fe₂O₃. Pink: Al; Yellow, Si; Red: O; Purple: Fe.

Table 5-10. EXAFS fitting parameters of Fe/MOR, using different modes.

Model	Path	N^a	R (Å) ^b	σ^2 ($10^{-3} \cdot \text{Å}^2$) ^c	ΔE_0 (eV) ^d	R factor (%) ^e
s-Fe/MOR ^f	Fe-O ₁	2.64 ± 0.54	1.85 ± 0.03	5.8 ± 2.7	-6.0 ± 2.5	0.60
	Fe-O ₂	4.69 ± 1.02	2.03 ± 0.02			
s-Fe/MOR ^g	Fe-O ₁	2.60	1.85	7.2 ± 1.9	-5.7 ± 0.3	1.01
	Fe-O ₂	5.31	2.04			
	Fe-Al/Si	0.60 ± 0.34	2.77 ± 0.04			
bi-Fe/MOR	Fe-O ₁	2.80	1.85	7.3 ± 1.8	-4.9 ± 0.7	0.93
	Fe-O ₂	5.43	2.04			
	Fe-Fe	-0.31 ± 0.19	2.52 ± 0.15			
Tri-Fe/MOR	Fe-O ₁	2.90	1.85	7.1 ± 1.9	-4.6 ± 0.8	1.08
	Fe-O ₂	5.52	2.03			
	Fe-Fe	-0.33 ± 0.20	2.73 ± 0.04			
Fe ₂ O ₃	Fe-O ₁	2.29	1.85	6.0 ± 1.5	-5.5 ± 0.6	0.65
	Fe-O ₂	4.39	2.04			
	Fe-Fe	0.30 ± 0.17	3.00 ± 0.04			

^aN: coordination numbers; ^bR: bond distance; ^c σ^2 : Debye-Waller factors; ^d ΔE_0 : the inner potential correction. ^eR factor: goodness of fit. S_0^2 was set as 0.87, based on the fitting of reference. R-range: 1.0-3.0. ^fOnly fitting first shell of the s-Fe/MOR. ^gSecond shell was considered.

5.5 PDMS coating of Fe/MOR

Lippard and coworkers found that in MMO enzymes, the di-iron active site is situated in a hydrophobic cavity and the related gating mechanism enables their near-perfect selectivity to methanol for direct methane oxidation [163]. However, considering the rigid structure of zeolites, it is difficult to directly imitate the bio-enzymatic process based on the flexible enzymatic components with a zeolitic system. For the purpose of preserving the formed methanol from over-oxidation, it would be fantastic to achieve its rapid release by a fast diffusion out of the pore and away from the active site. However, the polar methanol adsorbed easier at the polar surface of a zeolite and thus is prone to over-oxidation than the non-polar methane molecule, Bokhoven and coworkers [11] commented that in unprotected systems (without employing any measures to stabilize methanol or suppress its further oxidation), a low selectivity towards methanol at higher methane conversions is found for all catalysts, which indicates the general limits of the catalytic DMTM process. Special concepts are required to obtain the product in higher yield and selectivity.

Xiao and coworkers [44] have recently prepared hydrophobic ZSM-5 with AuPd alloy nanoparticles encapsulated inside the zeolite micropores for in situ H_2O_2 generation that triggered the direct methane oxidation. A hydrophobic external “molecular fence” was prepared by anchoring organosilanes at the outer surface of ZSM-5. The hydrophobic molecular fence permitted the diffusion of hydrophobic species like methane, oxygen, and hydrogen to PdAu active sites, while locally concentrating the formed H_2O_2 that allowed its rapid interaction with methane. This way, it helps for efficient methanol production and prevents over-oxidation (>92% selectivity).

Herein, we adopted a general and facile approach by using polydimethylsiloxane (PDMS)-coating treatment to form a hydrophobic layer on the surface of Fe/MOR. Compared with other postmodification methods, such a PDMS-coating approach is facile and shows significant superiority to retain inherent porosity (i.e., high surface area, pore texture, and crystalline structure) [164-166]. The PDMS coating on the catalyst was conducted by a vapor deposition technique, which will form semi-coated not fully coated catalysts. Semi-coated zeolite particles could preferentially reside in the gas-liquid interface, increasing the mass transfer process. Our initial idea was that hydrophobic coating facilitates the enrichment of hydrophobic substrates (methane) to increase the $m(CH_4)/m(H_2O_2)$ ratio inside the pores of the zeolite and thereby promote

interaction with Fe sites, which will further boost the activity. And the hydrophobicity may also play a role to help the desorption of the polar methanol molecule, leading to better selectivity.

5.5.1 Preparation method

Polydimethylsiloxane (PDMS) coating was conducted on 0.35Fe/MOR-500 by a simple vapor deposition technique. Firstly, after mixing the two-part polymers of base elastomer and curing agent (PDMS, SYLGARD[®] 184, Sigma Aldrich) thoroughly, the mixture was then put in a glass container and dried at 70 °C for 1 h to get the solid form of PDMS, which was cut it into small pieces for the later coating (Figure 5-16a). Typically, a certain amount of Fe/MOR powder (spreading to layer as thin as possible) was put on a glass dish, placed in a sealed glass container with some fresh PDMS stamp (Figure 5-16b). After vacuuming to remove the air inside, the glass container was maintained at 235 °C for 1 h in a digital-temperature controlled oven and then allowed to cool to room temperature naturally to give PDMS-coated Fe/MOR. The volatile and low molecular weight silicone molecules would deposit on the surface of Fe/MOR and subsequently cross-link, to result in the formation of a hydrophobic silicone coating.

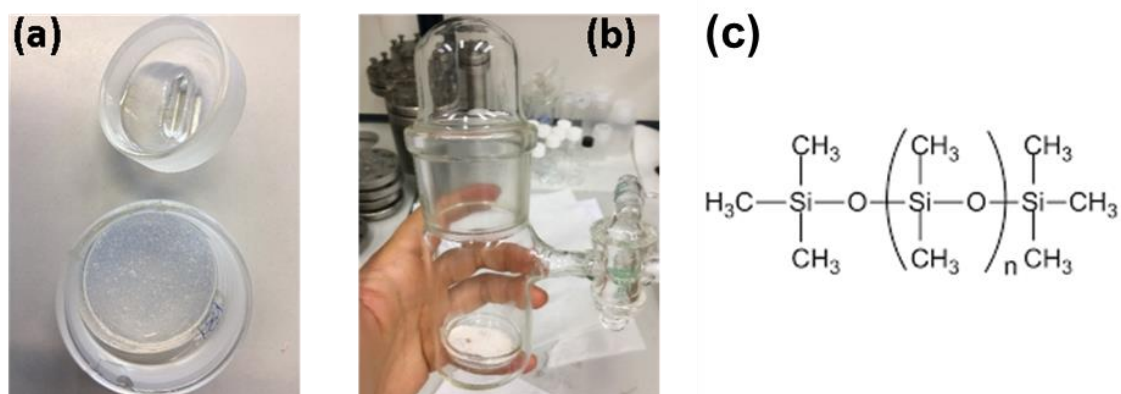


Figure 5-16. (a) Photograph of solid form of PDMS. (b) Photograph of reaction container for PDMS coating with MOR powder in the glass dish and PDMS stamp on the outside wall of the glass dish. (c) Chemical structure of PDMS.

5.5.2 Investigation of the activity

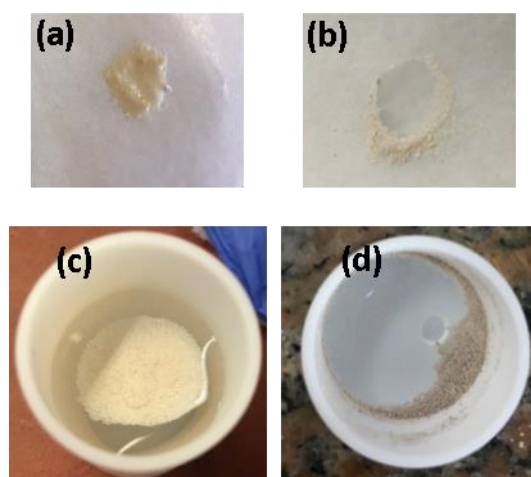


Figure 5-17. (a) Photograph of water dropped on 0.35Fe/MOR; (b) Photograph of water dropped on PDMS@0.35Fe/MOR; (c) Photograph of PDMS@0.35Fe/MOR (PDMS coating, 200 °C, 1 h) in 0.5 M H₂O₂ aqueous solution; (d) Photograph of PDMS@0.35Fe/MOR (PDMS coating, 235 °C, 3 h) in 0.5 M H₂O₂ aqueous solution.

At first, 2 or 3 drops of water were dropped on the Fe/MOR and PDMS coated Fe/MOR, which were placed on a weighing paper. Photographs presented in [Figure 5-17a](#) clearly show that Fe/MOR zeolite was immediately wet according to the hydrophilic nature of zeolites. After PDMS coating for 1 h, surface modification induces the increase of the contact angle of water drops, suggesting that the PDMS coating transforms the surface character of MOR zeolite from hydrophilic to hydrophobic ([Figure 5-17b](#)). The vessel was charged with Fe/MOR-500 or PDMS@Fe/MOR-500 catalyst and 10 mL of 0.5 M H₂O₂ aqueous solution during the catalytic reaction. Photographs presented in [Figure 5-17 \(c and d\)](#) show the PDMS coated Fe/MOR zeolites with different coating times and temperatures in the H₂O₂ solution. Due to the hydrophobic surface, these PDMS-coated Fe/MOR zeolites were not soaked into the solution like the Fe/MOR but floated on the surface. In [Figure 5-17d](#), PDMS@Fe/MOR obtained with a longer coating time and higher coating temperature (235 °C, 3 h) shows obviously a thick PDMS layer with a darker color and displays gradually enhanced hydrophobicity. [Table 5-11](#) shows the catalytic results of the 0.35Fe/MOR with or without the hydrophobic PDMS layer. However, it is a pity that we did not see a significant difference in the catalysts' catalytic performance. Because the PDMS coated MOR zeolites were found totally soaked into the solution and completely wet after the reaction test, we suppose that the PDMS layer was decomposed during the reaction because of the strong oxidizing power of •OH generated from H₂O₂.

Table 5-11. Catalytic activity of 0.35Fe/MOR with/without PDMS coating.

Entry	Cat.	Product yield(μmol)/Selectivity(%)					H ₂ O ₂		TOF /h ⁻¹
		MeOH	MeOOH	OHCH ₂ OOH	HCOOH	CO ₂	Conv. (%)	Util. (%)	
1	pdms@0.35Fe/MOR ^a	26.4	56.9	59.3	106.3	45.3	47.4	28.6	397
		9.0%	19.3%	20.2%	36.1%	15.4%			
2	pdms@0.35Fe/MOR ^b	27.4	51.2	55.0	87.4	49.9	55.3	23.0	353
		10.1%	18.9%	20.3%	32.2%	18.4%			
3	0.35Fe/MOR	23.6	53.5	52.9	111.2	52.5	57.2	25.0	385
		8.0%	18.2%	18.0%	37.9%	17.9%			

Reaction condition: 30 bar CH₄, 10 mL 0.5 M H₂O₂, autoclave reactor, 600 rpm, 80 °C, 0.5 h, 20 mg catalysts. 0.35Fe/MOR-500, Fe loading 0.35 wt.%; ^aPDMS coating, 200 °C, 1 h; ^bPDMS coating, 235 °C, 3 h.

5.6 Summary

Zeolite topology has been found to play a crucial role in activity because it provides the appropriate geometric constraints around Fe to maintain Fe-oxo sites. In our work, MOR was used as support to confine Fe sites for the direct methane oxidation to C1 oxygenates at 80 °C and 30 bar of CH₄ using an aqueous 0.5 M H₂O₂ solution as oxidant. The presence of disparate Fe species to different extent, such as mononuclear, oligonuclear clusters and metal oxides particles, has been confirmed for Fe/zeolites. The nature and proportion of Fe species in Fe/zeolites depend critically on many factors, such as the preparation method, Fe content, or calcination temperature. We have used four different preparation methods, namely incipient wetness impregnation (IWI), liquid ion exchange (IE), solid-state ion exchange (SSIE) and FeCl₃ sublimation to prepare Fe/MOR catalysts. We can clearly see that Fe/MOR catalysts obtained by these methods all gave a similar yield of C1 oxygenates around 250 μmol under suitable conditions, which proved the superiority of MOR zeolite as iron support for direct methane oxidation by using H₂O₂ as oxidant. Among these methods, the modified liquid ion-exchange method was found to better control Fe loading in MOR-type zeolite with Fe(acac)₃ as a precursor in CH₃CN solution to get around 0.30 wt.% Fe content, which showed the highest TOF. What's more, in the activity tests of Fe/MOR with different Fe content, we found that around 0.30 wt.% Fe was optimal loading content for Fe/MOR catalysts, which exhibited the best yield and TOF of up to 500 h⁻¹ to C1 oxygenates. The TEM images and XAS analysis confirmed that the Fe sites in 0.35Fe/MOR existed in the form of mononuclear Fe sites. UV-vis measurements indicated that 0.60Fe/MOR obtained by increasing the Fe precursor concentration showed an apparent peak in the range above 400 nm that is ascribed to Fe-oxo nanoparticles. We proposed that the further addition of Fe in MOR mainly contributes

to increasing the fraction of Fe nanoparticles, which tend to trigger the undesirable side-reactions, in particular, H_2O_2 decomposition resulting in a significant decrease in reaction efficiency.

6. Direct methane oxidation over Fe/MFI nanosheet catalysts by H₂O₂

6.1 Motivation

In the past decade, Hammond et al. [64] found that commercial H-ZSM-5 with a SiO₂/Al₂O₃ molar ratio of 30 containing 0.014 wt.% Fe impurity exhibited a surprising activity with TOFs of up to 2200 h⁻¹ towards C1 oxygenates at 50 °C using H₂O₂ aqueous solution as oxidant. They hold that the active iron site is an extra-framework binuclear core as identified by EXAFS and DFT calculations. Until now, the level of activity exhibited by ZSM-5 containing a trace amount of Fe has proven to be unique, and no other catalysts are reported to surpass its activity.

In 2021, Zhu et al. [105] found that 0.03 wt.% Fe/ZSM-5(66) synthesized via ion-exchange method triggered highly efficient methane conversion at 80 °C and 5 M H₂O₂ aqueous solution, reaching 8% methane conversion with a TOF of 84200 h⁻¹ to oxygenates and 91% selectivity to HCOOH. On the basis of a series of experimental characterizations and DFT calculations, they found that both mononuclear and binuclear Fe species confined in the channel of the ZSM-5 can generate Fe-O centers with high activity for dissociating C-H bonds. As shown in Figure 6-1a, they found that when the Fe loading further increased to 2.2 wt.%, the yield and selectivity to C1 oxygenates were almost unchanged compared to those over 0.03 wt.% Fe/ZSM-5, but the TOF decreased dramatically to around 1000 h⁻¹. UV-vis DRS depicted in Figure 6-1b revealed that the Fe species in 0.03 wt.% Fe/ZSM-5 mostly existed in the form of mononuclear Fe in the framework (λ_1) and extra-framework (λ_2) oligomeric Fe in the channels of the ZSM-5 [56]. However, 2.2 wt.% Fe/ZSM-5 contained not only highly dispersed Fe (λ_1 and λ_2) but also larger FeO_x aggregates (λ_3 and λ_4). Combining with other characterizations, they assumed that larger Fe₂O₃ aggregates appeared at high Fe loadings, which are unlikely to be active for the reaction but may hinder the diffusion of reactants to the active sites, thereby inhibiting the catalytic activity. Therefore, they believed that the atomically dispersed Fe species within the nano-channel of the ZSM-5 are the active sites for methane conversion to HCOOH.

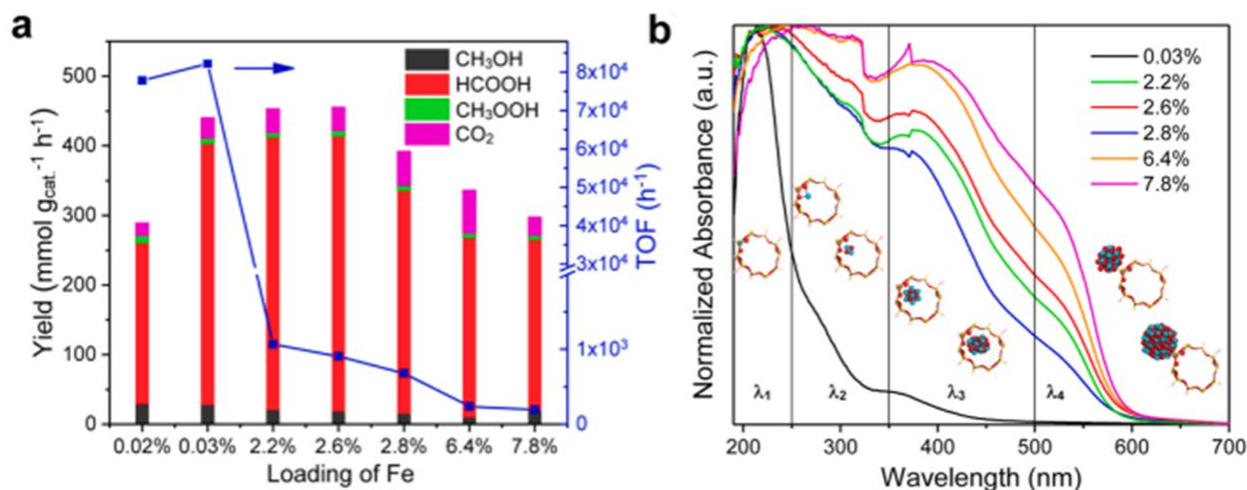


Figure 6-1. (a) Catalytic performances (yield and TOF) of the Fe/ZSM-5 samples with different Fe loadings. Reaction condition: 10 mL of H₂O with 5 M H₂O₂, 20 mg of catalyst, 3 MPa of CH₄, 80 °C, 0.5 h. (b) UV-vis DRS of Fe/ZSM-5 catalysts with different Fe loading amounts.

Zeolite topology is quite important for the activity, which provides an appropriate geometric constraint around Fe to maintain ultrafine Fe-oxo sites that act as active sites. We have analyzed the maximum pore size (the diameter of the largest-free-sphere that can diffuse) of ZSM-5 and molecular size of binuclear Fe sites proposed in Fe/ZSM-5 [64] and drew Figure 6-2 to help to understand the formation of Fe active site in ZSM-5 framework. Figures 6-2a and 6-2b show the maximum diameter of a sphere (a 10 MR) in the ZSM-5 framework. We used Diamond software to draw the proposed binuclear Fe and determine its rough size (see Figure 6-2c). We can see that ZSM-5 provides an ideal pore size to constrain binuclear Fe that leads to unique activity for direct methane oxidation. However, this advantage also results in severe drawbacks. Even the biggest micropores of ZSM-5 with aperture diameters around only 4.7 Å definitely cause diffusion limitations [167] that restrict the diffusion of Fe(NO₃)₃ or Fe(acac)₃ precursors to get high loading and more dispersed Fe sites, adversely affecting catalytic activity. Therefore, we expected that 2D Pentasil (MFI) nanosheets could increase the catalytic performance. 2D structures with reduced thickness are favorable to reducing diffusion path lengths when loading Fe, especially large size Fe(acac)₃ as a precursor [167]. Moreover, a higher exposed external surface enhances liquid/solid mass transfer, which might also contribute to achieving high loading of mono and binuclear Fe sites. Furthermore, primary products, especially methanol, are expected quickly diffuse off the nanosheet to avoid further over-reaction.

Zeolite topology is found to be decisive for the activity, which may provide the appropriate geometric constraint around Fe to maintain ultrafine Fe-oxo sites that act as active sites. The exact geometrical parameters of the MFI structure can be found in the zeolite structure database (Figure 6-2) [168]. The maximum size of the diffusion channel (10 MR) of the MFI structure is 4.7 Å (see

Figures 6-2a and 6-2b). Based on DFT calculations, Hammond et al. proposed the structure of the binuclear cluster in the MFI structure, namely $[\text{Fe}_2(\mu_2\text{-OH})_2(\text{OH})_2(\text{H}_2\text{O})_2]^{2+}$ [64]. The rough size of this binuclear cluster was measured at around 4.8 Å (see Figure 6-2d) and it is found to fit precisely into the pores of the ZSM. This pore size restriction may explain why the extra-framework iron sites in the MFI structure tend to form binuclear clusters. However, the confined environment, while favoring the formation of active sites for methane oxidation, may at the same time cause the aggregation of more giant clusters and hinder further increasing the loading of active binuclear clusters.

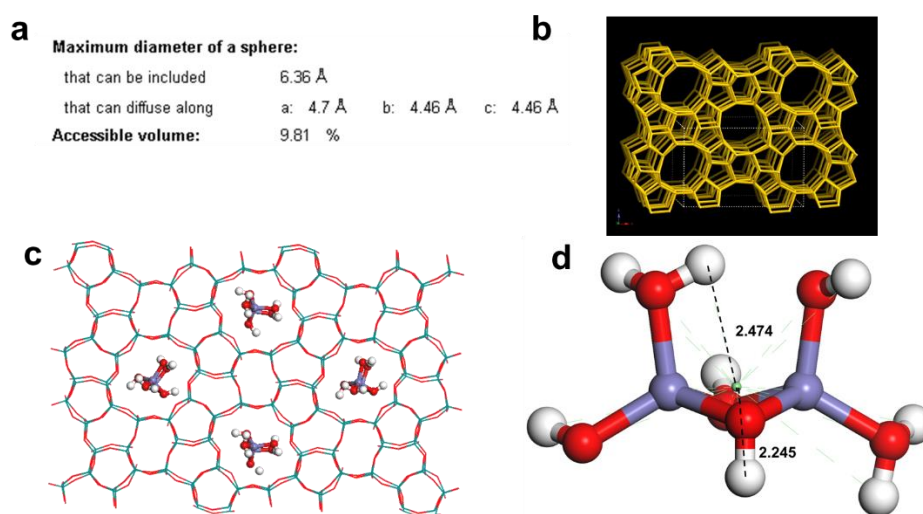


Figure 6-2. (a) Maximum diameter of a sphere in ZSM-5 [168]. (b) ZSM-5 framework viewed along [010] (c) The scheme of proposed binuclear Fe sites in ZSM-5. (d) The size and structure of binuclear Fe sites proposed in Fe/ZSM-5 (The black dotted line indicates the distance between the H atom and the center of cluster.) [64].

Even though the Fe impurity achieves the highest TOF in ZSM-5, the overall activity is still limited to the very low Fe loading. Increasing the Fe loadings to get a higher amount of active Fe sites is an effective method to increase the methane oxidation performance of Fe/MFI catalyst. Therefore, we expect to reduce 3D-MFI into 2D nanosheets to enhance the catalytic performance. 2D zeolite structure with reduced thickness is favorable to reduce diffusion path lengths when loading Fe, especially using large size $\text{Fe}(\text{acac})_3$ as a precursor [167]. Moreover, the reduced diffusion path is good for mass diffusion of the reactant and timely departure of the product to avoid the over-oxidation.

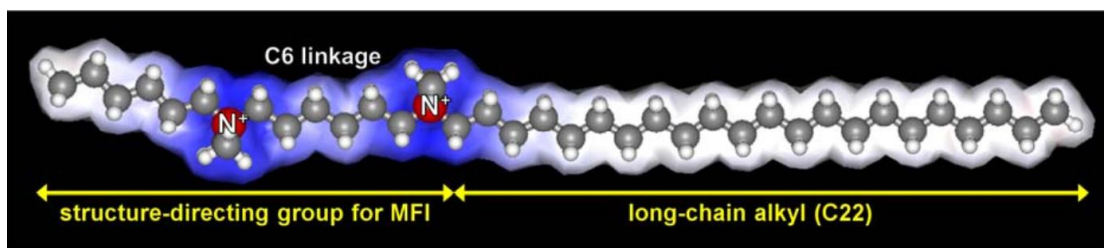


Figure 6-3. ‘Bifunctional’ cationic surfactant (C₂₂₋₆₋₆) directing porous structures in meso- and micro-length scales simultaneously.[169]

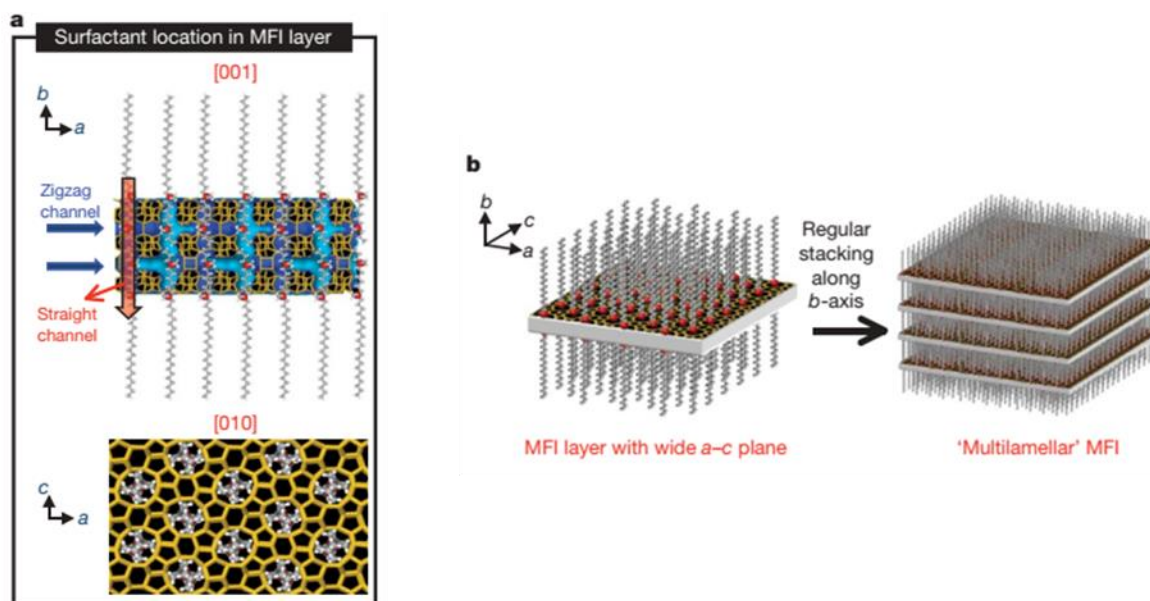


Figure 6-4. (a) Proposed structure model for the single MFI nanosheet. Two quaternary ammonium groups showed as a red sphere. (b) Many MFI nanosheets form multilamellar stacking along the b-axis.[169]

Considering the above mentioned reasons, layered zeolites, with shortened diffusion path and larger external surface area, maybe promising for the reaction. Ryong Ryoo and coworkers [169,170] established the synthesis of MFI nanosheets by designing a di-quaternary ammonium-type surfactant, [C₂₂H₄₅-N⁺(CH₃)₂-C₆H₁₂-N⁺(CH₃)₂-C₆H₁₃] (designated as C₂₂₋₆₋₆). The surfactant consisted of a long-chain alkyl group (C₂₂) and two quaternary ammonium groups spaced by a C₆ alkyl linkage (see Figure 6-3). The diammonium head groups directed the formation of microporous MFI crystalline structure as a structure-directing agent (SDA), while the long-chain tails having hydrophobic interaction induced the formation of mesoscale micellar structure. They proposed that the surfactant molecules are aligned along the straight micropores of the MFI framework (see Figure 6-4a). The hydrophilic end of the micelles led to the formation of an ultrathin zeolite framework of only 2 nm thickness. The hydrophobic end inhibited the growth of zeolites. Alternating MFI layers and surfactant layers formed multilamellar stacking along the b-axis (see Figure 6-4b).

In their work, MFI zeolites with a Si/Al ratio of 30 to ∞ can be obtained using the di-ammonium surfactant as the SDA. In a typical synthesis, the as-synthesized MFI zeolite has a plate-like morphology with multilamellar stacked and three-dimensionally intergrown (see Figure 6-5a). The overall thickness of a plate is typically 20–40 nm. High-resolution A TEM cross-section of a plate (see Figure 6-5c) unveiled that each plate consisted of lamellar stacking of alternating layers of MFI zeolite framework (2 nm) and surfactant micelle (2.8 nm). Three pentasil sheets make up one MFI framework layer with only 2 nm thickness, corresponding to the b-axis dimension ($b = 1.9738$

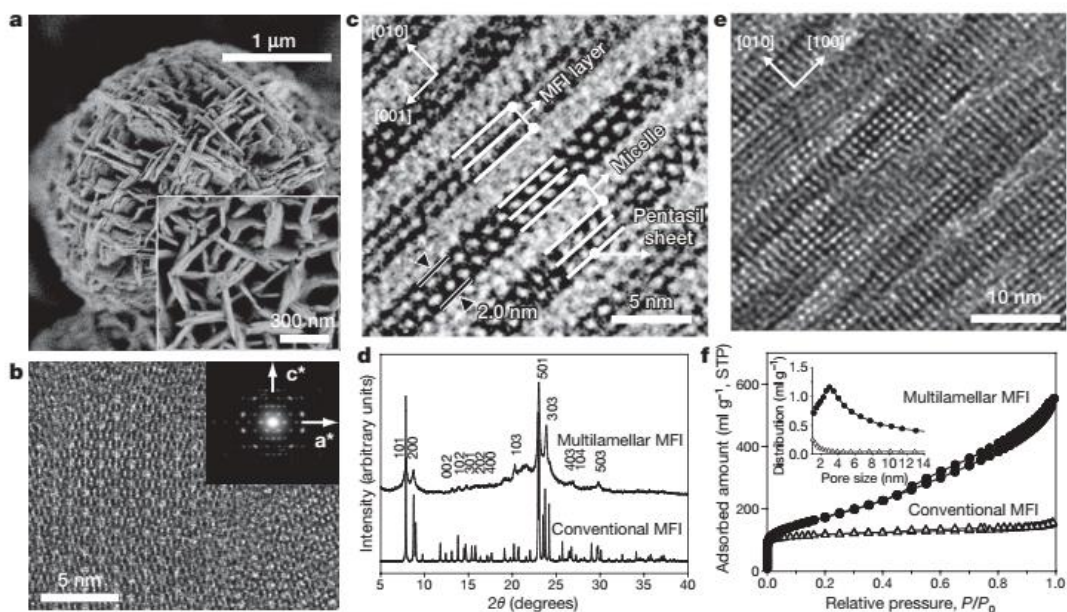


Figure 6-5. MFI nanosheets with a multilamellar structure. (a–d) As-synthesized sample; (e and f) calcined sample. (a) SEM image. (b) TEM and electron diffraction on the wide plane of the plate ([010] incidence of MFI). (c) TEM cross-section of the plate. (d) Powder XRD pattern. (e) TEM image of calcined sample. (f) N₂ adsorption–desorption isotherm. [169]

nm) of a single MFI unit cell. The powder XRD pattern of the as-synthesized MFI (see Figure 6-5d) showed that only h0l diffraction reflexes have adequate sharpness for indexing, which indicated that the obtained MFI framework has wide a–c planes and extremely small thickness along the b-axis. Since the surfactant layer actually acted as interlamellar support (see Figure 6-4b), calcination led to the removal of the surfactant and resulted in partial condensation of the MFI layers in the calcined sample that can be seen from its TEM image (see Figure 6-5e). What's more, the intergrown crystal plates (Figure 6-5a) could act as a ‘pillar’ supporting each other to maintain the mesoporous structure. N₂ adsorption-desorption isotherm (see Figure 6-5f) confirmed the highly mesoporous structure of the calcined sample with a significantly enhanced BET area of 520 m² g⁻¹ compared to conventional MFI zeolite of 420 m² g⁻¹. Due to the irregular distortion of zeolite

layers (see [Figure 6-5e](#)), the mesopore size distribution was quite comprehensive (see [Figure 6-5f](#)).

6.2 Synthesis methods

6.2.1 Synthesis of organic surfactant $C_{22-6-6}Br_2$

The organic surfactant $[C_{22}H_{45}-N^+(CH_3)_2-C_6H_{12}-N^+(CH_3)_2-C_6H_{13}]Br_2$ (designated as $C_{22-6-6}Br_2$) was synthesized in the following steps from Choi et al. [169,170]. 1-bromodocosane (7.8 g, 20 mmol, TCI) and *N,N,N',N'*-tetramethyl-1,6-diaminohexane (34.4 g, 200 mmol, Sigma Aldrich) were dispersed in 100 mL of acetonitrile/toluene mixture (1:1 v/v) in a 500 mL round-bottom flask, which was placed in 70 °C oil bath and reacted overnight under magnetic stirring. After cooling to room temperature, the obtained product was $[C_{22}H_{45}-N^+(CH_3)_2-C_6H_{12}-N^+(CH_3)_2]Br$ (designated as $C_{22-6-0}Br$). The compound $C_{22-6-0}Br$ was filtered, washed with diethyl ether, and dried in an oven at 80 °C to remove the organic solvent. Then the synthesized $C_{22-6-0}Br$ (5.6 g, 10 mmol) and 1-bromohexane (2.5 g, 20 mmol, Sigma Aldrich) were dissolved in 30 mL acetonitrile in a 100 mL round-bottom flask, which was refluxed at around 85 °C overnight. After cooling to room temperature, the obtained product was filtered, washed with diethyl ether, and dried in an oven at 80 °C to remove the organic solvent. The product was identified as $[C_{22}H_{45}-N^+(CH_3)_2-C_6H_{12}-N^+(CH_3)_2-C_6H_{13}]Br_2$ and confirmed by 1H NMR as shown in [Figure 6-6](#).

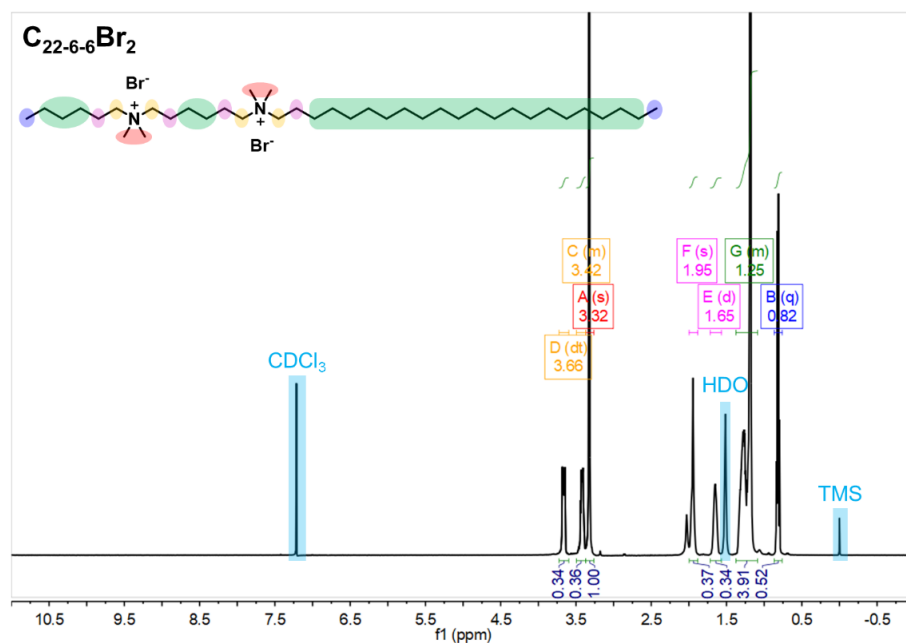


Figure 6-6. 1H NMR spectrum of the synthesized ligand $C_{22-6-6}Br_2$.

6.2.2 Synthesis of MFI-nanosheet zeolite

As we know, Fe/ZSM-5 catalyst with a low Si/Al ratio exhibited better activity due to the essential Brønsted acids sites. However, high Al content will disturb the multilamellar ordering [170]. In order to balance these two opposing influences, we have chosen a Si/Al ratio of 50 to synthesize multilamellar MFI nanosheets, denoted as MFI-nanosheet(50). Because our oven for the hydrothermal thesis could not achieve the tumbling of 60 rpm, which aimed to intensively mix the silica gel and the surfactant as depicted by Ryong Ryoo and coworkers [169,170]. Our MFI-nanosheet(50) was prepared following the recipe reported by Emdadi et al. [171]. Typically, 0.7 g NaOH was added into 3.1 g DI water, which was fully dissolved by ultrasound treatment and cooled to ambient temperature. 0.4 g H₂SO₄ was added into 4.2 g DI water, which was cooled to ambient temperature for later use. Then, the basic solution was added dropwise into the acidic solution under vigorous stirring, which was transferred into a 150 mL PTFE lined autoclave. After cooling the mixture to ambient temperature, 0.19 g Al₂(SO₄)₃·16H₂O was dissolved into the mixture under vigorous stirring. After fully dissolving, the magnetic stir bar was removed and changed to a mechanical stirrer. Then, 6.3 g TEOS was added slowly into the mixture, which was stirred vigorously at room temperature for 20 h using a mechanical stirrer to get homogeneous dispersion without bulk solids. Finally, 2.2 g C₂₂₋₆₋₆Br₂ was dissolved in 15 g DI water to get a clear solution by ultrasound treatment, which was then added into the reactor chamber under mechanical stirring for another 2 h at room temperature. The resultant gel was crystallized for 5 days under tumbling in an oven (30 rpm) at 150 °C. After crystallization, the zeolite product was filtered, washed with lots of DI water, and dried at 80 °C overnight. The obtained product without further calcination was denoted as MFI-nanosheet(50). Samples were calcined at 550 °C with 100 °C/h for 4 h in the air to remove the SDA, which was denoted as MFI-nanosheet(50)-550. For the MFI-nanosheet(∞) zeolite with a Si/Al molar ratio of ∞ , the entire synthesis procedure is the same as for MFI-nanosheet(50) except for the addition of Al₂(SO₄)₃·16H₂O when preparing the gel.

6.2.3 Fe loading on MFI nanosheets and 3D ZSM-5 zeolite

6.2.3.1 Fe loading on MFI nanosheets and 3D ZSM-5 by post-modification

Fe was loaded by the modified liquid ion exchange (mIE) method (see [part 5.3](#)) on MFI-nanosheet(50)-550. Typically, 200 mg MFI-nanosheet(50)-550 or commercial H-ZSM-5 and a certain amount of Fe(acac)₃ or Fe(NO₃)₃·9H₂O or FeCl₃·6H₂O were added to 8 mL of CH₃CN in a glass vial, which was ultrasonicated for 2 min and placed in an oven at 85 °C for 24 h. After the

heat treatment, the samples were centrifuged and washed with a sequence of acetone, deionized water, and acetone and were then dried at 80 °C in an oven for 5 h. Finally, the samples were calcined in an oven at 550 °C with a heating ramp of 100 °C/h and kept for 4 h in air, which were denoted as Fe/MFI-nanosheet-550 post (see Figure 6-7) and Fe/ZSM-5(50)-550.

For the solid-state ion-exchange (SSIE) method, 200 mg MFI-nanosheet(50)-550 or commercial H-ZSM-5(50) were mixed and intensively grounded with a certain amount of Fe(acac)₃, corresponding to a nominal loading of 0.5 wt.% Fe in an agate mortar for 1 h under ambient condition. The obtained uniform mixture was calcined in an oven at 550 °C with a heating ramp of 100 °C/h and kept for 4 h in air. The obtained catalysts are denoted as Fe/MFI-nanosheet(50)-550_{SSIE} or Fe/ZSM-5(50)_{SSIE}.

6.2.3.2 Fe loading on MFI nanosheets by direct modification

Fe was loaded by modified liquid ion-exchange (mIE) method with a Fe(acac)₃ as precursor on as-synthesized MFI-nanosheet samples without calcination, which was defined as a direct modification. Typically, 200 mg as-synthesized MFI-nanosheet(50) or MFI-nanosheet(∞) and certain amount of Fe(acac)₃ were added to 8 mL of CH₃CN in a glass vial, which was treated with ultrasound for 2 min and was placed in an oven at 85 °C for 12 h. The shorter loading time is because MFI-nanosheet without calcination still contains SDA, which is helpful to Fe loading. After the heat treatment, the samples were centrifuged and washed with a sequence of acetone, deionized water, and acetone and were then dried at 80 °C in an oven for 5 h. Finally, the samples were calcined in an oven at 550 °C with a heating ramp of 100 °C/h and kept for 4 h in air, which were denoted as Fe/MFI-nanosheet-550 direct (see Figure 6-7).

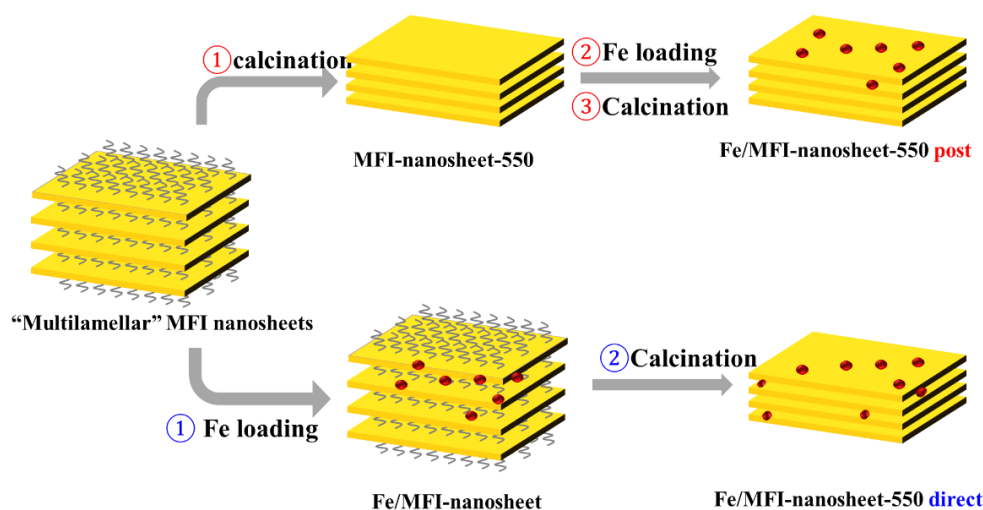


Figure 6-7. Scheme of the Fe loading procedure by modified liquid ion-exchange (mIE) method using CH₃CN as solvent.

6.2.4 Pillaring of multilamellar MFI nanosheets

Pillaring was performed by infiltration of tetraethyl orthosilicate (TEOS) solution into the surfactant layer between adjacent MFI nanosheets [170,172]. Typically, 5 g of TEOS was added to 1 g of as-synthesized multilamellar MFI-nanosheet(50) in a glass vial with a magnetic stirrer, which was subsequently flushed with He gas for 1 min and was closed with the lid. The mixture was stirred in an 85 °C oil bath for 16 h. The product was filtered off and washed with deionized water, soaked into water for 1 h, and filtered off and washed with water again. Finally, the product was centrifuged, dried at 80 °C overnight, and calcined in an oven at 550 °C with a heating ramp of 100 K/h for 4 h in air, which was denoted as MFI-pillared(50)-550.

6.3 Characterizations of 2D MFI nanosheets

6.3.1 ICP results

Table 6-1 shows the ICP results of different batches of MFI-nanosheet(50)-550 samples after calcination. From the ICP results, we learned that our synthesis method could give MFI nanosheets with a reproducible composition containing no Fe impurity. The Si/Al molar ratio was around 46, which is a little lower than the ratio in the gel.

Table 6-1. ICP results of different batches of MFI-nanosheet(50)-550.

Sample Batch	Fe wt. %	Si wt. %	Al wt. %	Na wt. %	n(Si/Al)
MFI-nanosheet(50)-550 21.08.12	<10ppm	39.1	0.82	0.37	45.9
MFI-nanosheet(50)-550 21.05.12	<10ppm	38.7	0.81	0.24	46.3
MFI-nanosheet(50)-550 21.04.29	<10ppm	40.5	0.83	0.22	46.8

Table 6-2 shows the ICP results of the Fe modified MFI-nanosheet catalysts by direct modification as described in part 6.2.3.2. The column denoted as “preparation condition” shows the used Fe precursor and the nominal Fe salt amounts when preparing. The ICP results indicated that the preparation procedure did not influence the Si/Al molar ratio.

Table 6-2. ICP results of Fe modified MFI-nanosheet catalysts by direct synthesis method.

Sample Name	Preparation condition	Fe wt. %	Si wt. %	Al wt. %	Na wt. %	n(Si/Al)
0.333Fe/MFI-nanosheet(50)-550 direct	0.5 wt. %, Fe(acac) ₃ mIE, 85 °C, 12 h	0.333	38.2	0.81	0.16	45.4
0.664Fe/MFI-nanosheet(50)-550 direct	0.8 wt. %, Fe(acac) ₃ mIE, 85 °C, 12 h	0.664	40.3	0.84	0.25	46.1

0.222Fe/MFI-nanosheet(50)-550 direct	0.3 wt.%, Fe(NO ₃) ₃ mIE, 85 °C, 12 h	0.222	38.3	0.81	0.24	45.5
0.372Fe/MFI-nanosheet(50)-550 direct	0.5 wt.%, Fe(NO ₃) ₃ mIE, 85 °C, 12 h	0.372	40.3	0.86	0.30	45.3
0.560Fe/MFI-nanosheet(∞)-550 direct	0.8 wt.%, Fe(acac) ₃ mIE, 85 °C, 12 h	0.560	45.0	0	0.33	∞

Table 6-3 shows the ICP results of the Fe modified MFI-nanosheet(50)-550 catalyst by post-modification as described in part 6.2.3.1. The column denoted as the “preparation condition” shows the synthesis methods, the used Fe precursors and the nominal Fe loading amounts when preparing. The ICP results indicate that the two times high-temperature calcination and activation procedure when loading Fe influences the Si/Al molar ratio to some degree.

Table 6-3. ICP results of Fe modified MFI-nanosheet(50)-550 catalysts by post-synthesis methods.

Sample Name	Preparation condition	Fe wt. %	Si wt. %	Al wt. %	Na wt. %	n(Si/Al)
0.079Fe/MFI-nanosheet (50)-550 post	mIE, 85 °C, 24 h 0.5 wt.%, FeCl ₃	0.079	39.1	0.78	0.21	48.1
0.128Fe/MFI-nanosheet (50)-550 post	mIE, 85 °C, 24 h 0.5 wt.%, Fe(acac) ₃	0.128	39.5	0.74	0.16	51.0
0.345Fe/MFI-nanosheet (50)-550 post	mIE, 85 °C, 24 h 0.5 wt.%, Fe(NO ₃) ₃	0.345	41.0	0.83	0.14	47.3
0.496Fe/MFI-nanosheet (50)-550 _{SSIE}	SSIE, r.t. 1 h 0.5 wt.%, Fe(acac) ₃	0.496	41.4	0.76	0.22	52.3

Table 6-4 shows the ICP results of the Fe modified H-ZSM-5(50) catalyst by post-synthesis method as described in part 6.2.3.2. The column denoted as the “preparation condition” shows the used Fe precursors and the nominal Fe loading when preparing. The ICP results indicate that the preparation procedure does not influence the Si/Al molar ratio for commercial H-ZSM-5(50).

Table 6-4. ICP results of Fe modified H-ZSM-5(50) catalyst by post-synthesis methods.

Sample Name	Preparation condition	Fe wt. %	Si wt. %	Al wt. %	Na wt. %	n(Si/Al)
H-ZSM-5(50)-550	-	<10ppm	42.3	0.89	0.04	45.8
0.060Fe/ZSM-5(50)-550	mIE, 85 °C, 24 h 0.5 wt.%, FeCl ₃	0.060	40.8	0.85	0.03	46.2
0.114Fe/ZSM-5(50)-550	mIE, 85 °C, 24 h 0.5 wt.%, Fe(acac) ₃	0.114	43.8	0.90	0.04	46.7
0.288Fe/ZSM-5(50)-550	mIE, 85 °C, 24 h 0.5 wt.%, Fe(NO ₃) ₃	0.288	39.4	0.82	0.06	46.0
H-ZSM-5(95)-550	-	0.017	44.9	0.45	0	95.3
0.136Fe/ZSM-5(95)-550	mIE, 85 °C, 24 h 0.5 wt.%, Fe(NO ₃) ₃	0.136	45.6	0.47	0.1	94.0
0.494Fe-ZSM-5(50)-550 _{SSIE}	SSIE, r.t., 1 h 0.5 wt.%, Fe(acac) ₃	0.494	40.3	0.87	0	44.7

6.3.2 SEM and TEM images

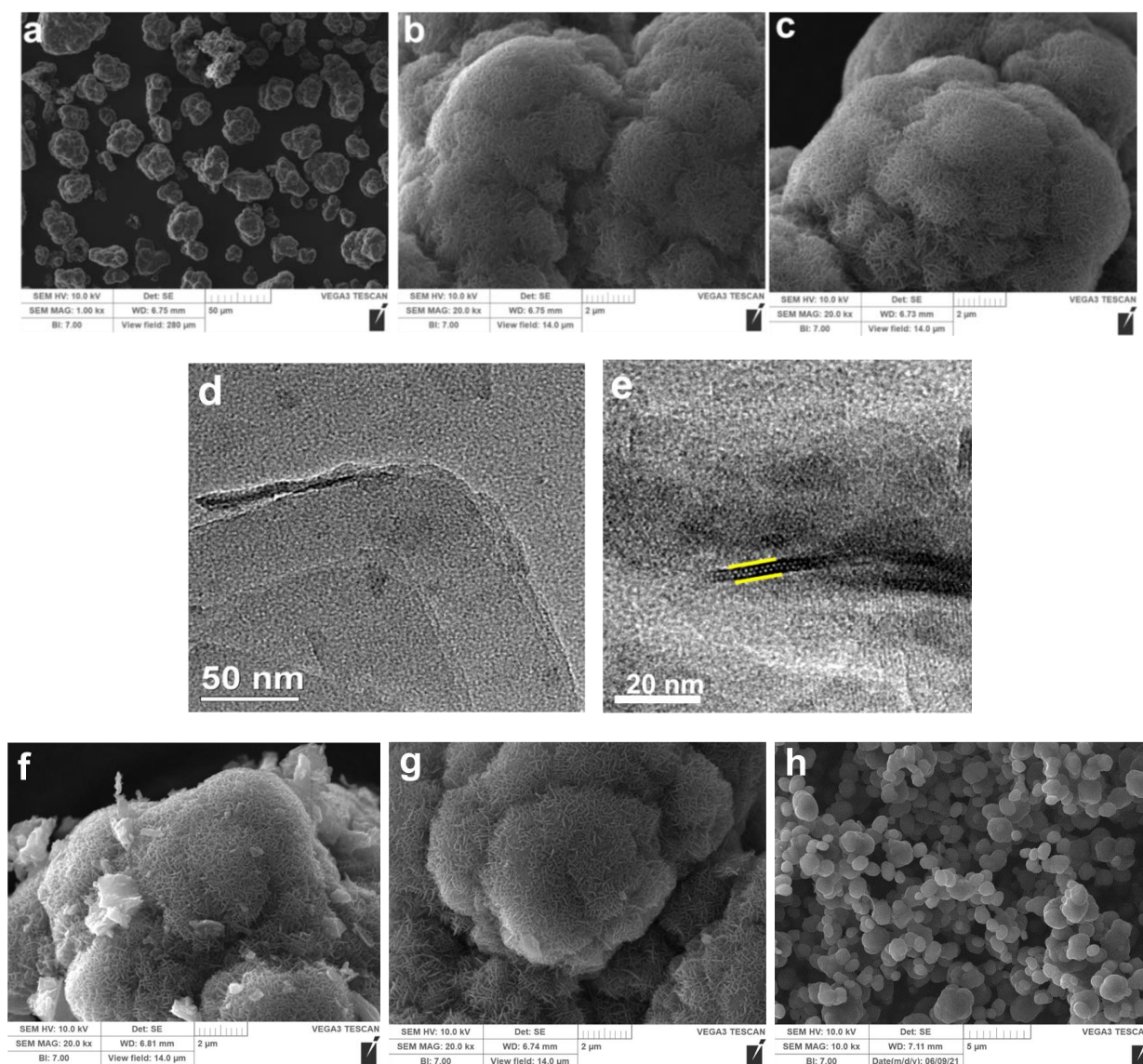


Figure 8. (a) and (b) SEM images of as-synthesized MFI-nanosheet(50); (c) SEM image of MFI-nanosheet(50)-550, high-temperature calcination in the air; (d) and (e) TEM images of calcined MFI nanosheets with a unilamellar structure, MFI-pillared-550; (f) SEM image of Fe/MFI-nanosheet-550 post; (g) SEM image of Fe/MFI-nanosheet-550 direct; (h) ZSM-5(50)-550.

As shown in [Figures 6-8a](#) and [6-8b](#), the as-synthesized MFI-nanosheet(50) has a plate-like morphology that was multilamellar stacked and three-dimensionally intergrown (see [Figure 6-8b](#)) to give big particles (see [Figure 6-8a](#)). [Figures 6-8c](#) is the SEM image of MFI-nanosheet(50)-550, which indicates that high-temperature calcination in the air did not change the morphology of MFI nanosheets, but plates were thinner. Besides multilamellar form, MFI zeolite could also be prepared in the form of unilamellar nanosheets by pillaring with TEOS. TEM images in [Figure 6-8d](#) and [6-8e](#) revealed that the material is composed of a single MFI layer, which further proved the success of obtaining MFI nanosheets. [Figures 6-8f](#) and [6-8g](#) show the SEM images of Fe/MFI-

nanosheet(50)-550(post) and Fe/MFI-nanosheet(50)-550(direct) catalysts, respectively, which were prepared as described in [part 6.2.3](#). There were lots of bulk particles of MFI zeolite found in Fe/MFI-nanosheet(50)-550(post) that were prepared by Fe loading on calcined MFI-nanosheet(50)-550 and then had high-temperature activation at 550 °C. This result indicates that bulk structure appears after repeated high-temperature calcination of MFI nanosheets. There is no difference between [Figure 6-8c](#) and [6-8g](#) of Fe/MFI-nanosheet(50)-550(direct) catalyst, indicating that the Fe loading process on the as-synthesized sample did not change the morphology of MFI nanosheets.

6.3.3 XRD

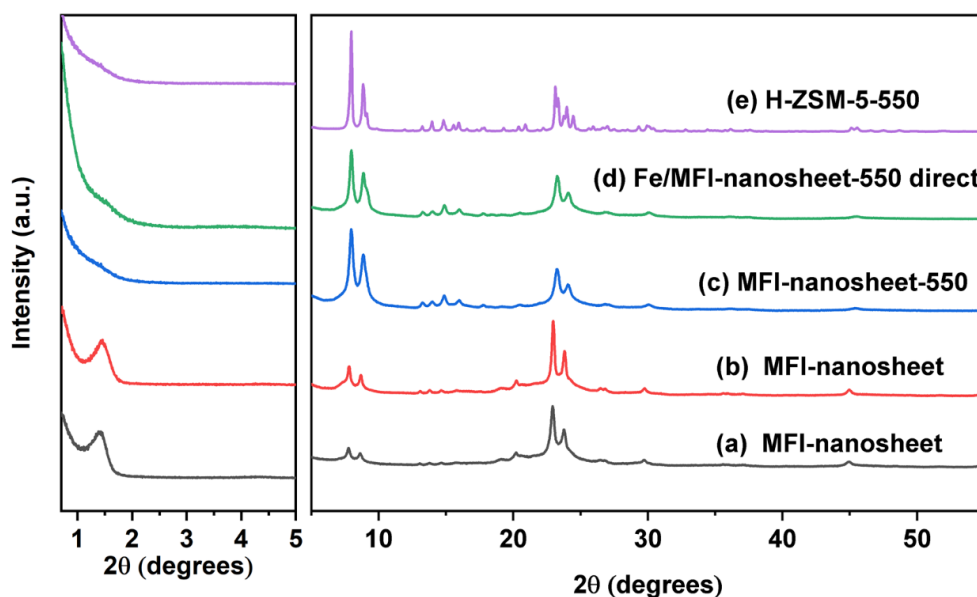


Figure 6-9. Low-angle and high-angle XRD patterns for as-synthesized MFI-nanosheet(50) samples, MFI-nanosheet(50)-550 and H-ZSM-5(50)-550.

X-ray diffraction is a good method to identify lamellar structures ([Figure 6-9](#)) [170]. The high-angle XRD peaks indicated the formation of crystalline MFI structure. The reflexes in the low-angle XRD pattern can be assigned to the first-order reflections associated with the interlayer structure of multilamellar MFI zeolites [170]. The low-angle XRD peaks indicate a highly ordered multilamellar structure was obtained. In [Figure 6-9](#), XRD pattern of different batches of as-synthesized MFI-nanosheet(50) ([a](#) and [b](#)) showed both low-angle peaks corresponding to the interlamellar structure and the significantly broadened high-angle XRD peaks, which are characteristic of a crystalline MFI zeolite. As for the calcined samples ([c](#)) and ([d](#)), the ordered multilamellar structure disappeared while the broadened reflexes indicate the extremely small framework thickness along the b-axis.

6.3.4 Physical adsorption

As shown before in Figure 6-8, the intergrown plates in MFI nanosheets could act as a ‘pillar’ supporting each other to maintain a mesoporous structure. N₂ adsorption–desorption isotherm (see Figure 6-10) of MFI-nanosheet(50)-550 confirmed the mesoporous structure of the calcined sample with a BET area of 413 m² g⁻¹, which is lower than the reported 520 m² g⁻¹ in literature [169] because of the different synthesis methods. Due to the irregular distortion of zeolite layers (see Figure 6-5e), the mesopore size distribution was quite comprehensive.

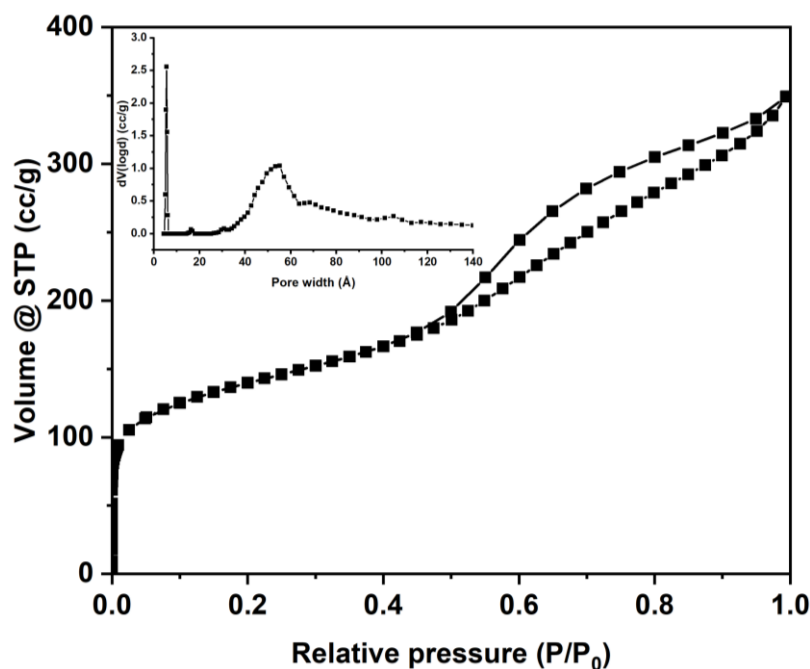


Figure 6-10. N₂ adsorption–desorption isotherm of MFI-nanosheet(50)-550. STP, standard temperature and pressure.

6.4 Investigation of the activity

6.4.1 Catalytic activity of Fe/MFI-nanosheet-550(post) catalysts

Table 6-5 shows the catalytic activity of MFI-nanosheet(50)-550 catalysts with Fe loaded by post-modification (mIE or SSIE), and 3D ZSM-5(50) zeolite also loaded with Fe by post-modification as reference (see Table 6-6). By comparing the catalytic results, it is evident that 3D ZSM-5 sample used as support exhibits much better activity in TOF and C1 productivity than 2D MFI nanosheets obtained by the same post-modification method. The significantly reduced activity for Fe modified MFI-nanosheet(50)-550 made us suspect that the 2D structure might generate different Fe sites to that in 3D ZSM-5 zeolite, which seems to be less active. There was

no big difference in the Fe loading amount on ZSM-5(50) and MFI-nanosheet(50)-550, no matter which Fe precursors were used. We assume that after removing SDA by calcination, originally multilamellar MFI nanosheets were subject to partial condensation, forming a thick plate with distorted layers that did not show advantageous diffusion abilities.

Table 6-5. Catalytic activity of Fe loaded MFI-nanosheet(50)-550 catalysts by post-modification.

No.	Cat.	Preparation Condition	Product yield(μmol)/Selectivity(%)					H_2O_2		TOF / h^{-1}
			MeOH	OHCH ₂ OOH	MeOOH	HCOOH	CO ₂	Conv. (%)	Util. (%)	
1	0.079Fe/MFI-nanosheet(50)-550 post	mIE, 85 °C, 24 h, 0.5 wt.%, FeCl ₃	8.8 7.8%	16.0 14.2%	15.2 13.5%	65.6 58.5%	6.6 5.9%	17.0	30.6	746
2	0.128Fe/MFI-nanosheet(50)-550 post	mIE, 85 °C, 24 h, 0.5 wt.%, Fe(acac) ₃	9.5 6.2%	15.6 10.2%	13.8 9.0%	99.8 65.2%	14.4 9.4%	26.3	27.7	605
3	0.345Fe/MFI-nanosheet(50)-550 post	mIE, 85 °C, 24 h, 0.5 wt.%, Fe(NO ₃) ₃	6.8 8.1%	15.4 18.6%	18.7 22.7%	32.5 39.4%	9.3 11.2%	13.7	23.5	119
4	0.496Fe/nanosheet(50)-550 _{SSIE}	SSIE, r.t. 1 h 0.5 wt.%, Fe(acac) ₃	5.7 4.6%	17.2 13.9%	15.0 12.1%	63.2 50.9%	23.1 18.6%	30.1	16.0	114

Reaction condition: 30 bar of CH₄, 10 mL of 0.5 M H₂O₂, 600 rpm, 50 °C, 0.5 h, 20 mg of catalyst.

Table 6-6. Catalytic activity of Fe loaded H-ZSM-5(50) catalyst by post-modification.

No.	Cat.	Preparation Condition	Product yield(μmol)/Selectivity(%)					H_2O_2		TOF / h^{-1}
			MeOH	OHCH ₂ OOH	Me OOH	HCOOH	CO ₂	Conv. (%)	Util. (%)	
1	0.06Fe/ZSM-5(50)-550	mIE, 85 °C, 24 h 0.5 wt.%, FeCl ₃	18.7 10.7%	14.4 8.2%	10.4 5.9%	121.8 69.3%	10.5 5.9%	20.3	42.2	1538
2	0.114Fe/ZSM-5(50)-550	mIE, 85 °C, 24 h 0.5 wt.%, Fe(acac) ₃	14.7 6.2%	16.4 6.9%	10.4 4.4%	162.8 68.9%	31.8 13.5%	29.3	37.8	1001
3	0.288Fe/ZSM-5(50)-550	mIE, 85 °C, 24 h 0.5 wt.%, Fe(NO ₃) ₃	20.5 4.8%	9.5 2.2%	4.4 1.0%	321.4 75.7%	69.0 16.2%	55.0	37.2	690
4	0.494Fe/ZSM-5(50)-550 _{SSIE}	SSIE, r.t., 1 h 0.5 wt.%, Fe(acac) ₃	8.3 3.9%	12.7 6.0%	8.3 3.9%	123.5 58.7%	57.8 27.5%	37.9	22.9	172
5	H-ZSM-5(50)-550	-	1.4 12.4%	0	6.9 62.1%	2.8 25.4%	0	1.3	26.2	-

Reaction condition: 30 bar of CH₄, 10 mL of 0.5 M H₂O₂, 600 rpm, 50 °C, 0.5 h, 20 mg of catalyst.

6.4.2 Catalytic activity of Fe/MFI-nanosheet-550(direct) catalysts

Fe modification of uncalcined MFI nanosheets still containing the SDA may be beneficial for obtaining highly-dispersed Fe sites. Comparing the actual Fe loading amount when using Fe(acac)₃ as a precursor to get the same nominal loading of 0.5 wt.% (see [Tables 6-5,6-6,6-7](#)), Fe loading on MFI-nanosheet still containing the SDA is much easier than loading on ZSM-5(50) and MFI-nanosheet(50)-550 not containing the SDA. [Table 6-7](#) shows the catalytic results of Fe/MFI-nanosheet-550(direct) catalysts. According to [No. 1](#), 0.333Fe/MFI-nanosheet(50)-550 with Fe(acac)₃ as a precursor exhibited good activity to C1 oxygenates with a TOF of 326 h⁻¹. However,

increasing Fe loading to 0.664 wt.% (see No. 2) resulted in a decreased TOF but higher CO₂ selectivity. These results did not satisfy our initial idea that we could increase loading with mono and binuclear Fe sites and achieve higher productivity by improving diffusion of the precursor, thus getting better catalytic performance. Fe/MFI-nanosheet-550(direct) indeed exhibited better activity than Fe/MFI-nanosheet-550(post), but was still much less active than its 3D counterpart.

Table 6-7. Catalytic activity of Fe/MFI-nanosheet-550(direct) catalysts.

No.	Cat.	Preparation Condition	Product yield(μmol)/Selectivity(%)					H ₂ O ₂		TOF /h ⁻¹
			MeOH	OHCH ₂ OOH	MeOOH	HCOOH	CO ₂	Conv. (%)	Util. (%)	
1	0.333Fe/MFI-nanosheet(50)-550 direct	0.5wt.% Fe(acac) ₃ mIE, 85°C, 12h	11.4 5.0%	13.7 6.0%	8.7 3.8%	160.7 70.7%	32.7 14.4%	33.3	32.3	326
2	0.664Fe/MFI-nanosheet(50)-550 direct	0.8wt.% Fe(acac) ₃ mIE, 85 °C, 12h	10.7 3.2%	14.9 4.4%	7.1 2.1%	222.4 65.4%	84.8 24.9%	54.4	26.7	215

Reaction condition: 30 bar CH₄, 10 mL 0.5 M H₂O₂, 600 rpm, 50°C, 0.5 h, 20 mg catalyst.

Table 6-8 shows further catalytic studies of Fe/MFI-nanosheet(50)-550(direct). In No. 1 a blank experiment is conducted, i.e., only H₂O₂ without the addition of the solid catalyst, gives only trace activity (1 μmol), indicating the decisive role of the solid catalyst. The presence of that trace activity can be ascribed to the self-decomposition of the H₂O₂. As can be seen from No. 2, there was no H₂O₂ conversion on MFI-nanosheet(50)-550 without Fe sites, indicating that there was even no Fe impurity and the presence of blank catalyst inhibits the self-decomposition of H₂O₂. According to No. 3, there were no C1 oxygenates generated after replacing CH₄ with N₂, which verifies that all the carbon products originate from CH₄. Another aspect, the high consumption of H₂O₂ under the N₂ atmosphere implies that the CH₄ atmosphere plays a positive role in suppressing the self-decomposition of H₂O₂. There were no products detected in the reaction solution without the addition of H₂O₂, suggesting that H₂O₂ solution as oxidant is essential for the reaction (see No. 4). When using 0.560Fe/MFI-nanosheet(∞)-550 sample without Al, the product yield was greatly reduced, implying the Al atoms' significance and the related Brønsted acid sites (see No. 5).

Table 6-8. Catalytic studies of Fe/MFI-nanosheet-550(direct) catalysts.

No.	Cat.	Preparation Condition	Product yield(μmol)/Selectivity(%)					H ₂ O ₂		TOF /h ⁻¹
			MeOH	OHCH ₂ OOH	MeOOH	HCOOH	CO ₂	Conv. (%)	Util. (%)	
1	Without catalyst	-	0.4 36.7%	0	0.6 53.3%	0.1 10%	0	3.9	0.63	-

2	MFI-nanosheet(50)-550	-	0.5	0	0.5	0	0	0	0	-
3	0.333Fe/MFI-nanosheet(50)-550 direct ^a	0.5 wt.%, Fe(acac) ₃ mIE, 85 °C, 12h	0	0	0	0	0	39.5	0	-
4	0.333Fe/MFI-nanosheet(50)-550 direct ^b	0.5 wt.%, Fe(acac) ₃ mIE, 85 °C, 12h	0	0	0	0	0	0	0	-
5	0.560Fe/MFI-nanosheet(∞)-550 direct	0.8 wt.%, Fe(acac) ₃ mIE, 85 °C, 12h	0.7 11.0%	0	0.3 4.8%	0.7 10.3%	5.0 73.8%	8.2	0.8	1.8

Reaction condition: 30 bar of CH₄, 10 mL of 0.5 M H₂O₂, 600 rpm, 50 °C, 0.5 h, 20 mg of catalyst.

^aReplacing CH₄ with 30 bar of N₂; ^bReplacing H₂O₂ aqueous solution with 10 mL of H₂O.

6.5 Characterizations of catalysts

6.5.1 XAS analysis

Further characterizations were applied to elucidate the structure of Fe species in both MFI nanosheets and 3D ZSM-5, trying to explain the activity difference. XAS measurements were performed to investigate Fe's coordination environment and oxidation state. The X-ray absorption near-edge structure (XANES) spectra of Fe K-edge in 0.288Fe/ZSM-5(50)-550 and 0.664Fe/MFI-nanosheet(50)-550(direct) both sit quite close to Fe₂O₃, suggesting + 3 valence of Fe in both catalysts (Figure 6-11a). The Fourier transform-extended X-ray absorption fine structure (FT-EXAFS) spectra (Figure 6-11b) and the fitting results (Figure 6-12) were conducted to determine the coordination environments. In Figure 6-11b and 6-12a, 0.664Fe/MFI-nanosheet(50)-550(direct) shows one dominant peak below 2 Å, which can be ascribed to Fe-O scattering path. There are no apparent observations of the Fe-Fe scattering path, proven by Fe foil (2.21 Å) and Fe₂O₃ (2.56 Å), confirming the absence of Fe-Fe bond and atomically dispersion of Fe sites in 0.664Fe/MFI-nanosheet(50)-550(direct). However, as shown in Figure 6-11b and 6-12b, 0.288Fe/ZSM-5(50)-550 sample with much lower Fe content exhibited a much stronger peak at 2.6 Å for the Fe-O-Fe bonds, which indicated the existence of iron oxide clusters on 3D ZSM-5 zeolite. Further wavelet transformed (WT) EXAFS spectra in Figure 6-13 also gave the same conclusion, which gives a more descriptive evaluation. Compared to 0.664Fe/MFI-nanosheet(50)-550(direct) (Figure 6-13a), there is a strong Fe-Fe path for 0.288Fe/ZSM-5(50)-550 sample in Figure 6-13b, indicating the atomic state of Fe species in MFI nanosheet. Although both mononuclear and binuclear Fe sites have been reported to be the active sites in Fe/ZSM-5 catalyst, our current results seem to show binuclear Fe sites being more active.

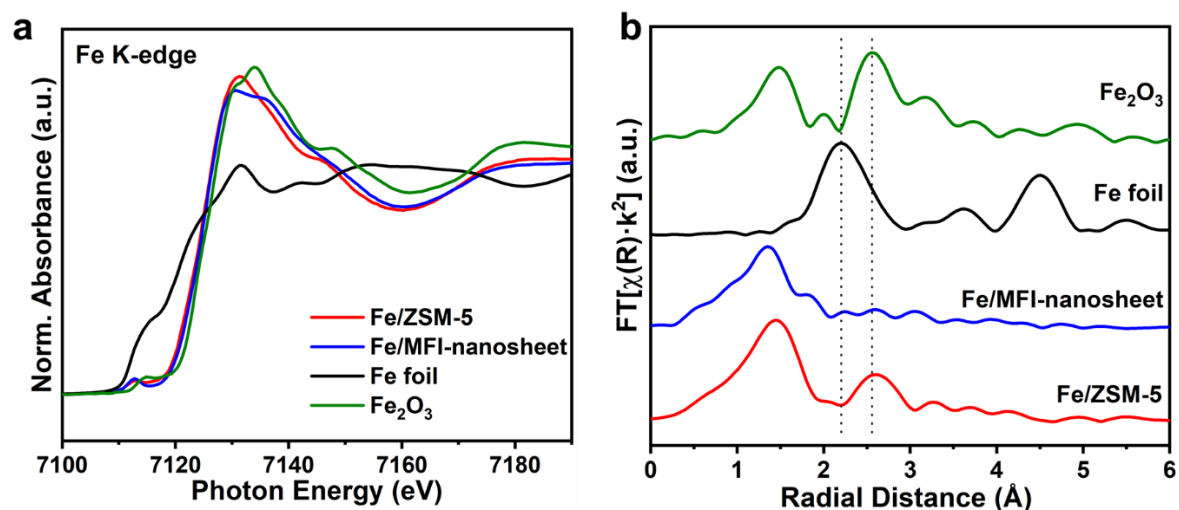


Figure 6-11. (a) Fe K-edge XANES spectra and (b) FT-EXAFS spectra of 0.288Fe/ZSM-5(50)-550, 0.664Fe/MFI-nanosheet(50)-550(direct), Fe foil and Fe₂O₃.

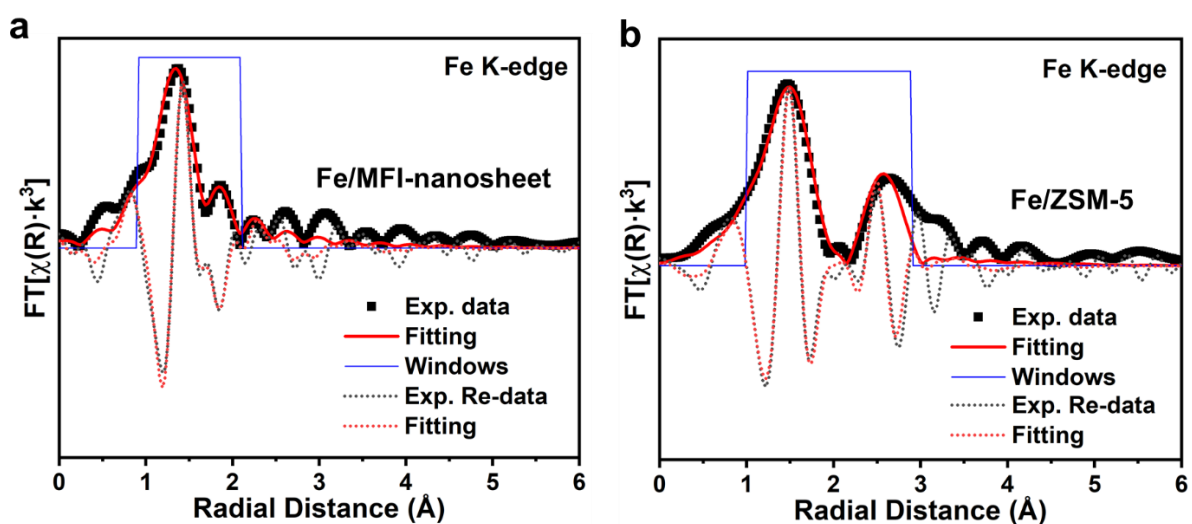


Figure 6-12. EXAFS fitting in R-space of (a) 0.664Fe/MFI-nanosheet(50)-550 and (b) 0.288Fe/ZSM-5(50)-550.

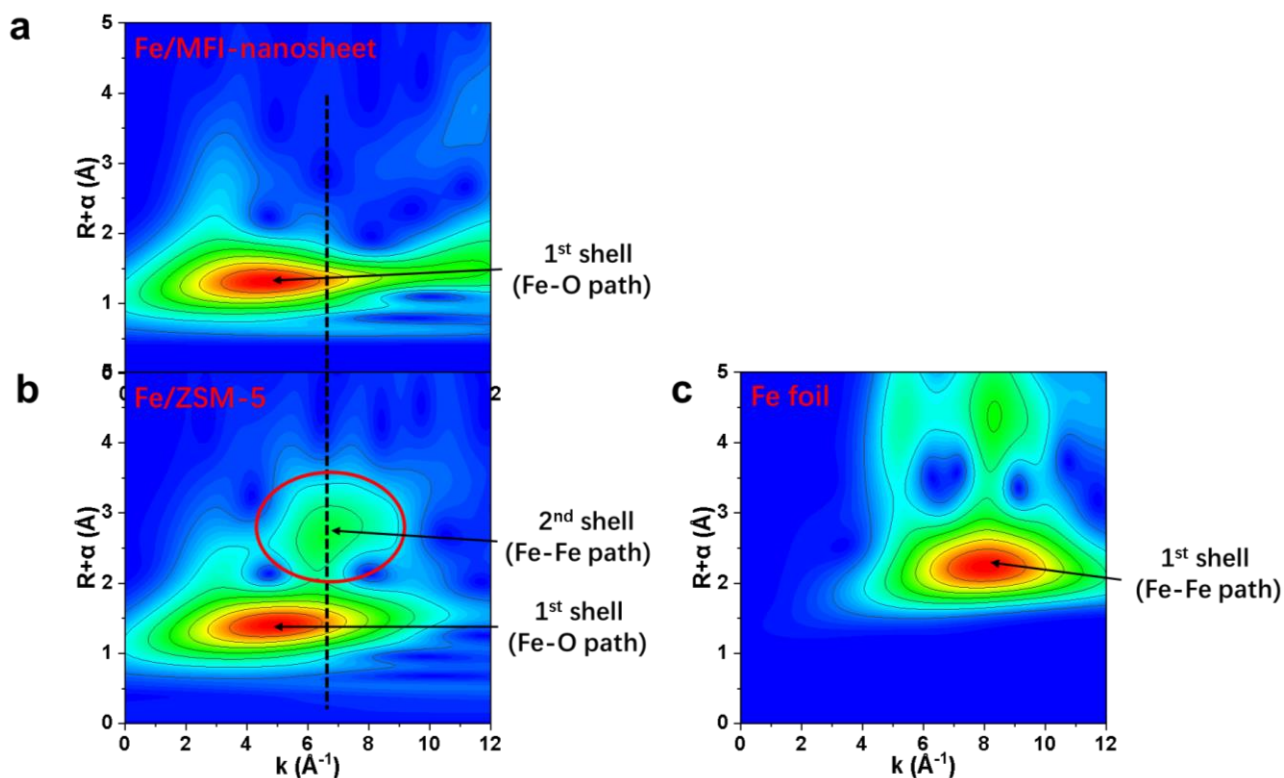


Figure 6-13. WT-EXAFS of (a) 0.664Fe/MFI-nanosheet(50)-550, (b) 0.288Fe/ZSM-5(50)-550 and (c) Fe foil.

6.5.2 UV-vis analysis

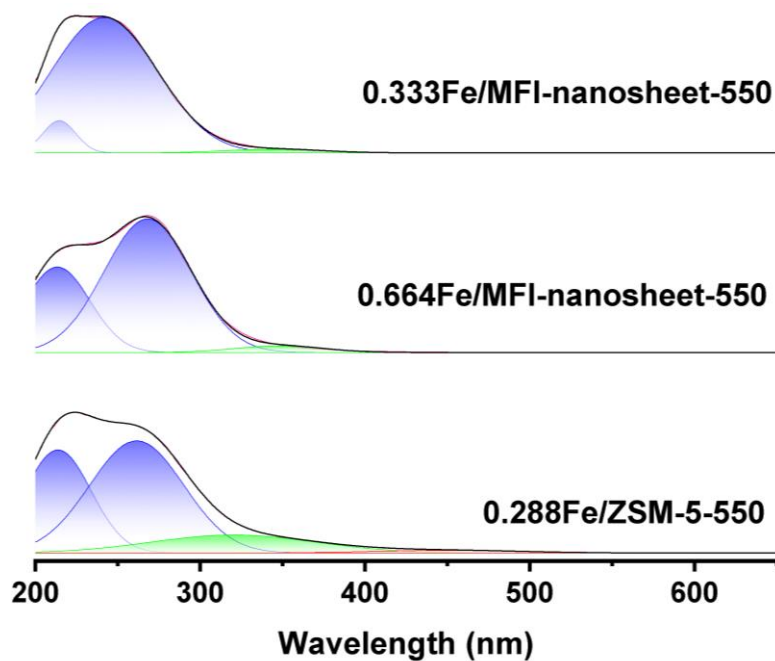


Figure 6-14. UV-vis DRS spectra of Fe/MFI catalysts.

Table 6-9. Deconvolution data of Fe/MFI catalysts.

Catalysts	Relative contribution of different range (%) ^a		
	I ₁ (200~300 nm)	I ₂ (300~400 nm)	I ₃ (>400 nm)
0.333Fe/MFI-nanosheet(50)-550(direct)	97.81	2.19	0
0.664Fe/MFI-nanosheet(50)-550(direct)	97.05	2.95	0
0.288Fe/ZSM-5(50)-550	91.20	7.66	1.14

^aObtained by using Origin software (GaussAmp Fit), $R^2 > 0.999$.

Spectroscopic studies were also conducted to distinguish the Fe species (see Figure 6-14 and Table 6-9). UV-vis DRS showed that 97.81% of the iron at 0.333 wt.% Fe content for the MFI nanosheet sample was present as mononuclear sites of different coordination. When further increasing the Fe content to 0.664 wt.%, there was no big difference in the Fe sites fraction and still no appearance of Fe₂O₃ particles, which is very difficult to achieve with 3D ZSM-5 sample. This proves that nanosheet structure can provide highly dispersed Fe sites even at high Fe loading. However, for 0.288Fe/ZSM-5(50)-550 sample aggregation can be observed due to a higher proportion of the oligomeric clusters and even the appearance of Fe₂O₃ nanoparticles. The different types of Fe active sites in MFI nanosheet and 3D ZSM-5 may cause different catalytic performances.

6.5.3 Solid state ²⁷Al-MAS-NMR spectroscopy

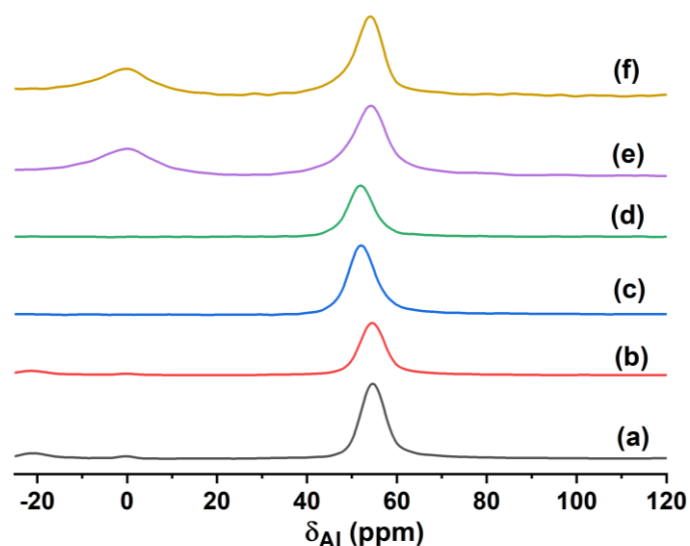


Figure 6-15. Solid state ²⁷Al-MAS-NMR spectra of (a) H-ZSM-5(50)-550; (b) 0.288Fe/ZSM-5(50)-550; (c) MFI-nanosheet(50) (20.05.12); (d) MFI-nanosheet(50) (20.08.12); (e) 0.333Fe/MFI-nanosheet(50)-550(direct); (f) 0.664Fe/MFI-nanosheet(50)-550(direct).

Solid state ^{27}Al -MAS-NMR spectroscopy (Figure 6-15) was applied to distinguish the framework aluminum (Al_F) from the extra-framework aluminum (Al_{EF}) with Al_F of tetra-coordination giving a resonance at about 55 ppm and Al_{EF} of hexa-coordination at 0 ppm [173]. A simple integration of the peak areas could be used to determine the relative ratio of the two species. In Figure 6-15, H-ZSM-5(50)-550 (a) and 0.288Fe/ZSM-5(50)-550 (b) almost exclusively exhibit tetracoordinated Al, and only a small amount of hexa-coordinated extra-framework aluminum. According to solid-state ^{27}Al NMR spectra of as-synthesized MFI-nanosheet(50) samples, almost all Al atoms in the zeolite samples were located inside the zeolite frameworks of different batches (c) and (d), which proved the success of the synthesis. However, the peak intensity of Al_{EF} for the calcined samples was significantly increased due to the $\text{Al}_{EF}/\text{Al}_F$ ratio of around 0.75 for both 0.333Fe/MFI-nanosheet(50)-550 (e) and 0.664Fe/MFI-nanosheet(50)-550 (f), which can be explained by the dealumination during the high-temperature calcination. The reduced framework thickness for MFI nanosheets with the higher external surface area was assumed to enhance the dealumination. According to the experimental findings reported by Triantafyllidis et al. [174], the Al_{EF} does not contribute to the acidity, which may be the reason for the decreasing activity of Fe modified MFI nanosheet sample.

6.5.4 Py-FTIR analysis

To characterize the acidic properties of zeolitic materials under study, pyridine adsorption combined with FTIR spectroscopy (Py-FTIR) was employed [175]. After pyridine adsorption on samples at 25 °C for 0.5h, absorption bands for degassed at 150 °C for 1 h were observed in the IR spectrum centered around 1447, 1490 and 1540 cm^{-1} (see Figure 6-16) [176,177]. The IR band centered around 1452–1447 cm^{-1} can be attributed to the interaction of pyridine with metal ions (Lewis (L) acid sites, such as Al^{3+}). The IR band centered around 1545–1540 cm^{-1} corresponds to the chemisorption of pyridine on Brønsted (B) acid sites. Therefore, a band located around 1490 cm^{-1} is assigned to pyridine adsorption on both adsorbed species. The amount of B acid sites and L acid sites was quantified using the following equations [178], and the results are presented in Table 6-10:

$$C_{(\text{Brønsted})} = \text{IMEC}_{(\text{Brønsted})}^{-1} \times \text{IA}_{(\text{Brønsted})} \times \frac{\pi R^2}{w} \quad (1)$$

$$C_{(\text{Lewis})} = \text{IMEC}_{(\text{Lewis})}^{-1} \times \text{IA}_{(\text{Lewis})} \times \frac{\pi R^2}{w} \quad (2)$$

where C is the concentration ($\mu\text{mol/g}$ catalyst) of acid sites; $\text{IMEC}(\text{B}, \text{L})$ are the integrated molar extinction coefficients ($\text{cm}/\mu\text{mol}$) ($\text{IMEC}(\text{B}) = 1.67\text{cm}/\mu\text{mol}$, $\text{IMEC}(\text{L}) = 2.22\text{cm}/\mu\text{mol}$); $\text{IA}(\text{B}, \text{L})$

are the integrated absorbances (cm^{-1}); πR^2 is the area of catalyst disk (cm^2) and W is the weight of disk (mg).

As shown by entry 4 and 5 in Table 6-10, there is no difference for B and L acid sites densities of ZSM-5(50)-550 and 0.288Fe/ZSM-5(50)-550. Compared with 3D zeolites, 2D MFI nanosheets (entry 1 to 3) with similar Si/Al molar ratios obviously have more L acid sites and fewer B acid sites, due to the observed dealumination. As known, B acid sites play an essential role in the activity for H₂O₂-mediated methane oxidation reaction. Therefore, we assume that the high-temperature calcination caused the dealumination from Al_F to Al_{EF}, which transformed the B acid sites into L acid sites undermining the activity of Fe/MFI-nanosheet(50)-550 catalysts. In order to verify this hypothesis, we prepared 0.136Fe/ZSM-5(95)-550 catalyst with higher a Si/Al ratio of 95 to keep the B acid sites density same as the Fe/MFI-nanosheet(50)-550 samples (see entry 6 in Table 10). Table 6-11 shows that 0.136Fe/ZSM-5(95)-550 catalyst prepared by the same method as 0.288Fe/ZSM-5(50)-550 exhibited very low activity, which proved the influence of the B acid sites. However, its activity is even much less than 0.333Fe/MFI-nanosheet(50)-550, which has a similar B acid sites density. Thus, we assume that Fe/MFI-nanosheet(50)-550 catalysts host different Fe sites as 3D ZSM-5 zeolite that depends less on B acid sites when conducting the reaction.

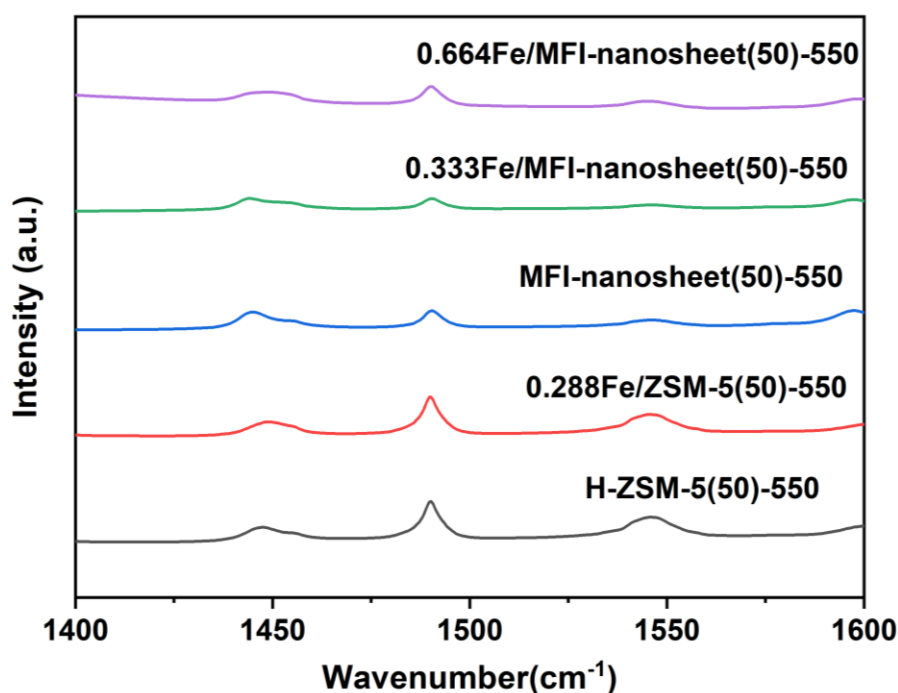


Figure 6-16. Py-FTIR spectra of various catalysts degassed at 150 °C for 1 h.

Table 6-10. Acidic properties of the MFI zeolite materials.^a

Entry	Sample name	Density (mg/cm ²)	IA(B)	IA(L)	B density (umol/g)	L density (umol/g)
1	MFI-nanosheet(50)-550	28.23	3.371	8.393	0.199	0.660
2	0.333Fe/MFI-nanosheet(50)-550	16.92	1.854	6.736	0.183	0.884
3	0.664Fe/MFI-nanosheet(50)-550	18.83	3.423	5.705	0.304	0.673
4	H-ZSM-5(50)-550	38.48	11.61	6.543	0.504	0.377
5	0.288Fe/ZSM-5(50)-550	37.52	10.43	6.473	0.464	0.383
6	H-ZSM-5(90)-550	29.42	3.842	1.769	0.218	0.133

^aLewis acid and Brønsted acid sites were calculated according to the 1447 and 1540 cm⁻¹ peak areas, respectively, of pyridine adsorption at 150 °C.

Table 6-11. Catalytic activity of Fe/ZSM-5(95)-550 catalyst.

No.	Cat.	Preparation Condition	Product yield(μmol)/Selectivity(%)					H ₂ O ₂		TOF /h ⁻¹
			MeOH	OHCH ₂ OOH	MeOOH	HCOOH	CO ₂	Conv. (%)	Util. (%)	
1	0.136Fe/ZSM-5(95)-550	mIE, 85 °C, 24 h 0.5 wt.%, Fe(NO ₃) ₃	2.9 9.3%	6.8 21.8%	11.0 35.4%	7.7 24.7%	2.8 8.8%	1.8	56.3	117
2	H-ZSM-5(95)-550	-	1.4 8.5%	6.8 39.8	7.6 4.5%	1.2 7.2%	0	1.7	30.3	561

Reaction condition: 30 bar of CH₄, 10 mL of 0.5 M H₂O₂, 600 rpm, 50 °C, 0.5 h, 20 mg of catalyst.

6.6 Summary

Since MFI zeolite was reported to be able to host binuclear Fe to exhibit unique activity on direct methane oxidation in H₂O₂, such distinctive performance has only been found in MFI structure. Most follow-up studies concentrated on optimizing synthesis and adjusting reaction parameters. Recently, mononuclear Fe species was also reported as the active site in Fe/ZSM-5 zeolites by correlating a wide variety of characterization results with catalytic performance data. The special topology and microporous structure of MFI that can confine atomically dispersed Fe, also suffered the diffusion problem to limit the Fe loading. We planned to shift from the 3D MFI to a hierarchical 2D structure, aiming to increase the amount of Fe active sites and boost mass transfer to improve oxygenates further productivity of Fe/MFI catalyst. 2D MFI nanosheet was synthesized successfully and characterized by low-angle XRD and physical adsorption to prove the presence of both mesoporous and microporous structures. The Fe was loaded onto 2D MFI with high loading of 0.664 wt.% and still maintained highly dispersed Fe sites without obvious aggregation. Both the UV-vis DRS and XAS analysis confirmed that the Fe sites in 0.664Fe/MFI-nanosheet(50)-550(direct) existed in the form of mononuclear Fe sites. However, 2D MFI nanosheet as support was found less active than its 3D counterpart, which goes against our original idea. Therefore, we proposed that 2D MFI nanosheet is not conducive to forming more active

binuclear sites. What's more, the dealumination occurred on calcined MFI-nanosheet sample, caused a decrease of Brønsted (B) acid sites and undermined activity. Therefore, we concluded that mononuclear Fe is also the active site in Fe/MFI catalyst based on the research in our work.

7. Conclusion

Direct methane oxidation remains a significant challenge because of the large energy barrier for activating the C-H bond and the inevitable over-oxidation of the products to CO₂. Atomically dispersed metal sites, especially iron and copper, are favored for promoting methane oxidation. Anchoring Fe in confined space is an effective strategy to restrict the migration and aggregation to get undesired Fe-oxo aggregates. Thus, zeolites and MOF materials with microporous structures, large specific surfaces and high exposure to active sites have been widely used as supports. Selective oxidation of methane to C1 oxygenates using H₂O₂ as oxidant over Fe-containing zeolites (MOR, MFI) and MOFs in an autoclave reactor was studied in the presented work. Without methanol protection, the Fe-H₂O₂ mediated system mainly leads to HCOOH as products.

Fe/MFI catalyst has been proved to show good catalytic performance to get HCOOH. However, MFI zeolite can only host a limited number of active Fe sites, generally lower than 0.5 wt.%. Such a low Fe loading of MFI already causes the formation of considerable Fe-oxo aggregates, which mainly promote the undesired side-reactions, total oxidation and H₂O₂ decomposition, and restrict the enhancement of the overall activity. Based on their well-defined structure and much higher porosity, MOF materials have been demonstrated to achieve highly dispersed metal sites with around 1-3 wt.% loading. However, the activities are still inferior to that of zeolite catalysts. In addition, the stability of MOF catalysts needs to be carefully verified. We provided concrete examples to show MOFs catalyst design and catalytic performance.

Besides MOF materials, two zeolite catalysts, Fe/MFI-nanosheet and Fe/MOR, were thoroughly investigated regarding their catalytic performance and the active Fe sites. The modified liquid ion-exchange method was found to better control Fe loading of MOR with Fe(acac)₃ as the precursor and CH₃CN as the solvent to get around 0.30 wt.% Fe content, which showed an excellent TOF of 555 h⁻¹. The UV-vis DRS and XAS analysis confirmed that the Fe sites in 0.35Fe/MOR existed in the form of mononuclear Fe sites, which contributed to the activity. However, compared with the classic Fe/MFI catalyst that can exhibit good activity at 50 °C, it requires 80 °C to activate H₂O₂ on Fe/MOR. Zeolite topology is believed to be decisive for the activity, which may provide the appropriate geometric constraint around Fe to maintain ultras-small Fe-oxo clusters as active sites. However, a deep understanding of the relation between the zeolite topology and the formation of active Fe sites is still lacking.

Both mono and binuclear Fe have been reported as the active Fe sites in Fe/MFI. However, how to selectively increase the number of active Fe sites is still unsolved. The special topology of MFI can not only confine atomically dispersed Fe, but can also cause diffusion problems and can limit

the number of accessible active Fe sites. Hierarchical 2D MFI nanosheets were successfully synthesized, which achieved a high loading of 0.664 wt.% with highly dispersed Fe sites without obvious aggregation. Both UV-vis DRS and XAS analyses confirmed that the mononuclear Fe sites are active in MFI nanosheets. However, 2D MFI nanosheet as support was found less active than its 3D counterpart, which could be due to the fact that dealumination occurred on calcined MFI-nanosheet sample, causing a decrease of Brønsted sites. Another explanation could be that mononuclear Fe is less active than binuclear Fe in MFI.

Based on the results and experience of the current study, some prospects for future work are recommended:

1. How to controllably obtain active sites, such as mono-, bi-, or tri-nuclear Fe sites, in zeolite is the key to follow-up work;
2. Exploring an effective way to increase the number of active sites in zeolite to improve the apparent activity is critical.
3. In situ characterizations, such as time-of-flight mass spectrometry and isotope labeling experiments, are necessary to track the evolution of liquid products and study the reaction mechanism.
4. Density functional theory (DFT) calculations are required to study the process of methane activation on mononuclear Fe in MOR and MFI nanosheets.

8. Reference

- [1] <http://naturalgas.org/overview/background/>
- [2] <https://www.statista.com/statistics/265329/countries-with-the-largest-natural-gas-reserves/>
- [3] Caballero, A., & Perez, P. J. (2013). Methane as raw material in synthetic chemistry: The final frontier. *Chemical Society Reviews*, 42(23), 8809-8820.
- [4] Taifan, W., & Baltrusaitis, J. (2016). CH₄ conversion to value added products: Potential, limitations and extensions of a single step heterogeneous catalysis. *Applied Catalysis B: Environmental*, 198, 525-547.
- [5] Haynes, C. A., & Gonzalez, R. (2014). Rethinking biological activation of methane and conversion to liquid fuels. *Nature chemical biology*, 10(5), 331-339.
- [6] <https://www.ipcc.ch/site/assets/uploads/2018/02/ar4-wg1-chapter2-1.pdf>
- [7] U.S. Environmental Protection Agency. Summary Report: Global Anthropogenic Non-CO₂ Greenhouse Gases Emissions: 1990–2030 (U.S. Environmental Protection Agency, Washington, DC, 2012).
- [8] Sun, L., Wang, Y., Guan, N., & Li, L. (2020). Methane activation and utilization: Current status and future challenges. *Energy Technology*, 8(8), 1900826.
- [9] (a) Waters, T., O'Hair, R. A., & Wedd, A. G. (2003). Catalytic gas phase oxidation of methanol to formaldehyde. *J. Am. Chem. Soc.*, 125(11), 3384-3396. (b) Sun, C., Du, J., Liu, J., Yang, Y., Ren, N., Shen, W., ... & Tang, Y. (2010). A facile route to synthesize durable mesopore containing ZSM-5 catalyst for methanol to propylene reaction. *Chemical communications*, 46(15), 2671-2673.
- [10] Arndtsen, B. A., Bergman, R. G., Mobley, T. A., & Peterson, T. H. (1995). Selective intermolecular carbon-hydrogen bond activation by synthetic metal complexes in homogeneous solution. *Accounts of chemical research*, 28(3), 154-162.
- [11] Ravi, M., Ranocchiari, M., & van Bokhoven, J. A. (2017). The direct catalytic oxidation of methane to methanol—A critical assessment. *Angew. Chem., Int. Ed.*, 56(52), 16464-16483.
- [12] Gol'Dshleger, N. F., Es' Kova, V. V., Shilov, A. E., & Shteinman, A. A. (1972). Reactions of alkanes in solutions of platinum chloride complexes. *Zhurnal Fizicheskoi Khimi*, 46, 1353-1354.
- [13] Periana, R. A., Taube, D. J., Gamble, S., Taube, H., Satoh, T., & Fujii, H. (1998). Platinum catalysts for the high-yield oxidation of methane to a methanol derivative. *Science*, 280(5363), 560-564.
- [14] Díaz-Urrutia, C., & Ott, T. (2019). Activation of methane: A selective industrial route to methanesulfonic acid. *Science*, 363(6433), 1326-1329.
- [15] Rosenzweig, A. C., Frederick, C. A., & Lippard, S. J. (1993). Crystal structure of a bacterial non-haem iron hydroxylase that catalyses the biological oxidation of methane. *Nature*, 366(6455), 537-543.
- [16] (a) Tinberg, C. E., & Lippard, S. J. (2011). Dioxygen activation in soluble methane monooxygenase. *Accounts of chemical research*, 44(4), 280-288. (b) Koo, C. W., & Rosenzweig, A. C. (2021). Biochemistry of aerobic biological methane oxidation. *Chemical Society Reviews*, 50(5), 3424-3436.
- [17] Lieberman, R. L., & Rosenzweig, A. C. (2005). Crystal structure of a membrane-bound metalloenzyme that catalyses the biological oxidation of methane. *Nature*, 434(7030), 177-182.
- [18] Shiota, Y., Juhász, G., & Yoshizawa, K. (2013). Role of tyrosine residue in methane activation at the dicopper site of particulate methane monooxygenase: a density functional theory study. *Inorganic chemistry*, 52(14), 7907-7917.
- [19] Ross, M. O., MacMillan, F., Wang, J., Nisthal, A., Lawton, T. J., Olafson, B. D., ... & Hoffman, B. M. (2019). Particulate methane monooxygenase contains only mononuclear copper centers. *Science*, 364(6440), 566-570.

- [20] Ro, S. Y., Schachner, L. F., Koo, C. W., Purohit, R., Remis, J. P., Kenney, G. E., ... & Rosenzweig, A. C. (2019). Native top-down mass spectrometry provides insights into the copper centers of membrane-bound methane monooxygenase. *Nature communications*, 10(1), 1-12.
- [21] (a) Banerjee, R., Proshlyakov, Y., Lipscomb, J. D., & Proshlyakov, D. A. (2015). Structure of the key species in the enzymatic oxidation of methane to methanol. *Nature*, 518(7539), 431-434. (b) Wang, W., Liang, A. D., & Lippard, S. J. (2015). Coupling oxygen consumption with hydrocarbon oxidation in bacterial multicomponent monooxygenases. *Accounts of chemical research*, 48(9), 2632-2639.
- [22] Wang, V. C. C., Maji, S., Chen, P. P. Y., Lee, H. K., Yu, S. S. F., & Chan, S. I. (2017). Alkane oxidation: methane monooxygenases, related enzymes, and their biomimetics. *Chemical reviews*, 117(13), 8574-8621.
- [23] Panov, G. I., Sobolev, V. I., & Kharitonov, A. S. (1990). The role of iron in N₂O decomposition on ZSM-5 zeolite and reactivity of the surface oxygen formed. *Journal of molecular catalysis*, 61(1), 85-97.
- [24] Starokon, E. V., Dubkov, K. A., Pirutko, L. V., & Panov, G. I. (2003). Mechanisms of iron activation on Fe-containing zeolites and the charge of α -oxygen. *Topics in catalysis*, 23(1), 137-143.
- [25] Snyder, B. E., Vanelderen, P., Bols, M. L., Hallaert, S. D., Böttger, L. H., Ungur, L., ... & Solomon, E. I. (2016). The active site of low-temperature methane hydroxylation in iron-containing zeolites. *Nature*, 536(7616), 317-321.
- [26] Bols, M. L., Hallaert, S. D., Snyder, B. E., Devos, J., Plessers, D., Rhoda, H. M., ... & Sels, B. F. (2018). Spectroscopic identification of the α -Fe/ α -O active site in Fe-CHA zeolite for the low-temperature activation of the methane C-H bond. *J. Am. Chem. Soc.*, 140(38), 12021-12032.
- [27] (a) Xu, R., Liu, N., Dai, C., Li, Y., Zhang, J., Wu, B., ... & Chen, B. (2021). H₂O-Built Proton Transfer Bridge Enhances Continuous Methane Oxidation to Methanol over Cu-BEA Zeolite. *Angew. Chem. Int. Ed.* 2021, 60, 16634-16640. (b) Memioglu, O., & Ipek, B. (2021). A potential catalyst for continuous methane partial oxidation to methanol using N₂O: Cu-SSZ-39. *Chemical Communications*, 57(11), 1364-1367.
- [28] (a) Starokon, E. V., Parfenov, M. V., Pirutko, L. V., Abornev, S. I., & Panov, G. I. (2011). Room-temperature oxidation of methane by α -oxygen and extraction of products from the FeZSM-5 surface. *The Journal of Physical Chemistry C*, 115(5), 2155-2161. (b) Shi, Y., Liu, S., Liu, Y., Huang, W., Guan, G., & Zuo, Z. (2020). Quasicatalytic and catalytic selective oxidation of methane to methanol over solid materials: a review on the roles of water. *Catalysis Reviews*, 62(3), 313-345.
- [29] Groothaert, M. H., Smeets, P. J., Sels, B. F., Jacobs, P. A., & Schoonheydt, R. A. (2005). Selective oxidation of methane by the bis (μ -oxo) dicopper core stabilized on ZSM-5 and mordenite zeolites. *J. Am. Chem. Soc.*, 127(5), 1394-1395.
- [30] (a) Tomkins, P., Ranocchiari, M., & van Bokhoven, J. A. (2017). Direct conversion of methane to methanol under mild conditions over Cu-zeolites and beyond. *Accounts of chemical research*, 50(2), 418-425. (b) Freakley, S. J., Dimitratos, N., Willock, D. J., Taylor, S. H., Kiely, C. J., & Hutchings, G. J. (2021). Methane Oxidation to Methanol in Water. *Accounts of Chemical Research*, 5129-5133.
- [31] Newton, M. A., Knorpp, A. J., Sushkevich, V. L., Palagin, D., & van Bokhoven, J. A. (2020). Active sites and mechanisms in the direct conversion of methane to methanol using Cu in zeolitic hosts: a critical examination. *Chemical Society Reviews*, 49(5), 1449-1486.
- [32] Sun, L., Wang, Y., Wang, C., Xie, Z., Guan, N., & Li, L. (2021). Water-involved methane-selective catalytic oxidation by dioxygen over copper zeolites. *Chem* 7, 1557-1568.
- [33] Narsimhan, K., Iyoki, K., Dinh, K., & Román-Leshkov, Y. (2016). Catalytic oxidation of methane into methanol over copper-exchanged zeolites with oxygen at low temperature. *ACS central science*, 2(6), 424-429.

- [34] Narsimhan, K., Mansouri, A., Bozbag, S. E., Krumeich, F., Park, M. B., Alayon, E. M. C., ... & van Bokhoven, J. A. (2016). Isothermal Cyclic Conversion of Methane into Methanol over Copper-Exchanged Zeolite at Low Temperature. *Angew. Chem. Int. Ed.*, 55, 5467-5471.
- [35] Yang, J., Du, X., & Qiao, B. (2021). Methane oxidation to methanol over copper-containing zeolite. *Chem*, 7(9), 2270-2272.
- [36] Wood, B. R., Reimer, J. A., Bell, A. T., Janicke, M. T., & Ott, K. C. (2004). Methanol formation on Fe/Al-MFI via the oxidation of methane by nitrous oxide. *Journal of Catalysis*, 225(2), 300-306.
- [37] Chow, Y. K., Dummer, N., Carter, J., Meyer, R., Armstrong, R., Williams, C., ... & Hutchings, G. J. (2018). A kinetic study of methane partial oxidation over Fe-ZSM-5 using N₂O as an oxidant. *ChemPhysChem*, 19(4), 402-411.
- [38] Liu, Z., Huang, E., Orozco, I., Liao, W., Palomino, R. M., Rui, N., ... & Senanayake, S. D. (2020). Water-promoted interfacial pathways in methane oxidation to methanol on a CeO₂-Cu₂O catalyst. *Science*, 368(6490), 513-517.
- [39] Sushkevich, V. L., Palagin, D., Ranocchiari, M., & van Bokhoven, J. A. (2017). Selective anaerobic oxidation of methane enables direct synthesis of methanol. *Science*, 356(6337), 523-527.
- [40] Koishybay, A., & Shantz, D. F. (2020). Water is the oxygen source for methanol produced in partial oxidation of methane in a flow reactor over Cu-SSZ-13. *J. Am. Chem. Soc.*, 142(28), 11962-11966.
- [41] Edwards, J. K., Solsona, B. E., Landon, P., Carley, A. F., Herzing, A., Kiely, C. J., & Hutchings, G. J. (2005). Direct synthesis of hydrogen peroxide from H₂ and O₂ using TiO₂-supported Au-Pd catalysts. *Journal of Catalysis*, 236(1), 69-79.
- [42] Ab Rahim, M. H., Forde, M. M., Jenkins, R. L., Hammond, C., He, Q., Dimitratos, N., ... & Hutchings, G. J. (2013). Oxidation of methane to methanol with hydrogen peroxide using supported gold-palladium alloy nanoparticles. *Angew. Chem., Int. Ed.*, 52(4), 1280-1284.
- [43] Agarwal, N., Freakley, S. J., McVicker, R. U., Althabban, S. M., Dimitratos, N., He, Q., ... & Hutchings, G. J. (2017). Aqueous Au-Pd colloids catalyze selective CH₄ oxidation to CH₃OH with O₂ under mild conditions. *Science*, 358(6360), 223-227.
- [44] Jin, Z., Wang, L., Zuidema, E., Mondal, K., Zhang, M., Zhang, J., ... & Xiao, F. S. (2020). Hydrophobic zeolite modification for in situ peroxide formation in methane oxidation to methanol. *Science*, 367(6474), 193-197.
- [45] Yang, X. F., Wang, A., Qiao, B., Li, J., Liu, J., & Zhang, T. (2013). Single-atom catalysts: a new frontier in heterogeneous catalysis. *Accounts of chemical research*, 46(8), 1740-1748.
- [46] Wang, A., Li, J., & Zhang, T. (2018). Heterogeneous single-atom catalysis. *Nature Reviews Chemistry*, 2(6), 65-81.
- [47] Kokalj, A., Bonini, N., Sbraccia, C., de Gironcoli, S., & Baroni, S. (2004). Engineering the reactivity of metal catalysts: a model study of methane dehydrogenation on Rh (111). *J. Am. Chem. Soc.*, 126(51), 16732-16733.
- [48] Kwon, Y., Kim, T. Y., Kwon, G., Yi, J., & Lee, H. (2017). Selective activation of methane on single-atom catalyst of rhodium dispersed on zirconia for direct conversion. *J. Am. Chem. Soc.*, 139(48), 17694-17699.
- [49] Huang, W., Zhang, S., Tang, Y., Li, Y., Nguyen, L., Li, Y., ... & Tao, F. (2016). Low-temperature transformation of methane to methanol on Pd₁O₄ single sites anchored on the internal surface of microporous silicate. *Angew. Chem. Int. Ed.*, 55, 13441-13445.
- [50] Bai, S., Liu, F., Huang, B., Li, F., Lin, H., Wu, T., ... & Huang, X. (2020). High-efficiency direct methane conversion to oxygenates on cerium dioxide nanowires supported rhodium single-atom catalyst. *Nature communications*, 11(1), 1-9. <https://doi.org/10.1038/s41467-020-14742-x>
- [51] Xie, J., Jin, R., Li, A., Bi, Y., Ruan, Q., Deng, Y., ... & Tang, J. (2018). Highly selective oxidation of methane to methanol at ambient conditions by titanium dioxide-supported iron species. *Nature Catalysis*, 1(11), 889-896.

- [52] Cui, X., Li, H., Wang, Y., Hu, Y., Hua, L., Li, H., ... & Bao, X. (2018). Room-temperature methane conversion by graphene-confined single iron atoms. *Chem*, 4(8), 1902-1910.
- [53] Zhou, H., Liu, T., Zhao, X., Zhao, Y., Lv, H., Fang, S., ... & Wu, Y. (2019). A supported nickel catalyst stabilized by a surface digging effect for efficient methane oxidation. *Angew. Chem. Int. Ed.*, 58(51), 18388-18393.
- [54] Wu, B., Yang, R., Shi, L., Lin, T., Yu, X., Huang, M., ... & Sun, Y. (2020). Cu single-atoms embedded in porous carbon nitride for selective oxidation of methane to oxygenates. *Chemical Communications*, 56(93), 14677-14680.
- [55] Shen, Q., Cao, C., Huang, R., Zhu, L., Zhou, X., Zhang, Q., ... & Song, W. (2020). Single chromium atoms supported on titanium dioxide nanoparticles for synergic catalytic methane conversion under mild conditions. *Angew. Chem. Int. Ed.*, 59(3), 1216-1219.
- [56] Hammond, C., Dimitratos, N., Lopez-Sanchez, J. A., Jenkins, R. L., Whiting, G., Kondrat, S. A., ... & Hutchings, G. J. (2013). Aqueous-phase methane oxidation over Fe-MFI zeolites; promotion through isomorphous framework substitution. *ACS Catalysis*, 3(8), 1835-1844.
- [57] Qin, R., Liu, P., Fu, G., & Zheng, N. (2018). Strategies for stabilizing atomically dispersed metal catalysts. *Small Methods*, 2(1), 1700286.
- [58] Cui, W. G., & Hu, T. L. (2021). Incorporation of active metal species in crystalline porous materials for highly efficient synergetic catalysis. *Small*, 17(22), 2003971.
- [59] C. Baerlocher and L. B. McCusker, Database of Zeolite Structures, <http://www.iza-structure.org/databases/>.
- [60] Li, Y., & Yu, J. (2021). Emerging applications of zeolites in catalysis, separation and host-guest assembly. *Nature Reviews Materials*, 6(12), 1156-1174.
- [61] Hunger, M. (2010). Catalytically active sites: generation and characterization. *Zeolites and catalysis: synthesis, reactions and applications*, 2, 493-546.
- [62] Kosinov, N., Liu, C., Hensen, E. J., & Pidko, E. A. (2018). Engineering of transition metal catalysts confined in zeolites. *Chemistry of Materials*, 30(10), 3177-3198.
- [63] Rahman, A. K. M. L., Kumashiro, M., & Ishihara, T. (2011). Direct synthesis of formic acid by partial oxidation of methane on H-ZSM-5 solid acid catalyst. *Catalysis Communications*, 12(13), 1198-1200.
- [64] Hammond, C., Forde, M. M., Ab Rahim, M. H., Thetford, A., He, Q., Jenkins, R. L., ... & Hutchings, G. J. (2012). Direct catalytic conversion of methane to methanol in an aqueous medium by using copper-promoted Fe-ZSM-5. *Angew. Chem., Int. Ed.*, 2012, 51, 5129-5133
- [65] Hammond, C., Dimitratos, N., Jenkins, R. L., Lopez-Sanchez, J. A., Kondrat, S. A., Hasbi ab Rahim, M., ... & Hutchings, G. J. (2013). Elucidation and evolution of the active component within Cu/Fe/ZSM-5 for catalytic methane oxidation: from synthesis to catalysis. *ACS Catalysis*, 3(4), 689-699.
- [66] Shahami, M., & Shantz, D. F. (2019). Zeolite acidity strongly influences hydrogen peroxide activation and oxygenate selectivity in the partial oxidation of methane over M, Fe-MFI (M: Ga, Al, B) zeolites. *Catalysis Science & Technology*, 9(11), 2945-2951.
- [67] Yu, T., Li, Z., Jones, W., Liu, Y., He, Q., Song, W., ... & Luo, W. (2021). Identifying key mononuclear Fe species for low-temperature methane oxidation. *Chemical Science*, 12(9), 3152-3160.
- [68] Yu, T., Li, Z., Lin, L., Chu, S., Su, Y., Song, W., ... & Luo, W. (2021). Highly Selective Oxidation of Methane into Methanol over Cu-Promoted Monomeric Fe/ZSM-5. *ACS Catalysis*, 11, 6684-6691.
- [69] Yu, T., Su, Y., Wang, A., Weckhuysen, B. M., & Luo, W. (2021). Efficient Synthesis of Monomeric Fe Species in Zeolite ZSM-5 for the Low-Temperature Oxidation of Methane. *ChemCatChem*, 13(12), 2766-2770.
- [70] D. Tito-Ferro, I. Rodríguez-Iznaga, B. Concepción-Rosabal, G. Berlier, F. Chávez-Rivas, A. Penton-Madriral, F. F. CastellónBarraza and V. Petranovskii. (2016) Iron exchanged natural

- mordenite: UV-Vis diffuse reflectance and Mössbauer spectroscopy characterisation. *International Journal of Nanotechnology*, 13(1-3), 112-125.
- [71] Grundner, S.; Markovits, M. A.; Li, G.; Tromp, M.; Pidko, E. A.; Hensen, E. J.; Jentys, A.; Sanchez-Sanchez, M.; Lercher, J. A. (2015) Single-site trinuclear copper oxygen clusters in mordenite for selective conversion of methane to methanol. *Nature Communications*, 6, 7546–7554.
- [72] Fang, Z., Murayama, H., Zhao, Q., Liu, B., Jiang, F., Xu, Y., ... & Liu, X. (2019). Selective mild oxidation of methane to methanol or formic acid on Fe–MOR catalysts. *Catalysis Science & Technology*, 9(24), 6946-6956.
- [73] Yaghi, O. M., & Li, H. (1995). Hydrothermal synthesis of a metal-organic framework containing large rectangular channels. *J. Am. Chem. Soc.*, 117(41), 10401-10402.
- [74] Yaghi, O. M., Li, G., & Li, H. (1995). Selective binding and removal of guests in a microporous metal–organic framework. *Nature*, 378(6558), 703-706.
- [75] Furukawa, H., Cordova, K. E., O’Keeffe, M., & Yaghi, O. M. (2013). The chemistry and applications of metal-organic frameworks. *Science*, 341(6149), 1230444.
- [76] Kitagawa, S. (2014). Metal–organic frameworks (MOFs). *Chemical Society Reviews*, 43(16), 5415-5418.
- [77] Yaghi, O. M., Kalmutzki, M. J., & Diercks, C. S. (2019). Introduction to reticular chemistry: metal-organic frameworks and covalent organic frameworks. John Wiley & Sons.
- [78] Freund, R., Canossa, S., Cohen, S. M., Yan, W., Deng, H., Guillerm, V., ... & Diercks, C. S. (2021). 25 years of Reticular Chemistry. *Angew. Chem., Int. Ed.*, 60(45), 23946-23974.
- [79] Li, B., Wen, H. M., Cui, Y., Zhou, W., Qian, G., & Chen, B. (2016). Emerging multifunctional metal–organic framework materials. *Advanced Materials*, 28(40), 8819-8860.
- [80] Li, H., Li, L., Lin, R. B., Zhou, W., Zhang, Z., Xiang, S., & Chen, B. (2019). Porous metal-organic frameworks for gas storage and separation: Status and challenges. *EnergyChem*, 1(1), 100006.
- [81] Jiao, L., Wang, Y., Jiang, H. L., & Xu, Q. (2018). Metal–organic frameworks as platforms for catalytic applications. *Advanced Materials*, 30(37), 1703663.
- [82] Huang, Y., Ren, J., & Qu, X. (2019). Nanozymes: classification, catalytic mechanisms, activity regulation, and applications. *Chemical reviews*, 119(6), 4357-4412.
- [83] Zhao, M., Wang, H. B., Ji, L. N., & Mao, Z. W. (2013). Insights into metalloenzyme microenvironments: biomimetic metal complexes with a functional second coordination sphere. *Chemical Society Reviews*, 42(21), 8360-8375.
- [84] Jiao, L., Wang, J., & Jiang, H. L. (2021). Microenvironment modulation in metal–organic framework-based catalysis. *Accounts of Materials Research*, 2(5), 327-339.
- [85] Yuan, S., Feng, L., Wang, K., Pang, J., Bosch, M., Lollar, C., ... & Zhou, H. C. (2018). Stable metal–organic frameworks: design, synthesis, and applications. *Advanced Materials*, 30(37), 1704303.
- [86] Van Vleet, M. J., Weng, T., Li, X., & Schmidt, J. R. (2018). In situ, time-resolved, and mechanistic studies of metal–organic framework nucleation and growth. *Chemical reviews*, 118(7), 3681-3721.
- [87] Hönicke, I. M., Senkovska, I., Bon, V., Baburin, I. A., Bönisch, N., Raschke, S., ... & Kaskel, S. (2018). Balancing mechanical stability and ultrahigh porosity in crystalline framework materials. *Angew. Chem., Int. Ed.*, 57(42), 13780-13783.
- [88] Kim, M., Cahill, J. F., Fei, H., Prather, K. A., & Cohen, S. M. (2012). Postsynthetic ligand and cation exchange in robust metal–organic frameworks. *J. Am. Chem. Soc.*, 134(43), 18082-18088.
- [89] Tanabe, K. K., & Cohen, S. M. (2011). Postsynthetic modification of metal–organic frameworks—a progress report. *Chemical Society Reviews*, 40(2), 498-519.

- [90] Islamoglu, T., Goswami, S., Li, Z., Howarth, A. J., Farha, O. K., & Hupp, J. T. (2017). Postsynthetic tuning of metal–organic frameworks for targeted applications. *Accounts of chemical research*, 50(4), 805-813.
- [91] Yang, Q., Xu, Q., & Jiang, H. L. (2017). Metal–organic frameworks meet metal nanoparticles: synergistic effect for enhanced catalysis. *Chemical Society Reviews*, 46(15), 4774-4808.
- [92] Osadchii, D. Y., Olivos-Suarez, A. I., Szécsényi, Á., Li, G., Nasalevich, M. A., Dugulan, I. A., ... & Gascon, J. (2018). Isolated Fe sites in metal organic frameworks catalyze the direct conversion of methane to methanol. *ACS Catalysis*, 8(6), 5542-5548.
- [93] Loiseau, T., Serre, C., Huguenard, C., Fink, G., Taulelle, F., Henry, M., ... & Férey, G. (2004). A rationale for the large breathing of the porous aluminum terephthalate (MIL-53) upon hydration. *Chemistry-A European Journal*, 10(6), 1373-1382.
- [94] Kazaryan, A., & Baerends, E. J. (2015). Ligand field effects and the high spin–high reactivity correlation in the H abstraction by non-heme iron (IV)–oxo complexes: A DFT frontier orbital perspective. *ACS Catalysis*, 5(3), 1475-1488.
- [95] Szécsényi, Á., Li, G., Gascon, J., & Pidko, E. A. (2018). Unraveling reaction networks behind the catalytic oxidation of methane with H₂O₂ over a mixed-metal MIL-53(Al, Fe) MOF catalyst. *Chemical science*, 9(33), 6765-6773.
- [96] Liu, J., Ye, J., Li, Z., Otake, K. I., Liao, Y., Peters, A. W., ... & Hupp, J. T. (2018). Beyond the active site: tuning the activity and selectivity of a metal–organic framework-supported Ni catalyst for ethylene dimerization. *J. Am. Chem. Soc.*, 140(36), 11174-11178.
- [97] Zhao, W., Shi, Y., Jiang, Y., Zhang, X., Long, C., An, P., ... & Tang, Z. (2021). Fe-O Clusters Anchored on Nodes of Metal-Organic Frameworks for Direct Methane Oxidation. *Angew. Chem., Int. Ed.*, 60(11), 5811-5815.
- [98] Katz, M. J., Brown, Z. J., Colón, Y. J., Siu, P. W., Scheidt, K. A., Snurr, R. Q., ... & Farha, O. K. (2013). A facile synthesis of UiO-66, UiO-67 and their derivatives. *Chemical Communications*, 49(82), 9449-9451.
- [99] Pędziwiatr, P. (2018). Decomposition of hydrogen peroxide-kinetics and review of chosen catalysts. *Acta Innovations*, (26), 45-52.
- [100] Chen, R., Chen, J., Zhang, J., & Wan, X. (2018). Combination of Tetrabutylammonium Iodide (TBAI) with tert-Butyl Hydroperoxide (TBHP): An Efficient Transition-Metal-Free System to Construct Various Chemical Bonds. *The Chemical Record*, 18(9), 1292-1305.
- [101] Yuan, Q., Deng, W., Zhang, Q., & Wang, Y. (2007). Osmium-catalyzed selective oxidations of methane and ethane with hydrogen peroxide in aqueous medium. *Advanced Synthesis & Catalysis*, 349(7), 1199-1209.
- [102] Xiao, Y. S., Chen, L. Y., Lu, R. X., & Tang, C. Q. (2015). Selective oxidation of methane to methanol with organic oxidants catalyzed by iodine in non-aqueous acetic acid medium. In *Applied Mechanics and Materials (Vol. 723, pp. 624-628)*. Trans Tech Publications Ltd.
- [103] Borade, R., Sayari, A., Adnot, A., & Kaliaguine, S. (1990). Characterization of acidity in ZSM-5 zeolites: an X-ray photoelectron and IR spectroscopy study. *Journal of Physical Chemistry*, 94(15), 5989-5994.
- [104] Marturano, P., Drozdová, L., Kogelbauer, A., & Prins, R. (2000). Fe/ZSM-5 prepared by sublimation of FeCl₃: the structure of the Fe species as determined by IR, 27Al MAS NMR, and EXAFS spectroscopy. *Journal of Catalysis*, 192(1), 236-247.
- [105] Zhu, K., Liang, S., Cui, X., Huang, R., Wan, N., Hua, L., ... & Deng, D. (2021). Highly efficient conversion of methane to formic acid under mild conditions at ZSM-5-confined Fe-sites. *Nano Energy*, 82, 105718.
- [106] Winkler, M., Schnierle, M., Ehrlich, F., Mehnert, K. I., Hunger, D., Sheveleva, A. M., ... & van Slageren, J. (2021). Electronic structure of a diiron complex: a multitechnique experimental study of [(dppf) Fe (CO)₃]⁺⁰. *Inorganic Chemistry*, 60(5), 2856-2865.

- [107] Dinh, K. T.; Sullivan, M. M.; Serna, P.; Meyer, R. J.; Dincă, M.; Román-Leshkov, Y. Viewpoint on the Partial Oxidation of Methane to Methanol Using Cu- and Fe-Exchanged Zeolites. *ACS Catalysis*, 2018, 8, 8306–8313.
- [108] Rosen, A. S., Notestein, J. M., & Snurr, R. Q. (2019). Structure–Activity Relationships That Identify Metal–Organic Framework Catalysts for Methane Activation. *ACS Catalysis*, 9(4), 3576–3587.
- [109] Gaab, M., Trukhan, N., Maurer, S., Gummaraju, R., & Müller, U. (2012). The progression of Al-based metal-organic frameworks—From academic research to industrial production and applications. *Microporous and mesoporous materials*, 157, 131–136.
- [110] Reinsch, H., van der Veen, M. A., Gil, B., Marszalek, B., Verbiest, T., De Vos, D., & Stock, N. (2013). Structures, sorption characteristics, and nonlinear optical properties of a new series of highly stable aluminum MOFs. *Chemistry of Materials*, 25(1), 17–26.
- [111] Fei, H., & Cohen, S. M. (2015). Metalation of a thiocatechol-functionalized Zr (IV)-based metal–organic framework for selective C–H functionalization. *J. Am. Chem. Soc.*, 137(6), 2191–2194.
- [112] Karlin, K. D. (1993). Metalloenzymes, structural motifs, and inorganic models. *Science*, 261(5122), 701–708.
- [113] Shade, D., Marszalek, B., & Walton, K. S. (2021). Structural similarity, synthesis, and adsorption properties of aluminum-based metal-organic frameworks. *Adsorption*, 27(2), 227–236.
- [114] Xiao, D. J., Bloch, E. D., Mason, J. A., Queen, W. L., Hudson, M. R., Planas, N., ... & Long, J. R. (2014). Oxidation of ethane to ethanol by N₂O in a metal–organic framework with coordinatively unsaturated iron (II) sites. *Nature chemistry*, 6(7), 590–595.
- [115] Rosi, N. L., Kim, J., Eddaoudi, M., Chen, B., O'Keeffe, M., & Yaghi, O. M. (2005). Rod packings and metal–organic frameworks constructed from rod-shaped secondary building units. *J. Am. Chem. Soc.*, 127(5), 1504–1518.
- [116] Yuan, K., Song, T., Wang, D., Zou, Y., Li, J., Zhang, X., ... & Hu, W. (2018). Bimetal–organic frameworks for functionality optimization: MnFe-MOF-74 as a stable and efficient catalyst for the epoxidation of alkenes with H₂O₂. *Nanoscale*, 10(4), 1591–1597.
- [117] Liu, Q., Cong, H., & Deng, H. (2016). Deciphering the spatial arrangement of metals and correlation to reactivity in multivariate metal–organic frameworks. *J. Am. Chem. Soc.*, 138(42), 13822–13825.
- [118] Loiseau, T., Lecroq, L., Volkringer, C., Marrot, J., Férey, G., Haouas, M., Taulelle, F., Bourrelly, S., Llewellyn, P. L., & Latroche, M. (2006). MIL-96, a porous aluminum trimesate 3D structure constructed from a hexagonal network of 18-membered rings and μ_3 -oxo-centered trinuclear units. *J. Am. Chem. Soc.*, 128(31), 10223–10230.
- [119] Férey, G., Serre, C., Mellot-Draznieks, C., Millange, F., Surblé, S., Dutour, J., & Margiolaki, I. (2004). A hybrid solid with giant pores prepared by a combination of targeted chemistry, simulation, and powder diffraction. *Angew. Chem., Int. Ed.*, 43, 6296–6301.
- [120] Férey, G., Mellot-Draznieks, C., Serre, C., Millange, F., Dutour, J., Surblé, S., & Margiolaki, I. (2005). A chromium terephthalate-based solid with unusually large pore volumes and surface area. *Science*, 309(5743), 2040–2042.
- [121] Barthelet, K., Riou, D., & Férey, G. (2002). [V^{III}(H₂O)]₃O(O₂CC₆H₄CO₂)₃·(Cl, 9H₂O)(MIL-59): a rare example of vanadocarboxylate with a magnetically frustrated three-dimensional hybrid framework. *Chemical Communications*, (14), 1492–1493.
- [122] Serre, C. M. D. C., Mellot-Draznieks, C., Surblé, S., Audebrand, N., Filinchuk, Y., & Férey, G. (2007). Role of solvent-host interactions that lead to very large swelling of hybrid frameworks. *Science*, 315(5820), 1828–1831.
- [123] Horcajada, P., Surblé, S., Serre, C., Hong, D. Y., Seo, Y. K., Chang, J. S., Greneche, J. M., Margiolaki, I. & Férey, G. (2007). Synthesis and catalytic properties of MIL-100 (Fe), an iron (III) carboxylate with large pores. *Chemical Communications*, 27, 2820–2822.

- [124] Guesh, K., Caiuby, C. A. D., Mayoral, A., Díaz-García, M., Díaz, I., Sanchez-Sanchez, M. Sustainable Preparation of MIL-100(Fe) and Its Photocatalytic Behavior in the Degradation of Methyl Orange in Water. *Cryst. Growth Des.* 2017, 17, 1806-1813.
- [125] Yoon, J. W., Seo, Y. K., Hwang, Y. K., Chang, J. S., Leclerc, H., Wuttke, S., ... & Férey, G. (2010). Controlled reducibility of a metal–organic framework with coordinatively unsaturated sites for preferential gas sorption. *Angew. Chem., Int. Ed.*, 49(34), 5949-5952.
- [126] Simons, M. C., Vitillo, J. G., Babucci, M., Hoffman, A. S., Boubnov, A., Beauvais, M. L., ... & Bhan, A. (2019). Structure, Dynamics, and Reactivity for Light Alkane Oxidation of Fe (II) Sites Situated in the Nodes of a Metal-Organic Framework. *J. Am. Chem. Soc.*, 141(45), 18142-18151.
- [127] Hall, J. N., & Bollini, P. (2020). Low-Temperature, Ambient Pressure Oxidation of Methane to Methanol Over Every Tri-Iron Node in a Metal-Organic Framework Material. *Chemistry-A European Journal*, 26(70), 16639-16643.
- [128] Wang, J. H., Zhang, Y., Li, M., Yan, S., Li, D., & Zhang, X. M. (2017). Solvent-Assisted Metal Metathesis: A Highly Efficient and Versatile Route towards Synthetically Demanding Chromium Metal–Organic Frameworks. *Angew. Chem., Int. Ed.*, 56(23), 6478-6482.
- [129] Tilstam, U. (2012). Sulfolane: A versatile dipolar aprotic solvent. *Organic Process Research & Development*, 16(7), 1273-1278.
- [130] Drago, R. S., Wayland, B., & Carlson, R. L. (1963). Donor properties of sulfoxides, alkyl sulfites, and sulfones. *J. Am. Chem. Soc.*, 85(20), 3125-3128.
- [131] Balducci, L., Bianchi, D., Bortolo, R., D'Aloisio, R., Ricci, M., Tassinari, R., & Ungarelli, R. (2003). Direct oxidation of benzene to phenol with hydrogen peroxide over a modified titanium silicalite. *Angew. Chem., Int. Ed.*, 42, 4937-4940.
- [132] Xiao, P., Wang, Y., Nishitoba, T., Kondo, J. N., & Yokoi, T. (2019). Selective oxidation of methane to methanol with H₂O₂ over an Fe-MFI zeolite catalyst using sulfolane solvent. *Chemical Communications*, 55(20), 2896-2899.
- [133] Couck, S., Liu, Y. Y., Leus, K., Baron, G. V., Van der Voort, P., & Denayer, J. F. (2015). Gas phase adsorption of alkanes, alkenes and aromatics on the sulfone-DUT-5 Metal Organic Framework. *Microporous and Mesoporous Materials*, 206, 217-225.
- [134] Senkovska, I., Hoffmann, F., Fröba, M., Getzschmann, J., Böhlmann, W., & Kaskel, S. (2009). New highly porous aluminium based metal-organic frameworks: Al(OH)(ndc)(ndc= 2, 6-naphthalene dicarboxylate) and Al(OH)(bpdc)(bpdc= 4, 4'-biphenyl dicarboxylate). *Microporous and Mesoporous Materials*, 122(1-3), 93-98.
- [135] Cavka, J. H., Jakobsen, S., Olsbye, U., Guillou, N., Lamberti, C., Bordiga, S., & Lillerud, K. P. (2008). A new zirconium inorganic building brick forming metal organic frameworks with exceptional stability. *J. Am. Chem. Soc.*, 130(42), 13850-13851.
- [136] Manna, K., Ji, P., Lin, Z., Greene, F. X., Urban, A., Thacker, N. C., & Lin, W. (2016). Chemoselective single-site Earth-abundant metal catalysts at metal-organic framework nodes. *Nature communications*, 7(1), 1-11.
- [137] Nouar, F., Breeze, M. I., Campo, B. C., Vimont, A., Clet, G., Daturi, M., ... & Serre, C. (2015). Tuning the properties of the UiO-66 metal organic framework by Ce substitution. *Chemical Communications*, 51(77), 14458-14461.
- [138] Zecchina, A., Rivallan, M., Berlier, G., Lamberti, C. & Richiardi, G. (2007). Structure and nuclearity of active sites in Fe-zeolites: comparison with iron sites in enzymes and homogeneous catalysts. *Phys. Chem. Chem. Phys.* 9, 3483-3499.
- [139] Park, K. S., Ni, Z., Côté, A. P., Choi, J. Y., Huang, R., Uribe-Romo, F. J., ... & Yaghi, O. M. (2006). Exceptional chemical and thermal stability of zeolitic imidazolate frameworks. *Proceedings of the National Academy of Sciences*, 103(27), 10186-10191.
- [140] Chaudhari, A. K., Ryder, M. R., & Tan, J. C. (2016). Photonic hybrid crystals constructed from in situ host–guest nanoconfinement of a light-emitting complex in metal–organic framework pores. *Nanoscale*, 8(12), 6851-6859.

- [141] Cravillon, J., Nayuk, R., Springer, S., Feldhoff, A., Huber, K., & Wiebcke, M. (2011). Controlling zeolitic imidazolate framework nano- and microcrystal formation: insight into crystal growth by time-resolved in situ static light scattering. *Chemistry of Materials*, 23(8), 2130-2141.
- [142] Huang, X. C., Lin, Y. Y., Zhang, J. P., & Chen, X. M. (2006). Ligand-directed strategy for zeolite-type metal-organic frameworks: zinc(II)imidazolates with unusual zeolitic topologies. *Angew. Chem., Int. Ed.*, 45(10), 1557-1559.
- [143] Liu, S., Wang, J., & Yu, J. (2016). ZIF-8 derived bimodal carbon modified ZnO photocatalysts with enhanced photocatalytic CO₂ reduction performance. *RSC advances*, 6(65), 59998-60006.
- [144] Kuo, C. H., Tang, Y., Chou, L. Y., Sneed, B. T., Brodsky, C. N., Zhao, Z., & Tsung, C. K. (2012). Yolk-shell nanocrystal@ZIF-8 nanostructures for gas-phase heterogeneous catalysis with selectivity control. *J. Am. Chem. Soc.*, 134(35), 14345-14348.
- [145] Schoedel, A., & Zaworotko, M. J. (2014). [M₃(μ₃-O)(O₂CR)₆] and related trigonal prisms: versatile molecular building blocks for crystal engineering of metal-organic material platforms. *Chemical Science*, 5(4), 1269-1282.
- [146] Horcajada, P., Serre, C., Vallet-Regí, M., Sebban, M., Taulelle, F., & Férey, G. (2006). Metal-organic frameworks as efficient materials for drug delivery. *Angew. Chem., Int. Ed.*, 45, 5974-5978.
- [147] Sonnauer, A., Hoffmann, F., Fröba, M., Kienle, L., Duppel, V., Thommes, M., ... & Stock, N. (2009). Giant pores in a chromium 2, 6-naphthalenedicarboxylate open-framework structure with MIL-101 topology. *Angew. Chem. Int. Ed.*, 48, 3791-3794.
- [148] Taylor-Pashow, K. M., Della Rocca, J., Xie, Z., Tran, S., & Lin, W. (2009). Postsynthetic modifications of iron-carboxylate nanoscale metal-organic frameworks for imaging and drug delivery. *J. Am. Chem. Soc.*, 131(40), 14261-14263.
- [149] (a) Feng, D., Wang, K., Wei, Z., Chen, Y. P., Simon, C. M., Arvapally, R. K., ... & Zhou, H. C. (2014). Kinetically tuned dimensional augmentation as a versatile synthetic route towards robust metal-organic frameworks. *Nature communications*, 5(1), 1-9.
- [150] Peng, L., Asgari, M., Mievilte, P., Schouwink, P., Bulut, S., Sun, D. T., ... & Queen, W. L. (2017). Using predefined M₃(μ₃-O) clusters as building blocks for an isostructural series of metal-organic frameworks. *ACS applied materials & interfaces*, 9(28), 23957-23966.
- [151] Dhakshinamoorthy, A., Li, Z., & Garcia, H. (2018). Catalysis and photocatalysis by metal organic frameworks. *Chemical Society Reviews*, 47(22), 8134-8172.
- [152] Barona, M., Ahn, S., Morris, W., Hoover, W., Notestein, J. M., Farha, O. K., & Snurr, R. Q. (2019). Computational Predictions and Experimental Validation of Alkane Oxidative Dehydrogenation by Fe₂M MOF Nodes. *ACS Catalysis*, 10(2), 1460-1469.
- [153] Guillerme, V., Gross, S., Serre, C., Devic, T., Bauer, M., & Férey, G. (2010). A zirconium methacrylate oxocluster as precursor for the low-temperature synthesis of porous zirconium (IV) dicarboxylates. *Chemical communications*, 46(5), 767-769.
- [154] Pérez-Ramírez, J., Groen, J. C., Brückner, A., Kumar, M. S., Bentrup, U., Debbagh, M. N., & Villaescusa, L. A. (2005). Evolution of isomorphously substituted iron zeolites during activation: comparison of Fe-beta and Fe-ZSM-5. *Journal of Catalysis*, 232(2), 318-334.
- [155] Grundner, S., Luo, W., Sanchez-Sanchez, M., & Lercher, J. A. (2016). Synthesis of single-site copper catalysts for methane partial oxidation. *Chemical Communications*, 52(12), 2553-2556.
- [156] Chow, Y. K., Dummer, N. F., Carter, J. H., Williams, C., Shaw, G., Willock, D. J., ... & Hutchings, G. J. (2018). Investigating the influence of acid sites in continuous methane oxidation with N₂O over Fe/MFI zeolites. *Catalysis Science & Technology*, 8(1), 154-163.
- [157] Qi, G., Gatt, J. E., & Yang, R. T. (2004). Selective catalytic oxidation (SCO) of ammonia to nitrogen over Fe-exchanged zeolites prepared by sublimation of FeCl₃. *Journal of Catalysis*, 226(1), 120-128.

- [158] Schwidder, M., Kumar, M. S., Klementiev, K., Pohl, M. M., Brückner, A., & Grünert, W. (2005). Selective reduction of NO with Fe-ZSM-5 catalysts of low Fe content: I. Relations between active site structure and catalytic performance. *Journal of Catalysis*, 231(2), 314-330.
- [159] Kumar, M. S., Schwidder, M., Grünert, W., Bentrup, U., & Brückner, A. (2006). Selective reduction of NO with Fe-ZSM-5 catalysts of low Fe content: Part II. Assessing the function of different Fe sites by spectroscopic in situ studies. *Journal of Catalysis*, 239(1), 173-186.
- [160] Hensen, E. J. M., Zhu, Q., Hendrix, M. M. R. M., Overweg, A. R., Kooyman, P. J., Sychev, M. V., & Van Santen, R. A. (2004). Effect of high-temperature treatment on Fe/ZSM-5 prepared by chemical vapor deposition of FeCl₃: I. Physicochemical characterization. *Journal of Catalysis*, 221(2), 560-574.
- [161] P. F. Xie, Y. J. Luo, Z. Ma, C. Y. Huang, C. X. Miao, Y. H. Yue, W. M. Hua, Z. Gao, Catalytic decomposition of N₂O over Fe-ZSM-11 catalysts prepared by different methods: Nature of active Fe species, *Journal of Catalysis*, 2015, 330, 311-322.
- [162] Choi, S. H., Wood, B. R., Ryder, J. A., & Bell, A. T. (2003). X-ray absorption fine structure characterization of the local structure of Fe in Fe-ZSM-5. *The Journal of Physical Chemistry B*, 107(43), 11843-11851.
- [163] Lee, S. J.; McCormick, M. S.; Lippard, S. J.; Cho, U. S. (2013) Control of substrate access to the active site in methane monooxygenase. *Nature*, 494, 380-384.
- [164] Huang, G., Yang, Q., Xu, Q., Yu, S. H., & Jiang, H. L. (2016). Polydimethylsiloxane coating for a palladium/MOF composite: highly improved catalytic performance by surface hydrophobization. *Angew. Chem., Int. Ed.*, 55, 7379-7383.
- [165] Zhang, W., Hu, Y., Ge, J., Jiang, H. L., & Yu, S. H. (2014). A facile and general coating approach to moisture/water-resistant metal-organic frameworks with intact porosity. *J. Am. Chem. Soc.*, 136(49), 16978-16981.
- [166] Yuan, J., Liu, X., Akbulut, O., Hu, J., Suib, S. L., Kong, J., & Stellacci, F. (2008). Superwetting nanowire membranes for selective absorption. *Nature nanotechnology*, 3(6), 332-336.
- [167] Tao, Y., Kanoh, H., Abrams, L., & Kaneko, K. (2006). Mesopore-modified zeolites: preparation, characterization, and applications. *Chemical reviews*, 106(3), 896-910.
- [168] <https://europe.iza-structure.org/IZA-SC/framework.php?STC=MFI>
- [169] Choi, M., Na, K., Kim, J., Sakamoto, Y., Terasaki, O., & Ryoo, R. (2009). Stable single-unit-cell nanosheets of zeolite MFI as active and long-lived catalysts. *Nature*, 461(7261), 246-249.
- [170] Na, K., Choi, M., Park, W., Sakamoto, Y., Terasaki, O., & Ryoo, R. (2010). Pillared MFI zeolite nanosheets of a single-unit-cell thickness. *J. Am. Chem. Soc.*, 132(12), 4169-4177.
- [171] Emdadi, L., Tran, D. T., Zhang, J., Wu, W., Song, H., Gan, Q., & Liu, D. (2017). Synthesis of titanosilicate pillared MFI zeolite as an efficient photocatalyst. *RSC advances*, 7(6), 3249-3256.
- [172] Maheshwari, S., Jordan, E., Kumar, S., Bates, F. S., Penn, R. L., Shantz, D. F., & Tsapatsis, M. (2008). Layer structure preservation during swelling, pillaring, and exfoliation of a zeolite precursor. *J. Am. Chem. Soc.*, 130(4), 1507-1516.
- [173] Rodríguez-González, L., Hermes, F., Bertmer, M., Rodríguez-Castellón, E., Jiménez-López, A., & Simon, U. (2007). The acid properties of H-ZSM-5 as studied by NH₃-TPD and 27Al-MAS-NMR spectroscopy. *Applied Catalysis A: General*, 328(2), 174-182.
- [174] Triantafyllidis, K. S., Nalbandian, L., Trikalitis, P. N., Ladavos, A. K., Mavromoustakos, T., & Nicolaidis, C. P. (2004). Structural, compositional and acidic characteristics of nanosized amorphous or partially crystalline ZSM-5 zeolite-based materials. *Microporous and Mesoporous Materials*, 75(1-2), 89-100.
- [175] Le Van Mao, R., Le, T. S., Fairbairn, M., Muntasar, A., Xiao, S., & Denes, G. (1999). ZSM-5 zeolite with enhanced acidic properties. *Applied Catalysis A: General*, 185(1), 41-52.
- [176] Sun, S., Barnes, A. J., Gong, X., Lewis, R. J., Dummer, N. F., Bere, T., ... & Hutchings, G. J. (2021). Lanthanum modified Fe-ZSM-5 zeolites for selective methane oxidation with H₂O₂. *Catalysis Science & Technology*, 11(24), 8052-8064.

- [177] Gong, T., Zhang, X., Bai, T., Zhang, Q., Tao, L., Qi, M., ... & Zhang, L. (2012). Coupling conversion of methanol and C4 hydrocarbon to propylene on La-modified HZSM-5 zeolite catalysts. *Industrial & engineering chemistry research*, 51(42), 13589-13598.
- [178] Li, D., Bui, P., Zhao, H. Y., Oyama, S. T., Dou, T., & Shen, Z. H. (2012). Rake mechanism for the deoxygenation of ethanol over a supported Ni₂P/SiO₂ catalyst. *Journal of catalysis*, 290, 1-12.